

Journal of
Mechanics of
Materials and Structures

Volume 1, N° 7

September 2006



mathematical sciences publishers

JOURNAL OF MECHANICS OF MATERIALS AND STRUCTURES

<http://www.jomms.org>

EDITOR-IN-CHIEF Charles R. Steele

ASSOCIATE EDITOR Marie-Louise Steele
Division of Mechanics and Computation
Stanford University
Stanford, CA 94305
USA

SENIOR CONSULTING EDITOR Georg Herrmann
Ortstrasse 7
CH-7270 Davos Platz
Switzerland

BOARD OF EDITORS

D. BIGONI University of Trento, Italy
H. D. BUI École Polytechnique, France
J. P. CARTER University of Sydney, Australia
R. M. CHRISTENSEN Stanford University, U.S.A.
G. M. L. GLADWELL University of Waterloo, Canada
D. H. HODGES Georgia Institute of Technology, U.S.A.
J. HUTCHINSON Harvard University, U.S.A.
C. HWU National Cheng Kung University, R.O. China
IWONA JASIUŁ University of Illinois at Urbana-Champaign
B. L. KARIHALOO University of Wales, U.K.
Y. Y. KIM Seoul National University, Republic of Korea
Z. MROZ Academy of Science, Poland
D. PAMPLONA Universidade Católica do Rio de Janeiro, Brazil
M. B. RUBIN Technion, Haifa, Israel
Y. SHINDO Tohoku University, Japan
A. N. SHUPIKOV Ukrainian Academy of Sciences, Ukraine
T. TARNAI University Budapest, Hungary
F. Y. M. WAN University of California, Irvine, U.S.A.
P. WRIGGERS Universität Hannover, Germany
W. YANG Tsinghua University, P.R. China
F. ZIEGLER Technische Universität Wien, Austria

PRODUCTION


PAULO NEY DE SOUZA Production Manager
SHEILA NEWBERY Senior Production Editor
SILVIO LEVY Scientific Editor

See inside back cover or <http://www.jomms.org> for submission guidelines.

JoMMS (ISSN 1559-3959) is published in 10 issues a year. The subscription price for 2006 is US \$400/year for the electronic version, and \$500/year for print and electronic. Subscriptions, requests for back issues, and changes of address should be sent to Mathematical Sciences Publishers, Department of Mathematics, University of California, Berkeley, CA 94720-3840.

JoMMS peer review and production are managed by EditFLOW™ from Mathematical Sciences Publishers.

PUBLISHED BY

 **mathematical sciences publishers**
<http://www.mathscipub.org>

A NON-PROFIT CORPORATION

Typeset in L^AT_EX

©Copyright 2006. Journal of Mechanics of Materials and Structures. All rights reserved.

ANTIPLANE DEFORMATION OF ORTHOTROPIC STRIPS WITH MULTIPLE DEFECTS

REZA TEYMORI FAAL, SHAHRIAR J. FARIBORZ AND HAMID REZA DAGHYANI

Stress analysis is carried out in an orthotropic strip containing a Volterra-type screw dislocation. The distributed dislocation technique is employed to obtain integral equations for a strip weakened by cracks and cavities under antiplane traction. These equations are of Cauchy singular kind, which are solved numerically by generalizing a numerical method available in the literature. Several examples are solved to demonstrate the validity and applicability of the procedure.

1. Introduction

In composite materials, defects in the form of cracks and cavities generate regions of high stress gradient. These regions are the primary locus of failure in structures, even under moderate applied load. Therefore, stress analysis in the vicinity of defects is imperative as the first stage of the design process.

Stress analysis in a strip with cracks under antiplane deformation has been investigated frequently. Here, we review some recent pertinent articles. Zhou et al. [1998] showed that in the vicinity of two collinear cracks perpendicular to the edges of an isotropic strip, the cracks were symmetrical with respect to the centerline of the strip and subjected to antiplane traction. Li [2003] obtained a closed-form solution for orthotropic strips. Stress analysis in an isotropic strip weakened by two collinear cracks situated on the centerline under antiplane shear was carried out by [Zhou and Ma 1999]. In the above articles, the application of boundary conditions resulted in a set of integral equations which are solved by the Schmidt's method. Wu and Dzenis [2002] obtained closed-form solutions for mode III stress intensity factors for an interfacial edge crack between two bonded semi-infinite dissimilar elastic strips. Li [2005] considered an interfacial crack between two bonded dissimilar semi-infinite orthotropic strips where the crack surface was under antiplane traction. Closed form stress intensity factors were obtained for a strip with either clamped or traction-free boundaries.

In this study, we perform stress analysis in an orthotropic strip weakened by cracks and cavities under antiplane deformation. We obtain the solution of Volterra-type screw dislocation by means of Fourier transformation, and use the solution to derive integral equations for cracks. Cavities are considered as closed curved cracks without singularity. The integral equations are solved numerically for the dislocation density function by generalizing the method developed by [Erdogan et al. 1973] to take into account cavities, embedded cracks, and edge cracks. Finally, we obtain the stress intensity factor for cracks, and the hoop stress for cavities for several examples.

We regret to inform that Hamid Reza Daghyani passed away in 2006.

Keywords: antiplane deformation, orthotropic strip, multiple defects, Cauchy-type singularity.

2. Strip with screw dislocation

The distributed dislocation technique is an efficient means of treating multiple curved cracks with smooth geometries. However, determining stress fields due to a single dislocation in the region has been a major obstacle to the utilization of this method. We now take up this task for an orthotropic strip containing a screw dislocation. We consider an orthotropic elastic strip with finite thickness h in the y -direction and extended infinitely in the x -direction. The x -axis is situated at the distance h_1 below the upper edge of the strip. The only nonzero displacement component under antiplane deformation is the out of plane component $w(x, y)$. Consequently, the constitutive relationships are

$$\sigma_{zy} = G_{zy} \frac{\partial w}{\partial y}, \quad (1)$$

$$\sigma_{zx} = G_{zx} \frac{\partial w}{\partial x}. \quad (2)$$

In the above equalities, G_{zx} and G_{zy} are the orthotropic shear moduli of elasticity of material. The equilibrium equations $\sigma_{ij,j} = 0$, in view of Equations (1)–(2), reduce to

$$G_{zx} \frac{\partial^2 w}{\partial x^2} + G_{zy} \frac{\partial^2 w}{\partial y^2} = 0. \quad (3)$$

The traction-free condition on the strip edges implies that

$$\sigma_{zy}(x, h_1) = 0, \quad \sigma_{zy}(x, h_1 - h) = 0. \quad (4)$$

A Volterra-type screw dislocation with Burgers vector δ is situated at the origin of coordinates with the dislocation line $x = 0, y > 0$. The conditions representing the dislocation are

$$\lim_{|x| \rightarrow \infty} w = 0, \quad (5)$$

$$w(0^+, y) - w(0^-, y) = \delta H(y), \quad (6)$$

where $H(y)$ is the Heaviside step function. The conditions of continuity and self-equilibrium of stress in the strip containing dislocation imply that

$$w(x, 0^-) = w(x, 0^+), \quad \sigma_{zy}(x, 0^-) = \sigma_{zy}(x, 0^+). \quad (7)$$

Since the problem is symmetric with respect to the y -axis, we may consider only the region $x > 0$. Equation (3) is solved by Fourier sine transformation, which for a sufficiently regular function $f(x)$ is defined as

$$F(\lambda) = \int_0^\infty f(x) \sin \lambda x \, dx. \quad (8)$$

The inversion of the Fourier sine transform yields

$$f(x) = \frac{2}{\pi} \int_0^\infty F(\lambda) \sin \lambda x \, d\lambda. \quad (9)$$

The application of Equation (8) to Equation (3) with the aid of Equation (5) leads to a second order ordinary differential equation, in each region $0 \leq y \leq h_1$ and $h_1 - h \leq y \leq 0$. The solution satisfying

Equation (6) is readily known, namely

$$W(\lambda, y) = \begin{cases} a_1 e^{\lambda G y} + b_1 e^{-\lambda G y} + \frac{\delta}{2\lambda}, & 0 \leq y \leq h_1, \\ a_2 e^{\lambda G y} + b_2 e^{-\lambda G y}, & h_1 - h \leq y \leq 0, \end{cases} \tag{10}$$

where $G = \sqrt{G_{zx}/G_{zy}}$. The application of conditions (4) and (7) to Equation (10) results in

$$a_1 = \frac{\delta e^{-2\lambda G h_1} (e^{2\lambda G h} - e^{2\lambda G h_1})}{4\lambda(1 - e^{2\lambda G h})}, \quad b_1 = \frac{\delta (e^{2\lambda G h} - e^{2\lambda G h_1})}{4\lambda(1 - e^{2\lambda G h})}, \tag{11}$$

$$a_2 = \frac{\delta e^{2\lambda G h} (e^{-2\lambda G h_1} - 1)}{4\lambda(1 - e^{2\lambda G h})}, \quad b_2 = \frac{\delta (1 - e^{2\lambda G h_1})}{4\lambda(1 - e^{2\lambda G h})}. \tag{12}$$

The displacement field in view of Equations (9)–(12) becomes

$$w(x, y) = \frac{\delta}{2\pi} \int_0^\infty \left(\frac{(e^{2\lambda G h} - e^{2\lambda G h_1})(e^{\lambda G (y-2h_1)} + e^{-\lambda G y})}{\lambda(1 - e^{2\lambda G h})} + \frac{2}{\lambda} \right) \sin \lambda x \, d\lambda, \quad 0 \leq y \leq h_1, \tag{13}$$

$$w(x, y) = \frac{\delta}{2\pi} \int_0^\infty \left(\frac{(e^{-2\lambda G h_1} - 1)(e^{\lambda G (y+2h)} + e^{-\lambda G (y-2h_1)})}{\lambda(1 - e^{2\lambda G h})} \right) \sin \lambda x \, d\lambda, \quad h_1 - h \leq y \leq 0. \tag{14}$$

Note that the rigid body motion of strip, that is, the unboundedness of the integrand in Equation (13) as $\lambda \rightarrow \infty$, may cause difficulties in carrying out the above integrations. Consequently, it is expedient to obtain the displacement field from the stress components instead. Substituting Equations (13)–(14) into

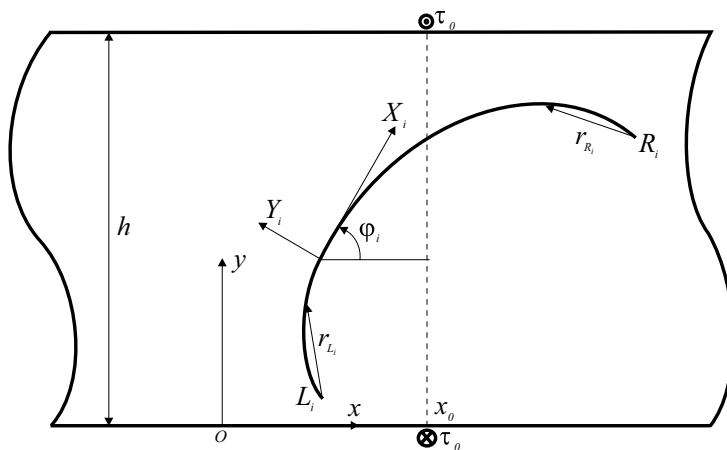


Figure 1. Schematic view of the strip with a curved crack.

Equations (1)–(2) yields

$$\sigma_{zy}(x, y) = \frac{\delta G G_{zy}}{2\pi} \int_0^\infty \frac{(e^{2\lambda Gh} - e^{2\lambda Gh_1})(e^{\lambda G(y-2h_1)} - e^{-\lambda Gy})}{1 - e^{2\lambda Gh}} \sin \lambda x \, d\lambda, \quad 0 \leq y \leq h_1, \quad (15)$$

$$\sigma_{zx}(x, y) = \frac{\delta G_{zx}}{2\pi} \int_0^\infty \frac{(e^{2\lambda Gh} - e^{2\lambda Gh_1})(e^{\lambda G(y-2h_1)} + e^{-\lambda Gy})}{1 - e^{2\lambda Gh}} \cos \lambda x \, d\lambda, \quad 0 \leq y \leq h_1, \quad (16)$$

$$\sigma_{zy}(x, y) = \frac{\delta G G_{zy}}{2\pi} \int_0^\infty \frac{(e^{-2\lambda Gh_1} - 1)(e^{\lambda G(y+2h)} - e^{-\lambda G(y-2h_1)})}{1 - e^{2\lambda Gh}} \sin \lambda x \, d\lambda, \quad h_1 - h \leq y \leq 0, \quad (17)$$

$$\sigma_{zx}(x, y) = \frac{\delta G_{zx}}{2\pi} \int_0^\infty \frac{(e^{-2\lambda Gh_1} - 1)(e^{\lambda G(y+2h)} + e^{-\lambda G(y-2h_1)})}{1 - e^{2\lambda Gh}} \cos \lambda x \, d\lambda, \quad h_1 - h \leq y \leq 0. \quad (18)$$

The integrals in Equations (15)–(18) can be evaluated employing contour integration and the residue theorem. The stress components are obtained in series form which are summed, leading, in the whole strip region, to

$$\sigma_{zy}(x, y) = \frac{\delta G_{zy} \sinh \kappa x}{4h} \left(\frac{1}{\cosh \kappa x - \cos \kappa G y} - \frac{1}{\cosh \kappa x - \cos \kappa G (y - 2h_1)} \right), \quad (19)$$

$$\sigma_{zx}(x, y) = \frac{\delta G G_{zy}}{4h} \left(\frac{\sin \kappa (y - 2h_1)}{\cosh \kappa x - \cos \kappa G (y - 2h_1)} - \frac{\sin \kappa y}{\cosh \kappa x - \cos \kappa G y} \right), \quad (20)$$

where $\kappa = \pi/Gh$. Substituting the stress component σ_{zy} into Equation (1), integrating the resultant expression with respect to y , and ignoring the rigid body displacement, the displacement field becomes

$$w(x, y) = \frac{\delta}{2\pi} \left(\tan^{-1} \left(\tan \frac{\kappa G y}{2} \coth \frac{\kappa x}{2} \right) - \tan^{-1} \left(\tan \frac{\kappa G (y - 2h_1)}{2} \coth \frac{\kappa x}{2} \right) \right). \quad (21)$$

The stress components (19)–(20) readily satisfy the boundary conditions in Equation (4). Furthermore, choosing the proper branch of the multiple-valued function which is the first term in the right-hand side of Equation (21), it is easy to verify that Equation (6) holds. In the particular case of screw dislocation in the isotropic half-plane, letting $G = 1$ and $h_2 \rightarrow \infty$ in Equations (19)–(21), the displacement and stress fields become

$$w(x, y) = \frac{\delta}{2\pi} \left(\tan^{-1} \left(\frac{y}{x} \right) - \tan^{-1} \left(\frac{y - 2h_1}{x} \right) \right),$$

$$\left\{ \begin{matrix} \sigma_{zx}(x, y) \\ \sigma_{zy}(x, y) \end{matrix} \right\} = \frac{\delta}{2\pi} \mu \left(\frac{1}{(y - 2h_1)^2 + x^2} \begin{Bmatrix} y - 2h_1 \\ -x \end{Bmatrix} - \frac{1}{y^2 + x^2} \begin{Bmatrix} y \\ -x \end{Bmatrix} \right), \quad \text{for } -\infty < y \leq h_1,$$

where μ is the shear modulus of elasticity of the isotropic half-plane. The above solutions are identical to those in [Weertman and Weertman 1992].

To investigate the behavior of stress fields at the dislocation position from Equation (19) we may observe that

$$\tau_{zy}(x, 0) \sim \frac{\delta G G_{zy}}{2\pi x} \quad \text{as } x \rightarrow 0.$$

Note that the above Cauchy-type singularity at the dislocation location is a distinct feature of stress fields in the two-dimensional regions containing a dislocation.

3. Orthotropic strip with multiple cracks and cavities

The dislocation solutions accomplished in Section 2 can be used to analyze strips with multiple cracks and cavities. The cavities are considered as closed-curve cracks without singularity. We consider a strip weakened by M cavities, N_1 embedded cracks, and N_2 edge cracks. Henceforth, we designate cavities, embedded cracks, and edge cracks with the respective subscripts

$$\begin{aligned} i &\in \{1, 2, \dots, M\}, \\ j &\in \{M + 1, M + 2, \dots, M + N_1\}, \\ k &\in \{M + N_1 + 1, M + N_1 + 2, \dots, N\}, \end{aligned}$$

where $N = M + N_1 + N_2$ and represents the total number of defects. The stress components on the local coordinates X_i - Y_i as seen in Figure 1 located on the surface of i -th crack in terms of stress components in x - y coordinates become

$$\sigma_{zY_i} = \sigma_{zy} \cos \varphi_i - \sigma_{zx} \sin \varphi_i, \tag{22}$$

$$\sigma_{zX_i} = \sigma_{zx} \cos \varphi_i + \sigma_{zy} \sin \varphi_i, \tag{23}$$

where φ_i is the angle between X_i and x axes. Suppose dislocations with unknown density B_{zj} are distributed on the infinitesimal segment $d\lambda_j$ located at a point with coordinates (x_j, y_j) on the surface of the j -th crack. The traction on the surface of i -th crack, due to the above distribution of dislocations, and using Equations (19), (20), (22), and (23), becomes

$$\begin{aligned} \sigma_{zY_i}(x_i, y_i) = \frac{G_{zy} B_{zj} d\lambda_j}{4h} &\left(\frac{\cos \varphi_i \sinh \kappa(x_i - x_j) + G \sin \varphi_i \sin \kappa G(y_i - y_j)}{\cosh \kappa(x_i - x_j) - \cos \kappa G(y_i - y_j)} \right. \\ &\left. - \frac{\cos \varphi_i \sinh \kappa(x_i - x_j) + G \sin \varphi_i \sin \kappa G(y_i + y_j - 2h)}{\cosh \kappa(x_i - x_j) - \cos \kappa G(y_i + y_j - 2h)} \right). \end{aligned} \tag{24}$$

Covering crack surfaces by dislocations, the principle of superposition can be invoked to obtain traction on a crack surface. We can thus integrate Equation (24) on the crack surfaces and superimpose the resultant tractions. Integration of Equation (24) is facilitated by describing crack configurations in parametric form $x_i = x_i(s)$, $y_i = y_i(s)$, for $i = 1, 2, \dots, N$, and where $-1 \leq s \leq 1$. The traction on the surface of the i -th crack yields

$$\sigma_{zY_i}(x_i(s), y_i(s)) = \sum_{j=1}^N \int_{-1}^1 b_{zj}(t) k_{ij}(s, t) dt, \tag{25}$$

where $b_{zj}(t)$ is the dislocation density on the nondimensionalized length $-1 \leq t \leq 1$. From Equation (24), the kernel $k_{ij}(s, t)$ is

$$\begin{aligned} k_{ij}(s, t) = \frac{G_{zy} \sqrt{(x'_j(t))^2 + (y'_j(t))^2}}{4h} &\left(\frac{\cos \varphi_i(s) \sinh \kappa(x_i(s) - x_j(t)) + G \sin \varphi_i(s) \sin \kappa G(y_i(s) - y_j(t))}{\cosh \kappa(x_i(s) - x_j(t)) - \cos \kappa G(y_i(s) - y_j(t))} \right. \\ &\left. - \frac{\cos \varphi_i(s) \sinh \kappa(x_i(s) - x_j(t)) + G \sin \varphi_i(s) \sin \kappa G(y_i(s) + y_j(t) - 2h)}{\cosh \kappa(x_i(s) - x_j(t)) - \cos \kappa G(y_i(s) + y_j(t) - 2h)} \right). \end{aligned} \tag{26}$$

Substituting the crack angle $\varphi_i(s) = \tan^{-1}(y'_i(s)/x'_i(s))$ as seen in [Figure 1](#), into [Equation \(26\)](#), the kernel is recast in the more convenient form

$$k_{ij}(s, t) = \frac{G_{zy}}{4h} \sqrt{\frac{(x'_j(t))^2 + (y'_j(t))^2}{(x'_i(s))^2 + (y'_i(s))^2}} \left(\frac{x'_i(s) \sinh \kappa(x_i(s) - x_j(t)) + G y'_i(s) \sin \kappa G(y_i(s) - y_j(t))}{\cosh \kappa(x_i(s) - x_j(t)) - \cos \kappa G(y_i(s) - y_j(t))} - \frac{x'_i(s) \sinh \kappa(x_i(s) - x_j(t)) + G y'_i(s) \sin \kappa G(y_i(s) + y_j(t) - 2h)}{\cosh \kappa(x_i(s) - x_j(t)) - \cos \kappa G(y_i(s) + y_j(t) - 2h)} \right). \quad (27)$$

Making use of [Equation \(27\)](#) we can conclude that $k_{ij}(s, t)$ has Cauchy-type singularity for $i = j$ as $t \rightarrow s$. To illustrate this behavior, applying L'Hopital's rule to [Equation \(27\)](#) gives

$$k_{ii}(s, t) = \frac{a_{-1}}{s - t} + \sum_{m=0}^{\infty} a_m (s - t)^m \quad \text{as } t \rightarrow s,$$

where the coefficient of the singular term $a_{-1} = GG_{zy}/2\pi$. The coefficients a_m , $m = 0, 1, \dots$ are regular functions of variable s in the interval $-1 \leq s \leq 1$ which are too lengthy to be given here. By Bueckner's principle, changing the sign of the left-hand side of [Equation \(25\)](#) gives the traction caused by the external loading on the uncracked strip at the presumed surface of cracks. In [Appendix A](#), we present the Green's function solution of applied traction for a self-equilibrating load on strip edges. Using [Equations \(22\)](#) and [\(A4\)](#), the following traction should be applied on the surface of i -th crack

$$\sigma_{zY_i}(x_i(s), y_i(s)) = \frac{\tau_0}{2Gh} \left(\frac{x'_i(s) \sin \kappa G(y_i(s) - h) + G y'_i(s) \sinh \kappa(x_i(s) - x_0)}{\left(\cosh \kappa(x_i(s) - x_0) + \cos \kappa G(y_i(s) - h) \right) \sqrt{(x'_i(s))^2 + (y'_i(s))^2}} - \frac{x'_i(s) \sin \kappa G y_i(s) + G y'_i(s) \sinh \kappa(x_i(s) - x_0)}{\left(\cosh \kappa(x_i(s) - x_0) + \cos \kappa G y_i(s) \right) \sqrt{(x'_i(s))^2 + (y'_i(s))^2}} \right).$$

Employing the definition of dislocation density function, the equation for crack opening displacement across the j -th crack is

$$w_j^+(s) - w_j^-(s) = \int_{-1}^s \sqrt{(x'_j(t))^2 + (y'_j(t))^2} b_{zj}(t) dt. \quad (28)$$

The displacement field is single-valued for the surfaces of embedded cracks and cavities. Consequently, the dislocation density functions are subjected to the following closure requirement for $j = 1, 2, \dots, M + N_1$

$$\int_{-1}^1 \sqrt{(x'_j(t))^2 + (y'_j(t))^2} b_{zj}(t) dt = 0. \quad (29)$$

The Cauchy singular integral [Equations \(25\)](#) and [\(29\)](#) are solved simultaneously to determine dislocation density functions. Cavities are defined as closed curved cracks with bounded dislocation density at both ends of the cracks. Thus, for $-1 < t < 1$, $j = 1, 2, \dots, M$ the dislocation density functions for cavities are expressed as

$$b_{zj}(t) = g_{zj}(t) \sqrt{1 - t^2}. \quad (30)$$

Stress fields for embedded cracks in orthotropic materials are singular at crack tips with square root singularity [Delale 1984]. Thus, the dislocation density functions are represented for $-1 < t < 1$, $j = M + 1, M + 2, \dots, M + N_1$ as

$$b_{zj}(t) = \frac{g_{zj}(t)}{\sqrt{1-t^2}}. \tag{31}$$

For edge cracks, taking the embedded crack tip at $t = -1$, for $-1 < t < 1$, $j = M + N_1 + 1, M + N_1 + 2, \dots, N$ we let

$$b_{zj}(t) = g_{zj}(t) \sqrt{\frac{1-t}{1+t}}. \tag{32}$$

[Liebowitz 1968] gives the stress intensity factors for i -th crack in terms of crack opening displacement as

$$k_{IIILi} = \frac{\sqrt{2}}{4} GG_{zy} \lim_{r_{Li} \rightarrow 0} \frac{w_i^-(s) - w_i^+(s)}{\sqrt{r_{Li}}}, \quad k_{IIIRi} = \frac{\sqrt{2}}{4} GG_{zy} \lim_{r_{Ri} \rightarrow 0} \frac{w_i^-(s) - w_i^+(s)}{\sqrt{r_{Ri}}}, \tag{33}$$

for $j = M + 1, M + 2, \dots, N$, where r is the distance from a crack tip. Setting the points L_i and R_i on the surface of the crack, as shown in Figure 1, yields

$$r_{Li} = \left[(x_i(s) - x_i(-1))^2 + (y_i(s) - y_i(-1))^2 \right]^{\frac{1}{2}}, \quad r_{Ri} = \left[(x_i(s) - x_i(1))^2 + (y_i(s) - y_i(1))^2 \right]^{\frac{1}{2}}. \tag{34}$$

Substituting Equation (31) into Equation (28), deriving the resultant equations, substituting Equation (34) into Equation (33), and finally employing L'Hopital's rule yields the stress intensity factors for embedded cracks

$$k_{IIILi} = \frac{GG_{zy}}{2} \left((x'_i(-1))^2 + (y'_i(-1))^2 \right)^{\frac{1}{4}} g_{zi}(-1), \quad k_{IIIRi} = \frac{-GG_{zy}}{2} \left((x'_i(1))^2 + (y'_i(1))^2 \right)^{\frac{1}{4}} g_{zi}(1),$$

where $i = M + 1, M + 2, \dots, M + N_1$. Analogously, for an edge crack the stress intensity factor is

$$k_{IIILi} = GG_{zy} \left((x'_i(-1))^2 + (y'_i(-1))^2 \right)^{\frac{1}{4}} g_{zi}(-1),$$

where $i = M + N_1 + 1, M + N_1 + 2, \dots, N$.

To calculate hoop stress on the surface of cavities, we employ the definition of dislocation density function valid for $-1 \leq s \leq 1$, $i = 1, 2, \dots, M$

$$\gamma_{zX_i}(x_i(s), y_i(s)) = b_{zi}(s). \tag{35}$$

From Hooke's law and Equation (35), for $-1 \leq s \leq 1$, $i = 1, 2, \dots, M$ the shear stress (see [Lekhnitskii 1963]) becomes

$$\sigma_{zX_i}(x_i(s), y_i(s)) = \frac{G_{zx} G_{zy}}{G_{zx} \sin^2 \varphi_i + G_{zy} \cos^2 \varphi_i} b_{zi}(s). \tag{36}$$

Substituting the crack angle $\varphi_i(s) = \tan^{-1}(y'_i(s)x'_i(s))$ into Equation (36) for $-1 \leq s \leq 1$, $i = 1, 2, \dots, M$ results in

$$\sigma_{zX_i}(x_i(s), y_i(s)) = \frac{G_{zx} \left((x'_i(s))^2 + (y'_i(s))^2 \right)}{(x'_i(s))^2 + G^2 (y'_i(s))^2} b_{zi}(s).$$

We define the nondimensionalized hoop stress for $-1 \leq s \leq 1$, $i = 1, 2, \dots, M$ as

$$\sigma_i(s) = \frac{h\sigma_{zX_i}(x_i(s), y_i(s))}{\tau_0},$$

where h is the strip thickness and τ_0 is the point load applied on the strip.

4. Solution of integral equations

The numerical solution of Equations (25) and (29) is carried out for a strip weakened by cavities, embedded cracks, and edge cracks. The numerical procedure developed by [Erdogan et al. 1973] cannot consider all these defects simultaneously. We have developed a minor generalization of the procedure to provide the needed results. Expanding the continuous functions $g_{zj}(t)$ in Equations (30), (31), and (32), respectively, by Tchebysheff polynomials of first kind $T_l(t)$, second kind $U_l(t)$, and the Jacobi polynomials $P_l^{(1/2, -1/2)}$ for $-1 \leq t \leq 1$ leads to

$$g_{zj}(t) = \begin{cases} \sum_{l=0}^{\infty} B_{jl}U_l(t), & j = 1, 2, \dots, M, \\ \sum_{l=0}^{\infty} B_{jl}T_l(t), & j = M + 1, \dots, M + N_1, \\ \sum_{l=0}^{\infty} B_{jl}P_l(t)^{(1/2, -1/2)}, & j = M + N_1 + 1, \dots, N. \end{cases} \quad (37)$$

Using Equation (37), the integral Equation (25) can be rewritten for $-1 \leq s \leq 1$, $i = 1, 2, \dots, N$ as

$$\begin{aligned} \sigma_{zY_i}(x_i(s), y_i(s)) &= \sum_{j=1}^M \sum_{l=0}^{\infty} B_{jl} \int_{-1}^1 k_{ij}(s, t)U_l(t)\sqrt{1-t^2} dt \\ &+ \sum_{j=M+1}^{M+N_1} \sum_{l=0}^{\infty} B_{jl} \int_{-1}^1 k_{ij}(s, t)\frac{T_l(t)}{\sqrt{1-t^2}} dt + \sum_{j=M+N_1+1}^N \sum_{l=0}^{\infty} B_{jl} \int_{-1}^1 k_{ij}(s, t)P_l(t)^{(1/2, -1/2)}\sqrt{\frac{1-t}{1+t}} dt. \end{aligned} \quad (38)$$

Following [Theocaris and Iokimidis 1977] we conclude that at $s = s_r$, $r = 1, 2, \dots, n - 1$, and $s = 1$ the following approximations hold

$$\int_{-1}^1 k_{ij}(s_r, t)\frac{T_l(t)}{\sqrt{1-t^2}} dt \approx \frac{\pi}{n} \sum_{k=1}^n k_{ij}(s_r, t_k)T_l(t_k), \quad (39)$$

$$\int_{-1}^1 k_{ij}(1, t)\frac{T_l(t)}{\sqrt{1-t^2}} dt \approx n\pi a_{-1}\delta_{ij} + \frac{\pi}{n} \sum_{k=1}^n k_{ij}(1, t_k)T_l(t_k), \quad (40)$$

where δ_{ij} is the Kronecker delta, $s_r = \cos(\pi r/n)$ for $r = 1, 2, \dots, n - 1$, and $t_k = \cos(\pi(2k - 1)/2n)$ for $k = 1, 2, \dots, n$. These are the zeros of $U_{n-1}(s_r)$ and $T_n(t_k)$, respectively. Employing identities for $l \in \mathbb{N}$

$$U_l(t)\sqrt{1-t^2} = \frac{T_l(t) - T_{l+2}(t)}{2\sqrt{1-t^2}}, \quad (41)$$

$$P_l(t)^{(1/2, -1/2)}\sqrt{\frac{1-t}{1+t}} = \frac{\Gamma(l + 1/2)}{\sqrt{\pi}l!} \left(\frac{T_{l-1}(t) + T_l(t) - T_{l+1}(t) - T_{l+2}(t)}{2(1+t)\sqrt{1-t^2}} \right), \quad (42)$$

and Equations (39)–(40), the remaining integrals in Equation (38) can be estimated as

$$\int_{-1}^1 k_{ij}(s_r, t)U_l(t)\sqrt{1-t^2} dt \approx \frac{\pi(1-t_k^2)}{n} \sum_{k=1}^n k_{ij}(s_r, t_k)U_l(t_k), \tag{43}$$

$$\int_{-1}^1 k_{ij}(1, t)U_l(t)\sqrt{1-t^2} dt \approx \frac{\pi(1-t_k^2)}{n} \sum_{k=1}^n k_{ij}(1, t_k)U_l(t_k), \tag{44}$$

$$\int_{-1}^1 k_{ij}(s_r, t)P_l(t)^{(1/2,-1/2)}\sqrt{\frac{1-t}{1+t}} dt \approx \frac{\pi(1-t_k)}{n} \sum_{k=1}^n k_{ij}(s_r, t_k)P_l(t_k)^{(1/2,-1/2)}, \tag{45}$$

$$\int_{-1}^1 k_{ij}(1, t)P_l(t)^{(1/2,-1/2)}\sqrt{\frac{1-t}{1+t}} dt \approx \frac{\pi(1-t_k)}{n} \sum_{k=1}^n k_{ij}(1, t_k)P_l(t_k)^{(1/2,-1/2)}. \tag{46}$$

The integral Equations (29) and (38) at the points $s = s_r, r = 1, 2, \dots, n - 1$ and $s = 1$, by virtue of Equations (41)–(46), can be expressed as

$$\begin{aligned} \sigma_{zY_i}(x_i(s_r), y_i(s_r)) &= \frac{\pi}{n} \sum_{j=1}^M \sum_{k=1}^n (1-t_k^2)k_{ij}(s_r, t_k)g_{zj}(t_k) + \frac{\pi}{n} \sum_{j=M+1}^{M+N_1} \sum_{k=1}^n k_{ij}(s_r, t_k)g_{zj}(t_k) \\ &+ \frac{\pi}{n} \sum_{j=M+N_1+1}^N \sum_{k=1}^n (1-t_k)k_{ij}(s_r, t_k)g_{zj}(t_k), \quad i = 1, \dots, N, \quad r = 1, \dots, n-1, \\ \sigma_{zY_i}(x_i(1), y_i(1)) &= \frac{\pi}{n} \sum_{j=1}^M \sum_{k=1}^n (1-t_k^2)k_{ij}(1, t_k)g_{zj}(t_k) + \frac{\pi}{n} \sum_{j=M+1}^{M+N_1} \sum_{k=1}^n k_{ij}(1, t_k)g_{zj}(t_k) \\ &+ \frac{\pi}{n} \sum_{j=M+N_1+1}^N \sum_{k=1}^n (1-t_k)k_{ij}(1, t_k)g_{zj}(t_k), \quad i = M+N_1+1, \dots, N. \end{aligned}$$

In matrix form the above system of algebraic equations is written

$$\begin{bmatrix} H_{11} & H_{12} & \dots & H_{1N} \\ H_{21} & H_{22} & \dots & H_{2N} \\ \vdots & \vdots & \ddots & \vdots \\ H_{N1} & H_{N2} & \dots & H_{NN} \end{bmatrix} \begin{bmatrix} g_{z1}(t_p) \\ g_{z2}(t_p) \\ \vdots \\ g_{zN}(t_p) \end{bmatrix} = \begin{bmatrix} q_1(s_r) \\ q_2(s_r) \\ \vdots \\ q_N(s_r) \end{bmatrix}. \tag{47}$$

The matrix and vector components in the system of Equation (47) are

$$H_{ij} = \begin{bmatrix} A_{j1}k_{ij}(s_1, t_1) & \dots & A_{j_{n-1}}k_{ij}(s_1, t_{n-1}) & A_{jn}k_{ij}(s_1, t_n) \\ \vdots & \ddots & \vdots & \vdots \\ A_{j1}k_{ij}(s_{n-1}, t_1) & \dots & A_{j_{n-1}}k_{ij}(s_{n-1}, t_{n-1}) & A_{jn}k_{ij}(s_{n-1}, t_n) \\ A_{j1}B_{ij}(t_1) & \dots & A_{j_{n-1}}B_{ij}(t_{n-1}) & A_{jn}B_{ij}(t_n) \end{bmatrix},$$

$$g_{zj} = [g_{zj}(t_1) \dots g_{zj}(t_n)]^T, \quad j = 1, 2, \dots, N,$$

$$q_i = [\sigma_{zY_i}(x_i(s_1), y_i(s_1)) \dots \sigma_{zY_i}(x_i(s_{n-1}), y_i(s_{n-1})) \ 0]^T, \quad i = 1, \dots, M+N_1,$$

$$q_i = [\sigma_{zY_i}(x_i(s_1), y_i(s_1)) \dots \sigma_{zY_i}(x_i(s_{n-1}), y_i(s_{n-1})) \ \sigma_{zY_i}(x_i(1), y_i(1))]^T, \quad i = M+N_1+1, \dots, N.$$

In the above equalities, superscript T stands for the transpose of a vector and A_{jk} and $B_{ij}(t)$ are

$$A_{jk} = \frac{\pi}{n} \begin{cases} 1 - t_k^2, & j = 1, \dots, M, \\ 1, & j = M + 1, \dots, M + N_1, \\ 1 - t_k, & j = M + N_1 + 1, \dots, N, \end{cases} \quad k = 1, 2, \dots, n,$$

$$B_{ij}(t) = \begin{cases} \delta_{ij} \sqrt{(x'_i(t))^2 + (y'_i(t))^2}, & i = 1, \dots, M + N_1, \\ k_{ij}(1, t), & i = M + N_1 + 1, \dots, N. \end{cases}$$

Note that the minor enhancement of [Erdogan et al. 1973] does not affect the convergence of numerical results.

5. Numerical examples and results

The validity of analysis is examined by considering an orthotropic strip with thickness h where the x -axis coincides with the lower edge of strip. The strip is weakened by a single crack located on the y -axis extending over $a \leq y \leq b$. The crack is under antiplane traction $\tau_0(s)$ on its surface. For this example, the integral Equation (25) simplifies to

$$\tau_0(s) = \frac{(b-a)GG_{zy}}{4h} \int_{-1}^1 \frac{\sin(\pi y(t)/h)}{\cos(\pi y(t)/h) - \cos(\pi y(s)/h)} b_z(t) dt, \tag{48}$$

where the crack equation for $-1 \leq s \leq 1$ is

$$y(s) = \frac{1}{2}(b + a + (b - a)s).$$

The integral Equation (48) is identical to Equation (30) derived by [Li 2005]. This may demonstrate that our method is valid for numerical analysis of cracks in strips.

For cavities, the formulations and also the numerical solution of integral equations are validated by considering an infinite isotropic plane weakened by two identical circular approaching cavities. The plane is under uniform antiplane traction τ_0 at infinity. The variation of the nondimensionalized stress component $\sigma_{zy}(d, 0)/\tau_0$ versus the distance between cavities is shown in Figure 2. The results are in reasonable agreement with those obtained by [Steif 1989]. As a final check of the formulation, we

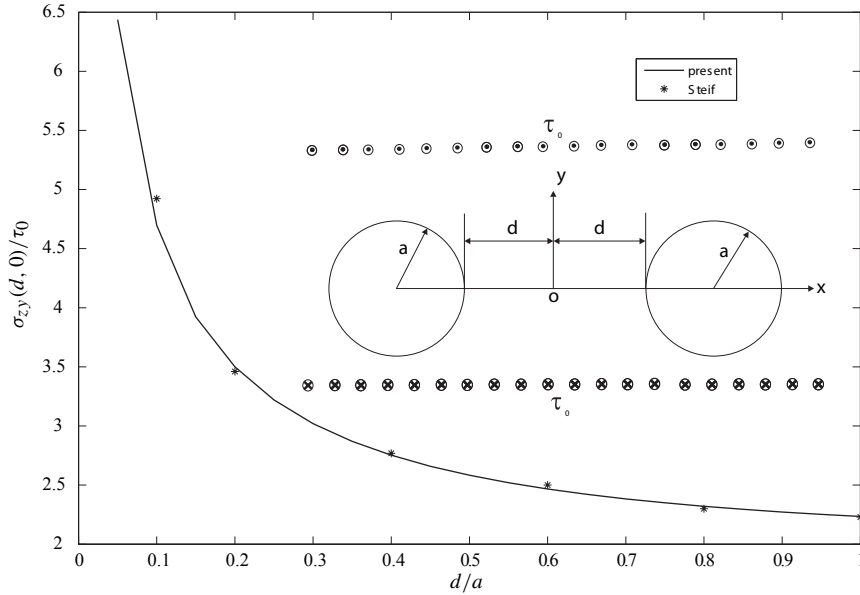


Figure 2. Comparison of hoop stress with Steif's results.

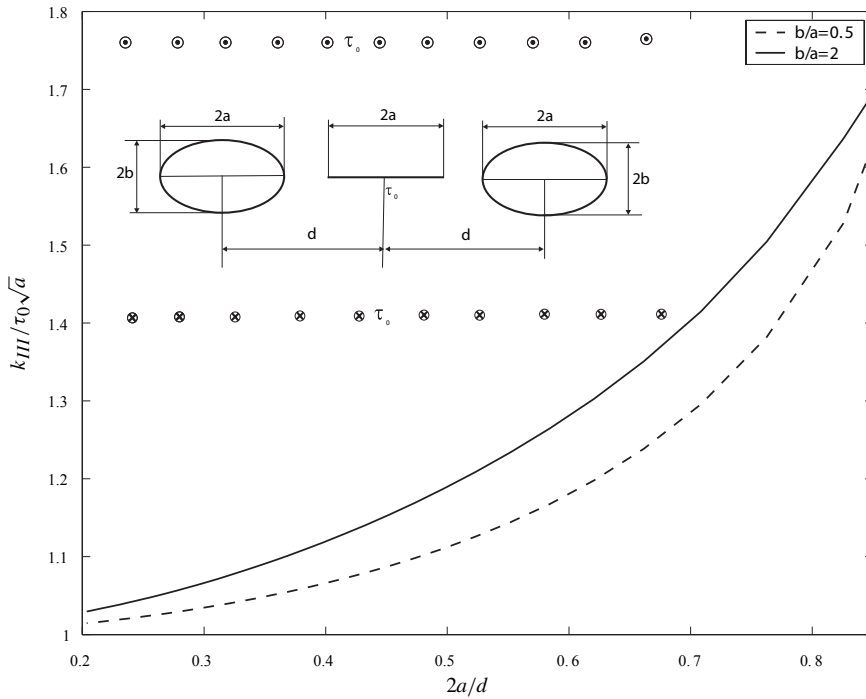


Figure 3. Variation of stress intensity factor with $2a/d$.

analyze an embedded crack located between two approaching elliptical cavities under far field traction (Figure 3), and show that the curves for $k/\tau_0\sqrt{a}$ versus $2a/d$ coincide with Isida's results in [Isida 1973].

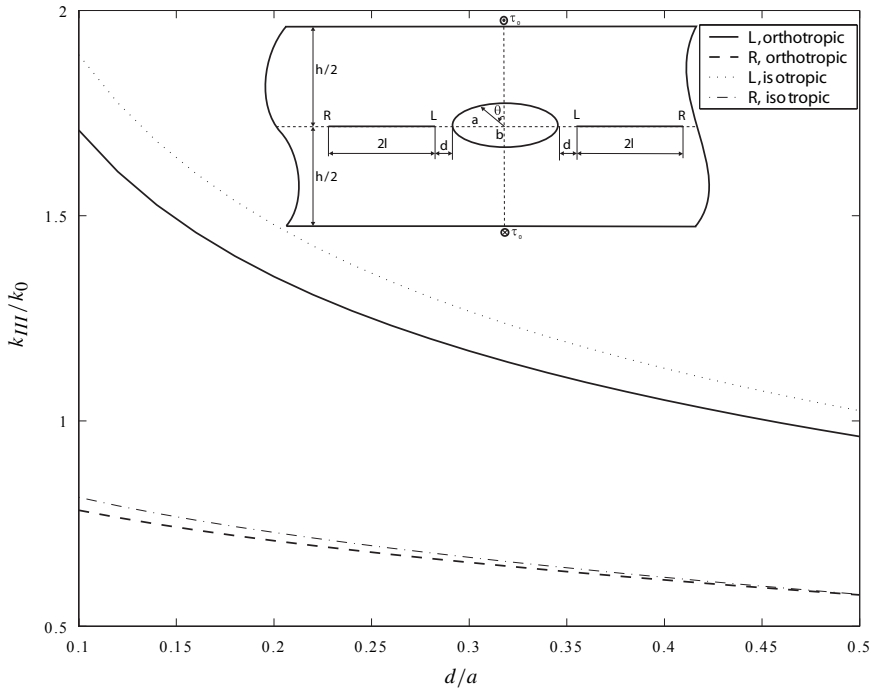


Figure 4. Variations of k_{III}/k_0 with d/a .

The procedure described in the preceding sections allows consideration of a strip with any number of cracks and cavities, and with differing orientations. We now furnish four examples to demonstrate the applicability of this method. In all examples, the ratio of the moduli of elasticity of the orthotropic strip is taken as $G = 1.135$ which is representative of that for carbon-carbon plies. Moreover, the strip is under antiplane point force with magnitude τ_0 on the edges. The stress intensity factors become dimensionless by using the divisor $k_0 = \tau_0 \sqrt{l/h}$, where l is the half length of embedded crack. For an edge crack, l is the crack length.

In the first example, we consider a pair of straight cracks with length $2l = h/3$ and an elliptical cavity with the length of major semi-axis $a = h/6$ and minor semi-axis $b = h/12$. The major axis of the cavity and the cracks are located on the centerline of the strip. Therefore, the problem is symmetric with respect to the y -axis. Figure 4 shows the variations of nondimensionalized stress intensity factors, k/k_0 , of crack tips against d/a for isotropic and orthotropic strips. As the crack tip approaches the elliptical cavity, k/k_0 at the tip L increases rapidly. In the orthotropic strip, weaker material stiffness in the y -direction compared to that of the x -direction reduces the stress intensity factor. The plot of dimensionless hoop stress on the elliptical cavity, $h\sigma_{zX}/\tau_0$, versus angle θ , where θ is measured from the minor-axis of elliptical cavity, are shown for the orthotropic strip in Figure 5. A similar trend for dimensionless hoop stress but with greater magnitude was observed for a cavity in the isotropic strip.

In the second example, we consider an orthotropic strip weakened by an edge crack with length $h/4$ perpendicular to the upper edge of strip, and a rotating embedded crack with length $2l = h/2$. The plots of dimensionless stress intensity factors, k/k_0 , versus the crack orientation, angle θ , are shown in Figure 6. The interaction between cracks is weak, In particular, variation of k/k_0 is small for the edge

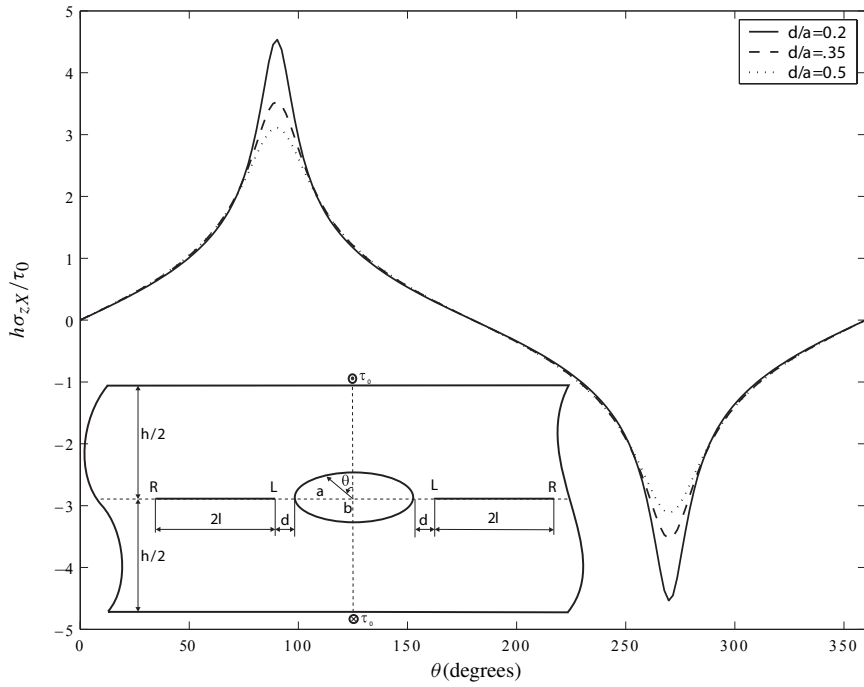


Figure 5. Dimensionless hoop stress on the elliptical cavity for the orthotropic strip versus θ for $d/a = 0.5$.

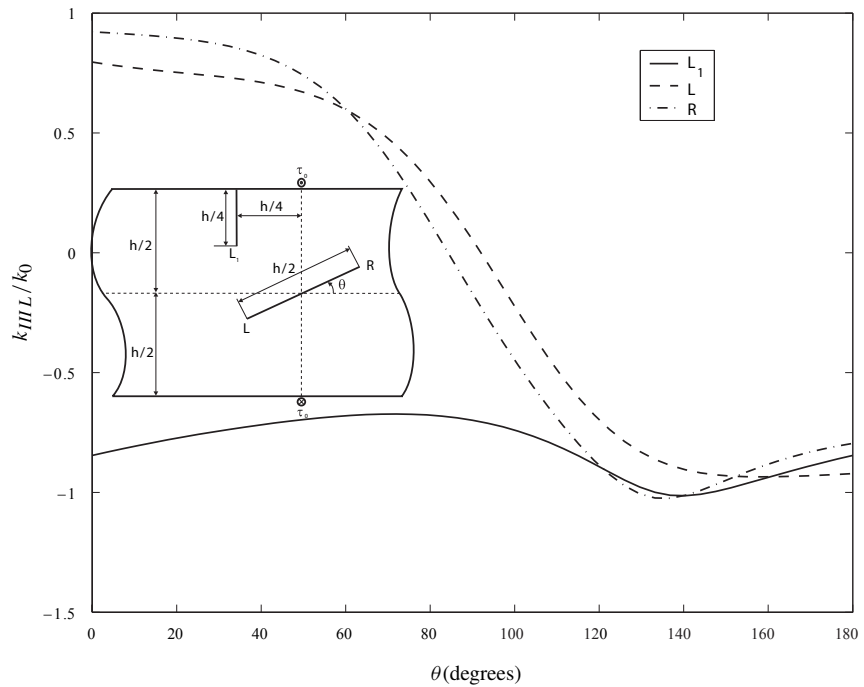


Figure 6. Variations of k_{III}/k_0 with θ for orthotropic strips.

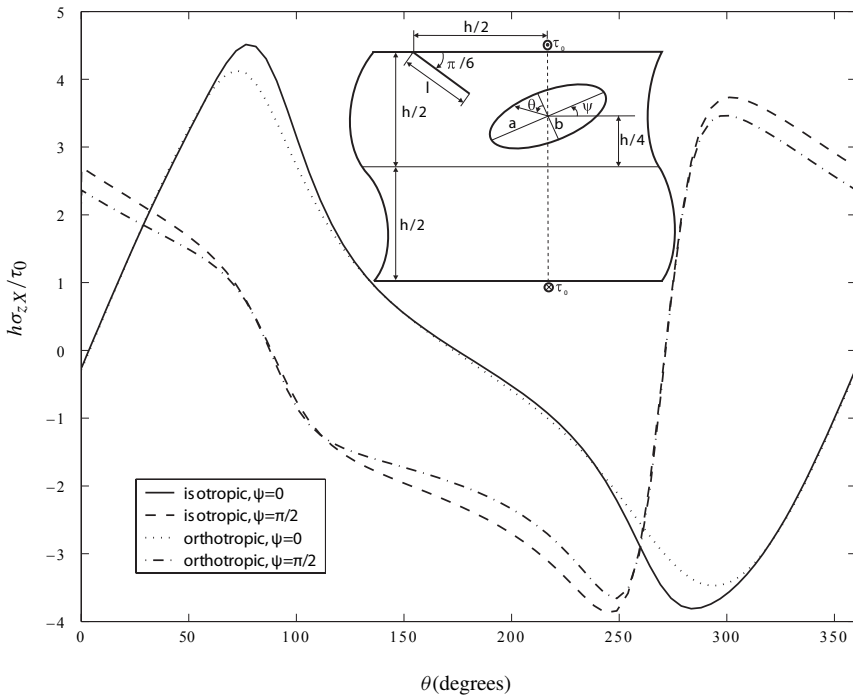


Figure 7. Dimensionless hoop stress on the elliptical cavity versus θ for different values of ψ .

crack. At $\theta = \pi/2$, the embedded crack experiences some stress due to interaction with the edge crack. For the isotropic strip, the plots of k/k_0 are very similar to those in Figure 6, but with slightly reduced magnitude.

In the third example, we consider a strip weakened by a stationary inclined edge crack with length $l = h/3$ and an elliptical cavity with the length of major semi-axis $a = h/8$ and minor semi-axis $b = h/12$. We let the cavity rotate around its center. Figure 7 shows the plot of dimensionless hoop stress for two different orientations of cavity, $\psi = 0$ and $\pi/2$, versus the angle θ , where θ is measured from the minor axis of elliptical cavity. Figure 8 shows dimensionless stress intensity factors, k/k_0 , for the crack tip versus the cavity orientation. For all cavity orientations, the magnitude of the stress intensity factor in the orthotropic strip is higher than that in the isotropic one.

In the fourth and last example, we consider a straight embedded crack with a fixed center, an inclined edge crack, and a circular cavity with radius $R = h/6$. The center of the cavity and the embedded crack are located on the line with distance $h/3$ from the lower edge of strip. The edge crack is in the radial direction of the cavity with a length half of the embedded crack. The distance from the center of the embedded crack to the center of cavity is $4h/3$. Figure 9 and shows the stress intensity factors for edge cracks with changing crack length in isotropic and orthotropic strips, and Figure 10 shows the same information, but for embedded cracks. The dimensionless hoop stress for the cavity, when $l/h = 1$, is shown in Figure 11. Hoop stress is greatest at the points closest to crack tips.

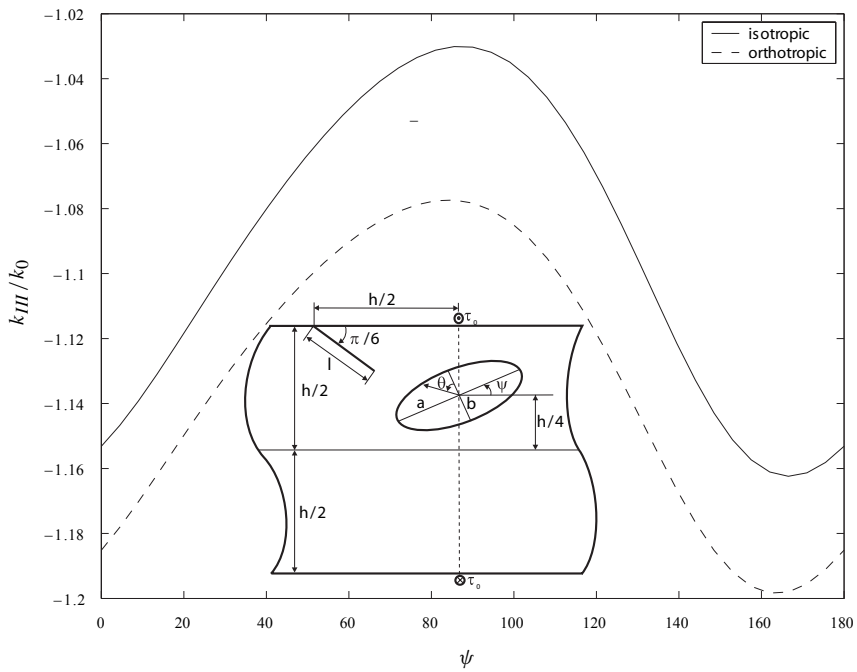


Figure 8. Variations of k_{III}/k_0 with ψ .

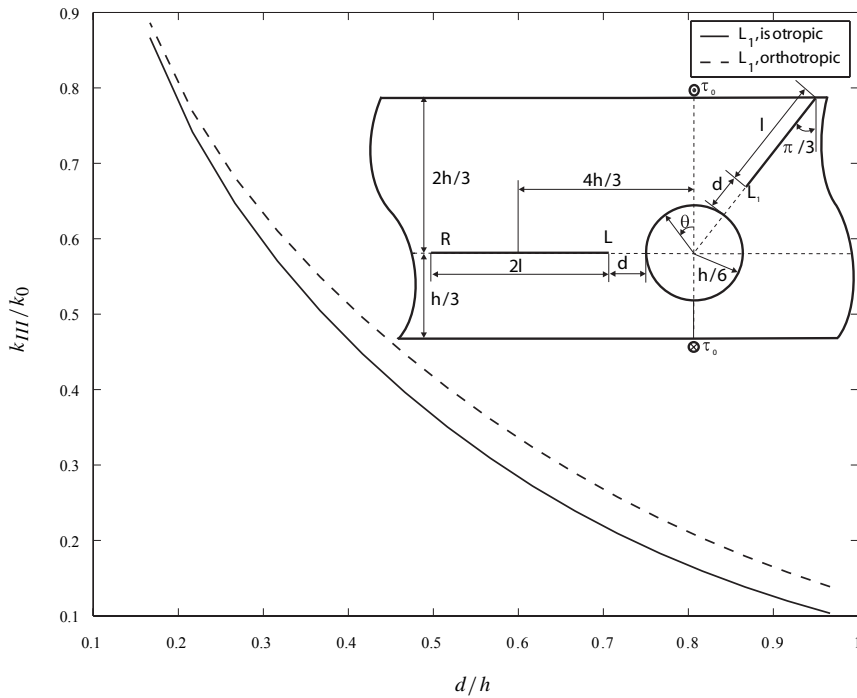


Figure 9. Variations of k_{III}/k_0 with d/h for the edge crack.

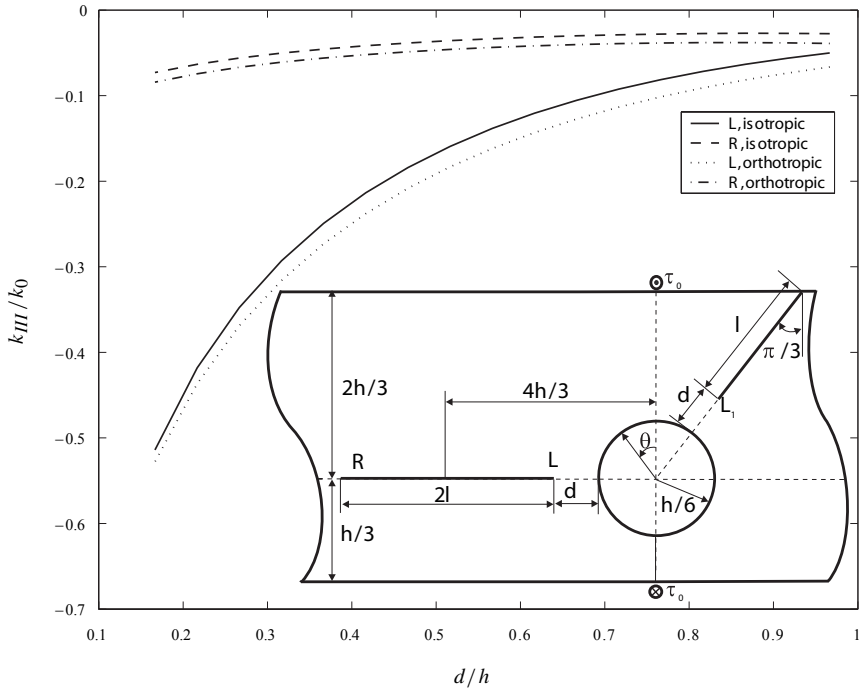


Figure 10. Variations of k_{III}/k_0 with d/h for the embedded crack.

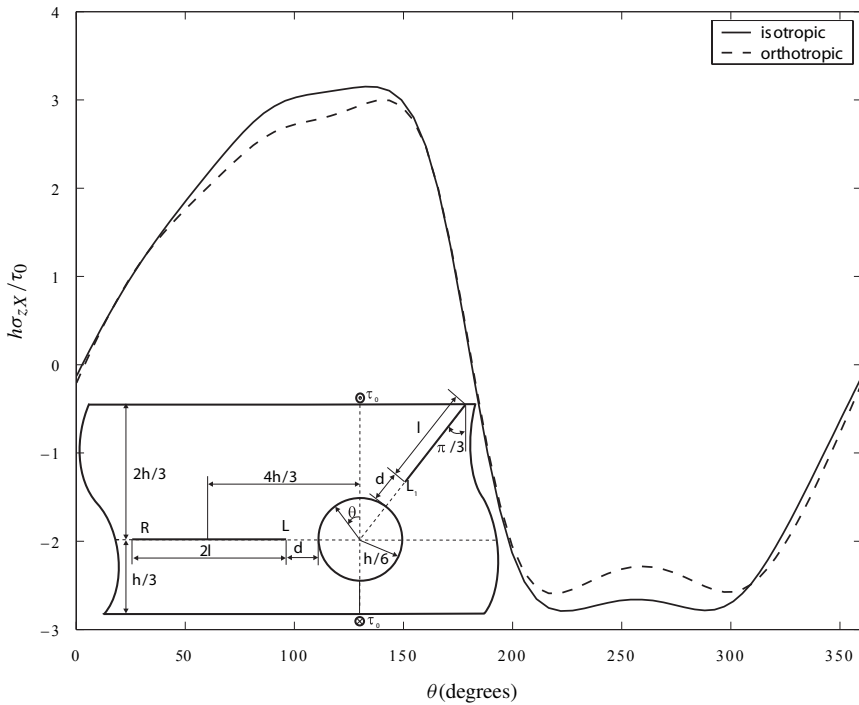


Figure 11. Dimensionless hoop stress on the circular cavity inside the strip versus θ for $l = h$.

Appendix A

The Green's function solution for elasticity problem of a strip under antiplane load may be obtained by applying the following self-equilibrating traction to the strip edges

$$\sigma_{zy}(x, h) = \tau_0 \delta(x - x_0) = \sigma_{zy}(x, 0). \quad (\text{A1})$$

The application of Fourier transform in x -direction to Equation (3) leads to a second order ordinary differential equation with the solution

$$W(\Omega, y) = E(\Omega)e^{\Omega Gy} + F(\Omega)e^{-\Omega Gy}. \quad (\text{A2})$$

The unknown coefficients in Equation (A2) are obtained by taking the Fourier transform of Equation (A1) and applying them to Equation (A2), yielding

$$W(\Omega, y) = \frac{\tau_0}{GG_{zy}} \frac{\cosh \Omega Gy - \cosh \Omega G(y-h)}{\Omega \sinh \Omega Gh} e^{-i\Omega x_0}. \quad (\text{A3})$$

Employing the inverse Fourier transform of Equation (A3) in conjunction with Equations (1)–(2) give the stress fields as

$$\sigma_{zx}(x, y) = \frac{i\tau_0 G}{2\pi} \int_{-\infty}^{\infty} \frac{\cosh \Omega Gy - \cosh \Omega G(y-h)}{\sinh \Omega Gh} e^{i\Omega(x-x_0)} d\Omega,$$

$$\sigma_{zy}(x, y) = \frac{\tau_0}{2\pi} \int_{-\infty}^{\infty} \frac{\sinh \Omega Gy - \sinh \Omega G(y-h)}{\sinh \Omega Gh} e^{i\Omega(x-x_0)} d\Omega.$$

To determine the above integrals, we can use contour integration. The results are

$$\sigma_{zx}(x, y) = \frac{\tau_0}{2h} \left(\frac{\sinh \kappa(x-x_0)}{\cosh \kappa(x-x_0) + \cos \kappa G(y-h)} - \frac{\sinh \kappa(x-x_0)}{\cosh \kappa(x-x_0) + \cos(\kappa Gy)} \right), \quad (\text{A4})$$

$$\sigma_{zy}(x, y) = \frac{\tau_0}{2Gh} \left(\frac{\sin \kappa Gy}{\cosh \kappa(x-x_0) + \cos \kappa Gy} - \frac{\sin \kappa G(y-h)}{\cosh \kappa(x-x_0) + \cos \kappa G(y-h)} \right). \quad (\text{A5})$$

References

- [Delale 1984] F. Delale, "Stress singularities in bonded anisotropic materials", *Int. J. Solids Struct.* **20**:1 (1984), 31–40.
- [Erdogan et al. 1973] F. Erdogan, G. D. Gupta, and T. S. Cook, "Numerical solution of integral equations", pp. 368–425 in *Methods of analysis and solutions of crack problems*, edited by G. C. Sih, Mechanics of Fracture **1**, Noordhoff, Leyden, 1973.
- [Isida 1973] M. Isida, "Method of Laurent series expansion for internal crack problems", pp. 56–130 in *Methods of analysis and solutions of crack problems*, edited by G. C. Sih, Mechanics of Fracture **1**, Noordhoff, Leyden, 1973.
- [Lekhnitskii 1963] S. G. Lekhnitskii, *Theory of elasticity of an anisotropic elastic body*, Holden-Day, San Francisco, 1963.
- [Li 2003] X. F. Li, "Closed-form solution for two collinear mode-III cracks in an orthotropic elastic strip of finite width", *Mech. Res. Commun.* **30**:4 (2003), 365–370.
- [Li 2005] X. F. Li, "Two perfectly-bonded dissimilar orthotropic strips with an interfacial orthotropic strips normal to the boundaries", *Appl. Math. Comp.* **163**:2 (2005), 961–975.
- [Liebowitz 1968] H. Liebowitz, *Fracture mechanics*, Academic Press, New York, 1968.
- [Steif 1989] P. S. Steif, "Stress concentration around a pair of circular holes", *J. Appl. Mech. (ASME)* **56** (1989), 719–721.

- [Theocaris and Iokimidis 1977] P. S. Theocaris and N. I. Iokimidis, “Numerical integration methods for the solution of singular integral equations”, *Q. Appl. Math.* **35** (1977), 173–183.
- [Weertman and Weertman 1992] J. Weertman and J. R. Weertman, *Elementary dislocation theory*, Oxford University Press, New York, 1992.
- [Wu and Dzenis 2002] X. F. Wu and Y. A. Dzenis, “Closed-form solution for a mode-III interfacial edge crack between two bonded dissimilar elastic strips”, *Mech. Res. Commun.* **29**:5 (2002), 407–412.
- [Zhou and Ma 1999] Z. G. Zhou and L. Ma, “Two collinear Griffith cracks subjected to anti-plane shear in infinitely long strip”, *Mech. Res. Commun.* **26**:4 (1999), 437–444.
- [Zhou et al. 1998] Z. G. Zhou, B. Wang, and S. Y. Du, “The stress field in the vicinity of two collinear cracks subject to antiplane shear in a strip of finite width”, *Mech. Res. Commun.* **25**:2 (1998), 183–188.

Received 11 Dec 2005. Revised 18 Feb 2006. Accepted 24 May 2006.

REZA TEYMORI FAAL: faal92@yahoo.com

Department of Mechanical Engineering, Amirkabir University of Technology (Tehran Polytechnic), 424 Hafez Avenue, Tehran 158754413, Iran

SHAHRIAR J. FARIBORZ: sjfariborz@yahoo.com

Department of Mechanical Engineering, Amirkabir University of Technology (Tehran Polytechnic), 424 Hafez Avenue, Tehran 158754413, Iran

HAMID REZA DAGHYANI: Deceased 2006

Department of Mechanical Engineering, Amirkabir University of Technology (Tehran Polytechnic), 424 Hafez Avenue, Tehran 158754413, Iran

SWITCHING DEFORMATION MODES IN POST-LOCALIZATION SOLUTIONS WITH A QUASIBRITTLE MATERIAL

PIERRE BÉSUELLE, RENÉ CHAMBON AND FRÉDÉRIC COLLIN

Localization in a quasibrittle material is studied using a local second-gradient model. Since localization takes place in a medium assumed to be initially homogeneous, nonuniqueness of the solutions of an initial boundary value problem is then also studied. Using enhanced models generalizes the classical localization analysis. In particular, it is necessary to study solutions more continuous (that is, continuous up to the degree one) than the ones used in analysis involving classical constitutive equations. Within the assumptions done, it appears that localization is possible in the second-gradient model if it is possible in the underlying classical model. Then the study of nonuniqueness is conducted for the numerical problem, using different first guesses in the full Newton–Raphson procedure solving the incremental nonlinear equations. Thanks to this method, we are able to simulate qualitatively the nonreproducibility of usual experiment in the postpeak regime.

1. Introduction

Modeling the degradation of materials is a very challenging task. If the degradation is sufficiently high — if the material exhibits some softening (here in a vague sense) — it is now well known that some unpleasant features appear both in experiments and in computations.

From the experimental point of view, as soon as the softening is reached, it seems that the behavior is poorly reproducible or nonreproducible. The first reason is that in main cases strain localization occurs which means that contrary to current assumptions, laboratory samples are not strained homogeneously up to the failure. Moreover localization patterns themselves are not easily reproduced. Let us first quote Desrues and Viggiani [2004], who performed some biaxial tests twice:

[E]very test is somewhat unique as for the patterns of strain localization (location of the shear band, appearance of nonpersistent and/or multiple bands).

Quite clearly such behavior is related to the loss of uniqueness of the problem (that is, in the reported case the biaxial test) which allows shear bands to emerge. But, what is clear in [Desrues and Viggiani 2004] is that there is a large variability in the observed patterns. This means that there is not only one alternative solution involving a unique localized band. If it is quite clear that if orientation and width of the bands are easily reproduced, on the contrary the number of bands and their position as well as their persistence cannot be predicted in advance. This has some consequences for the load versus displacement curves which can exhibit very different results in their postpeak parts (that is, when some localization can be

P.B. gratefully acknowledges financial support for a two-month stay for at the University of Liège through a Research Fellowship of the Fonds National de la Recherche Scientifique (FNRS) of Belgium.

Keywords: continuum with microstructure, second gradient, finite element, bifurcation, strain localization, mode switching, reproducibility.

expected). This is clearly illustrated in [Desrues and Hammad 1985] or in [Desrues 1984] where the two curves of duplicate tests are in many cases rather different as soon as the peak value is attained. Other similar observations about tests performed twice can be found in [Viggiani et al. 2001]. These results are often interpreted as the consequence of some (unfortunately unknown) initial imperfection in the studied samples, and based on the deterministic principle, it is argued that if the initial state is completely known the problem should disappear.

Following the previous ideas, numerical modeling of such postpeak phenomena is usually achieved by introducing some (deterministic) initial imperfection into the computation, and it is believed that uniqueness of the solution is restored. Consequently changing the imperfection can change the final solution of the computation since it is assumed that there is a correspondence between a given imperfection and the resulting solution. Unfortunately we demonstrated recently that this way of thinking may be erroneous; see [Chambon and Moullet 2004]. For the same imperfection several (properly converged) solutions can be found provided an appropriate searching algorithm is used. Recently, introducing an initial fluctuation of the mechanical properties has been used to deal with this problem, for instance in [Nübel and Huang 2004]. In the quoted paper the introduction of this initial fluctuation is achieved by initializing randomly the density for a model sensitive with respect to this parameter. The computations performed seem very similar to what is usually observed. However, even in this case, it seems that the author assumes implicitly that uniqueness is restored. Alternative solutions should be searched in order to clarify this point.

Another way is followed in the numerical experiments detailed in the present paper. We choose to solve the “perfect” (which means without any intentional imperfection) problem, and we try to exhibit several solutions for this problem. Usually the method used to find alternative solutions is related to a spectral analysis of the linearized velocity problem. Numerically this is achieved by searching when the least eigenvalue of the tangent stiffness matrix related to the velocity discretized problem goes to zero; see for instance [de Borst 1986] or [Ikeda and Murota 2002]. This method is based on a linearization of the problem which is completely sound if the nonlinear problem is incrementally linear. Since we use an elastoplastic model, elastic up to a given threshold and exhibiting a sudden softening as soon as this threshold is reached, there are many possible linearizations depending on the choice of the unloading area within the computed domain. Then the drawback of such a method is that the mode corresponding to the null eigenvalue which allows theoretically to follow the bifurcated solution can correspond for some point of the studied structure to a constitutive branch (loading or unloading) different to the one used to compute the linearized stiffness matrix. In this paper we prefer to follow the ideas initially applied in [Chambon et al. 2001b] where the solution for a time step is searched with a Newton–Raphson method with different first estimations which can (if the problem has more than one solution) yield different properly converged solutions.

On the other hand, it is now well known that localizations cannot be properly modeled with classical media since this implies rupture without energy consumption as proved by Pijaudier-Cabot and Bažant [1987]. Enhanced models are necessary. However, contrary to what is often believed, the use of an enhanced model does not guarantee uniqueness of the solution of the corresponding boundary value problems; this has been demonstrated in [Chambon et al. 1998; Chambon and Moullet 2004], the latter employing the same model used in this paper. But it seems that the result is more general. Challamel and Hijaj [2005] also found solutions for the same problem, but using a nonlocal, enhanced model.

In this paper a second-gradient theory is used in conjunction with the method to search alternative solutions recalled above. The first section of this paper is devoted to a brief recall of the model used and of the principle of its numerical implementation.

In order to be able to perform easily different computations, the element has been first implemented in the general purpose finite element code Lagamine developed at University of Liège [Charlier 1987], and we checked the accuracy of this implementation using extended tests. This is described in the second section of this paper.

Then a localization analysis is performed in the third section of the paper. Such an analysis is necessarily different from the original ones of [Rudnicki and Rice 1975] since the type of discontinuity assumed in the aforementioned reference cannot be used due to the second-order terms.

After briefly recalling the method, the fourth section deals with the numerical experiments of non-uniqueness and describes computations exhibiting switching modes. Such mode switching has already been studied by Ikeda et al. [1997] in a different context. It has been made mainly for the incrementally linear comparison solid, which on the one hand allows a sound mathematic treatment, but on the other discards modes involving a change in the loading branches of the constitutive equations. Here, as explained above, no assumption is done concerning the behavior but only a numerical treatment of the problem is made.

As for our notations, a component of a tensor (or vector) is denoted by the name of the tensor (or vector) accompanied by the indices. All tensorial indices are in lower position, since there is no need to distinguish between covariant and contravariant components. Upper indices have specific meanings defined in the text. The summation convention with respect to repeated tensorial indices is used.

2. Local second-gradient models

2.1. A microstructured continuum with kinematic constrains. Models with microstructure descend from the pioneer works of the Cosserat brothers [Cosserat and Cosserat 1909], via [Toupin 1962], [Mindlin 1964] and [Germain 1973]. They use an enriched kinematic description of the continuum, with respect to classical continua, recalled hereafter. In addition to the displacement field, u_i , a second-order tensor, the microkinematic gradient v_{ij} , is introduced. Particular subclasses of enriched models introduce a constraint on the microkinematic field. For example, Cosserat models can be viewed as a microstructured model for which the microstrain is vanishing, that is, the symmetric part of the tensor v_{ij} is zero. In the same spirit, (local) second-gradient models assume that the microkinetic gradient is equal to the displacement gradient $v_{ij} = \partial u_i / \partial x_j$, where x_j is the spatial coordinate. Recently, such models have been developed for geomaterials [Chambon et al. 2001a; Matsushima et al. 2002; Chambon and Moullet 2004] and for metals [Fleck and Hutchinson 1997].

For local second-gradient models, the virtual work principle can be summarized as follows. For every kinematically admissible virtual displacement fields u_i^* ,

$$\int_{\Omega} \left(\sigma_{ij} \varepsilon_{ij}^* + \Sigma_{ijk} \frac{\partial^2 u_i^*}{\partial x_j \partial x_k} \right) dv = \int_{\Omega} G_i u_i^* dv + \int_{\partial \Omega} \left(t_i u_i^* + T_{ij} \frac{\partial u_i^*}{\partial x_j} \right) ds, \quad (1)$$

where σ_{ij} is the Cauchy stress, ε_{ij}^* is the virtual macrostrain, Σ_{ijk} is the dual static variable associated to the second gradient of the virtual displacement, the so-called *double stress*; see [Germain 1973]. Further,

G_i is the body force per unit volume, t_i is the traction force per unit surface and T_{ij} is the double force per unit surface. However t_i and T_{ij} cannot be taken independently, since u_i^* and $\partial u_i^*/\partial x_j$ are not independent. More conveniently, the virtual work of external forces can be rewritten using the normal derivative $Du_i = n_k \partial u_i/\partial x_k$ on the boundary. Here and in the following n_k is the normal to the boundary (assumed to be regular).

$$\int_{\Omega} \left(\sigma_{ij} \varepsilon_{ij}^* + \Sigma_{ijk} \frac{\partial^2 u_i^*}{\partial x_j \partial x_k} \right) dv = \int_{\Omega} G_i u_i^* dv + \int_{\partial\Omega} (p_i u_i^* + P_i Du_i^*) ds, \tag{2}$$

where p_i and P_i are two independent variables which can be prescribed on the boundary.

For such a class of models, the balance equations and boundary conditions yield

$$\frac{\partial \sigma_{ij}}{\partial x_j} - \frac{\partial^2 \Sigma_{ijk}}{\partial x_j \partial x_k} + G_i = 0, \tag{3}$$

$$\sigma_{ij} n_j - n_k n_j D \Sigma_{ijk} - \frac{D \Sigma_{ijk}}{D x_k} n_j - \frac{D \Sigma_{ijk}}{D x_j} n_k + \frac{D n_l}{D x_l} \Sigma_{ijk} n_j n_k - \frac{D n_j}{D x_k} \Sigma_{ijk} = p_i, \tag{4}$$

$$\Sigma_{ijk} n_j n_k = P_i, \tag{5}$$

where Dq/Dx_j denotes the tangential derivatives of any quantity q :

$$\frac{Dq}{Dx_j} = \frac{\partial q}{\partial x_j} - n_j Dq. \tag{6}$$

2.2. Numerical implementation in a finite element code. A direct application of virtual work principle (2) to solve equations of a boundary value problem needs to use C^1 elements. To avoid this constraint, a weak form of equation (2) can be introduced with help of a Lagrange multipliers field λ_{ij} , which yields, for any time t and any kinematically admissible virtual fields u_i^* and v_{ij}^* ,

$$\int_{\Omega^t} \left(\sigma_{ij}^t \frac{\partial u_i^*}{\partial x_j^t} + \Sigma_{ijk}^t \frac{\partial v_{ij}^*}{\partial x_k^t} + \lambda_{ij}^t \left(\frac{\partial u_i^*}{\partial x_j^t} - v_{ij}^* \right) \right) dv = \int_{\Omega^t} G_i^t u_i^* dv + \int_{\partial\Omega^t} (p_i^t u_i^* + P_i Du_i^*) ds, \tag{7}$$

and for any virtual field λ_{ij}^* ,

$$\int_{\Omega^t} \lambda_{ij}^* \left(\frac{\partial u_i^t}{\partial x_j^t} - v_{ij}^t \right) dv = 0. \tag{8}$$

A complete description of the numerical treatment can be found in [Chambon and Moullet 2004]. The problem is discretized in time and for each finite step a full Newton–Raphson is applied to solve the resulting nonlinear problem. In order to get the equations suitable for Newton–Raphson technique, the unbalanced quantities are computed after the n -th iteration of the current time step. The same equations are applied for the $n + 1$ -th iteration, assuming these equations are well balanced. Then, by differentiation, one gets a proper linearization of the set of equations for the Newton–Raphson method. Equations are written in the actual configuration and the small strain assumption is not made, which introduces some geometrical terms in the linearized equations.

The finite element is organized with 8 nodes for the displacement field u_i , 4 nodes for the displacement gradient field v_{ij} , and a single node for the Lagrange multipliers field λ_{ij} . The element was introduced

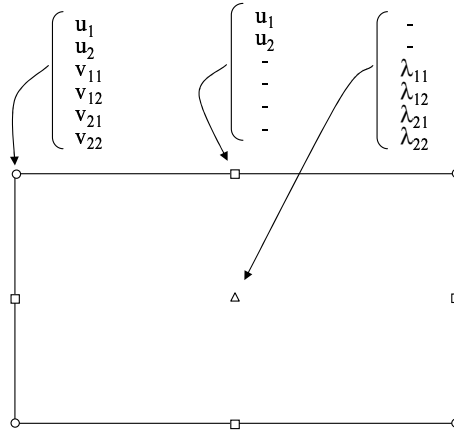


Figure 1. Nodal variables used in the finite element introduced in Lagamine.

in the finite element code Lagamine, initially developed at Liège University in Belgium [Charlier 1987]. The element used in Lagamine to implement our second-gradient model contains in fact 9 nodes each with 6 possible degrees of freedom. For the present application, some of these are not used (see Figure 1): only 36 degrees of freedom are activated by element [Bésuelle 2005].

The following algorithm is adopted for computing one time step from $t - \Delta t$ to t .

- (1) Initial configuration: stress $\sigma^{t-\Delta t}$, double stress $\Sigma^{t-\Delta t}$, coordinates $x^{t-\Delta t}$.
- (2) Assumption on the final configuration for the first iteration $n = 1$:
 - initialization of the increment of nodal values $[\Delta U_{\text{node}}^{t,n}]$,
 - update coordinates: $x^{t,n}$.
- (3) Beginning of the iteration n .
- (4) For each element:
 - for each integration point:
 - compute the strain rate, the rotation rate and the second-gradient rate,
 - compute $\Delta \sigma^{t,n}$ and $\Delta \Sigma^{t,n}$ using the constitutive equations,
 - update the stress and the double stress $\sigma^{t,n} = \sigma^{t-\Delta t} + \Delta \sigma^{t,n}$, $\Sigma^{t,n} = \Sigma^{t-\Delta t} + \Delta \Sigma^{t,n}$,
 - compute the consistent tangent stiffness matrices of constitutive laws.
 - compute the element stiffness matrix.
 - compute the element out of balance forces.
- (5) Compute the global stiffness matrix.
- (6) Compute the global out of balance forces.
- (7) Compute the corrections $[\delta U_{\text{node}}^{t,n}]$ of the increment of nodal values by solving the Newton–Raphson linearized system.
- (8) Check the accuracy of the computed solution:
 - if convergence: go to 9,

- if no convergence: update the new assumed final configuration, $n = n + 1$ and go to 3.

(9) End of the step.

3. Validation

3.1. Constitutive model: a quasibrittle material. The constitutive model used in this paper is the same as in [Matsushima et al. 2002] and [Chambon and Moullet 2004], and it can be decoupled into two independent relations. The first is classical, and links the stress to the displacement gradient; it is a Von Mises elastoplastic law based on the Prandt–Reuss model, with a strain softening regime. The second relation gives the double stress as a function of the gradient of the field v_{ij} (that is, the second gradient of the displacement); it is a linear elastic law. Concerning the constitutive equation used here, we emphasize that the classical part of the model involves no hardening but only sudden softening as soon as a threshold is attained. Moreover this part is not a hyperelastoplastic model, contrary to the ones used for bifurcation analyses in [Steinmann et al. 1997; Borja 2002; Ikeda et al. 2003]. From a thermodynamical point of view it would presumably be better to use the hyperelastoplastic model, but in the second-gradient context it is then necessary to build up a new theory. This has already been done in [Tamagnini et al. 2001] and [Chambon et al. 2004], but the implementation of such a model in a finite element code has not yet been made.

The classical relation is

$$\dot{\sigma} = 3 K \dot{\epsilon},$$

$$\overset{\nabla}{s}_{ij} = \begin{cases} 2 G_1 \dot{\epsilon}_{ij} & \text{for } \|\epsilon\| \leq e_{\text{lim}}, \\ 2 G_1 \left(\dot{\epsilon}_{ij} - \frac{G_1 - G_2}{G_1} \frac{s_{kl} \dot{\epsilon}_{kl}}{\|s\|^2} s_{ij} \right) & \text{for } \|\epsilon\| > e_{\text{lim}}, \end{cases} \quad (9)$$

where $\overset{\nabla}{s}_{ij}$ is the Jaumann rate of the deviatoric Cauchy stress tensor, $\dot{\epsilon}_{ij}$ is the deviatoric strain rates, $\dot{\sigma}$ is the mean stress rate and $\dot{\epsilon}$ is the mean strain rate. K , G_1 and G_2 are the bulk modulus, the shear moduli before peak and after peak, respectively. $\|\epsilon\|$ is the second invariant of the Green–Lagrange deformation tensor, e_{lim} is a deformation parameter of the model which corresponds to the deviatoric stress peak.

The bulk modulus K is assumed to be constant. The elastic shear modulus available for unloading is assumed to be constant, while an exponential function is assumed as follows for the shear modulus after the yield point so that the material could reach its residual state smoothly:

$$G_2 = \bar{G}_2 \exp\left(\frac{\bar{G}_2}{G_1 e_{\text{lim}} - \sigma_{\text{res}}} (\|\epsilon\| - e_{\text{lim}})\right), \quad (10)$$

where \bar{G}_2 is the value of the shear modulus just after yielding and σ_{res} is the residual deviatoric stress.

The second-gradient law has been chosen as simple as possible. It is a particular case of the more general isotropic linear relation derived in [Mindlin 1964], involving six parameters corresponding to five independent coefficients. The following relation is slightly different from the one in [Matsushima

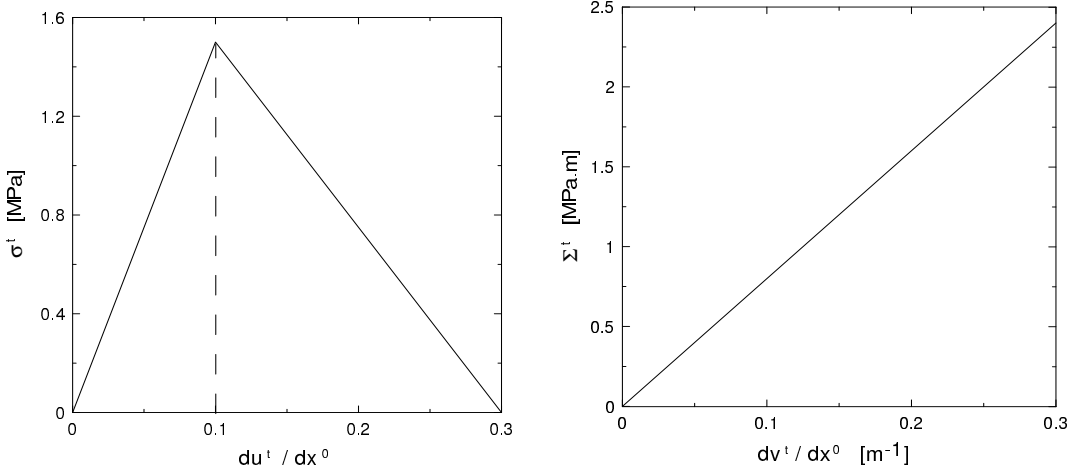


Figure 2. Constitutive relations in the one-dimensional case: (left) first grade term; (right) second grade term.

et al. 2002] and [Chambon and Moullet 2004], in that some inaccuracies have been corrected:

$$\begin{bmatrix} \overset{\nabla}{\Sigma}_{111} \\ \overset{\nabla}{\Sigma}_{112} \\ \overset{\nabla}{\Sigma}_{121} \\ \overset{\nabla}{\Sigma}_{122} \\ \overset{\nabla}{\Sigma}_{211} \\ \overset{\nabla}{\Sigma}_{212} \\ \overset{\nabla}{\Sigma}_{221} \\ \overset{\nabla}{\Sigma}_{222} \end{bmatrix} = \begin{bmatrix} D & 0 & 0 & 0 & 0 & D/2 & D/2 & 0 \\ 0 & D/2 & D/2 & 0 & -D/2 & 0 & 0 & D/2 \\ 0 & D/2 & D/2 & 0 & -D/2 & 0 & 0 & D/2 \\ 0 & 0 & 0 & D & 0 & -D/2 & -D/2 & 0 \\ 0 & -D/2 & -D/2 & 0 & D & 0 & 0 & 0 \\ D/2 & 0 & 0 & -D/2 & 0 & D/2 & D/2 & 0 \\ D/2 & 0 & 0 & -D/2 & 0 & D/2 & D/2 & 0 \\ 0 & D/2 & D/2 & 0 & 0 & 0 & 0 & D \end{bmatrix} \begin{bmatrix} \partial \dot{v}_{11} / \partial x_1 \\ \partial \dot{v}_{11} / \partial x_2 \\ \partial \dot{v}_{12} / \partial x_1 \\ \partial \dot{v}_{12} / \partial x_2 \\ \partial \dot{v}_{21} / \partial x_1 \\ \partial \dot{v}_{21} / \partial x_2 \\ \partial \dot{v}_{22} / \partial x_1 \\ \partial \dot{v}_{22} / \partial x_2 \end{bmatrix}, \quad (11)$$

where \dot{v}_{ij} is the material time derivative of v_{ij} , and $\overset{\nabla}{\Sigma}_{ijk}$ is the Jaumann double stress derivative, defined by $\overset{\nabla}{\Sigma}_{ijk} = \dot{\Sigma}_{ijk} + \Sigma_{ljk}\omega_{li} + \Sigma_{imk}\omega_{mj} + \Sigma_{ijp}\omega_{pk}$, where ω_{li} is the spin tensor.

3.2. One-dimensional simulation. In order to validate the implementation of the element in Lagamine, first a one-dimensional compression is computed. This problem has analytic solutions under the assumption of small strain; see [Chambon et al. 1998]. The bar is 1 meter long. The degrees of freedom u_1 , v_{11} , v_{12} and v_{21} are blocked at each node, the direction 2 being the direction of compression. In order to study the symmetrical localized solution composed of a central patch in the softening loading part and two end patches in the elastic unloading part, two elements at the middle of the bar have a e_{lim} -value reduced by 2%. The constitutive parameters are the same as those used in [Matsushima et al. 2002]:

$$\begin{aligned} G_1 &= 16.875 \text{ MPa}, & \bar{G}_2 &= 0 \text{ MPa}, & e_{lim} &= 0.082, \\ K &= -7.5 \text{ MPa}, & D &= 0.08 \text{ MN}. \end{aligned} \quad (12)$$

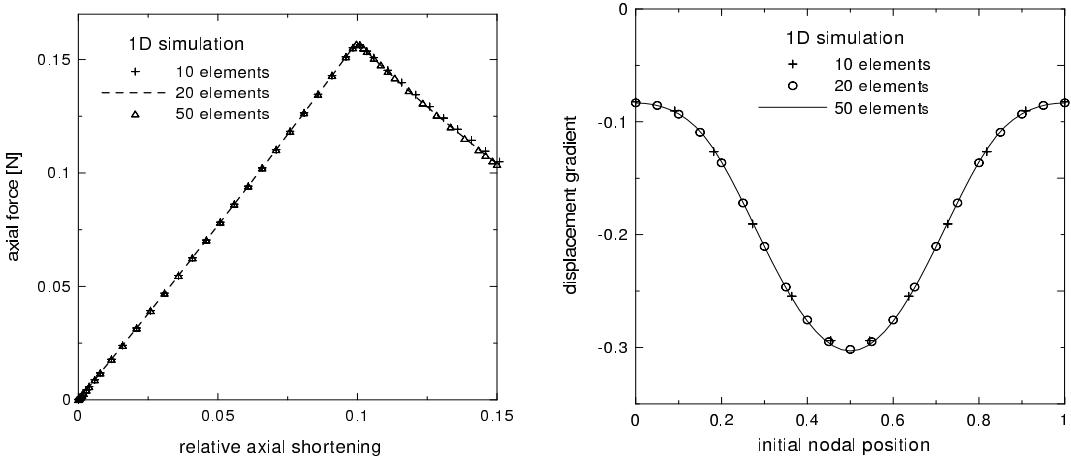


Figure 3. Comparison of three mesh refinements in one-dimensional simulations: (left) evolution of the resulting force versus the axial shortening, and (right) displacement gradient along the bar.

The two constitutive relations are plotted in Figure 2. To observe the influence of the mesh on the numerical solutions, three mesh refinements are used, with 11, 20 and 50 elements, respectively. The three solutions are very close (Figure 3), in terms of force versus bar shortening and deformation profile.

3.3. Two-dimensional simulation. A biaxial test is computed in this section as an example of a two-dimensional problem. Figure 4 shows the initial configuration of the specimen. It is 0.5 m wide and 1 m high (and 1 m thick). The (classical) surface tractions per unit area at both sides of the specimen are set equal to zero. The external additional double forces per unit area P_i are assumed to be zero all along the boundaries. At the top there is a smooth rigid plate remaining horizontal. Through this plate

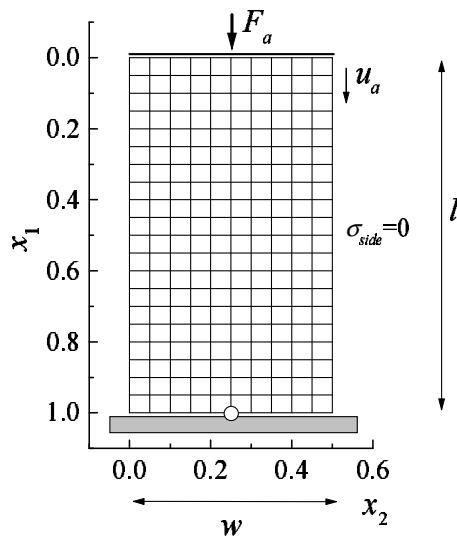


Figure 4. Initial configuration and boundary condition for biaxial test.

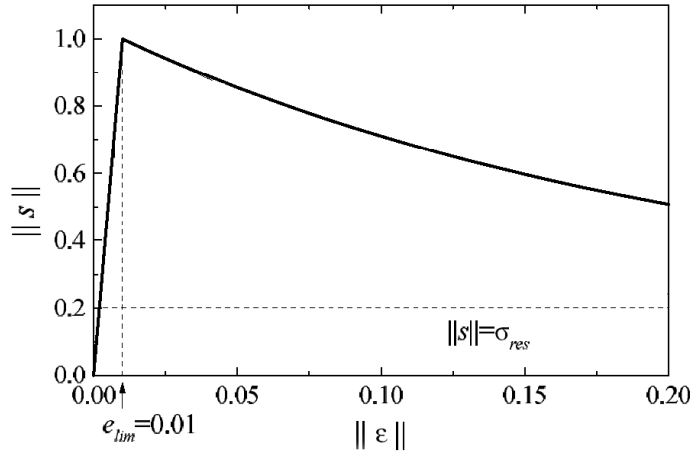


Figure 5. Classical part of the constitutive relation.

a compressive force F_a is applied. The vertical displacement of this top plate is denoted by u_a . At the bottom, there is another rigid and smooth plate, which remains horizontal too. The central point of the bottom plate is fixed to avoid rigid body displacement. The classical part of the constitutive relation is plotted in [Figure 5](#). The parameters are chosen as follows:

$$\begin{aligned} G_1 &= 50 \text{ MPa}, & \bar{G}_2 &= -2 \text{ MPa}, & e_{\text{lim}} &= 0.01, \\ K &= 97.3856 \text{ MPa}, & \sigma_{\text{res}} &= 0.2 \text{ MPa}, & D &= 0.2 \text{ kN}. \end{aligned} \quad (13)$$

Several meshes are compared: structured meshes with 10×20 , 15×30 , 20×40 and 40×80 elements, and an unstructured mesh with 300 elements. The left bottom element of the mesh has a e_{lim} -value reduced of 10% in order to force a localization band in this area. Here, we try to find similar solutions; that is, we don't try to find more than one alternative solution contrary to what is done in the following sections.

The implementation of our element in a general purpose code allows us to go further in the validation procedure. For example, we can work with unstructured meshes, an impossibility until now. Moreover, the use of a general code makes it possible to compare more precisely the similarities (and likely the differences) between different computations. It is often especially difficult to compare solutions of the same problem obtained with different meshes. In the following computations, in order to determine the width of the shear band, instead of comparing contours of some variable (often obtained by some interpolation procedure), we have chosen to look directly at the part of the computed body which loads plastically (inside the localized band). For this purpose, we have marked by a small open square the (plastically) loading Gauss points. In the area where there are no such marks the material unloads elastically.

The localization patterns of solutions ([Figure 6](#)) are very close, and the band thickness depends very little on the mesh size. We want here to emphasize a new result: an unstructured mesh changes neither the orientation nor the width of the band even if its position seems to be a little shifted. However, we have to keep in mind that, since we use an imperfection related to an element, the problems solved in

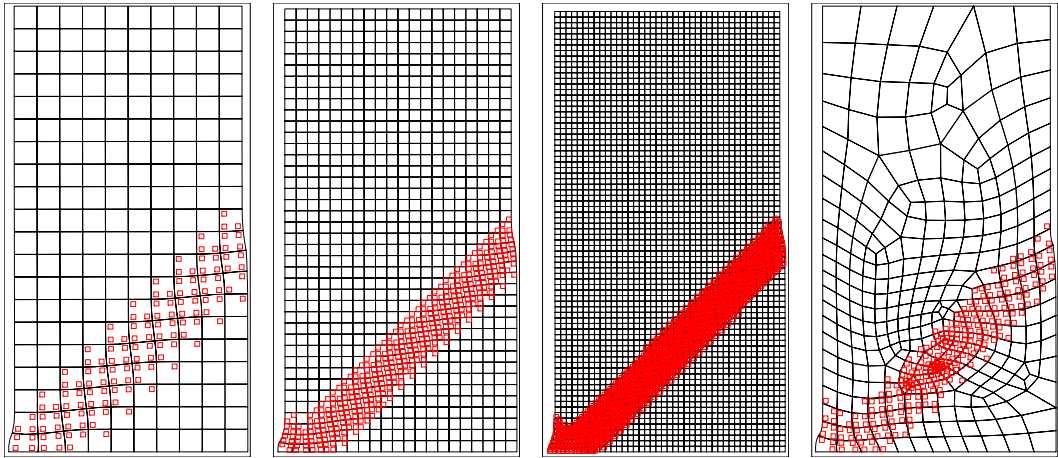


Figure 6. Comparison of the localization patterns for the four meshes 10×20 , 20×40 , 40×80 and an unstructured mesh with 300 elements, respectively. The imperfection is located in the left bottom element. The squares correspond to the integration points which are in the softening loading part; the other integration points are in the elastic regime.

the four cases are not exactly the same. The curves of the loading force versus the specimen shortening (Figure 7) are also very close. The step of band propagation from the imperfection concerns the force peak zone, and as soon as the band is completely propagated through the specimen, the force decreases. When the number of elements is sufficiently high (about 300 elements), or, more objectively, when there are at least about three elements in the band thickness, the curves are perfectly superimposed.

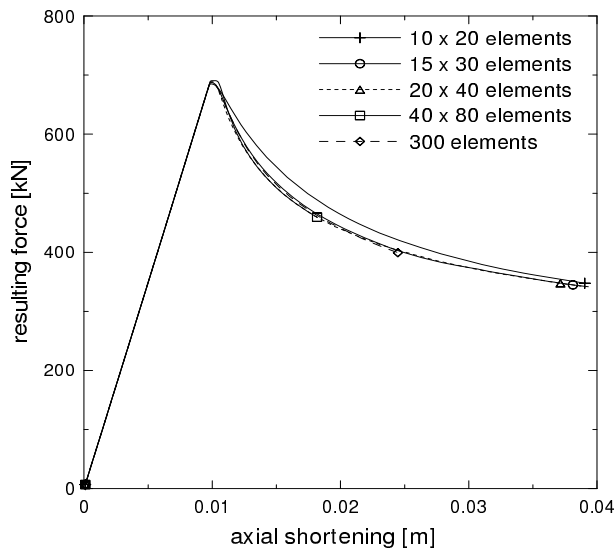


Figure 7. Comparison of the resulting force versus axial shortening curves for the same meshes.

4. Nonuniqueness of solutions

The aim of this section is to show that as soon as strain localization is possible, there can exist several solutions to a boundary value problem, despite of the use of a second-gradient model. Moreover, consistent with experimental observations, it is possible that the computed solutions switch from one pattern to another.

Generalizing Hill's uniqueness theorem [Hill 1958], Chambon and Moullet [2004] demonstrated that, under certain assumptions on the model, local second-gradient models (in the small strain framework) enjoy a uniqueness property. These results, applied to the biaxial problem, allow us to prove that uniqueness of solution is preserved in the elastic regime. In the biaxial problem described above, this unique solution is the homogeneous elastic response for which the response of the second-gradient model is similar to the response of a classical law. When the state of stress reaches the peak of the law, the uniqueness theorem cannot be applied, and, consistent with the numerical results in [Chambon et al. 1998] and in [Chambon and Moullet 2004], more than one solution is possible. It is then interesting to try to generalize the shear band analysis in the spirit of [Rudnicki and Rice 1975].

We present here a bifurcation analysis to search the condition for existence of a localized band. Applied to the second-gradient model used here, such an analysis is a generalization of the pioneering work of Rice [1976] and Rudnicki and Rice [1975]. We will show that for second-gradient models, at least when classical and second-gradient parts are decoupled, the bifurcation analysis is reduced to a bifurcation analysis on the classical part of the constitutive relation. However, the result is weaker in the sense that as soon as the criterion is met, localized solutions are possible, but not in all cases. Let us emphasize this point. This means that the second-gradient model and the underlying classical model have the same prebifurcation curve since second-gradient effects are only active for inhomogeneous fields. But the bifurcation point of the second-gradient model is located beyond the bifurcation point of the classical model, with the difference depending on the size of the modeled sample. It is likely that from the limit case of an infinite sample, both models have the same bifurcation point. Clearly the postbifurcation behavior is different for the two models.

The classical part of the rate law is assumed to be bilinear, and the second gradient law linear. We restrict this analysis by assuming that the so-called small strain assumption holds. So we use the ordinary material stress rates instead of some objective ones like the Jaumann stress rates:

$$\dot{\sigma}_{ij} = K_{ijkl}^e \frac{\partial \dot{u}_k}{\partial x_l} \quad \text{or} \quad \dot{\sigma}_{ij} = K_{ijkl}^{ep} \frac{\partial \dot{u}_k}{\partial x_l} \quad \text{depending on} \quad \frac{\partial \dot{u}_k}{\partial x_l},$$

$$\dot{\Sigma}_{ijk} = A_{ijklmn} \frac{\partial^2 \dot{u}_l}{\partial x_m \partial x_n}.$$

The nonhomogeneous solution is assumed to have the form of a planar band with unit normal n_i . Inside and outside the band, the velocity gradient depends only on the position across the band. The velocity gradient inside and outside the band must have the form

$$\frac{\partial \dot{u}_i^\zeta}{\partial x_j} = \frac{\partial \dot{U}_i}{\partial x_j} + g_i^\zeta n_j,$$

where $\zeta = 1$ inside the band, and $\zeta = 0$ outside. The displacement gradient $\partial \dot{U}_i / \partial x_j$ is assumed homogeneous, and $g_i^\zeta = g_i^\zeta(\alpha)$ are arbitrary vectors depending on the position $\alpha = x_k n_k$ across the band. g_i^1 characterizes the strain field inside the band and g_i^0 corresponds to the near field on each side of the band. To insure the strain continuity, we assume that

$$g_i^1 = g_i^0 \tag{14}$$

at the boundaries of the band. This point deserves a discussion. This is a salient difference with the localization analysis for classical materials. To some extent, we use a second-gradient theory in order to have more regular solutions. From the theoretical point of view, solutions have to be C^1 continuous. Moreover, contrary to what happens for a classical model, a discontinuity of the strain rate could imply that some forces are infinite. Consequently a classical shear band analysis cannot apply a priori to the models used here.

The C^1 continuity requirement is not imposed in the localization analysis developed in [Huang et al. 2005; Iordache and Willam 1998]. In this case, a discontinuity of the Cosserat rotation rate is assumed, which should imply an infinite curvature. However, these studies used *pure* Cosserat models, which means that there is no link between microrotation and macrorotation (see for instance [Chambon et al. 2001a] for a study of the difference between the pure Cosserat model and second-gradient Cosserat model). An analysis allowing discontinuities might be interesting, but an analysis with C^1 continuous fields should be made as well, as we suggested in [Chambon et al. 2001a]. Our opinion is corroborated by the results of Iordache and Willam [1998]. These authors found that the analysis with discontinuities gives results corresponding to compaction or extension bands—for the case for which Cosserat effects are vanishing, which means finally for a classical model.

For simplicity’s sake, we assume that the direction of g_i^ζ over the band is constant and then

$$g_i^\zeta(\alpha) = g^\zeta(\alpha) m_i^\zeta,$$

where $g^\zeta(\alpha)$ are scalar functions and m_i^ζ are constant unit vectors. To simplify the notation, we consider that the solutions on each side of the band are the same (symmetry with respect to the band) and we do not make any difference between the solution on one side and that on the other.

In each point of the body, the stress and double stress fields satisfy conditions of equilibrium in (3). Because the prebifurcation field is presumed uniform, the stress rate and double stress rate at the onset of localization satisfy

$$\frac{\partial \dot{\sigma}_{ij}^\zeta}{\partial x_j} - \frac{\partial^2 \dot{\Sigma}_{ijk}^\zeta}{\partial x_j \partial x_k} = 0. \tag{15}$$

Moreover, at the boundaries of the band, conditions (4) and (5) must be satisfied (the tangential derivative on the boundaries of the band are zero because the displacement gradient depends only on α):

$$\dot{\sigma}_{ij}^0 n_j - \frac{\partial \dot{\Sigma}_{ijk}^0}{\partial x_p} n_p n_j n_k = \dot{\sigma}_{ij}^1 n_j - \frac{\partial \dot{\Sigma}_{ijk}^1}{\partial x_p} n_p n_j n_k, \tag{16}$$

$$\dot{\Sigma}_{ijk}^0 n_j n_k = \dot{\Sigma}_{ijk}^1 n_j n_k, \tag{17}$$

where $(\cdot)^0$ and $(\cdot)^1$ denote quantities outside and inside the band, respectively.

The equilibrium condition inside and outside the band can be written

$$K_{ijkl}^{\zeta} n_j n_l (g_k^{\zeta})' - A_{ijklmn} n_j n_k n_m n_n (g_l^{\zeta})''' = 0, \quad (18)$$

where $(g_k^{\zeta})'$ is the derivative of $g_k^{\zeta}(\alpha)$ in the direction orthogonal to the band. It seems reasonable to assume that $K_{ijkl}^1 = K_{ijkl}^{ep}$ and $K_{ijkl}^0 = K_{ijkl}^e$.

The limit conditions at the two boundaries of the band depend on the constitutive relation which is considered on each side of the interface. For classical constitutive laws, it can be shown that the softer response (that is, the one corresponding to the tensor \mathbf{K}^{ep}) can be considered on each side of the interface to track the first bifurcation condition (see [Bésuelle and Rudnicki 2004] for a review).

Here, Equation (17) becomes:

$$A_{ijklmn} n_j n_k n_m n_n ((g_l^0)' - (g_l^1)') = 0. \quad (19)$$

Since function $g_i(\alpha)$ is continuous at the boundaries of the band (see Equation (14)) and since the material is loading inside the band and unloading outside, this means that it undergoes a neutral loading:

$$K_{ijkl}^{ep} \left. \frac{\partial \dot{u}_k^0}{\partial x_l} \right|_{\alpha=\alpha_a \text{ or } \alpha_b} = K_{ijkl}^e \left. \frac{\partial \dot{u}_k^0}{\partial x_l} \right|_{\alpha=\alpha_a \text{ or } \alpha_b}. \quad (20)$$

Then the limit condition (16) can be written

$$K_{ijkl}^{ep} n_j n_l (g_k^0 - g_k^1) - A_{ijklmn} n_j n_k n_m n_n ((g_l^0)'' - (g_l^1)') = 0. \quad (21)$$

Finally the problem can be summarized as follows:

- outside the band, the following condition, which comes from Equation (15), must be satisfied:

$$\mathcal{H}_{ij}^e (g_j^0)' - \mathcal{A}_{ij} (g_j^0)''' = 0; \quad (22)$$

- inside the band, once more coming from Equation (15), we observe that

$$\mathcal{H}_{ij}^{ep} (g_j^1)' - \mathcal{A}_{ij} (g_j^1)''' = 0; \quad (23)$$

- there must exist two values α^a and α^b for which the following conditions are satisfied:

$$\mathcal{A}_{ij} ((g_j^0)' - (g_j^1)') = 0, \quad (24)$$

which comes from Equation (19), and

$$\mathcal{A}_{ij} ((g_j^0)'' - (g_j^1)') = 0, \quad (25)$$

which comes from Equation (21),

where $\mathcal{H}_{ik}^{ep} = K_{ijkl}^{ep} n_j n_l$, $\mathcal{H}_{ik}^e = K_{ijkl}^e n_j n_l$ and $\mathcal{A}_{il} = A_{ijklmn} n_j n_k n_m n_n$. Note that $|\alpha^a - \alpha^b|$ corresponds to the band thickness.

Since Equations (22)–(23) are ordinary linear differential equations, one can search solutions of the form $g_i^{\zeta}(\alpha) = \gamma_{\zeta} \exp(\lambda_{\zeta} \alpha) m_i^{\zeta}$, where γ_{ζ} are nonzero constants (if $\gamma_{\zeta} = 0$, there is no localization) and λ_{ζ} are the two unknowns of the problem. Then one has to solve

$$(\mathcal{H}_{ij}^{ep} - (\lambda_1)^2 \mathcal{A}_{ij}) m_j^1 = 0 \quad (26)$$

and

$$(\mathcal{H}_{ij}^e - (\lambda_0)^2 \mathcal{A}_{ij}) m_j^0 = 0. \tag{27}$$

There is then a solution corresponding to a nonuniform field if

$$\det(\mathcal{H}_{ij}^{ep} - \Lambda_1 \mathcal{A}_{ij}) = 0, \tag{28}$$

and

$$\det(\mathcal{H}_{ij}^e - \Lambda_0 \mathcal{A}_{ij}) = 0, \tag{29}$$

where $\Lambda_\zeta = (\lambda_\zeta)^2$.

A localized solution corresponds to a strain field involving an extremum. Then this implies $\Lambda_1 < 0$ for an harmonic form for $g^1(\alpha)$ inside the band (while one expects $\Lambda_0 > 0$ outside the band for a hyperbolic form). In fact, we are also guided in this reasoning by the one dimensional analytical solutions obtained by Chambon et al. [1998] and by El Hassan [1997], who demonstrated that the hyperbolic form corresponds to a kind of boundary layer.

Equation (28) is an algebraic equation of degree 3. The third-order term reads $\det(\mathcal{A})$ whereas the zero-order terms reads $\det(\mathcal{H}^{ep})$. If $\Lambda_a, \Lambda_b, \Lambda_c$ are the solutions of this equation, then consequently

$$\det(\mathcal{A}) \Lambda_a \Lambda_b \Lambda_c = \det(\mathcal{H}^{ep}). \tag{30}$$

As a consequence of the choice of an isotropic tensor for the second-order part of the model, we have $\mathcal{A} = D \mathbf{I}$, where \mathbf{I} is the identity tensor. This can be easily checked for the particular value of A_{ijklmn} detailed in Equation (11). So, $\det(\mathcal{A}) = D^3$.

Before the onset of localization, the roots are expected to be positive (no localized solutions). So without any additional assumption, the bifurcation condition as in classical (bilinear) constitutive equation [Chambon et al. 2000] is

$$\det(\mathcal{H}^{ep}) \leq 0. \tag{31}$$

If we assumed the incremental continuity of the classical part of the law, then a necessary and sufficient condition for the sign of one root to change (that is, to have a vanishing root) is

$$\det(\mathcal{H}^{ep}) = 0, \tag{32}$$

which corresponds to the classical bifurcation condition for a classical bilinear law. In this case the result can be found directly by inspecting the annulment of the zero-order term of Equation (28). Moreover, $\det(\mathcal{H}^e) > 0$, and so the solution g_i^0 outside the band is hyperbolic.

As far as the band thickness is concerned, it is given by finding α_a and α_b that satisfy the double condition (24)–(25), which can be reduced here to

$$((g^1)' - (g^0)')|_{\alpha=\alpha_a \text{ or } \alpha_b} = 0 \quad \text{and} \quad ((g^1)'' - (g^0)'')|_{\alpha=\alpha_a \text{ or } \alpha_b} = 0.$$

Note that we assume in the particular form (11) that the parameter D is constant and positive. With other models such as the ones detailed in [Chambon et al. 2001a], plasticity can also occur in the second-gradient part of the model and in this case, D can evolves during the loading. Since the order of magnitude of the thickness of the band is given by the inverse of λ_ζ , the evolution of the thickness of the band is related to the variations of D and of $\det(\mathcal{H}^{ep})$ according to Equation (30).

Coming back to the model defined by Equation (11), where D is assumed to be constant, the thickness of the emerging band corresponding to condition (32) is infinite and decreases when $\det(\mathcal{H}^{\text{ep}})$ decreases. Since an infinite thickness for a finite size boundary value problem is not realistic, the onset of localization can be somewhat delayed when second-gradient models are used. Consequently this criterion is not completely similar to the one of classical media. It is a necessary condition of localization, however since second-gradient models implicitly include an internal length, it is possible that this criterion could be met but without loss of uniqueness for some "small" (with respect to the internal length) problems.

For the particular law adopted in Equations (9)–(11), the bifurcation criterion is satisfied after the deviatoric stress peak.

5. Switching mode of deformation

5.1. Algorithm for nonuniqueness search. When several solutions for a given boundary value problem exist, it can be difficult to know that they exist and to find the other (or some of the other) solutions, especially when the boundary value problem is nonlinear.

As we recall from Section 1, it is not satisfactory to search the null space of one eigenvalue of the tangent stiffness matrix related to the linearized discretized velocity problem. This way is useful for incrementally linear problems such as the ones induced by using a large strain elastic theory, but is only a guess for incrementally nonlinear problems arising when a constitutive equation incorporates some unloading branches.

For numerical computations involving classical constitutive equations, we have developed an algorithm to search several (eventual) solutions to a problem. It takes advantage of the fact that at the beginning of a time step, for the first iteration, the nodal quantities denoted $[\Delta U_{\text{node}}^n]$ in the algorithm presented in Section 2.2 can be freely chosen. The standard choice is to use nodal values related to the ones obtained at the end of the previous time step. Such a choice applied to an initially homogeneous problem generally (though not in all cases) leads to the homogeneous solution. If a random initialization is adopted for $[\Delta U_{\text{node}}^n]$, then it is possible to find nonhomogeneous solutions. In fact, for classical continua, our experience (see [Chambon et al. 2001b]) is that as soon as uniqueness is lost, the duplication of numerical experiments can yield different solutions, changing only some numerical parameters such as the time step size or the first guess of a given time step. Since all of them are properly converged, this means that they are all different solutions of the same initial boundary value problem defined by the same history of boundary conditions.

Recently, this algorithm has been adapted to second-gradient models [Chambon and Moullet 2004]. It has also been implemented in Lagamine, leading to the following numerical results.

5.2. Numerical loss of uniqueness. We present in Figure 8 several localized solutions (well converged) found after a few random initializations. The random initialization algorithm has been activated after a specimen shortening of 0.012 m while the stress peak corresponds to a shortening of 0.01 m. In order to clearly visualize the localized zones, the (plastically) loading Gauss points are marked with small open squares. As in experiments, the width of the bands is completely reproducible. On the contrary, the position, the number, and, more generally, the patterning between several bands are quite different from one numerical experiment to another.

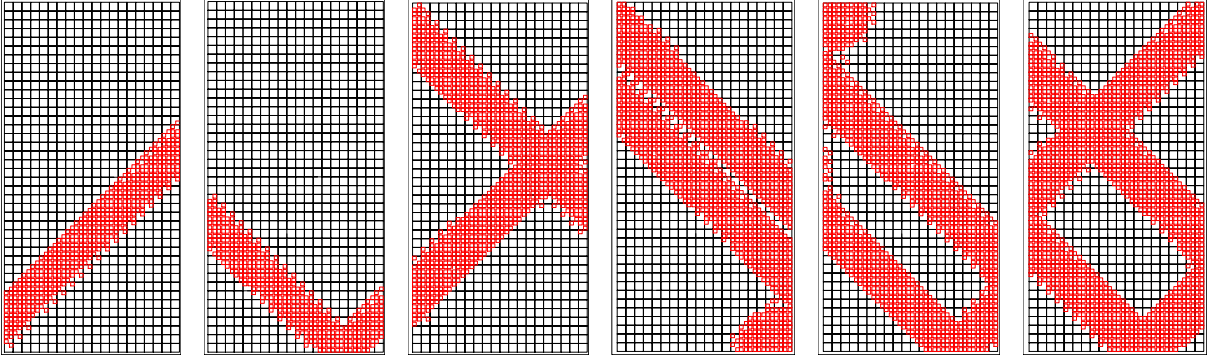


Figure 8. Example of localized solutions obtained after a random initialization, showing solutions with 1, 2 or 3 bands. The squares correspond to the integration points which are in the softening loading part; the other integration points are in the elastic part.

Figure 9 presents the global curves of the resulting force versus the axial shortening; they are clearly organized in several packages, each package being characterized by the number of deformation bands. This observation is similar to what has been seen in the one-dimensional case in [Chambon et al. 1998]. It is clear that the more numerous the bands are, the larger are the areas where plastic loading takes place, and, consequently, the closer the global curves are to the homogeneous case. We can observe that there is no difference between the case with bands crossing the specimen directly from a lateral surface to the opposite one and with band reflection, either on the top or on the bottom rigid plate.

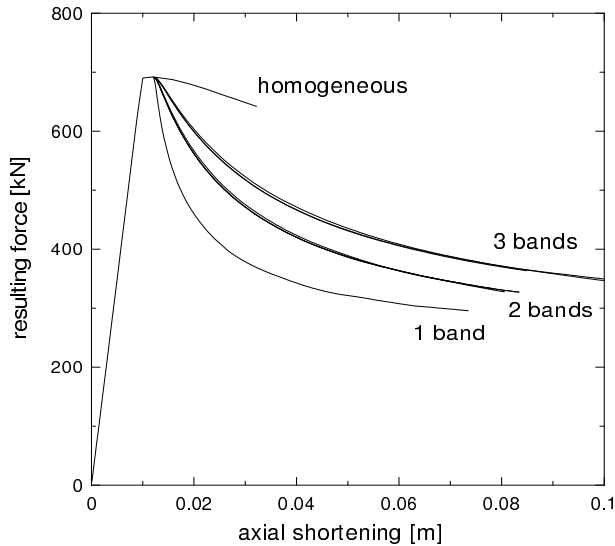


Figure 9. Comparison of the force versus axial shortening evolution of 10 simulations after a random initialization at a shortening of 0.012 m. Curves show that the responses depend on the number of bands. The higher the number of bands, the closer to the homogeneous response the curve is.

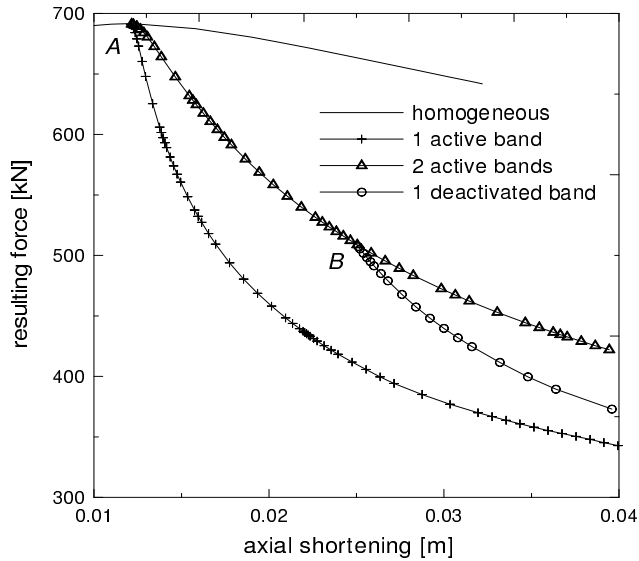


Figure 10. Comparison of the force versus axial shortening evolution in the postpeak regime of (converged) solutions with 1 active band, 2 active bands; and solution after the deactivation of one band. Step A corresponds to the random initialization, and step B corresponds to an *ad hoc* initialization in order to deactivate one band.

So, clearly these results show the nonuniqueness of solutions after the stress peak. The position and the number of bands are not prescribed by this boundary value problem, and we retrieve a variability of the responses similar to what is observed in experiments.

5.3. Numerical mode switching. From the initial homogeneous problem, after the onset of localization, several patterns of localization are possible for the numerical problem. The question addressed in this section is: is a given pattern stable, once activated? In fact, we will show that the pattern can evolve during the loading. If a solution has several bands which are active during the loading process, a solution for the next increment of loading is to keep all the bands active, but other solutions with fewer active bands are also possible. Since the areas outside the bands unload elastically, new bands cannot in fact appear, but it is possible that at a given time, some existing bands start to unload and become inactive.

To check this possibility, we use a method similar to the random initialization algorithm. The first guess used to start the Newton–Raphson iterative procedure is an *ad hoc* set of nodal values $[\Delta U_{\text{node}}^{t_n}]$ corresponding to a deactivation of some bands. An example of such a computation is shown for a two-band solution in Figure 10. A random initialization has been made for a specimen shortening of 0.012 m (step A), giving a two band solution, and the *ad hoc* initialization (step B) has been performed at a shortening of 0.025 m, to deactivate one of the bands. Then, the curve evolves from the two active band solutions to the one active band solution. The deformed meshes and the loading zones are shown in Figure 11 for an axial specimen shortening of 0.04 m. Figure 11, left, shows the result corresponding to a pattern of two active bands. The right hand side of the figure corresponds to a pattern where a band (the upper one) has been deactivated at step B. This figure shows clearly that the area corresponding to the deactivated band is still plastically deformed although it exhibits elastic unloading.

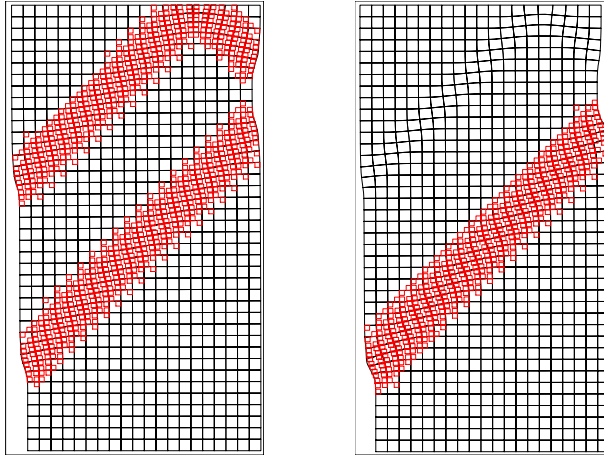


Figure 11. Pattern of active localization bands after the random initialization and (left) without deactivation of band, (right) after deactivation of the upper band. Deformed meshes correspond to the true deformation after a specimen shortening of 0.04 m, without displacement amplification.

6. Conclusion

To properly model localization patterns, the validation of the local second gradient theory has been extended. Localization analysis for this kind of model has been established. This theory is now mature and can be used in computation with some confidence. Similarly, the way of (partially) solving the bifurcation problem by means of different initializations of the Newton–Raphson iteration for a given time step has been extended to multiple bifurcations.

From a qualitative point of view, we are able to retrieve numerically the main features of observations made on experimental data. Especially, the great variability of the postpeak behavior of a sample is modeled realistically. These results have some consequences. First, the postpeak part of the curve cannot be interpreted as the result of a homogeneous response. Consequently, modeling the degradations of material needs enhanced models; moreover, the postpeak part of the curve can be used to get some material parameters only if the complete velocity field is known.

Clearly the results presented here have to be developed. Geomaterials are mainly polyphasic media, which implies the extension of the present model and methods to poromechanics. This has already been done; see [Collin et al. 2006] for details. Similarly, it is interesting to apply the methods presented to a classical constitutive equation less simple (elastic and sudden softening) than the one used here. This is work in progress [Bésuelle and Chambon 2006].

Finally a question arises. Is the loss of uniqueness observed and modeled for laboratory tests significant only for those tests for which homogeneity is required? In other words, can we find similar nonuniqueness problems for engineering situations? Answering such questions is not so easy, but some preliminary results [Al Holo 2005; Chambon and Al Holo 2006] indicate that for some problems, such as the borehole stability problem, the loss of uniqueness is important and may indicate poor reproducibility.

7. Acknowledgments

The authors thank R. Charlier (Liège) and D. Caillerie (Grenoble) for their helpful contributions.

References

- [Al Holo 2005] S. Al Holo, *Etude numérique de la localisation à l'aide d'un modèle de second gradient: Perte d'unicité et évolution de la zone localisée*, Ph.D. thesis, University of Grenoble, France, 2005.
- [Bésuelle 2005] P. Bésuelle, “Implémentation d'un nouveau type d'élément fini dans le code Lagamine pour une classe de lois à longueur interne”, Internal report, FNRS (Belgium), 2005. 1–17.
- [Bésuelle and Chambon 2006] P. Bésuelle and R. Chambon, “Modelling the post-localization regime with local second gradient models: non uniqueness of solutions and non persistent shear bands”, pp. 209–221 in *Modern trends in geomechanics*, edited by W. Wu and H. S. Yu, Springer, Berlin, 2006.
- [Bésuelle and Rudnicki 2004] P. Bésuelle and J. W. Rudnicki, “Localization: shear bands and compaction bands”, pp. 219–321 in *Mechanics of fluid-saturated rocks*, edited by Y. Guéguen and M. Boutéca, International Geophysics Series **89**, Elsevier, 2004.
- [Borja 2002] R. I. Borja, “Bifurcation of elastoplastic solids to shear band mode at finite strain”, *Comput. Methods Appl. Mech. Eng.* **191**:46 (2002), 5287–5314.
- [de Borst 1986] R. de Borst, *Non linear analysis of frictional materials*, Ph.D. thesis, University of Delft, Netherlands, 1986.
- [Challamel and Hijaj 2005] N. Challamel and M. Hijaj, “Non-local behavior of plastic softening beams”, *Acta Mech.* **178**:3–4 (2005), 125–146.
- [Chambon and Al Holo 2006] R. Chambon and S. Al Holo, “The borehole stability problem revisited”, 2006. in preparation.
- [Chambon and Moullet 2004] R. Chambon and J. C. Moullet, “Uniqueness studies in boundary value problems involving some second gradient models”, *Comput. Methods Appl. Mech. Eng.* **193**:27–29 (2004), 2771–2796.
- [Chambon et al. 1998] R. Chambon, D. Caillerie, and N. El Hassan, “One dimensional localisation studied with a second grade model”, *Eur. J. Mech. A: Solids* **17**:4 (1998), 637–656.
- [Chambon et al. 2000] R. Chambon, S. Crochepeyre, and J. Desrues, “Localization criteria for non-linear constitutive equations of geomaterials”, *Mech. Cohes. Frict. Mater.* **5**:1 (2000), 61–82.
- [Chambon et al. 2001a] R. Chambon, D. Caillerie, and T. Matsushima, “Plastic continuum with microstructure, local second gradient theories for geomaterials: localization studies”, *Int. J. Solids Struct.* **38**:46–47 (2001), 8503–8527.
- [Chambon et al. 2001b] R. Chambon, S. Crochepeyre, and R. Charlier, “An algorithm and a method to search bifurcation point in non linear problems”, *Int. J. Numer. Methods Eng.* **51**:3 (2001), 315–332.
- [Chambon et al. 2004] R. Chambon, D. Caillerie, and C. Tamagnini, “A strain space gradient plasticity theory for finite strain”, *Comput. Methods Appl. Mech. Eng.* **193**:27–29 (2004), 2797–2826.
- [Charlier 1987] R. Charlier, *Approche unifiée de quelques problèmes non linéaires de mécanique des milieux continus par la méthode des éléments finis*, Ph.D. thesis, University of Liège, Belgium, 1987.
- [Collin et al. 2006] F. Collin, R. Chambon, and R. Charlier, “A finite element method for poro mechanical modelling of geotechnical problems using local second gradient models”, *Int. J. Numer. Methods Eng.* **65**:11 (2006), 1749–1772.
- [Cosserat and Cosserat 1909] E. Cosserat and F. Cosserat, *Théorie des corps déformables*, Hermann, Paris, 1909.
- [Desrues 1984] J. Desrues, *La localisation de la déformation dans les matériaux granulaires*, Ph.D. thesis, University of Grenoble, France, 1984.
- [Desrues and Hammad 1985] J. Desrues and W. Hammad, “Shear banding dependency on mean stress level in sand”, pp. 57–68 in *Proceedings of the 2nd International Workshop on Localisation and Bifurcation*, edited by E. Dembicki et al., Techn. Univ. Gdansk, Poland, 1985.
- [Desrues and Viggiani 2004] J. Desrues and G. Viggiani, “Strain localization in sand: An overview of the experimental results obtained in Grenoble using stereophotogrammetry”, *Int. J. Numer. Anal. Methods Geomech.* **28**:4 (2004), 279–321.

- [El Hassan 1997] N. El Hassan, *Modélisation théorique et numérique de la localisation de la déformation dans les géomatériaux*, Ph.D. thesis, University of Grenoble, France, 1997.
- [Fleck and Hutchinson 1997] N. A. Fleck and J. W. Hutchinson, “Strain gradient plasticity”, pp. 295–361 in *Solid mechanics*, edited by J. W. Hutchinson and T. Y. Wu, Advances in Applied Mechanics **33**, Academic Press, San Diego, CA, 1997.
- [Germain 1973] P. Germain, “La méthode des puissances virtuelles en mécanique des milieux continus, I: Théorie du second gradient”, *J. Mécanique* **12**:2 (1973), 235–274.
- [Hill 1958] R. Hill, “A general theory of uniqueness and stability in elastic-plastic solids”, *J. Mech. Phys. Solids* **6**:3 (1958), 236–249.
- [Huang et al. 2005] W. Huang, M. Hijaj, and S. C. Sloan, “Bifurcation analysis for shear localization in non-polar and micropolar hypoplastic continua”, *J. Eng. Math.* **52**:1 (2005), 167–184.
- [Ikeda and Murota 2002] K. Ikeda and K. Murota, *Imperfect bifurcation in structures and materials*, Springer, Berlin, 2002.
- [Ikeda et al. 1997] K. Ikeda, K. Murota, Y. Yamakawa, and E. Yanagisawa, “Modes switching and recursive bifurcation in granular materials”, *J. Mech. Phys. Solids* **45**:11–12 (1997), 1929–1953.
- [Ikeda et al. 2003] K. Ikeda, Y. Yamakawa, and S. Tsutumi, “Simulation and interpretation of diffuse mode bifurcation of elastoplastic solids”, *J. Mech. Phys. Solids* **51**:9 (2003), 1649–1673.
- [Iordache and Willam 1998] M. M. Iordache and K. Willam, “Localized failure analysis in elastoplastic Cosserat continua”, *Comput. Methods Appl. Mech. Eng.* **151**:3–4 (1998), 559–586.
- [Matsushima et al. 2002] T. Matsushima, R. Chambon, and D. Caillerie, “Large strain finite element analysis of a local second gradient model: application to localization”, *Int. J. Numer. Methods Eng.* **54**:4 (2002), 499–521.
- [Mindlin 1964] R. D. Mindlin, “Micro-structure in linear elasticity”, *Arch. Ration. Mech. An.* **16**:1 (1964), 51–78.
- [Nübel and Huang 2004] K. Nübel and W. Huang, “A study of localized deformation pattern in granular media”, *Comput. Methods Appl. Mech. Eng.* **193**:27–29 (2004), 2719–2743.
- [Pijaudier-Cabot and Bažant 1987] G. Pijaudier-Cabot and Z. Bažant, “Nonlocal damage theory”, *J. Eng. Mech.* **113** (1987), 1512–1533.
- [Rice 1976] J. R. Rice, “The localization of plastic deformation”, pp. 207–220 in *14th International Congress on Theoretical and Applied Mechanics* (Delft), edited by W. T. Koiter, North-Holland, Amsterdam, 1976.
- [Rudnicki and Rice 1975] J. W. Rudnicki and J. R. Rice, “Conditions for the localization of deformation in pressure-sensitive dilatant materials”, *J. Mech. Phys. Solids* **23**:6 (1975), 371–394.
- [Steinmann et al. 1997] P. Steinmann, R. Larsson, and K. Runesson, “On the localization properties of multiplicative hyperelasto-plastic continua with strong discontinuities”, *Int. J. Solids Struct.* **34**:8 (1997), 969–990.
- [Tamagnini et al. 2001] C. Tamagnini, R. Chambon, and D. Caillerie, “A second gradient elastoplastic cohesive frictional model for geomaterials”, *C. R. Acad. Sci. II B Mec.* **329**:10 (2001), 735–739.
- [Toupin 1962] R. A. Toupin, “Elastic materials with couple-stresses”, *Arch. Ration. Mech. An.* **11**:1 (1962), 385–414.
- [Viggiani et al. 2001] G. Viggiani, M. Küntz, and J. Desrues, “An experimental investigation of the relationships between grain size distribution and shear banding in sand”, pp. 111–127 in *Continuous and discontinuous modelling of cohesive-frictional materials*, edited by P. A. Vermeer et al., Springer, Berlin, 2001.

Received 11 Dec 2005. Revised 20 Apr 2006. Accepted 5 May 2006.

PIERRE BÉSUELLE: Pierre.Besuelle@hmg.inpg.fr

Laboratoire 3S, Grenoble, Université Joseph Fourier, Institut National Polytechnique, C.N.R.S. U.M.R. 5521, B.P. 53X, 38041 Grenoble Cedex 9, France

RENÉ CHAMBON: Rene.Chambon@hmg.inpg.fr

Laboratoire 3S, Grenoble, Université Joseph Fourier, Institut National Polytechnique, C.N.R.S. U.M.R. 5521, B.P. 53X, 38041 Grenoble Cedex 9, France

FRÉDÉRIC COLLIN: F.Collin@ulg.ac.be

Geomac, FNRS-ULG, Liège, Belgium

INCREMENTAL MODELING OF T-STUB CONNECTIONS

MINAS E. LEMONIS AND CHARIS J. GANTES

An incremental model for predicting the mechanical characteristics of T -stub steel connections is presented in this paper. The response is calculated analytically on the basis of a simple beam representation for the flange and a deformational spring for the bolt. Contact phenomena in the flange are taken into account, and by means of an incremental procedure it becomes possible to follow the development of these phenomena throughout the loading history. Material nonlinearity is also accounted for, both in the flange and the bolt, assuming a bilinear constitutive model. We propose several refinements of the model, which enhance its effectiveness with respect to intricate characteristics of T -stub behavior, such as bolt-flange interaction and three-dimensional geometry. The performance of the model is validated by comparison to experimental results found in the literature and by a parametric study performed in parallel with three-dimensional finite element analyses.

1. Introduction

Advanced analysis of steel structures requires extensive information regarding the behavior of both the members and the joints. For the members, well established methodologies exist to account for nonlinearities in response. However, for joints, a similar level of methods is not available to predict response characteristics, and in particular the moment-rotation curve. This shortcoming is mainly due to the complex nature of joints, which are assemblages of multiple parts. Material and geometrical nonlinearities, contact phenomena, geometrical complexity and multiple typologies which govern the behavior of joints are an obstacle towards a systematic, theoretical, yet pragmatic treatment of this subject. To subdivide the problem, one can identify joint components with simplified behavior, and then reproduce the total response as an assembly of the partial responses of the individual components. In this context, various mechanical spring assemblies have been proposed for stiffness and strength calculations [Huber and Tschemmernegg 1998; CEN 2003], while a similar process has been suggested for other characteristics, such as rotational capacity and full moment-rotation curve [Kuhlmann and Kuhnemund 2000; Beg et al. 2004]. Generally, components of tensile, compressive and shear deformability can be identified in structural joints. The tensile components of common bolted joints, which provide the major source of deformability, have the form of equivalent T -stub connections [Yee and Melchers 1986; Weynand et al. 1995; Shi et al. 1996], as shown in Figure 1a.

Numerous research works are dedicated to the analytical estimation of strength and stiffness of T -stub connections. [Zoetemeijer 1974; Agerskov 1976; Yee and Melchers 1986], among others, contributed to a basis for the currently established and codified T -stub model [CEN 2003]. Regarding the complete

The research in this paper is part of a project which is cofunded by the European Social Fund (75%) and National Resources (25%). This contribution is gratefully acknowledged.

Keywords: T-stub connection, T-stub model, steel connections, contact phenomena, nonlinearity.

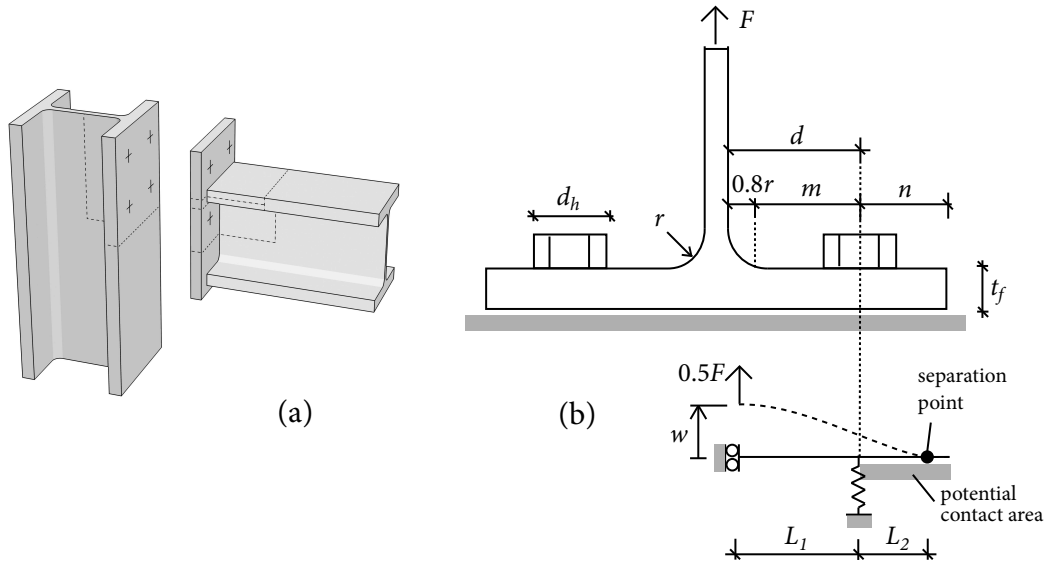


Figure 1. (a) *T*-stub components in a bolted beam-to-column joint and (b) *T*-stub definitions and the analytical model (b).

force-displacement curve, available methodologies include the bilinear model of [Jaspart 1991], the quadrilinear model of [Faella et al. 2000], the incremental model of [Swanson and Leon 2001] and the finite element beam model of [Girão Coelho et al. 2004]. An alternative approach for prediction of *T*-stub response is the advanced finite element modeling. Further contributions have been devoted to this subject which employ 2D plane elements [Mistakidis et al. 1997] or 3D brick elements [Sherbourne and Bahaari 1996; Bursi and Jaspart 1997; Wanzek and Gebbeken 1999]. The performance of such models is generally very good, since geometrical characteristics and nonlinearities are adequately modeled. However, the merit of these models for practical design purposes is limited, due to the special software requirements they pose, their high computational cost and the large amount of output data they produce.

In this paper we propose an incremental analytical model for the prediction of the complete force-displacement curve of the *T*-stub connection. The proposed model is designed for implementation in a computer program rather than hand calculation and assumes the following as relevant objectives: credible results, ease of programming, and minimum dependency on special software. To achieve credible results, our model is designed for implementation in a computer program rather than hand calculation. Published methodologies for prediction of the whole force-displacement curve generally require computer implementation [Faella et al. 2000; Swanson and Leon 2001; Girão Coelho et al. 2004]. In fact, *T*-stub behavior is so complicated that implementing a simplified method suitable for hand calculation would unavoidably compromise the credibility of the model. This becomes an even greater problem for the whole joint, since multiple components must be analyzed.

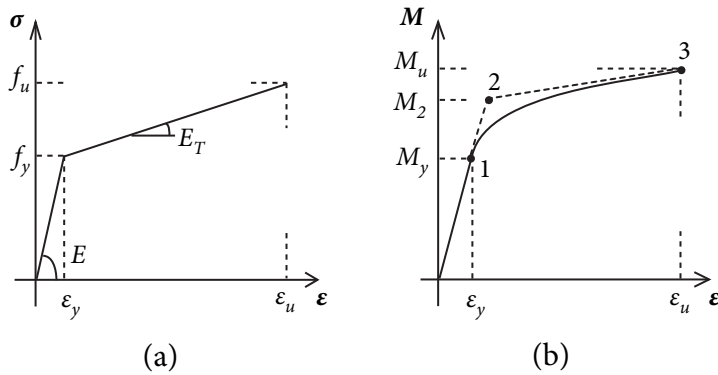


Figure 2. (a) Flange material modeling and (b) corresponding moment-outer fiber strain diagram.

2. Model description

T-stub connections are fairly complex to analyze. Their geometry is three-dimensional, and includes contact phenomena as well as interaction between the flanges and the bolts. Some compromises are taken into consideration to circumvent these difficulties. We first adopted a two-dimensional representation of the problem. This is opposed to the actual geometry which is three-dimensional due to the bolts and the holes at the flanges. As shown in Figure 1b, the analysis is based on classical beam theory, with the flanges modeled as beams and the bolts as springs of equivalent stiffness located at the axes of the physical bolts. Taking advantage of symmetry, we model only one half of the *T*-stub. The initially unknown distance of the flange edge, where the symmetry condition is enforced, from the bolt axis, is L_1 . The area extending from the bolt spring to the free end is considered as potential contact area where partial separation might occur. The separation length measured from the bolt axis is L_2 . Displacement w is identical to the vertical deflection of the flange mid-thickness at the symmetry plane which passes along the web.

2.1. Material nonlinearity. Both the flanges and the bolts feature a bilinear material law with strain hardening, shown in Figure 2a with E and E_T denoting the elasticity modulus and the hardening modulus respectively, ϵ_y , ϵ_u the yield and ultimate strain and f_y , f_u the yield and ultimate stress. Figure 2b shows the bending moment M – the outer fiber strain ϵ diagram for a rectangular cross section with this type of material. Point 1 of the diagram denotes the end of the elastic region, when the outer fibers of the cross section reach their yield strain ϵ_y . Beyond this point, and as larger parts of the cross section enter the plastic region, the curve gradually softens, up to the point of fracture, denoted by point 3 in the diagram.

It is assumed that fracture occurs when the outer fibers of the cross section reach their ultimate strain ϵ_u . Thus, the ultimate moment resistance can be expressed as

$$M_u = \frac{bt_f^2}{12} \left(3(E - E_T)\epsilon_y + 2E_T\epsilon_u - \frac{(E - E_T)\epsilon_y^3}{\epsilon_u^2} \right), \tag{1}$$

where b is the width of the flange, and the other symbols are shown in Figures 1b and 2a. When $\varepsilon_u \gg \varepsilon_y$, a hypothesis valid for steel, Equation (1) is simplified to become

$$M_u = \frac{bt_f^2}{12} (f_y + 2f_u). \quad (2)$$

We introduce an additional simplification regarding nonlinearity of the $M - \varepsilon$ curve. This curve is approximated by a bilinear representation, with the linear segments lying tangential to the original curve at points 1 and 3. The intersection of the two segments at point 2 in Figure 2b is proven to take place for a moment equal to

$$M_2 = \frac{bt_f^2}{4} f_y. \quad (3)$$

The bilinear simplification of the $M - \varepsilon$ curve allows one to distinguish the flange beam in parts where the bending moments have surpassed M_2 (and subsequently modulus E_T characterizes the material response), from the remaining parts, which remain elastic.

For the bolt, the bilinear material law results in a bilinear force versus elongation curve, since bolts are only subjected to tensile loading, so that calculation of the respective characteristics of the curve is straightforward.

2.2. Contact phenomena. A complex aspect of the T -stub behavior involves the contact of the flange surfaces. In existing methods [Jaspart 1991; Faella et al. 2000; Swanson and Leon 2001], the location of prying actions is predetermined and remains constant through the whole loading history. In our model, we make no assumption regarding the location of the prying actions. Instead, the part of the flange extending from the bolt location to the free end is considered as the potential contact area where partial separation might occur. A unique separation point appears somewhere within this area and the beam length beyond this point remains in complete contact with its base as shown in Figure 1b. Assuming that the base is infinitely rigid, this part of the beam remains straight, with zero curvature and, thus, zero moment. Due to continuity of the flange, the same conditions should apply locally to the separation point through the deformed part as well. Hence, both the rotation and the moment of the flange on both sides of the separation point should be zero. The calculation process takes advantage of these conditions to find the location of the separation point, as described later in this section.

The separation length L_2 changes during the loading progress, while additional parts of the flange or the bolt enter the plastic region, and we implement this behavior in the proposed incremental model. The conditions of zero moment and rotation apply throughout the response. Figure 3 shows the model used for the calculations, with the state of the total response in step i of the incremental process. The label A shows the edge near the web, located at a distance L_1 from the bolt axis, while B shows the bolt axis position, where the bolt spring is connected to the flange. Point C^i indicates the separation point at the current step i , with the current separation length L_2^i . Figure 3 also shows the incremental response between steps i and $i+1$, where the new separation point is indicated by C^{i+1} and the new separation length is L_2^{i+1} . For calculation of the new separation length L_2^{i+1} , a moment constraint is applied to the separation point C^{i+1} which allows for expression of the respective moment reaction as a function of the unknown L_2^{i+1} . However, as mentioned earlier, the separation point C^{i+1} must fulfill zero moment conditions. Therefore, we obtain an appropriate length L_2^{i+1} which causes the total moment to edge

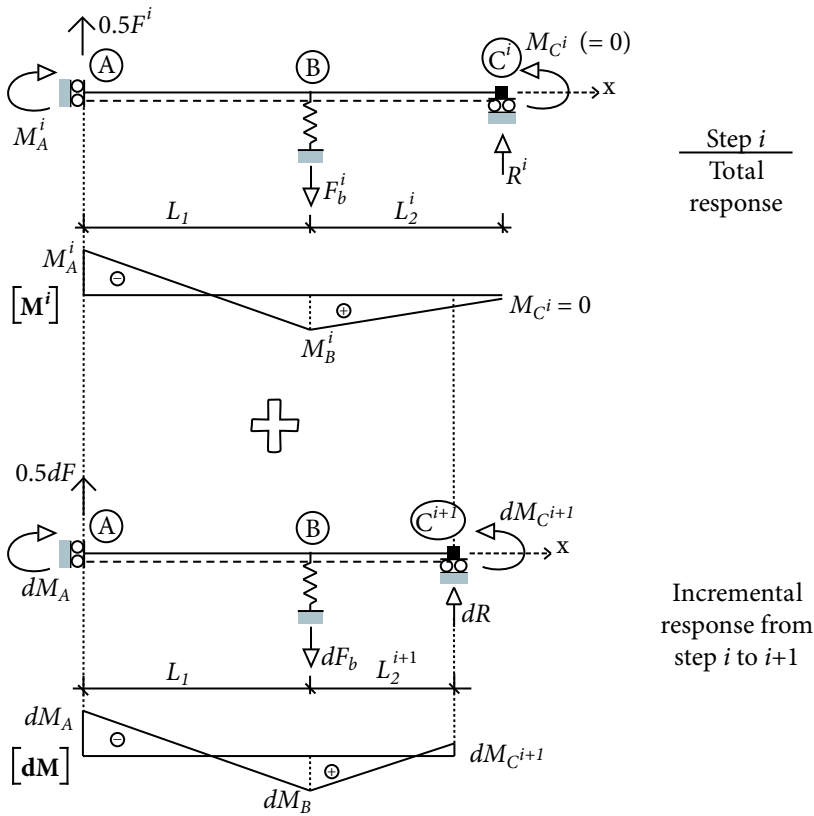


Figure 3. Incremental treatment of contact phenomena.

C^{i+1} to be zero. Note that the constraint symbol used in Figure 3 at the separation point represents a full moment support, but it differs from the conventional clamping symbol to signify the zero actual moment at this point. The enforcement of zero moment at the new separation point C^{i+1} , in the total response of step $i + 1$, is given by

$$M_{C^{i+1}} = M^i(x = L_1 + L_2^{i+1}) + dM_{C^{i+1}} = 0 \Rightarrow \tag{4}$$

$$M_B^i L_2^i - M_B^i L_2^{i+1} + dM_{C^{i+1}} L_2^i = 0. \tag{5}$$

The total moment M_B^i is known from the previous step but the incremental moment $dM_{C^{i+1}}$ is a function of the new separation length L_2^{i+1} . Further elaboration of Equation (5) will be given in Section 2.4, where the required quantities of the response will be available analytically.

2.3. Flange length L_1 . The modeled flange features a constant cross section. However, near the web, the real flange cross section gradually increases in height. The critical position for strength calculations, according to prEN 1993-1-8 [CEN 2003], lies at a distance $0.2r$ from the start of the flange-to-web fitting. However, using this length for stiffness calculations leads to overestimation of the response because the deformability of the remaining part of the fitting is ignored. Therefore, in our proposed model, we take

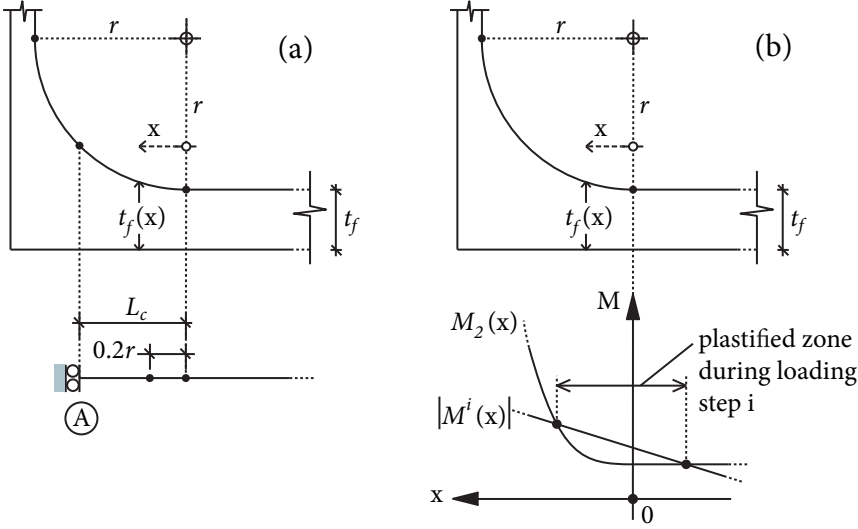


Figure 4. Approximation using the analytical model of (a) the flange-to-web fitting, and (b) definition of the plastified zone in the same region.

into account the total fitting length up to the web face. Because the real fitting has a variable cross section, an equivalent length L_c of constant cross section as shown in Figure 4a, is used so that the flexural stiffness of the two is equal as follows:

$$\int_0^r \frac{1}{EI(x)} dx = \int_0^{L_c} \frac{1}{EI} dx \Rightarrow \tag{6}$$

$$\int_0^r \frac{1}{(t_f(x))^3} dx = \int_0^{L_c} \frac{1}{t_f^3} dx. \tag{7}$$

The function $t_f(x)$ of the cross section height at a distance x from the start of the circular fitting, as shown in Figure 4a, is

$$t_f(x) = t_f + r - \sqrt{r^2 - x^2}. \tag{8}$$

The analytical integration of the left side of (7) is not readily available. Instead the trapezoidal rule can be applied as

$$\text{Int} = \int_0^r \frac{1}{t_f(x)^3} dx = \frac{r}{2k} \left(\frac{1}{t_f^3} + \frac{1}{(t_f + r)^3} + 2 \sum_{j=1}^{k-1} \frac{1}{t_{f,j}^3} \right), \tag{9}$$

where $t_{f,j} = t_f(x = j \frac{r}{k})$ and k the number of trapezoids to be used for the approximation. Typically, values of k equal to 4 or 5 provide sufficient accuracy. The equivalent fitting length should then be derived from (7) as

$$L_c = t_f^3 \text{Int}. \tag{10}$$

Figure 4b illustrates the relevant process of obtaining the plastified flange zone at the flange-to-web fitting, which will be investigated in the following section.

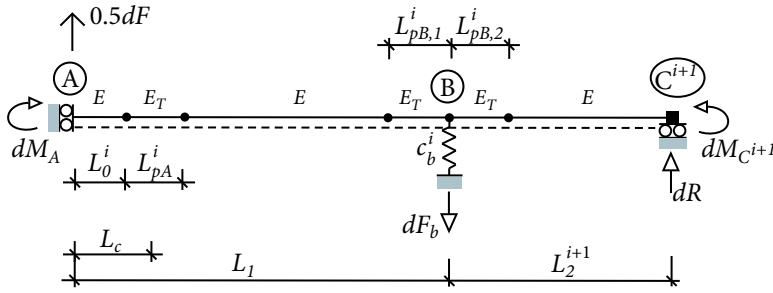


Figure 5. The proposed incremental model with all potential plastification zones in the flange.

2.4. Model response. The model is solved using the force method. As mentioned earlier, the incremental model features a moment constraint at C . Neglecting longitudinal forces, it is twice statically indeterminate. In **Figure 5**, the proposed incremental model is depicted in its more general form, with plastified parts in the flange-to-web fitting of length L_{pA}^i and at the bolt area of lengths $L_{pB,1}^i, L_{pB,2}^i$ where superscript i indicates the loading step. The resulting quantities of its response were obtained analytically and are summarized in **Table 1**. From this table, the incremental prying force dR , bolt force dF_b as well as moments $dM_{C^{i+1}}, dM_A$ and dM_B , which correspond to points C^{i+1}, A and B respectively, can be calculated for a given value of the applied incremental force dF . Then, the incremental displacement dw of the T -stub can be calculated from the partial displacements $dw_{j=0...2}$. **Section 4.3** provides details regarding the displacement dw_s . No special physical meaning is attributed to the parameters $s_{j=0...2}, p_{j=0...3}, q_{j=0...4}, G_1, G_2$ and λ listed in **Table 1**. These parameters are used to calculate the aforementioned incremental quantities of the model response, to reduce the complexity of the algebraic expressions.

Purely elastic response as well as special cases such as plastification near the flange-to-web fitting can be derived from the expressions of **Table 1** by substituting the respective plastification lengths with zero. This facilitates implementation of the model in computer code by avoiding multiple programming paths.

The plastification length L_{pA}^i is not adjacent to A but allows for a flange length L_0^i to remain elastic. This compensates for its increased moment resistance. The exact value of length L_{pA}^i and its position is obtained by solving

$$|M^i(x)| = M_2(x), \tag{11}$$

where $M^i(x)$, the total bending moment in the flange during loading step i at distance x from the start of the fitting, is defined as

$$M^i(x) = M_A^i + 0.5F^i(L_c - x). \tag{12}$$

The moment resistance $M_2(x)$ is calculated from Equation (3), where instead of the constant cross section height t_f , we use

$$t_f(x) = \begin{cases} t_f + r - \sqrt{r^2 - x^2}, & x > 0, \\ t_f, & x \leq 0. \end{cases} \tag{13}$$

If plastification occurs, solution of Equation (11) provides two roots as shown in **Figure 4b** for the definition of the length L_{pA}^i . Because part of the distance between the two roots obtained by (11) is located at the flange-to-web fitting, where the flange height is variable, a correction similar to the one

$$dR = \frac{3dF}{2} \frac{s_2(L_2^{i+1})^2 + s_1L_2^{i+1} + s_0}{q_4(L_2^{i+1})^4 + q_3(L_2^{i+1})^3 + q_2(L_2^{i+1})^2 + q_1L_2^{i+1} + q_0}$$

$$dM_{C^{i+1}} = -\frac{dF}{2} \frac{p_3(L_2^{i+1})^3 + p_2(L_2^{i+1})^2 + p_1L_2^{i+1} + p_0}{q_4(L_2^{i+1})^4 + q_3(L_2^{i+1})^3 + q_2(L_2^{i+1})^2 + q_1L_2^{i+1} + q_0}$$

$$dF_b = \frac{dF}{2} + dR$$

$$dM_A = -\frac{dF}{2}L_1 + dRL_2^{i+1} + dM_{C^{i+1}}, \quad dM_B = dRL_2^{i+1} + dM_{C^{i+1}}$$

$$dw = dw_0 + dRdw_1 + dM_{C^{i+1}}dw_2 (+dw_s)$$

$$dw_0 = \frac{dF}{6EI} \left(L_1^3 + \lambda \left((L_{pA}^i)^3 + (L_{pB,1}^i)^3 + 3L_{pA}^i(L_1 - L_0^i)(L_1 - L_0^i - L_{pA}^i) \right) + \frac{3EI}{c_b^i} \right)$$

$$dw_1 = -\frac{1}{2EI} \left(L_1^2L_2^{i+1} + \lambda L_2^{i+1}G_1 - \frac{2EI}{c_b^i} \right), \quad dw_2 = -\frac{1}{2EI} (L_1^2 + \lambda G_1), \quad dw_s = 0.5 \frac{dFL_1}{GA}$$

$$s_2 = c_b^i(L_1^2 + \lambda G_1)$$

$$s_1 = -4EI$$

$$s_0 = -4EI(L_1 + \lambda G_2) + c_b^i\lambda(L_{pB,2}^i)^2(L_1^2 + \lambda G_1)$$

$$p_3 = c_b^i(L_1^2 + \lambda G_1)$$

$$p_2 = -6EI$$

$$p_1 = -12EI(L_1 + \lambda G_2) + 3c_b^i\lambda(L_{pB,2}^i)^2(L_1^2 + \lambda G_1)$$

$$p_0 = -6EI(L_1^2 + \lambda(G_1 - (L_{pB,2}^i)^2)) - 2c_b^i\lambda(L_{pB,2}^i)^3(L_1^2 + \lambda G_1)$$

$$q_4 = c_b^i$$

$$q_3 = 4c_b^i(L_1 + \lambda G_2)$$

$$q_2 = -6c_b^i\lambda(L_{pB,2}^i)^2$$

$$q_1 = 12EI + 4c_b^i\lambda(L_{pB,2}^i)^3$$

$$q_0 = 12EI(L_1 + \lambda G_2) + 4c_b^i\lambda(L_{pB,2}^i)^3(L_1 + \lambda(G_2 - \frac{3L_{pB,2}^i}{4}))$$

$$G_1 = 2(L_1 - L_0^i)L_{pA}^i + (L_{pB,1}^i)^2 - (L_{pA}^i)^2$$

$$G_2 = L_{pA}^i + L_{pB,1}^i + L_{pB,2}^i \quad \lambda = \frac{E - E_T}{E_T}$$

Table 1. Analytical expressions for the incremental response from step i to $i + 1$.

mentioned in Section 2.3 is required, to correspond to the constant cross section height t_f used for the flange in the model. The only difference is in the computation of the integral in Equation (9), in which the minimum of two roots should be used as lower boundary and the maximum one as upper boundary.

A similar procedure can be used for determining the plastified lengths $L_{pB,1}^i$ and $L_{pB,2}^i$. In this case however, the flange cross section remains constant, so the computations for the two lengths are more straightforward.

Substituting $dM_{C^{i+1}}$ from Table 1 into Equation (5), the separation length L_2^{i+1} in the new step can be calculated from the following fifth order polynomial equation:

$$m_5(L_2^{i+1})^5 + m_4(L_2^{i+1})^4 + m_3(L_2^{i+1})^3 + m_2(L_2^{i+1})^2 + m_1L_2^{i+1} + m_0 = 0, \quad (14)$$

where the factors $m_{j=0\dots5}$ are:

$$\begin{aligned} m_5 &= -M_B^i q_4 \\ m_4 &= M_B^i L_2^i q_4 - M_B^i q_3 \\ m_3 &= M_B^i L_2^i q_3 - M_B^i q_2 - 0.5dFL_2^i p_3 \\ m_2 &= M_B^i L_2^i q_2 - M_B^i q_1 - 0.5dFL_2^i p_2 \\ m_1 &= M_B^i L_2^i q_1 - M_B^i q_0 - 0.5dFL_2^i p_1 \\ m_0 &= M_B^i L_2^i q_0 - 0.5dFL_2^i p_0 \end{aligned} \quad (15)$$

and the factors $q_{j=0\dots4}$, $p_{j=0\dots3}$ are the same as in Table 1.

Equation (14) is best solved using a Newton–Raphson scheme since the derivative is easily available. If the obtained solution from (14) exceeds the physical length n of the T -stub, then no partial contact occurs in the flange and instead a simple support at the flange edge should be applied. In that case, the incremental model is once statically indeterminate and its response differs from the one given in Table 1. The required quantities of the response, with simple support conditions at the flange edge are presented in Table 2. For a given value of the applied incremental force dF , we calculate the incremental forces dR and dF_b , moments, dM_A and dM_B , and subsequently, from the same table, the incremental displacement dw . As with Table 1, no special physical meaning is attributed to the parameters $s_{j=0\dots1}$, $q_{j=0\dots3}$, G_1 , G_2 and λ . Length L_2^{i+1} in Table 2 is equal to distance n from bolt axis to flange edge. However, the notation is retained for reasons of uniformity and continuity of the expressions.

Once simple support conditions apply to the edge, the flange rotation φ_C at this location becomes nonzero. The occurrence of partial contact again, at a later load increment, for example in case of subsequent plastification in the flange, should be allowed only after the negation of this previously accumulated rotation φ_C , together with a solution of (14) for a length L_2^{i+1} less than the physical length n .

3. Solution process

The objective of the solution process is to generate the load F vs. displacement w curve. The scheme of the incremental process is shown in Figure 6. At each cycle of the process, an incremental loading is determined and the incremental response and the new separation length are calculated. Then, the incremental response of the current load increment is appended to the last total response. At this point the

$$dR = \frac{3dF}{4} \frac{s_1 L_2^{i+1} + s_0}{q_3 (L_2^{i+1})^3 + q_2 (L_2^{i+1})^2 + q_1 L_2^{i+1} + q_0}$$

$$dF_b = \frac{dF}{2} + dR$$

$$dM_A = -\frac{dF}{2} L_1 + dR L_2^{i+1}, \quad dM_B = dR L_2^{i+1}$$

$$dw = dw_0 + dR dw_1 (+dw_s)$$

$$dw_0 = \frac{dF}{6EI} \left(L_1^3 + \lambda \left((L_{pA}^i)^3 + (L_{pB,1}^i)^3 + 3L_{pA}^i (L_1 - L_0^i) (L_1 - L_0^i - L_{pA}^i) \right) + \frac{3EI}{c_b^i} \right)$$

$$dw_1 = -\frac{1}{2EI} \left(L_1^2 L_2^{i+1} + \lambda L_2^{i+1} G_1 - \frac{2EI}{c_b^i} \right)$$

$$dw_s = 0.5 \frac{dF L_1}{GA}$$

$$s_1 = c_b^i (L_1^2 + \lambda G_1)$$

$$s_0 = -2EI$$

$$q_3 = c_b^i$$

$$q_2 = 3c_b^i (L_1 + \lambda G_2)$$

$$q_1 = -3c_b^i \lambda (L_{pB,2}^i)^2$$

$$q_0 = 3EI + c_b^i \lambda (L_{pB,2}^i)^3$$

$$G_1 = 2(L_1 - L_0^i) L_{pA}^i + (L_{pB,1}^i)^2 - (L_{pA}^i)^2$$

$$G_2 = L_{pA}^i + L_{pB,1}^i + L_{pB,2}^i \quad \lambda = \frac{E - E_T}{E_T}$$

$$L_2^{i+1} = \text{the distance } n \text{ from bolt axis to flange edge}$$

Table 2. Analytical expressions for the incremental response with simple support conditions at the flange edge from step i to $i + 1$.

total bending moments of the flange and the total bolt force are known and therefore decisions regarding the plastification or failure of flange regions or the bolt can be made. The new flange plastification lengths and the bolt stiffness are computed before a new cycle starts. The process continues until failure is detected either in the flange or in the bolt.

4. Model refinements

4.1. Bolt head size. In real T -stubs, the bolt acts on the flange through its head within an extended region of contact between flange and bolt head. However, in our model bolt action is concentrated at a

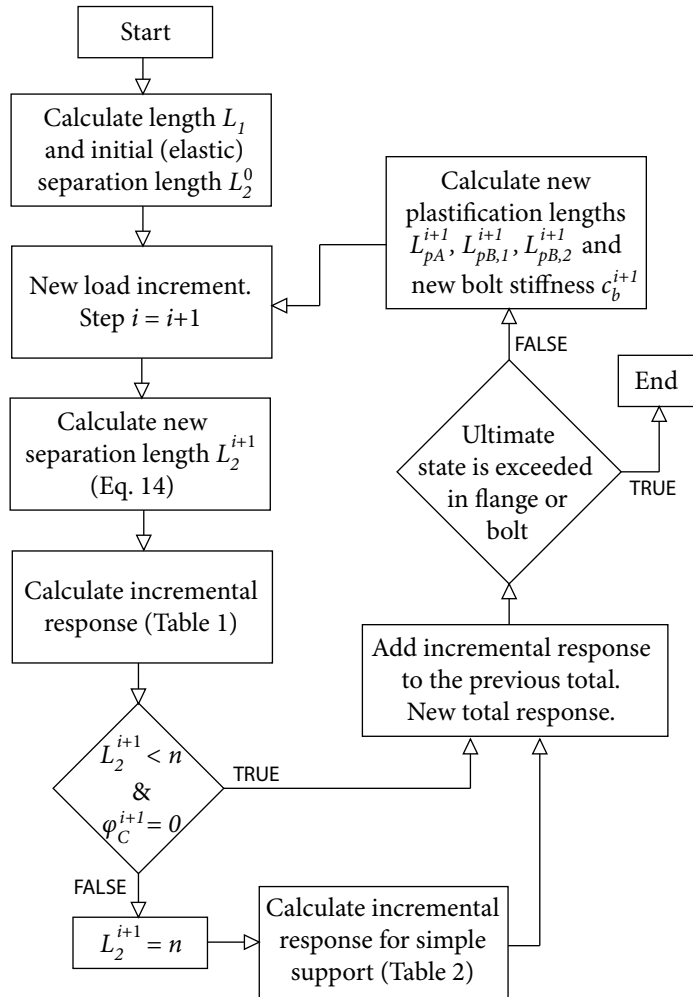


Figure 6. Solution process.

single point of the flange. As shown in Figure 7a, the solution derived from a concentrated bolt action overestimates the flange bending moment at the bolt location. Assuming a uniform distribution of the bolt force within a zone of length equal to the bolt head diameter d_h , the variation of the moment at the bolt location, compared to the case of concentrated action, is given by

$$\Delta M_B = \frac{F_b d_h}{8}. \tag{16}$$

This variation is taken into account when a decision regarding plastification or failure of the flange at the bolt location is taken.

Note that no special consideration made of the influence of the hole and the reduced cross section of the flange on the moment capacity of the flange. In theory, the beneficial action of the uniform distribution of the bolt force could be compensated by the unfavorable effect of the reduced flange cross

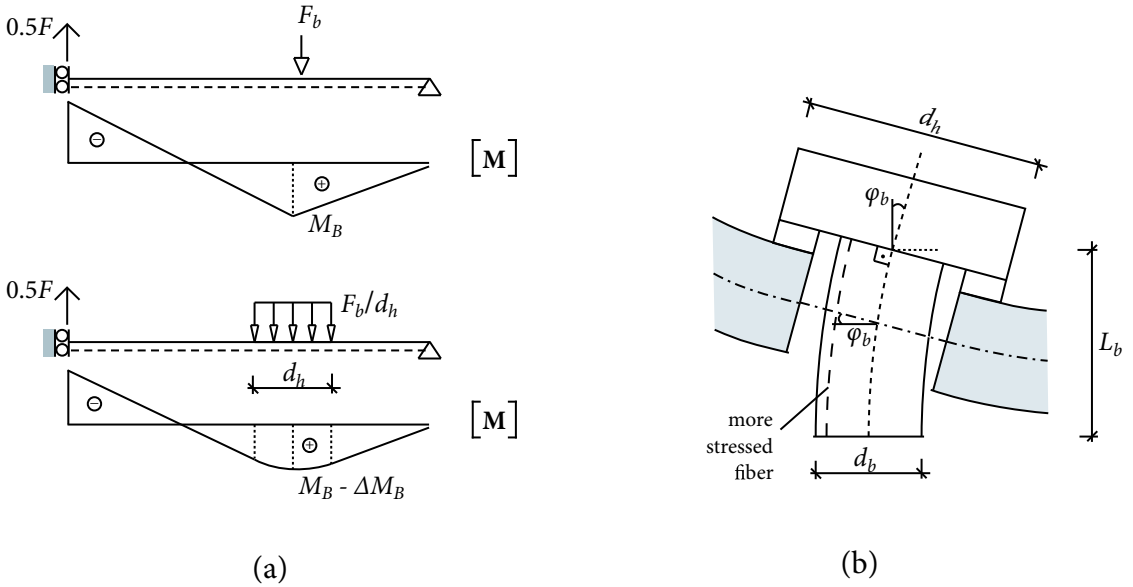


Figure 7. Influence of bolt head size (a) and definitions for the bolt bending treatment (b).

section. However, the behavior of the flange in the area near the bolt departs from simple bending, it is characterized by a complex three dimensional stress state, and it is affected by the interaction with the bolt head. Designation of a reduced moment capacity for the flange at the bolt area, based on its net cross section, lead to significant underestimate of the strength of the complete *T*-stub. Therefore, we do not propose such reduction to the flange moment capacity.

4.2. Bolt bending. The bolt shank of a real *T*-stub is subjected to combined tension and bending, whereas in the proposed model only axial tension is considered. This potentially leads to a considerable overestimation of the maximum axial load the bolt can carry. In *T*-stubs with strong flanges where the bolts are critical for the ultimate load capacity, a slight overestimation of the bolt resistance can lead to significant overestimation of the ultimate *T*-stub displacement.

To prevent this error we assume a revised criterion for the realization of the ultimate bolt state, which refers to the more stressed fiber of the bolt shank shown in [Figure 7b](#), as

$$\varepsilon_u > \varepsilon_t + \varepsilon_b, \tag{17}$$

where ε_u is the ultimate strain of the bolt material, ε_t the strain attributed to tensile action and ε_b the strain attributed to bending action. The value of ε_t can be obtained from

$$\varepsilon_t = \frac{w_b}{L_b}, \tag{18}$$

where L_b is the modeled shank length and w_b the elongation of the bolt shank, which can be calculated throughout the incremental process using the current bolt stiffness and the incremental axial bolt force dF_b . For ε_b , we assume that the total rotation of the bolt shank axis φ_b , is equal to the flange rotation at this position ([Figure 7b](#)) available analytically at each incremental step. Because the bending of the

shank is induced through rotation of its edges, constant bending moments along its length is assumed, and thus strain ε_b is related to rotation φ_b through

$$\varepsilon_b = \frac{d_b/2}{L_b} \varphi_b. \tag{19}$$

Note that for wide T -stubs the deformation of the flange is not uniform along its width. Near the bolts the flange deflection and rotation is reduced compared to a uniform deformation, as assumed in the model. In such cases the criterion in Equation (17) can lead to early failure. We tested our proposed model for T -stub configurations with b/m ratios up to 2.0 ~ 2.5, and obtained acceptable results, as shown in the following sections. For even wider T -stubs, further study is necessary to make a meaningful estimation of the bolt rotation.

4.3. Shear deformations. The expressions in Tables 1 and 2 account for the work in the flange due to bending actions only. This assumption is normally valid for long beams where work due to shear deformation may be neglected. For T -stubs, the dimensions of the flanges do not justify this simplification. Expressions similar to the ones in Tables 1 and 2 can be derived with the shear work included. However, such expressions are more complicated and are not presented in this paper. Instead, a simple circumvention is possible, in which we account for the shear work in the calculations of the resulting displacements only. Thus, the following quantity may be added to the displacements dw in Tables 1 and 2:

$$dw_s = \int_0^{L_1} \frac{0.5dF \cdot \bar{1}}{GA} dx = \frac{dFL_1}{2GA}. \tag{20}$$

4.4. Three-dimensional stress and strain state. In our model the flange is treated as a simple Bernoulli beam. Hence, any secondary stresses are neglected, such as the normal σ_{yy} and σ_{zz} with y and z axes as defined in Figure 8. However, this assumption for the stress state is accurate enough only near the two side edges and for fairly thin flanges. Towards the middle areas of the width b , lateral strain ε_{zz} is suppressed, resembling plane strain conditions. Assuming that $\varepsilon_{zz} = 0$ and that σ_{yy} also remains practically zero due

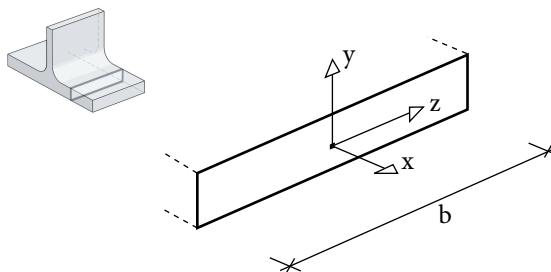


Figure 8. Flange cross sectional axis definitions.

to the flange being adequately thin, the three dimensional elastic stress-strain equations lead to

$$\sigma_{xx} = \frac{E}{1 - \nu^2} \varepsilon_{xx}, \quad (21)$$

$$\sigma_{zz} = \frac{\nu E}{1 - \nu^2} \varepsilon_{xx}. \quad (22)$$

Equation (21) suggests adoption of an equivalent modulus of elasticity for the flange

$$E^* = \frac{E}{1 - \nu^2}. \quad (23)$$

For Poisson's ratio ν equal to 0.3, an equivalent modulus E^* becomes approximately 10% larger than E . The interaction of normal stress σ_{xx} and the nonzero secondary σ_{zz} applied in the von Mises yield criterion leads to an equivalent yield stress:

$$f_y^* = \frac{f_y}{\sqrt{1 - \nu + \nu^2}}. \quad (24)$$

For $\nu = 0.3$, (24) leads to an approximately 13% increase of the equivalent yield stress of the flange.

To determine an equivalent modulus E_T^* in the plastic region, we adopt the deformation theory of plasticity [Chen and Han 1988], which implies a proportional loading history. The plastic strains are a function of the total stresses

$$\varepsilon_{xx}^p = \frac{\varepsilon_{\text{eff}}^p}{\sigma_{\text{eff}}} (\sigma_{xx} - \frac{1}{2}(\sigma_{yy} + \sigma_{zz})), \quad (25)$$

$$\varepsilon_{yy}^p = \frac{\varepsilon_{\text{eff}}^p}{\sigma_{\text{eff}}} (\sigma_{yy} - \frac{1}{2}(\sigma_{xx} + \sigma_{zz})), \quad (26)$$

$$\varepsilon_{zz}^p = \frac{\varepsilon_{\text{eff}}^p}{\sigma_{\text{eff}}} (\sigma_{zz} - \frac{1}{2}(\sigma_{xx} + \sigma_{yy})), \quad (27)$$

where $\varepsilon_{\text{eff}}^p$ and σ_{eff} are the effective plastic strain and the effective stress, respectively. Imposing $\varepsilon_{zz} = 0$ and $\sigma_{yy} = 0$, the nonzero plastic strains are

$$\varepsilon_{xx}^p = \frac{3}{4} \frac{\varepsilon_{\text{eff}}^p}{\sigma_{\text{eff}}} \sigma_{xx}, \quad (28)$$

$$\varepsilon_{yy}^p = -\frac{3}{4} \frac{\varepsilon_{\text{eff}}^p}{\sigma_{\text{eff}}} \sigma_{xx}, \quad (29)$$

while for the nonzero total normal stresses

$$\sigma_{zz} = \frac{1}{2} \sigma_{xx}. \quad (30)$$

The equivalent ultimate stress can be derived from (30) using the von Mises criterion

$$f_u^* = \frac{2\sqrt{3}}{3} f_u. \quad (31)$$

Finally, the equivalent modulus E_T^* can be defined as the slope of the line in the stress-strain plane leading from the equivalent yield state to the equivalent ultimate state

$$E_T^* = \frac{f_u^* - f_y^*}{\varepsilon_{xx,u} - \varepsilon_{xx,y}}, \tag{32}$$

where $\varepsilon_{xx,y}$ is the yielding strain obtained from (21) and $\varepsilon_{xx,u}$ is the ultimate strain obtained from (21) and (28) as

$$\varepsilon_{xx,u} = \frac{2\sqrt{3}}{3} \frac{f_u}{E} (1 - \nu^2) + \frac{\sqrt{3}}{2} (f_u - f_y) \frac{E - E_T}{EE_T}. \tag{33}$$

4.5. Flange-bolt interaction. In our proposed model, we assume a uniform flange deflection along its width b . However, in real T -stubs, especially wide ones, this assumption is not appropriate due to the bolt action which is exerted in a part only of the total width. This discrepancy affects the calculated displacements of the analytical model. Using an equivalent plate problem, [Faella et al. 2000] proposed a modified effective width b_{eff} for stiffness calculations. The plate features an infinite width which mainly applies to T -stubs which are considered as components of more complex connections where the dimensions of the plates are quite large compared to the individual T -stubs. Under these assumptions, b_{eff} is simply derived as

$$b_{\text{eff}} = 2.21m. \tag{34}$$

The length m is shown in Figure 1b and is equal to $d - 0.8r$. For completeness of the proposed model, we undertook a similar approach for plates of finite width. In particular, cantilevered plates with varying values of m/b loaded with a concentrated load in the middle of the free edge, opposite to the clamped one, were analyzed elastically using 2D plate finite elements. Comparing the numerically calculated displacements of the plates to those of a simple beam representation, for an equivalent width b_{eff} , we obtained

$$\frac{b}{b_{\text{eff}}} = \begin{cases} 0.92 + \frac{0.06}{(m/b)^2}, & m/b < 0.87, \\ 1, & m/b \geq 0.87. \end{cases} \tag{35}$$

Figure 9 shows a graphical representation of Equation (35) as well as the curve derived from Equation (34) from [Faella et al. 2000]. Considering that Equation (34) is based on an analysis of infinitely wide plates, it is expected that for low values of the ratio m/b , the two curves converge. However, for intermediate values of the ratio m/b , we observe a difference up to 20% in the equivalent width b_{eff} .

This equivalent width b_{eff} is used to calculate the resulting displacements due to flange deformation only. Decoupling of the total T -stub displacement w , which is calculated incrementally by means of Table 1 or 2, to flange and bolt contributions, can be performed at each incremental step since the bolt elongation is easily obtainable using the current bolt stiffness and the incremental axial force dF_b . The decoupled flange deflection should then be corrected with the multiplier b/b_{eff} from Equation (35), to better approximate the impact of three-dimensional flange deformation.

5. Model performance

5.1. Comparison with experimental tests. Performance of our proposed model is validated by comparison with results of published experimental tests, as well as by numerical parametric analyses. The

published tests we used are those for T -stubs T1 and T2 conducted by [Bursi and Jaspart 1997], for which all the necessary geometrical properties are provided in Table 3. T -stub T1 features a relatively weak flange which is critical for the response, unlike T -stub T2 which features a stronger flange in which both the bolts and the flange are critical for the response. With reference to prEN 1993-1-8 [CEN 2003], those two behaviors correspond to the first and second failure mode, respectively. The bilinear material approximations applied for the incremental models are shown in Figure 10a and 10b. Engineering values are adopted since the original undeformed geometrical formulation is used for the calculations. Web material data are needed because in the experimental setup the displacements were measured at the web. The web deformability can be easily included in our model through an axially loaded spring of equivalent stiffness.

In Figures 11a and 11b, the force F vs. displacement w curves for the proposed analytical model and the experimental tests T1 and T2 are presented. Also, the curves derived by means of 3D finite element simulation performed with ADINA v.8 [ADINA 2004], as described later in section 5.2, are included in the same figure. For the finite element analyses, the ultimate state is realized when the von Mises stress in the critical regions of the flange or at the bolt shank approaches the respective material ultimate value. Likewise, for our proposed model, the ultimate state is realized when flange moments reach the ultimate moment M_u or when the criterion (17) regarding combined tension and bending of the bolt is violated.

The performance of the proposed model is shown to be quite satisfactory. For T -stub T1 initial stiffness, ultimate load, ultimate displacement and the overall curve converge to their experimental counterparts. The knee range is sharper in the proposed model as well as in the 3D finite element model. We

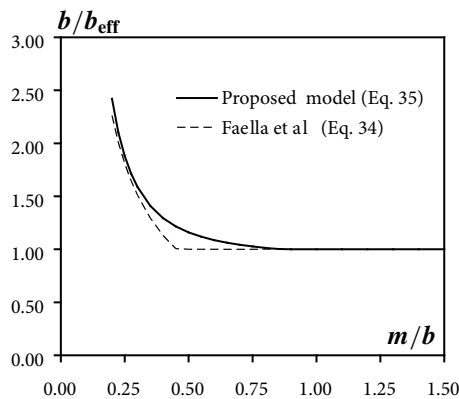


Figure 9. Curves for the estimation of the equivalent width b_{eff} .

	Flange					Bolt		
	b	t_f	r	d	n	d_b	d_h	L_b
T1	40.0	10.7	15.0	41.45	30.0	12.0	24.0	14.0
T2	40.0	16.0	18.0	40.25	30.0	12.0	24.0	16.0

Table 3. Geometrical characteristics for T -stubs in the parametric study (in mm).

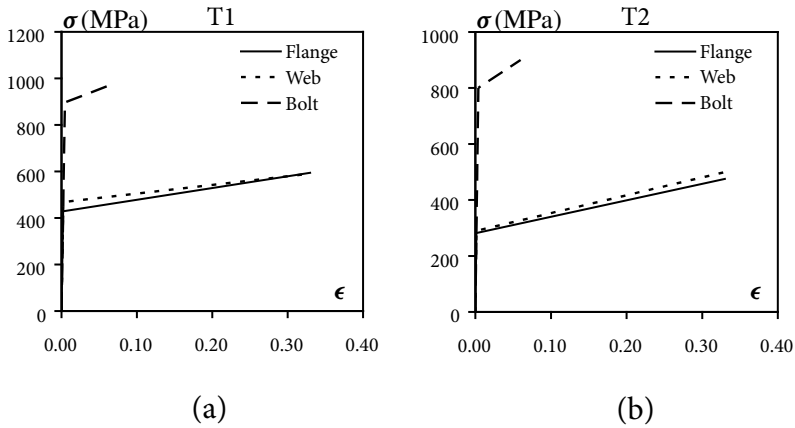


Figure 10. Bilinear material approximations for *T*-stubs (a) T1 and (b) T2.

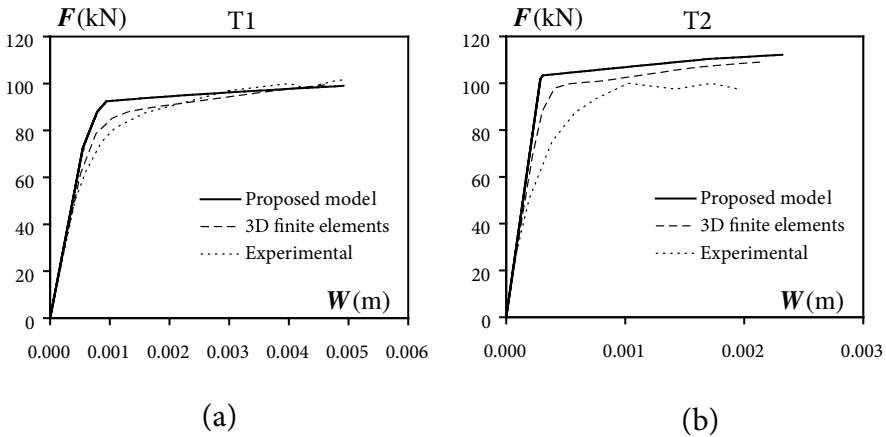


Figure 11. Force-displacement curves for *T*-stubs (a) T1 and (b) T2.

attribute this mainly to the bilinear approximation of the moment-curvature relationship for the flange and to the residual stresses present in the experimental flange. For *T*-stub T2, [Bursi and Jaspart 1997] mention that bolt thread stripping was observed and the experimental curve reflects this special failure type. Nevertheless, the curve of the proposed model lies fairly close to the 3D finite element one, for which thread detailing is also not modeled. A slight overestimation in the plastic branch can be observed. This is a result of the bolt bending action, which apart from the ultimate state, is neglected in the proposed model.

For flange contact, our proposed model for *T*-stub T2 reproduces simple support conditions at the flange edge which is validated by the finite element model and the physical test. For *T*-stub T1 the variation of the separation length L_2 through the loading history for the proposed model is shown in Figure 12a. After the first plastification in the flange area near the web, the separation length decreases

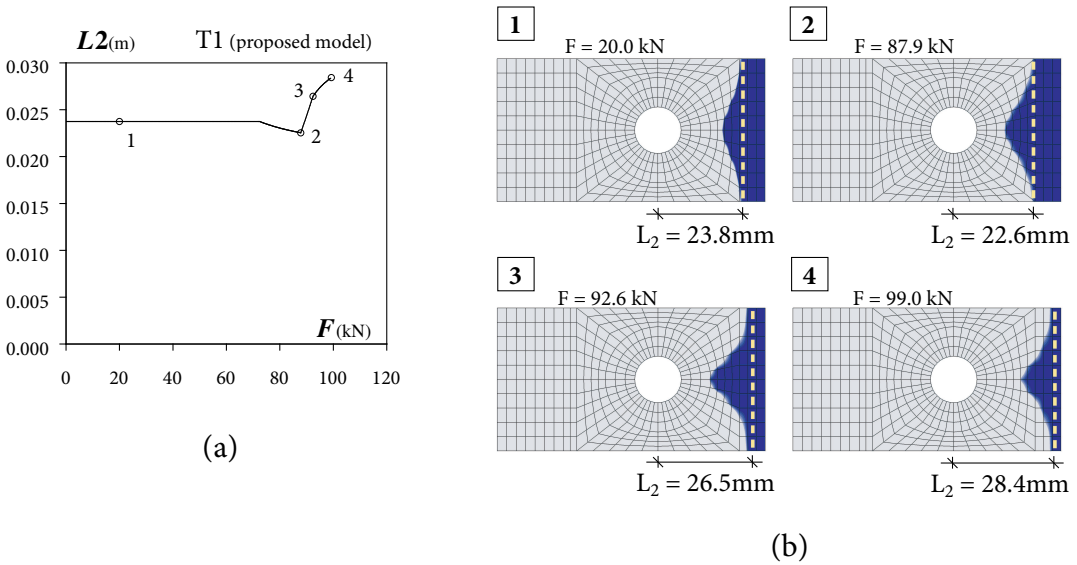


Figure 12. Development of flange contact phenomena in the proposed model (a) and in 3D finite element model (shown in dark shaded area) (b) for *T*-stub T1.

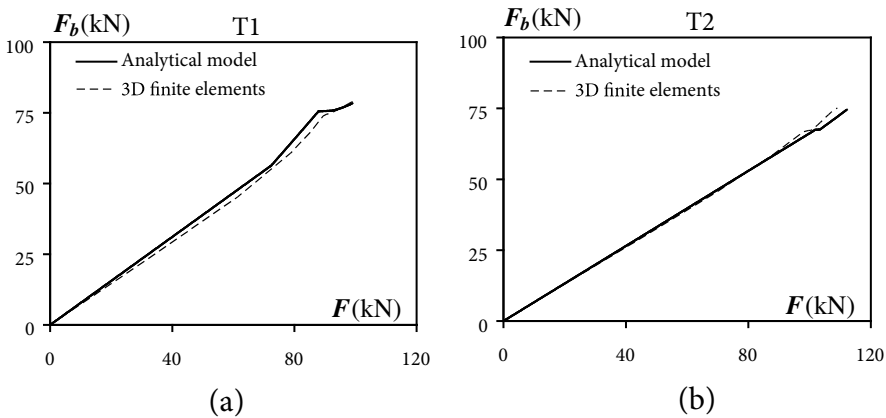


Figure 13. Bolt force versus external loading for *T*-stubs (a) T1 and (b) T2.

initially, but later when the bolt enters the plastic region, it increases. This behavior is confirmed by the results obtained by 3D finite element analysis shown in Figure 12b, where the contact area of the flange is plotted for various load levels. Note that the limits of the contact area provided by our model for the same loading levels are indicated with dashed lines.

In Figure 13, the axial force history for the bolt given by our model is compared to the 3D finite element results for both tests. The proposed model appears to perform very well in this context, especially considering the simplified method for including the bolt contribution, as compared to the more complex finite element method.

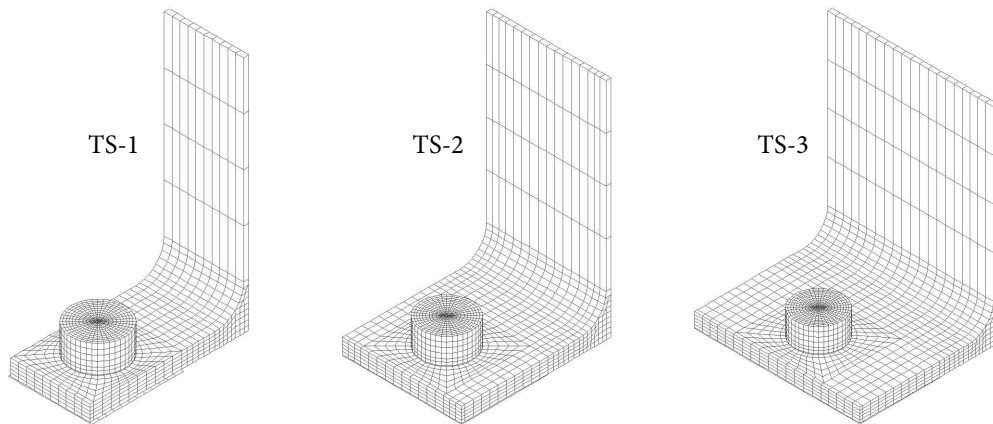


Figure 14. Typical finite element models for the parametric study.

5.2. Comparison through parametric finite element modeling. We also carried out a parametric study of the performance of our proposed model employing 3D finite element modeling with the software package ADINA v.8 [ADINA 2004]. The reliability of 3D finite element modeling for the *T*-stub connection has been confirmed in [Bursi and Jaspart 1997; Wanzek and Gebbeken 1999; Gantes and Lemonis 2003]. We validate its reliability here as well, through the comparison with the experimental tests T1 and T2 mentioned earlier. The flange and the bolts were modeled as separate bodies by means of eight node brick elements. The contact between them was modeled through 2D contact elements, equipped with constraint functions to enforce all contact conditions to the corresponding surfaces and a Coulomb friction coefficient equal to 0.25. In contrast, frictionless contact conditions were applied between the flange and its base which constitutes a symmetry plane of the whole problem. Through the thickness of the flange, five brick elements were employed, formulated with incompatible modes in order to circumvent the shear locking effect. Likewise, for the bolt circumference we implemented a large number of elements (40 or more). The loading was applied by prescribed displacements on the upper surface of the web with assumptions of large strains and large displacements globally imposed. Figure 14 shows the finite element plots for three of the models of the parametric study.

Table 4 lists the geometric properties of the *T*-stubs of the parametric study, while Table 5 lists the material properties, which remain unchanged for all *T*-stubs. The geometrical configurations in the parametric study include *T*-stubs with wide range of flange width and of relative strength between flange and bolts. The former allows investigation of the influence of the *T*-stub width to the flange-bolt interaction. We can also demonstrate the impact of the adopted beam representation in the ability of the model and its refinements to predict accurately the response of the three-dimensional problem.

Figure 15 shows the plots of force F against displacement w for the proposed analytical and the corresponding finite element models of the parametric study. In all cases the analytical curve closely matches the numerical one. The characteristic attributes of initial stiffness, ultimate strength and ultimate displacement are predicted within a fairly narrow margin of error. Performance is better for strength estimation than for initial stiffness and ultimate displacement. For the ultimate displacement, which is the most difficult characteristic to compute analytically, the maximum error does not exceed 30% for any

	Flange					Bolt		
	b	t_f	r	d	n	d_b	d_h	L_b
TS-1	50.0	10.0	18.0	66.75	30.0	20.0	34.0	14.0
TS-2	80.0	10.0	18.0	66.75	30.0	20.0	34.0	14.0
TS-3	120.0	10.0	18.0	66.75	30.0	20.0	34.0	14.0
TS-4	50.0	10.0	18.0	66.75	30.0	12.0	24.0	13.0
TS-5	80.0	10.0	18.0	66.75	30.0	12.0	24.0	13.0
TS-6	120.0	10.0	18.0	66.75	30.0	12.0	24.0	13.0
TS-7	50.0	15.0	18.0	65.50	30.0	20.0	34.0	19.0
TS-8	80.0	15.0	18.0	65.50	30.0	20.0	34.0	19.0
TS-9	120.0	15.0	18.0	65.50	30.0	20.0	34.0	19.0
TS-10	50.0	15.0	18.0	65.50	30.0	12.0	24.0	18.0
TS-11	80.0	15.0	18.0	65.50	30.0	12.0	24.0	18.0
TS-12	120.0	15.0	18.0	65.50	30.0	12.0	24.0	18.0

Table 4. Geometrical characteristics for T -stubs in the parametric study (in mm).

of the T -stubs and is much lower for most of them. Table 6 presents the mean value and the standard deviation of the relative errors in the parametric study for the three characteristic properties. A slight overestimation of the initial stiffness can be noticed from the results, while for the ultimate strength and displacement the mean error is very close to zero. Also, the low value of error standard deviation, observed for all three properties, indicates a consistent performance of the proposed model.

6. Conclusion

A new incremental T -stub model for the prediction of the complete force vs. displacement curve has been introduced in this paper. The model is designed for implementation in a computer program, and

	E	E_T	f_y	f_u
Flange	200000	782	355	510
Bolt	200000	2400	640	800

Table 5. Material properties for T -stubs in the parametric study (in MPa).

	Initial stiffness error	Strength error	Ultimate displacement error
Mean value	0.17	-0.02	0.03
Standard deviation	0.103	0.025	0.147

Table 6. Relative errors for the proposed model in the parametric study.

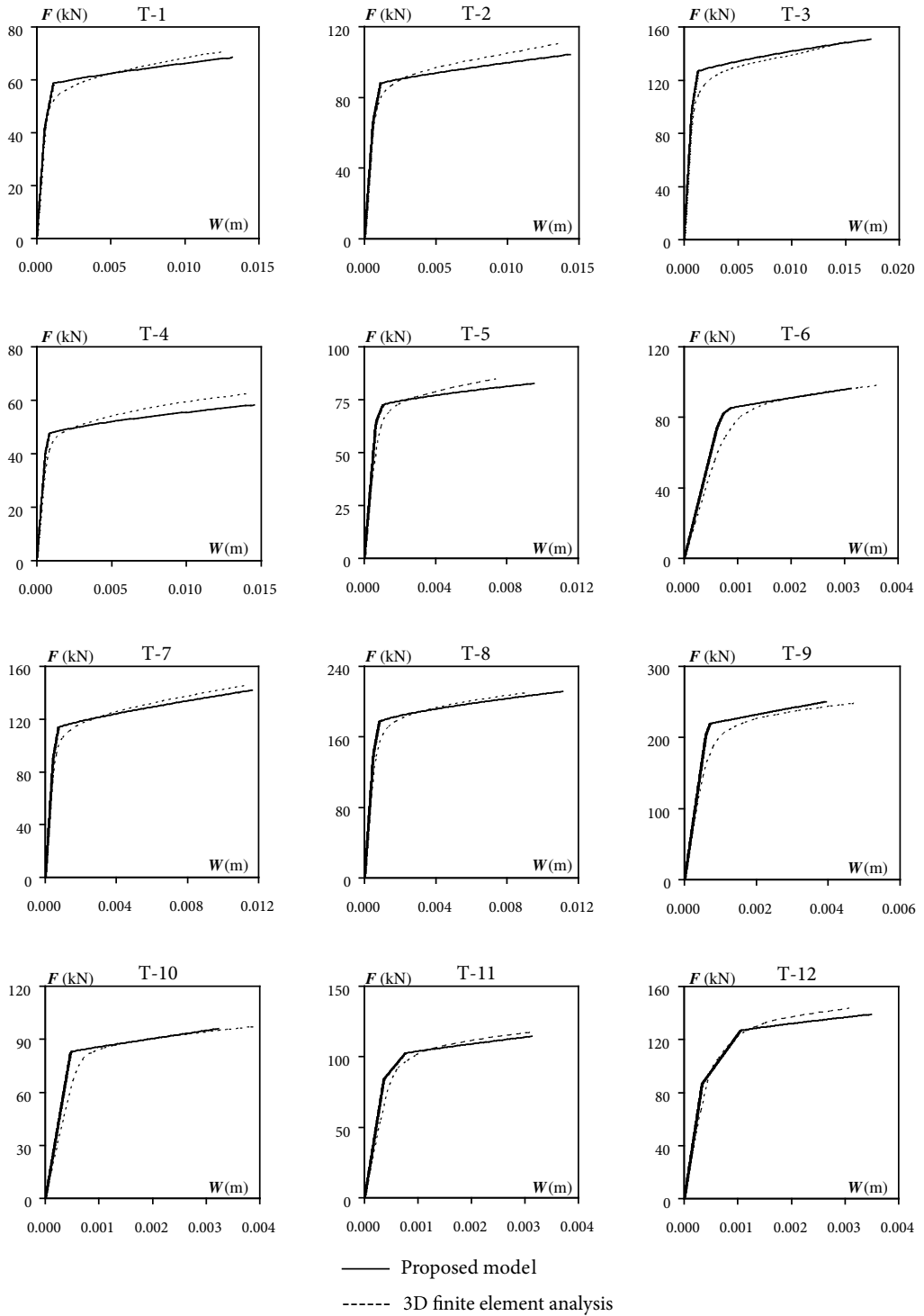


Figure 15. Force-displacement curves for the parametric study.

offers several advantages in this context by avoiding multiple cases and branches. The effectiveness of the model has been shown to be very satisfactory in evaluations comparing it to both experimental and numerical results. The solution time for a large number of load increments (500 or more) is negligible. Overall, the proposed model constitutes a valuable tool for the estimation of T -stub behavior, producing results comparable to much more complex and costly approaches such as 3D finite element analysis.

7. Notation

A	flange cross-sectional area
b	T -stub width
b_{eff}	effective T -stub width used for displacement calculations
c_b	axial stiffness of the bolt
d	distance between web face and bolt axis
d_b	bolt diameter
d_h	bolt head diameter
dF	incremental applied force
dF_b	incremental bolt force
dM_A	incremental bending moment at flange point A
dM_B	incremental bending moment at flange point B
$dM_{C^{i+1}}$	incremental bending moment at flange point C^{i+1}
dR	incremental prying force
dw	incremental transverse T -stub displacement
$dw_{j0...2}$	parameters for the calculation of incremental displacement
dw_s	incremental transverse T -stub displacement due to shear
E	Young modulus
E^*	equivalent Young modulus
E_T	strain hardening modulus
E_T^*	equivalent strain hardening modulus
F	applied force
F_b	bolt force
f_u	ultimate stress
f_u^*	equivalent ultimate stress
f_y	yield stress
f_y^*	equivalent yield stress

G	shear modulus
G_1, G_2	parameters for the calculation of T -stub incremental response
I	moment of inertia
i	superscript indicating the loading step number
j	index indicating the trapezoid in numerical calculation of Int
Int	integral derived from flexural stiffness equivalence in flange-to-web fitting
k	number of trapezoids in numerical calculation of Int
L_0	flange length from edge A to start of plastification length
L_1	flange length from edge A to bolt axis
L_2	flange separation length measured from bolt axis to edge C
L_b	bolt shank length
L_c	equivalent flange-to-web fitting length
L_{pA}	plastification length near edge A
$L_{pB,1}$	plastification length at point B and towards the web
$L_{pB,2}$	plastification length at point B and towards the flange edge
M	flange bending moment
$M(x)$	flange bending moment function of x
M_2	flange plastification moment in bilinear representation
$M_2(x)$	flange plastification moment function of x
M_A	bending moment at flange point A
M_B	bending moment at flange point B
$M_{C^i}, M_{C^{i+1}}$	bending moment at flange point C^i and C^{i+1}
M_u	flange ultimate moment
M_y	flange yield moment
m	distance between bolt axis and an offset of web face by $0.8r$
$m_{j0...5}$	parameters for the calculation of separation length
n	distance between bolt axis and flange edge
$p_{j0...3}$	parameters for the calculation of T -stub incremental response
$q_{j0...4}$	parameters for the calculation of T -stub incremental response
R	prying force
r	fillet radius of the flange-to-web fitting
$s_{j0...2}$	parameters for the calculation of T -stub incremental response

t_f	flange thickness
$t_f(x)$	flange thickness function of x in flange-to-web fitting
$t_{f,j}$	flange thickness in trapezoid j
w	transverse T -stub displacement
w_b	bolt shank elongation
ε	strain
ε_b	strain at tensile fiber of bolt shank due to bending
$\varepsilon_{\text{eff}}^p$	effective plastic strain
ε_t	strain at tensile fiber of bolt shank due to tension
ε_u	ultimate strain
ε_y	yield strain
$\varepsilon_{xx}, \varepsilon_{yy}, \varepsilon_{zz}$	normal strains along axes x , y and z
$\varepsilon_{xx}^p, \varepsilon_{yy}^p, \varepsilon_{zz}^p$	normal plastic strains along axes x , y and z
ΔM_B	variation of flange bending moment at bending moment due to distributed bolt action
λ	parameter for the calculation of T -stub incremental response
ν	Poisson's ratio
σ	stress
σ_{eff}	effective stress
$\sigma_{xx}, \sigma_{yy}, \sigma_{zz}$	normal stresses along axes x , y and z
ϕ_B	flange rotation at bolt axis
ϕ_C	flange rotation at flange edge

References

- [ADINA 2004] "ADINA theory and modeling guide, I: ADINA solids and structures", ADINA R&D Inc., Watertown, MA, 2004.
- [Agerskov 1976] H. Agerskov, "High strength bolted connections subjected to prying", *J. Struct. Div. (ASCE)* **102**:1 (1976), 161–175.
- [Beg et al. 2004] D. Beg, E. Zupancic, and I. Vayas, "On the rotation capacity of moment connections", *J. Constr. Steel Res.* **60**:3–5 (2004), 601–620.
- [Bursi and Jaspart 1997] O. S. Bursi and J. P. Jaspart, "Calibration of a finite element model for isolated bolted end-plate steel connections", *J. Constr. Steel Res.* **44**:3 (1997), 225–262.
- [CEN 2003] *Eurocode 3: Design of steel structures, 1.8: Design of joints*, Comité Européen de Normalisation (CEN), Brussels, Belgium, 2003. Stage 49 Draft.
- [Chen and Han 1988] W. F. Chen and D. J. Han, *Plasticity for structural engineers*, Springer, New York, 1988.
- [Girão Coelho et al. 2004] A. M. Girão Coelho, L. Simões da Silva, and F. Bijlaard, "Characterization of the nonlinear behaviour of single bolted T-stub connections", pp. 53–120 in *Proceedings of the Fifth International Workshop on Connections: Connections in steel structures, behavior, strength and design*, AISC-ECCS, Amsterdam, 2004.

- [Faella et al. 2000] C. Faella, V. Piluso, and G. Rizanno, *Structural steel semirigid connections: Theory, design and software*, CRC Press, Boca Raton, FL, 2000.
- [Gantes and Lemonis 2003] C. J. Gantes and M. E. Lemonis, “Influence of bolt length in finite element modeling of T-stub steel connections”, *Comput. Struct.* **81**:8–11 (2003), 595–604.
- [Huber and Tschemmerneegg 1998] G. Huber and F. Tschemmerneegg, “Modelling of beam-to-column joints”, *J. Constr. Steel Res.* **45**:2 (1998), 199–216.
- [Jaspart 1991] J. P. Jaspart, *Étude de la semi-rigidité des noeuds poutre-colonne et son influence sur la résistance et la stabilité des ossatures en acier*, Ph.D. thesis, University of Liège, Belgium, 1991.
- [Kuhlmann and Kuhnemund 2000] U. Kuhlmann and F. Kuhnemund, “Procedures to verify rotation capacity”, pp. 167–226 in *Semi-rigid connections in structural steelwork*, edited by M. Ivanyi and C. C. Banitopoulos, CISM Courses and Lectures **419**, Springer, Vienna, 2000.
- [Mistakidis et al. 1997] E. S. Mistakidis, C. C. Banitopoulos, C. D. Bisbos, and P. D. Panagiotopoulos, “Steel T-stub connections under static loading: An effective 2-D numerical model”, *J. Constr. Steel Res.* **44**:1–2 (1997), 51–67.
- [Sherbourne and Bahaari 1996] A. N. Sherbourne and M. R. Bahaari, “3D simulation of bolted connections to unstiffened columns, I: T-stub connections”, *J. Constr. Steel Res.* **40**:3 (1996), 169–187.
- [Shi et al. 1996] Y. J. Shi, S. L. Chan, and Y. L. Wong, “Modeling for moment-rotation characteristics for end-plate connections”, *J. Struct. Eng. (ASCE)* **122**:11 (1996), 1300–1306.
- [Swanson and Leon 2001] J. A. Swanson and R. T. Leon, “Stiffness modeling of bolted T-stub connection components”, *J. Struct. Eng. (ASCE)* **127**:5 (2001), 498–505.
- [Wanzek and Gebbeken 1999] T. Wanzek and N. Gebbeken, “Numerical aspects for the simulation of end plate connections”, pp. 13–31 in *Cost CI WG6 report: Numerical simulation of semi-rigid connections by the finite element method*, edited by K. S. Virdi, European Commission, Brussels, 1999.
- [Weynand et al. 1995] K. Weynand, J. Jaspart, and M. Steenhuis, “The stiffness model of revised annex J of Eurocode 3”, pp. 441–452 in *Connections in steel structures III: Proceedings of the Third International Workshop on Connections in Steel Structures* (Trento, Italy), edited by R. Bjorhovde et al., Pergamon, Tarrytown, NY, 1995.
- [Yee and Melchers 1986] Y. L. Yee and R. E. Melchers, “Moment-rotation curves for bolted connections”, *J. Struct. Eng. (ASCE)* **112**:3 (1986), 615–635.
- [Zoetemeijer 1974] P. Zoetemeijer, “A design method for the tension side of statically loaded, bolted beam-to-column connections”, *Heron* **20**:1 (1974), 1–59.

Received 29 Dec 2005. Revised 5 May 2006. Accepted 19 Jun 2006.

MINAS E. LEMONIS: mlemonis@central.ntua.gr

National Technical University of Athens, Laboratory of Steel Structures, 9 Iroon Polytechniou, 157 80, Zografou, Greece

CHARIS J. GANTES: chgantes@central.ntua.gr

National Technical University of Athens, Laboratory of Steel Structures, 9 Iroon Polytechniou, 157 80, Zografou, Greece

EFFECT OF THE ORDER OF PLATES ON THE BALLISTIC RESISTANCE OF DUCTILE LAYERED SHIELDS PERFORATED BY NONCONICAL IMPACTORS

G. BEN-DOR, A. DUBINSKY AND T. ELPERIN

In our previous studies using the two-term impactor-shield localized interaction model, we derived the rule determining the order of the plates with different mechanical properties in a multilayer shield that yields a maximum ballistic limit velocity against conical impactors. In the present study we show that this rule is valid also for ogive-shaped, nonconical impactors.

1. Introduction

Several topics associated with the investigation of layering and spacing of the shields are extensively covered in the literature on high-speed penetration mechanics. Many studies have compared ballistic characteristics of monolithic shields with those of the shields composed of several plates with the same total thickness and manufactured from the same material. The plates may be in contact or there may be air gaps between them. Therefore, as alternatives to the monolithic shield, many types of shields with different numbers of plates and different thicknesses of the plates and of the air gaps are feasible. Analyses of the effect of the order of plates manufactured from different materials on the ballistic characteristics of the shield have attracted particular interest. The simplest case of this problem is interchanging the plates in a two-layered shield. In the general case, the number of plates may vary and they may be manufactured from different materials. The combined effects of changing the order of plates and of using air gaps on the ballistic performance of the shield and various problems of optimization of the structure of the shield have also been studied in a number of investigations.

A brief survey of the state of the art presented below (mainly on penetration in metal shields) supports the assessment of [Radin and Goldsmith 1988] that “only limited results for multiple target materials exist in the literature. . . , and the results obtained cannot easily be correlated since different target and projectile materials, nose shapes, impact geometries and striker speeds were used”. Clearly, the latter assessment is not related to the problem of selecting the best shield among the given set of shields against the impactor with a given shape. This problem can be often solved experimentally, and the obtained results can be explained using relatively simple physical reasoning. The problem is to determine a more or less general law that will enable predicting the change of the ballistic characteristics of the shield by varying the structure of the shield. This problem has not been solved as yet, although a number of experimental and theoretical studies have been performed in this direction.

Honda et al. [1930] investigated experimentally the impact of steel plates by conical-nosed projectiles. It was found that a shield composed of thin plates had a lower ballistic resistance than a monolithic shield

Keywords: impact, layered shield, ballistic limit velocity, optimization, plate.

with the same thickness. However, a spaced shield with the thicknesses of the plates equal to the half-thickness of a monolithic shield performed better than a monolithic shield. Marom and Bodner [1979] conducted a combined analytical and experimental comparative study of monolithic, layered and spaced thin aluminum shields. They found that the ballistic resistance of a monolithic shield is higher than that of a multilayered shield with the plates in contact and lower than the ballistic resistance of a spaced shield. The study by [Radin and Goldsmith 1988] was also based on semiempirical models and experimental investigations. They found a monolithic aluminum shield to be superior to a layered shield with the same total thickness for conical-nose and blunt projectiles, while the spaced shields were less effective. Corran et al. [1983b; 1983a], using experimental results on penetration of mild steel plates by impactors having “increasingly rounded nose shape”, plotted the curve of perforation energy versus plate thickness for all considered variants of the shield and found a “kink” in the curve “at about 3.5 mm total thickness”. The occurrence of the kink was explained by the change of character of energy absorption. The authors arrived at the conclusions that the order of unequal plate thickness is important. No advantage was found in using multilayered targets below the kink. Above this point the best combinations may approach the best-fit line to the single layer tests below the kink. It was found that there is an advantage to placing the layers in contact.

Nixdorff [1984a; 1984b; 1987] compared the ballistic performance of a monolithic metal shield with a shield manufactured from the same material, having the same total thickness, and consisting of several plates in contact. Using the theory developed by Awerbuch and Bodner [1974], Nixdorff showed that separation of a homogeneous shield into several layers implies a reduction of the ballistic limit velocity (BLV) of the shield.

Zukas [1996] and Zukas and Scheffler [2001] found, on the basis of numerical simulations with metallic shields, that layering dramatically weakens thin [$b/(2R) < 1$] and intermediate thickness [$3 < b/(2R) < 10$] shields, while thick shields [$b/(2R) > 10$] show small changes in projectile residual properties [residual mass and residual velocity] when compared to their monolithic equivalent. Here b and R are the thickness of the shield and the shank radius of the impactor, respectively.

Madhu et al. [2003] conducted experiments with aluminum plates impacted normally and concluded that there is no significant change in the ballistic performance due to layering of such intermediate thickness of plates. They compared a monolithic shield with two- and three-layered shields of the same thickness. Gupta and Madhu [1997], using experimental results obtained for aluminum and steel plates, arrived at the same conclusion with respect to relatively thick plates. For thin shields, the layered combinations in contact yielded higher residual velocity as compared with a monolithic shield manufactured from either aluminum or steel. It was also found that for a spaced shield the residual velocity was higher than in the case of plates in contact, for the same impact velocity.

Weidemaier et al. [1993] conducted experiments and numerical simulations on the perforation of steel barriers by spherical impactors with a diameter of 17 mm. They studied a monolithic shield with a thickness of 43 mm and shields composed of plates in contact having the same total thickness. It was found that the ballistic characteristics of layered shields depended strongly on the order of the plates having different thicknesses and that layering could improve or impair the ballistic performance of the shield.

Almohandes et al. [1996] conducted a comprehensive experimental study on the perforation of mild steel by standard 7.62 mm bullets. They investigated shields with total thickness in the range of 8–14 mm that were layered in contact, spaced and monolithic. It was found that single shields were more effective

than laminated shields of the same total thickness, regardless of the configuration or striking velocity, and that the difference in performance diminished as the striking velocity increased. Moreover, the effectiveness of laminated targets—whether in contact or spaced—increased as the number of plates comprising each target decreased. Ballistic performance of laminated shields is further enhanced by using the thickest lamina as the rear lamina. The authors also studied shields with different structures in which fiberglass-reinforced polyester was used as the filler material, and showed that these shields performed better than weight-equivalent steel targets. The experimental results of Almohandes et al. [1996] were used by Liang et al. [2005] for validating their approximate penetration model. This model was used for comparative analysis of shields with different structures. It was concluded that the ballistic performance was the best for the double shield when the ratio of the thickness of the first layer to the total thickness was about 0.75, and the worst performance was obtained when this ratio was equal to 0.5. An air gap slightly influenced the resistance to perforation in multilayered targets.

Elek et al. [2005] developed a simple model to describe the perforation of monolithic and multilayered thin metallic plates by a flat-ended cylindrical impactor, and used their model for the analysis of the ballistic properties of multilayered spaced shields. The main results of this study may be summarized as follows. The suggested model predicted that the monolithic shield will have greater resistance than any other multilayered shield with standoff distance between the layers and equivalent total mass. The analysis of penetration in a two-layered shield showed that the maximum resistance could be obtained for very low ($< 20\%$ of total thickness) or very high ($> 80\%$ of total thickness) front-layer thickness. The increase of the number of the spaced layers in a multilayered shield, at constant total mass, caused a further decrease of the ballistic resistance. Deterioration of the ballistic performance of thin steel shields against flat-ended cylindrical impactors caused by layering had been noticed earlier by Zaid et al. [1973].

Shirai et al. [1997] investigated experimentally and numerically the impact resistance of reinforced concrete plates against projectile impact. They found that double-layered plates could be expected to have higher impact resistance than standard plates.

Park et al. [2005] suggested a multistage procedure for optimization of a two-layered shield. In the first stage, using numerical simulations to describe penetration into shields with different layer thicknesses $b^{(1)}$ and $b^{(2)}$, they determined the average temperature of a shield, T_{ave} , the average equivalent plastic strain ε_{ave} and the maximum equivalent plastic strain in a critical element of the shield ε_{max} . In the second stage, the approximate functions describing the dependencies, T_{ave} , ε_{ave} and ε_{max} vs. $b^{(1)}$ and $b^{(2)}$, were determined. In the third stage, using a reduction to a single-criterion problem by a linear combination of criteria, they solved a two-objective optimization problem. The authors considered two variants of the optimization criterion, T_{ave} or ε_{ave} and the weight of a shield. The constraints included the upper bounds or ε_{max} , and constraints on the thicknesses of the plates and the total thickness of a shield.

Aptukov [1985] and Aptukov et al. [1985], using Pontrjagin's maximum principle, determined the optimum distribution of the mechanical characteristics of a nonhomogeneous plate. The areal density of the shield along the trajectory of the impactor until it stopped was used as an optimization criterion, and cylindrical and cone-nosed impactors were considered. The two-term impactor-shield interaction model was employed, wherein the assumption about a linear dependence between the coefficients of the model was used. Using a cylindrical cavity expansion model, Aptukov et al. [1986] solved the discrete problem of optimization of a layered plate when the shield consisted of several layers of material and the material itself could be chosen from a given set of materials.

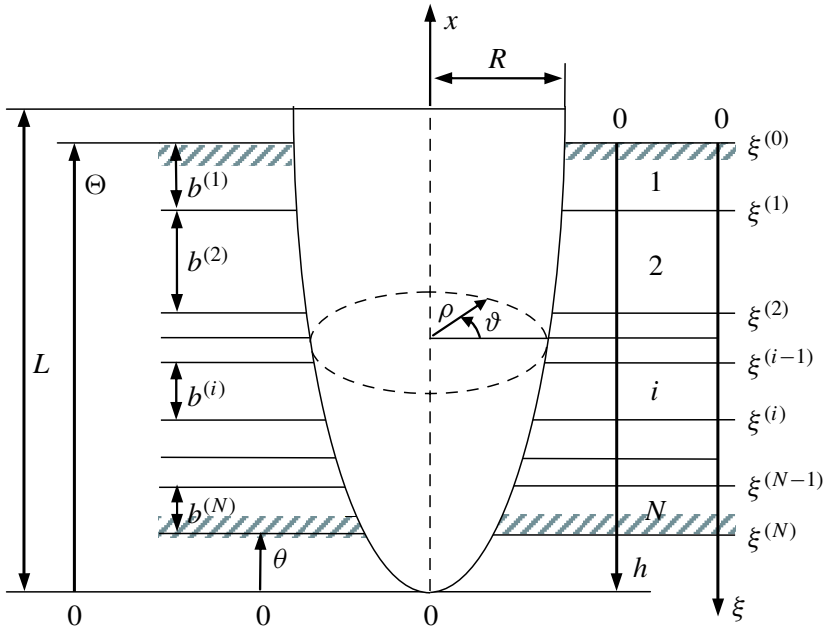


Figure 1. Notations.

Ben-Dor et al. [1998b; 1998a; 1999b; 1999a; 2000; 2006a] studied analytically the influence of air gaps between the plates and the order of plates on the BLV of a multilayered shield against conical-shaped impactors, and the results are summarized in [Ben-Dor et al. 2006a]. They found that, for the wide class of impactor-shield interaction models, the ballistic performance of the shield is independent of the widths of the air gaps and of the sequence of plates in the shield and that it is determined only by the total thickness of the plates if the plates are manufactured from the same material. Using the two-term impactor-shield interaction model, they found the criterion (depending on mechanical properties of the materials of the plates) determining the order of plates in a multilayer shield that provides the maximum BLV. In the present study we showed that this criterion remains valid for the impactors with a shape different from conical.

2. Mathematical model and statement of problem

Consider a high speed normal penetration of a rigid sharp striker (a body of revolution) into a ductile layered shield with a finite thickness. We assume that the conditions of penetration are determined mainly by the “ductile hole enlargement” model [Backman and Goldsmith 1978]. The basic notations are shown in Figure 1; and we assume that only the nose part of the cylinder-shaped impactor interacts with the shield. The coordinate h , the current depth of penetration, is defined as the distance between the leading edge of the nose of the impactor and the rear surface of the shield. The coordinate ξ is associated with the shield. In cylindrical coordinates, x, ρ, ϑ , associated with the impactor the surface of the nose is described by the following equation:

$$r = \Phi(x, \theta), \quad 0 \leq x \leq L, \quad 0 \leq \theta \leq 2\pi, \quad (1)$$

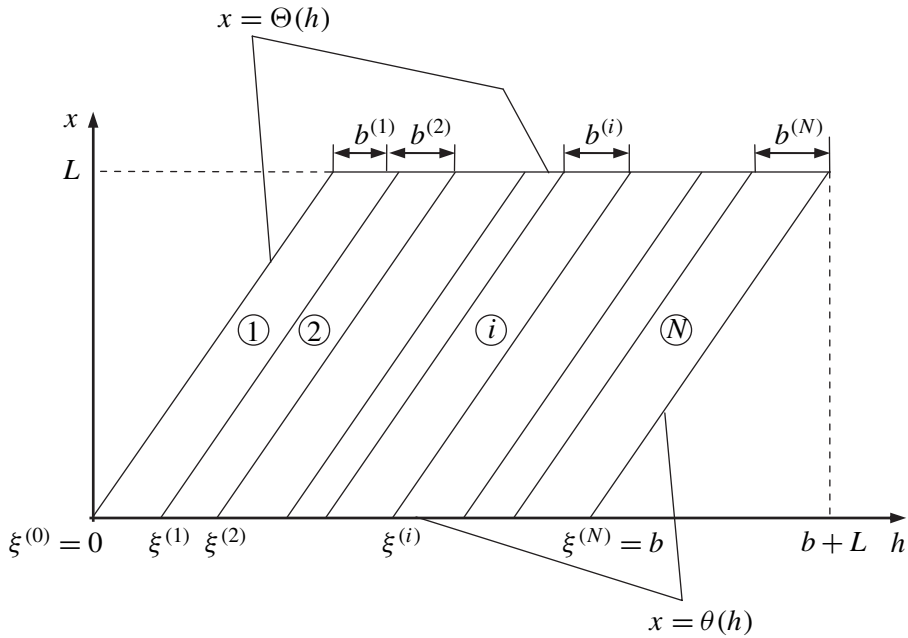


Figure 2. Model of the layered shield.

where L is the length of the impactor's nose, $\Phi(x)$ is an increasing, convex function. Assume that the shield consists of N layers (plates in-contact with different mechanical properties) with the thicknesses $b^{(1)}, b^{(2)}, \dots, b^{(N)}$. The plate with a number i is located between the cross-sections $\xi = \xi^{(i-1)}$ and $\xi = \xi^{(i)}$, where $i = 1, 2, \dots, N$ and $\xi^{(0)} = 0$. Let b be the total thickness of the shield that equals the sum of the thicknesses of all plates. It is assumed that the above parameters remain constant when the impactor penetrates into the shield. Then the part of the lateral surface of the impactor between the cross-sections $x = \theta(h)$ and $x = \Theta(h)$ (see Figure 1) interacts with some layers of the shield (see Figure 2) where

$$\theta(h) = \begin{cases} 0 & \text{if } 0 \leq h \leq b \\ h - b & \text{if } b \leq h \leq b + L \end{cases}, \quad \Theta(h) = \begin{cases} h & \text{if } 0 \leq h \leq L \\ L & \text{if } h \geq L \end{cases}. \quad (2)$$

The equation of motion of the impactor, $m(d^2h/dt^2) = -D$, can be rewritten as follows:

$$mv(dv/dh) = -D, \quad (3)$$

where the velocity of the impactor v is considered to be a function of h , m is the mass of the impactor, and D is the resistance force. We consider the range of impact velocities v_{imp} when the projectile perforates the shield. Perforation occurs when the position of the striker is $h = b + L$ and its residual velocity is v_{res} . The BLV, v_{bl} , is defined as the impact velocity of the impactor required to emerge from the shield with zero residual velocity.

We assume that the impactor-shield interaction at a given location at the surface of the impactor that is in contact with i -th plate can be represented as follows:

$$d\vec{F} = \left[a_2^{(i)} (-\vec{v}^0 \cdot \vec{n}^0)^2 v^2 + a_0^{(i)} \right] \vec{n}^0 dS, \tag{4}$$

where $d\vec{F}$ is the force acting at the surface element dS of the impactor, \vec{n}^0 is the inner normal unit vector at a given location on the impactor’s surface, \vec{v}^0 the unit vector of the impactor’s velocity, the parameters $a_0^{(i)}$ and $a_2^{(i)}$ depend on the properties of the material of the shield, and hereafter the superscript in round brackets indicates the number of the layer. Equation (4) comprises most of the widely used phenomenological models for homogeneous shields (for details see [Ben-Dor. et al. 2005; 2006a] and [Recht 1990]. In particular, in the model proposed and validated in the comprehensive experimental study by [Vitman and Stepanov 1959], $a_2^{(i)}$ and $a_0^{(i)}$ are material density of the shield and “dynamical hardness”, respectively. The values $a_0^{(i)}$ for some materials may be found in [Vitman and Ioffe 1948] (see also [Ben-Dor. et al. 2006b]).

In order to adapt Equation (4) for a layered shield let us define a step-functions ($\nu = 0, 2$):

$$a_\nu(\xi) = \begin{cases} a_\nu^{(1)} & \text{if } \xi^{(0)} \leq \xi < \xi^{(1)} \\ \dots & \\ a_\nu^{(i)} & \text{if } \xi^{(i-1)} \leq \xi < \xi^{(i)} \\ \dots & \\ a_\nu^{(N)} & \text{if } \xi^{(N-1)} \leq \xi \leq \xi^{(N)} \end{cases} . \tag{5}$$

Then Equation (4) can be rewritten as follows:

$$d\vec{F} = \left(a_2(\xi) (-\vec{v}^0 \cdot \vec{n}^0)^2 v^2 + a_0(\xi) \right) \vec{n}^0 dS. \tag{6}$$

The total force \vec{F} acting on the impactor at some location inside the shield is found by integrating the local force over the impactor-shield contact surface area, that is, over the portion of the impactor’s surface S that is determined by the inequalities $0 \leq \nu \leq 2\pi$ and $\theta(h) \leq x \leq \Theta(h)$. Taking into account the identity:

$$\xi = h - x, \tag{7}$$

and using the following formulas of differential geometry:

$$-\vec{v}^0 \cdot \vec{n}^0 = \Phi' / \sqrt{\Phi'^2 + 1}, \quad dS = \sqrt{\Phi'^2 + 1} dx d\nu, \quad \Phi' = d\Phi/dx, \tag{8}$$

we obtain the following expression for the drag force D :

$$\begin{aligned} D &= \vec{F} \cdot (-\vec{v}^0) = \iint_S \left(a_2(\xi) (-\vec{v}^0 \cdot \vec{n}^0)^2 v^2 + a_0(\xi) \right) (-\vec{v}^0 \cdot \vec{n}^0) dS \\ &= \frac{m}{2} [f_2(h)v^2 + f_0(h)], \end{aligned} \tag{9}$$

where

$$f_\nu(h) = \frac{4\pi}{m} \int_{\theta(h)}^{\Theta(h)} a_\nu(h-x) \Phi \psi_\nu(\Phi') dx, \quad \psi_\nu(z) = z \left(\frac{z}{\sqrt{z^2 + 1}} \right)^\nu, \quad \nu = 0, 2. \tag{10}$$

Substituting D from Equation (9) into Equation (3), after some algebra we obtain an ordinary linear differential equation with respect to v^2 :

$$dv^2/dh + f_2(h)v^2 + f_0(h) = 0. \quad (11)$$

The solution of Equation (11) with the initial condition $v(0) = v_{\text{imp}}$, which corresponds to the beginning of the motion of the impactor with the impact velocity v_{imp} , reads [Kamke 1959]:

$$v^2(h) = \frac{1}{q(h)}(v_{\text{imp}}^2 - g(h)), \quad (12)$$

where

$$q(h) = \exp\left(\int_0^h f_2(\eta)d\eta\right), \quad g(h) = \int_0^h f_0(H)q(H)dH. \quad (13)$$

Equation (12) yields the following formulas for the residual velocity, $v_{\text{res}} = v(b+L)$, and the BLV, v_{bl} :

$$v_{\text{res}}^2 = \frac{1}{q(b+L)}(v_{\text{imp}}^2 - g(b+L)), \quad v_{bl}^2 = g(b+L). \quad (14)$$

For further analysis it is convenient to rewrite the expression for v_{bl} using the dimensionless variables:

$$v_{bl}^2 = k \int_0^{\bar{b}+1} Q(\bar{h})d\bar{h} \int_{\bar{\theta}(\bar{h})}^{\bar{\Theta}(\bar{h})} \tilde{a}_0(\bar{h} - \bar{x})\bar{\Phi}\psi_0(\bar{\Phi}')d\bar{x}, \quad (15)$$

where L is chosen as a characteristic length, and

$$k = \frac{4\pi L^3}{m}, \quad \bar{x} = \frac{x}{L}, \quad \bar{\Phi} = \frac{\Phi}{L}, \quad \bar{\Phi}' = \frac{d\bar{\Phi}}{d\bar{x}}, \quad \bar{h} = \frac{h}{L}, \quad \bar{b} = \frac{b}{L}, \quad (16)$$

$$Q(\bar{h}) = \exp\left(k \int_0^{\bar{h}} d\bar{H} \int_{\bar{\theta}(\bar{H})}^{\bar{\Theta}(\bar{H})} \tilde{a}_2(\bar{H} - \bar{x})\bar{\Phi}\psi_2(\bar{\Phi}')d\bar{x}\right), \quad (17)$$

$$\tilde{a}_v(\bar{\xi}) = a_v(L\bar{\xi}), \quad v = 0, 2, \quad (18)$$

$$\bar{\theta}(\bar{h}) = \begin{cases} 0 & \text{if } 0 \leq \bar{h} \leq \bar{b} \\ \bar{h} - \bar{b} & \text{if } \bar{b} \leq \bar{h} \leq \bar{b} + 1 \end{cases}, \quad \bar{\Theta}(\bar{h}) = \begin{cases} \bar{h} & \text{if } 0 \leq \bar{h} \leq 1 \\ 1 & \text{if } \bar{h} \geq 1 \end{cases}. \quad (19)$$

It is shown by [Ben-Dor. et al. 1999b; Ben-Dor. et al. 1999a; Ben-Dor. et al. 2006a] that the maximum BLV of a layered shield against a conical impactor is attained if the plates are arranged in the increasing order of the parameter $\chi = a_0/a_2$. This means that if the plates are numbered, the shield must be constructed by successively adding the plates with the order numbers i_1, i_2, \dots, i_N , that satisfy the condition $\chi^{(i_1)} \leq \chi^{(i_2)} \leq \dots \leq \chi^{(i_N)}$, where $\chi^{(i)} = a_0^{(i)}/a_2^{(i)}$. The main goal of this study is to validate the latter result for nonconical impactors.

3. Ogive-shaped generatrix

Since the main goal of this study is to investigate the effect of deviation from a conical shape on the ballistic properties of a multilayer shield, the most convenient impactors for this purpose are ogive-shaped impactors having a generatrix with a constant curvature. Therefore it is natural to employ curvature as a parameter that characterizes a deviation from a conical shape. Curvature, a reciprocal of the radius of the largest circle that is tangent to a curve (on its concave side) at a point, is equal zero for a straight line, that is, a generatrix of a conical impactor.

The equation of the circle having the radius $\bar{\rho}_*$ (in dimensionless coordinates) with a center in the point $(\bar{x}_*, \bar{\Phi}_*)$ reads (see Figure 3):

$$(\bar{x} - \bar{x}_*)^2 + (\bar{\Phi} - \bar{\Phi}_*)^2 = \bar{\rho}_*^2, \tag{20}$$

where the arc of the generatrix must pass through the points $(0, 0)$ and $(1, \tau)$, and the following requirements must be satisfied:

$$0 \leq \bar{x} \leq 1, \quad 0 \leq \bar{\Phi} \leq \tau, \quad \bar{\Phi}_* \leq 0, \quad \bar{x}_* \geq 1, \quad \tau = R/L. \tag{21}$$

Omitting algebraic manipulations, let us write the equation of the generatrix in the form:

$$\bar{\Phi} = \frac{\tau}{2} - \frac{2\beta(\bar{x} - 0.5)^2 - 2\tau(\bar{x} - 0.5)\eta - 0.5\beta(\tau^2 + 1)}{\eta + \sqrt{\eta^2 + \beta^2(\tau^2 + 1) - 4\beta^2(\bar{x} - 0.5)^2 + 4\beta\tau\eta(\bar{x} - 0.5)}}, \tag{22}$$

where

$$\eta = \sqrt{\frac{4}{\tau^2 + 1} - \beta^2}, \quad \beta = \frac{1}{\bar{\rho}_*}, \quad 0 \leq \beta \leq \frac{2 \min(1, \tau)}{\tau^2 + 1}. \tag{23}$$

Equation (22) describes not only a circular arc but also a straight line, $\bar{\Phi} \leq \tau\bar{x}$, for a conical impactor. This formula for generatrix allows us to avoid computational problems arising for small β .

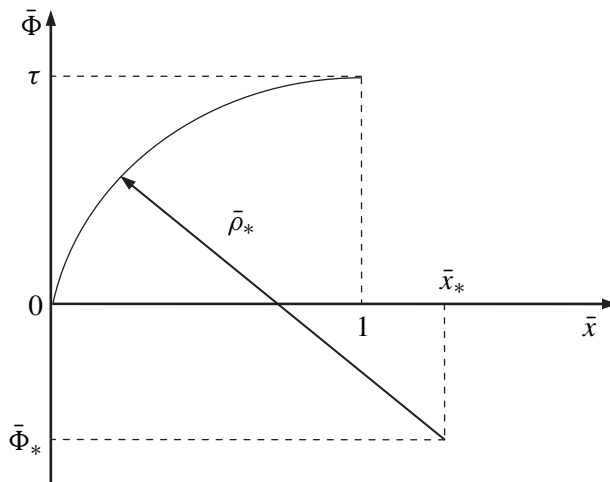


Figure 3. Ogive-shaped generatrix.

Equation (15) is quite involved and, consequently, it is not convenient for calculations and can introduce uncontrollable numerical error. All these problems can be avoided by using piecewise-linear approximation of the generatrix of a striker.

4. Piecewise-linear approximation of the generatrix

The equation of a piecewise linear generatrix can be written as follows (see Figure 4):

$$\bar{\Phi}(\bar{x}) = \begin{cases} \alpha_1 \bar{x} + \beta_1 & \text{if } 0 = \bar{x}_0 \leq \bar{x} \leq \bar{x}_1 \\ \dots & \\ \alpha_j \bar{x} + \beta_j & \text{if } \bar{x}_{j-1} \leq \bar{x} \leq \bar{x}_j \\ \dots & \\ \alpha_M \bar{x} + \beta_M & \text{if } \bar{x}_{M-1} \leq \bar{x} \leq \bar{x}_M = 1 \end{cases}, \tag{24}$$

where

$$\alpha_j = \frac{\bar{\Phi}_j - \bar{\Phi}_{j-1}}{\bar{x}_j - \bar{x}_{j-1}}, \quad \beta_j = \frac{\bar{x}_j \bar{\Phi}_{j-1} - \bar{x}_{j-1} \bar{\Phi}_j}{\bar{x}_j - \bar{x}_{j-1}}, \quad j = 1, 2, \dots, M. \tag{25}$$

The domain determined by Equation (19) can be represented as a union of $N \times M$ sub-domains $S_j^{(i)}$ (see Figure 5). The parallelogram $A_j^{(i)} B_j^{(i)} C_j^{(i)} E_j^{(i)}$ with the vertices at the points $A_j^{(i)} (\bar{\xi}^{(i-1)} + \bar{x}_{j-1}, \bar{x}_{j-1})$, $B_j^{(i)} (\bar{\xi}^{(i-1)} + \bar{x}_j, \bar{x}_j)$, $C_j^{(i)} (\bar{\xi}^{(i)} + \bar{x}_j, \bar{x}_j)$ and $E_j^{(i)} (\bar{\xi}^{(i)} + \bar{x}_{j-1}, \bar{x}_{j-1})$, bounds the sub-domain $S_j^{(i)}$. The

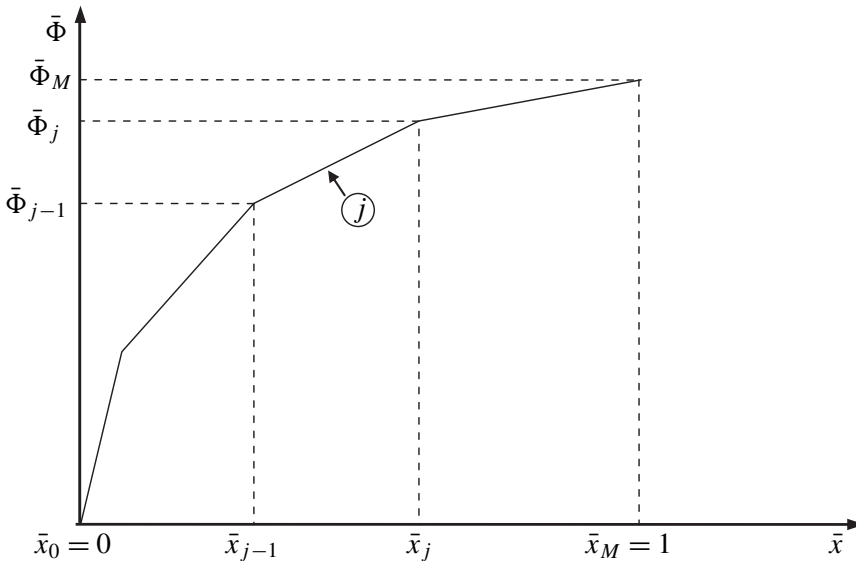


Figure 4. Piecewise linear generatrix.

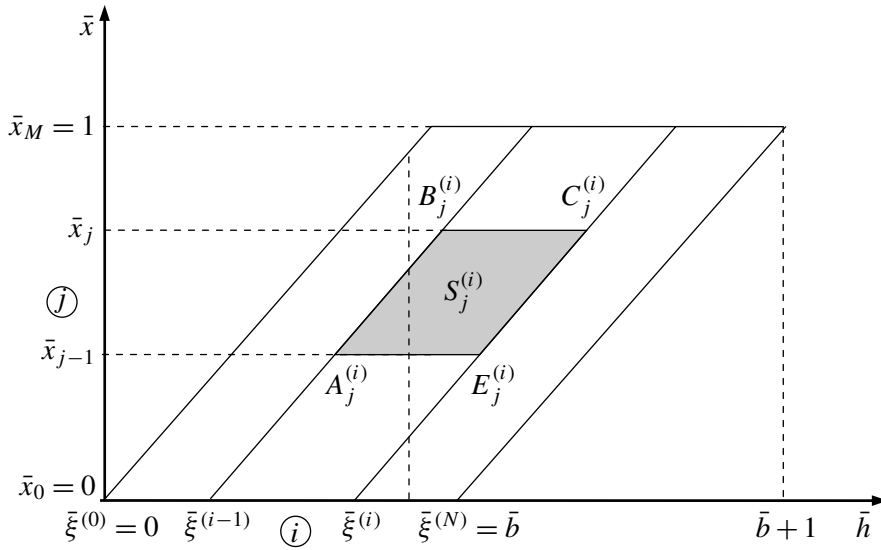


Figure 5. Domain of impactor/shield interaction for layered shield and impactor with linear generatrix.

sub-domains $S_j^{(i)}$ are determined as follows:

$$\begin{cases} \bar{\xi}^{(i-1)} + \bar{x}_{j-1} \leq \bar{h} \leq \bar{\xi}^{(i)} + \bar{x}_j \\ \bar{\theta}_j^{(i)}(h) \leq \bar{x} \leq \bar{\Theta}_j^{(i)}(h) \end{cases}, \tag{26}$$

where

$$\bar{\theta}_j^{(i)}(h) = \begin{cases} 0 & \text{if } \bar{h} \leq \bar{\xi}^{(i-1)} + \bar{x}_{j-1} \\ \bar{x}_{j-1} & \text{if } \bar{\xi}^{(i-1)} + \bar{x}_{j-1} \leq \bar{h} \leq \bar{\xi}^{(i)} + \bar{x}_{j-1} \\ \bar{x} - \bar{\xi}^{(i)} & \text{if } \bar{\xi}^{(i)} + \bar{x}_{j-1} \leq \bar{h} \leq \bar{\xi}^{(i)} + \bar{x}_j \\ 0 & \text{if } \bar{h} \geq \bar{\xi}^{(i)} + \bar{x}_j \end{cases}, \tag{27}$$

$$\bar{\Theta}_j^{(i)}(h) = \begin{cases} 0 & \text{if } \bar{h} \leq \bar{\xi}^{(i-1)} + \bar{x}_{j-1} \\ \bar{x}_{j-1} - \bar{\xi}^{(i-1)} & \text{if } \bar{\xi}^{(i-1)} + \bar{x}_{j-1} \leq \bar{h} \leq \bar{\xi}^{(i-1)} + \bar{x}_j \\ \bar{x}_j & \text{if } \bar{\xi}^{(i-1)} + \bar{x}_j \leq \bar{h} \leq \bar{\xi}^{(i)} + \bar{x}_j \\ 0 & \text{if } \bar{h} \geq \bar{\xi}^{(i)} + \bar{x}_j \end{cases}. \tag{28}$$

Then the integral in Equation (17) can be represented as sum of integrals over sub-domains $S_j^{(i)}$:

$$\begin{aligned}
 \frac{1}{k} \ln[Q(\bar{h})] &= \sum_{\substack{1 \leq i \leq N \\ 1 \leq j \leq M}} \int_0^{\bar{h}} d\bar{H} \int_{\bar{\theta}_j^{(i)}(\bar{H})}^{\bar{\Theta}_j^{(i)}(\bar{H})} \tilde{a}_2(\bar{H} - \bar{x}) \bar{\Phi} \psi_2(\bar{\Phi}') d\bar{x} \\
 &= \sum_{\substack{1 \leq i \leq N \\ 1 \leq j \leq M}} \tilde{a}_2^{(i)} \psi_2(\alpha_j) \int_0^{\bar{h}} d\bar{H} \int_{\bar{\theta}_j^{(i)}(\bar{H})}^{\bar{\Theta}_j^{(i)}(\bar{H})} (\alpha_j \bar{x} + \beta_j) d\bar{x} \\
 &= \sum_{\substack{1 \leq i \leq N \\ 1 \leq j \leq M}} \tilde{a}_2^{(i)} \psi_2(\alpha_j) [\Omega_j^{(i)}(\bar{h}) - \omega_j^{(i)}(\bar{h})],
 \end{aligned} \tag{29}$$

where

$$\begin{aligned}
 \omega_j^{(i)}(\bar{h}) &= \int_{\bar{\xi}^{(i-1)} + \bar{x}_{j-1}}^{\bar{h}} \left\{ 0.5\alpha_j [\bar{\theta}_j^{(i)}(\bar{H})]^2 + \beta_j \bar{\theta}_j^{(i)}(\bar{H}) \right\} d\bar{H}, \\
 \Omega_j^{(i)}(\bar{h}) &= \int_{\bar{\xi}^{(i-1)} + \bar{x}_{j-1}}^{\bar{h}} \left\{ 0.5\alpha_j [\bar{\Theta}_j^{(i)}(\bar{H})]^2 + \beta_j \bar{\Theta}_j^{(i)}(\bar{H}) \right\} d\bar{H}.
 \end{aligned} \tag{30}$$

The integrals in Equation (30) can be calculated taking into account the definition of functions $\bar{\theta}_j^{(i)}(h)$ and $\bar{\Theta}_j^{(i)}(h)$:

$$\omega_j^{(i)}(\bar{h}) = \begin{cases} 0 & \text{if } h \leq \bar{\xi}^{(i-1)} + \bar{x}_{j-1}, \\ (0.5\alpha_j \bar{x}_{j-1}^2 + \beta_j \bar{x}_{j-1})(\bar{h} - \bar{\xi}^{(i-1)} - \bar{x}_{j-1}) & \text{if } \bar{\xi}^{(i-1)} + \bar{x}_{j-1} \leq h \leq \bar{\xi}^{(i)} + \bar{x}_{j-1}, \\ (\alpha_j/6)((\bar{h} - \bar{\xi}^{(i)})^3 - \bar{x}_{j-1}^3) + 0.5\beta_j((\bar{h} - \bar{\xi}^{(i)})^2 - \bar{x}_{j-1}^2) & \text{if } \bar{\xi}^{(i)} + \bar{x}_{j-1} \leq h \leq \bar{\xi}^{(i)} + \bar{x}_j, \\ \omega_j^{(i)}(\bar{\xi}^{(i)} + \bar{x}_j) & \text{if } h > \bar{\xi}^{(i)} + \bar{x}_j, \end{cases} \tag{31}$$

$$\Omega_j^{(i)}(\bar{h}) = \begin{cases} 0 & \text{if } h \leq \bar{\xi}^{(i-1)} + \bar{x}_{j-1}, \\ (\alpha_j/6)((\bar{h} - \bar{\xi}^{(i-1)})^3 - \bar{x}_{j-1}^3) + 0.5\beta_j((\bar{h} - \bar{\xi}^{(i-1)})^2 - \bar{x}_{j-1}^2) & \text{if } \bar{\xi}^{(i-1)} + \bar{x}_{j-1} \leq h \leq \bar{\xi}^{(i-1)} + \bar{x}_j, \\ (\alpha_j/6)(\bar{x}_j^3 - \bar{x}_{j-1}^3) + 0.5\beta_j(\bar{x}_j^2 - \bar{x}_{j-1}^2) + \bar{x}_j(0.5\alpha_j \bar{x}_j + \beta_j)(\bar{h} - \bar{\xi}^{(i-1)} \bar{x}_j) & \text{if } \bar{\xi}^{(i-1)} + \bar{x}_j \leq h \leq \bar{\xi}^{(i)} + \bar{x}_j, \\ \Omega_j^{(i)}(\bar{\xi}^{(i)} + \bar{x}_j) & \text{if } h > \bar{\xi}^{(i)} + \bar{x}_j. \end{cases} \tag{32}$$

The expression for the BLV, Equation (15), can be rewritten similarly to Equation (29):

$$\begin{aligned} \frac{v_{bl}^2}{k} &= \sum_{\substack{1 \leq i \leq N \\ 1 \leq j \leq M}} \int_{\bar{\xi}^{(i-1)} + \bar{x}_{j-1}}^{\bar{\xi}^{(i)} + \bar{x}_j} Q(\bar{H}) d\bar{H} \int_{\bar{\theta}_j^{(i)}(\bar{H})}^{\bar{\Theta}_j^{(i)}(\bar{H})} \tilde{a}_0(\bar{H} - \bar{x}) \bar{\Phi} \psi_0(\bar{\Phi}') d\bar{x} \\ &= \sum_{\substack{1 \leq i \leq N \\ 1 \leq j \leq M}} \tilde{a}_0^{(i)} \psi_0(\alpha_j) \int_{\bar{\xi}^{(i-1)} + \bar{x}_{j-1}}^{\bar{\xi}^{(i)} + \bar{x}_j} Q(\bar{h}) [\Omega_j^{(i)}(\bar{h}) - \omega_j^{(i)}(\bar{h})] d\bar{h}. \end{aligned} \tag{33}$$

Thus, determining the BLV is reduced to calculating one-dimensional integrals.

5. Result of numerical calculations and discussion

In numerical calculations we considered a two-layer shield where “the first” plate and “the second” plate are manufactured from the soft steel and aluminum, respectively. We used the model given by Equation (4) with $a_0^{(1)} = 1850$ MPa, $a_2^{(1)} = 7830$ kg/m³, $a_0^{(2)} = 350$ MPa and $a_2^{(2)} = 2765$ kg/m³, where the values of the “dynamical hardness” $a_0^{(i)}$ are adopted from [Vitman and Ioffe 1948]. All calculations were performed for BLVs less than 1000 m/s. The latter constraint approximately determines the range of validity of this model.

The following numbers are assigned to the materials of the plates. The superscript [1 – 2] means that the order of the plates in the shield is such that the plate manufactured from material #1 (soft steel) is perforated before the plate manufactured from material #2 (aluminum), the superscript [2 – 1] indicates the reverse order of the plates. Since parameter $\chi = a_0/a_2$ decreases with the increase of the number of the material ($\chi^{(2)} = 0.127 \cdot 10^6$ m²/s², $\chi^{(1)} = 0.236 \cdot 10^6$ m²/s²), then $v_{bl}^{[2-1]} \geq v_{bl}^{[1-2]}$ for conical-nosed impactors. The goal of our calculations was to estimate the effect of the parameter β , that characterizes the deviation from the conical shape on the index $\delta = v_{bl}^{[2-1]}/v_{bl}^{[1-2]}$, that quantifies the efficiency of changing the order of plates on the BLV. Typical results of these calculations are showed in Figures 6-7. It must be noted that $\beta = 0$ for a conical impactor.

In all these figures we showed the dependence δ versus β , and different curves correspond to different ratios of the thicknesses of the plates in a shield. The curves in Figure 6 are plotted for $\tau = 0.5$, for $\tau = 1$ in Figure 7. Clearly, in the second case and for relatively large values of β when the shape of the bluntness is close to spherical, the penetrator is not a sharp-shaped body, and the plots have only a formal meaning.

Figure 6a corresponds to the dimensionless total thickness of the shield $\bar{b} = 8.0$ and $k = 0.0004$ m³/kg. The curves of the dependencies δ vs. β are concave, i.e., at the beginning the increase of the curvature of the generatrix of a striker causes reduction of the index δ , while further increase of β is accompanied by the increase of the index δ . Notably, for relatively large β , the magnitude of the index δ may become larger than that for a cone-shaped impactor. When the shape of the impactor is specified (β is given) the effect of the change of the order of the plates (the magnitude of the index δ) depends essentially upon the ratio of the thicknesses of the plates. In the considered case for all ogive-shaped impactors this effect is maximal when $b^{(1)}/b \approx 0.3$.

In Figure 6b we showed two sets of plots, the first for $k = 0.0007$ m³/kg and $\bar{b} = 8.0$, and the second for $k = 0.0004$ m³/kg and $\bar{b} = 12.0$. The first set differs from that in Figure 6a by the increased value

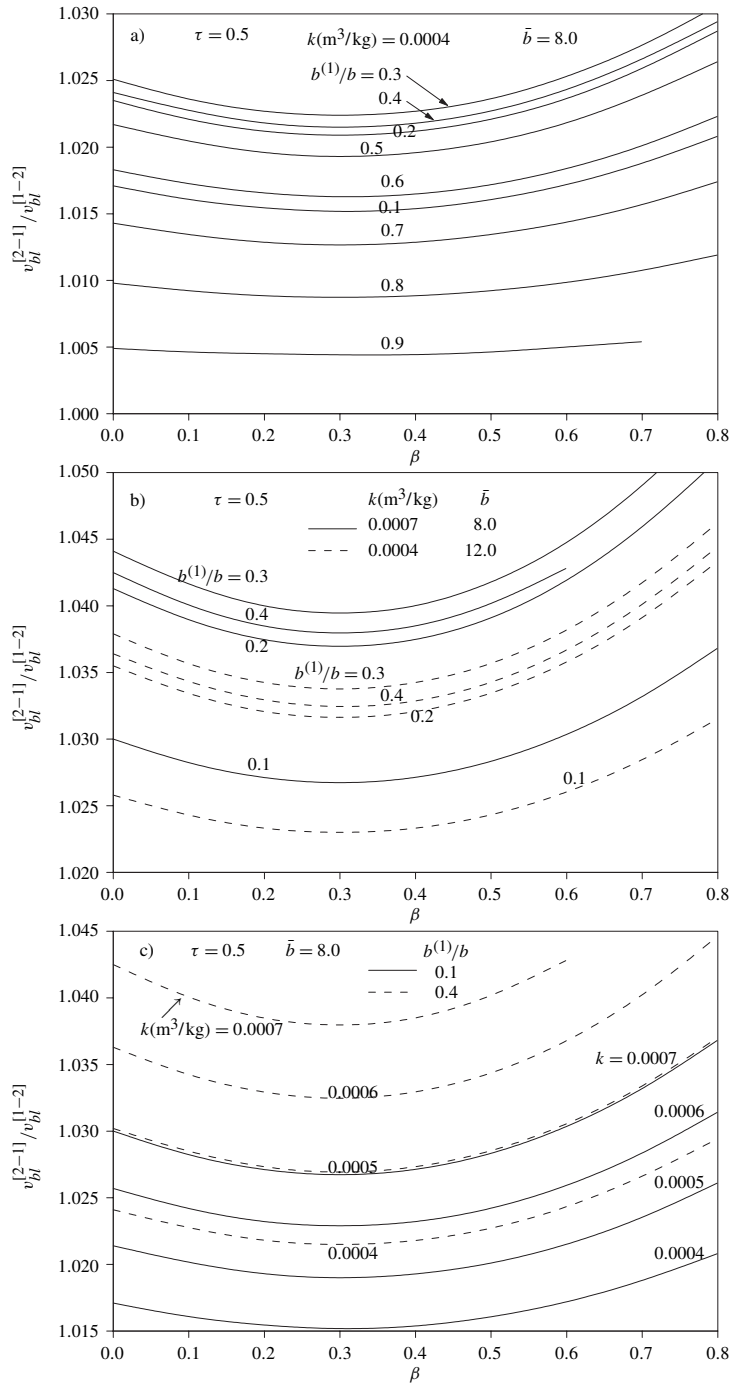


Figure 6. Influence of the curvature of the impactor's generatrix on the effect of rearranging the plates in the shield; $v_{bl}^{[1-2]}$ and $v_{bl}^{[2-1]}$ are the BLVs for the "direct" and the "reverse" order of the plates in the shield, respectively; β is the dimensionless curvature of the impactor's nose; $\tau = 0.5$.

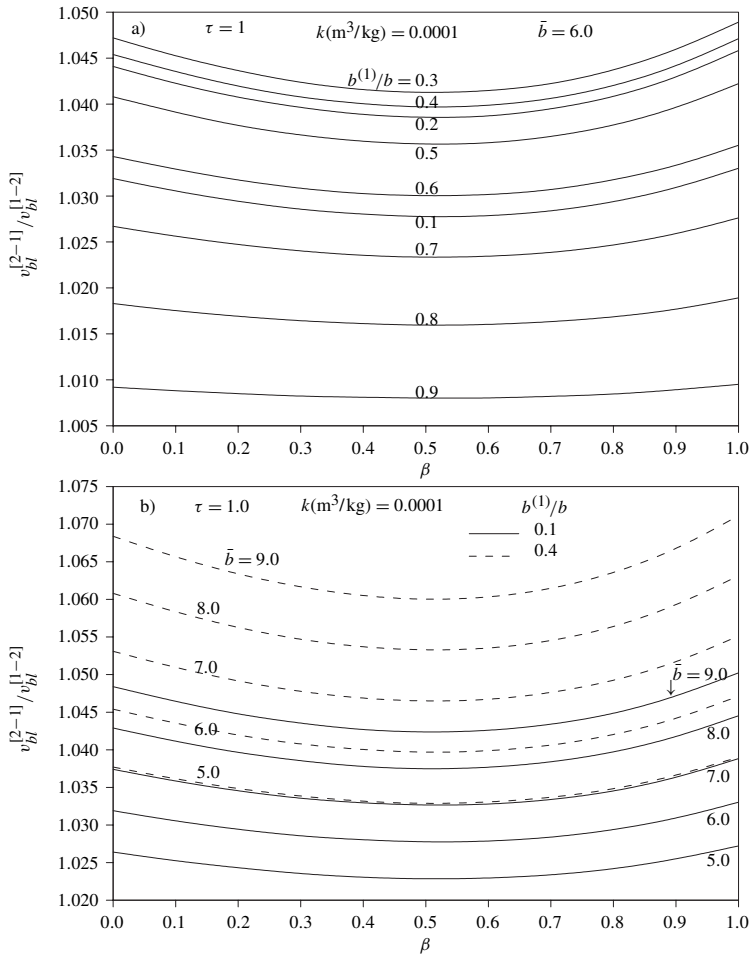


Figure 7. Influence of the curvature of the impactor’s generatrix on the effect of rearranging the plates in the shield; $v_{bl}^{[1-2]}$ and $v_{bl}^{[2-1]}$ are the BLVs for the “direct” and the “reverse” order of the plates in the shield, respectively; β is the dimensionless curvature of the impactor’s nose; $\tau = 1.0$

of k , while in the second set of curves we increased \bar{b} . Comparing the results showed in Figures 6a-6b demonstrates that increase of the magnitude of each of these two parameters, k and \bar{b} , results in the increase of the ratio of BLVs, δ , for every β . The effect of k on β is shown explicitly in Figure 6c.

Figure 7a for $\tau = 1$ demonstrates the same dependencies as Figure 6a. In Figure 7b we showed the effect of the total thickness of the shield for two values of the ratio $b^{(1)}/b$ (0.1 and 0.4) on the dependence $\delta = \delta(\beta)$. Inspection of these plots shows that the increase of the total width \bar{b} causes the increase of the ratio δ .

Our calculations demonstrated that replacement of the conical head of the impactor by a convex ogive-shaped head can be accompanied either by the increase or decrease of the efficiency of changing the order

of the plates in a shield. However we did not encounter situations in which the optimal order of the plates in the shield is different for these two different impactor shapes.

6. Energy absorption

Using the relationships for the impact energy and residual energy of the impactor E_{imp} and E_{res} , respectively:

$$E_{\text{imp}} = 0.5 m v_{\text{imp}}^2, \quad E_{\text{res}} = 0.5 m v_{\text{res}}^2 \quad (34)$$

and Equation (14) rewritten as

$$v_{\text{res}}^2 = \frac{1}{q_*} [v_{\text{imp}}^2 - v_{bl}^2], \quad q_* = q(b + L) = Q(\bar{b} + 1), \quad (35)$$

yields the following formula for the relative energy absorbed by a shield:

$$e_{\text{abs}} = \frac{E_{\text{imp}} - E_{\text{res}}}{E_{\text{imp}}} = \frac{q_* - 1}{q_*} + \frac{1}{q_*} \left(\frac{v_{bl}}{v_{\text{imp}}} \right)^2. \quad (36)$$

Assume that Equation (36) is written for the *initial* shield with a certain plate order. Consider also a *modified* shield with an altered plate order where the corresponding parameters in the modified shield are denoted by a tilde. Since q_* is independent of the order of the plates in the shield [Ben-Dor. et al. 1999b], we may write equation similar to Equation (36) for the modified shield:

$$\tilde{e}_{\text{abs}} = \frac{E_{\text{imp}} - \tilde{E}_{\text{res}}}{E_{\text{imp}}} = \frac{q_* - 1}{q_*} + \frac{1}{q_*} \left(\frac{\tilde{v}_{bl}}{v_{\text{imp}}} \right)^2. \quad (37)$$

Then

$$e_{\text{abs}} - \tilde{e}_{\text{abs}} = \frac{1}{q_*} \left(\frac{\tilde{v}_{bl}}{v_{\text{imp}}} \right)^2 (\mu^2 - 1), \quad \mu = \frac{v_{bl}}{\tilde{v}_{bl}}. \quad (38)$$

Taking into account that

$$\mu^2 - 1 \equiv (\mu - 1)^2 + 2(\mu - 1) \approx 2(\mu - 1), \quad (39)$$

for $|\mu - 1| \ll 1$, Equation (38) can be rewritten as follows:

$$e_{\text{abs}} - \tilde{e}_{\text{abs}} \approx \zeta (1 - \mu), \quad \zeta = \frac{2}{q_*} \left(\frac{\tilde{v}_{bl}}{v_{\text{imp}}} \right)^2. \quad (40)$$

Since $v_{bl}^0 \leq v_{\text{imp}}$ and $q_* > 1$, then $\zeta < 2$. Therefore, the model employed in this study predicts that rearranging the plates in the shield causes a change in the relative magnitude of the absorbed energy that does not exceed the doubled ratio of the corresponding BLVs.

7. Concluding remarks

Using approximate model for ductile layered shields, we analyzed the effect of re-arranging plates in the shield against nonconical rigid impactors. We found that the criterion for the optimal arrangement of the plates in a shield, determined previously for conical impactors, is valid also for nonconical impactors. The theoretical results we obtained can be employed in further experimental studies on the optimization of impactors and shields.

References

- [Almohandes et al. 1996] A. A. Almohandes, M. S. AbdelKader, and A. M. Eleiche, “Experimental investigation of the ballistic resistance of steel-fiberglass reinforced polyester laminated plates”, *Compos. Part B Eng.* **27**:5 (1996), 447–458.
- [Aptukov 1985] V. N. Aptukov, “Optimal structure of inhomogeneous plate with continuous distribution of properties over the thickness”, *Mech. Solids* **20**:3 (1985), 148–151.
- [Aptukov et al. 1985] V. N. Aptukov, G. I. Petrukhin, and A. A. Pozdeev, “Optimal deceleration of a rigid body by an inhomogeneous plate for the case of normal impact”, *Mech. Solids* **20**:1 (1985), 155–160.
- [Aptukov et al. 1986] V. N. Aptukov, V. L. Belousov, and M. A. Kanibolotskii, “Optimization of the structure of a layered slab with the penetration of a rigid striker”, *Mech. Compos. Mater.* **22**:2 (1986), 179–183.
- [Awerbuch and Bodner 1974] J. Awerbuch and S. R. Bodner, “Analysis of the mechanics of perforation of projectiles in metallic plates”, *Int. J. Solids Struct.* **10**:6 (1974), 671–684.
- [Backman and Goldsmith 1978] M. E. Backman and W. Goldsmith, “The mechanics of penetration of projectiles into targets”, *Int. J. Eng. Sci.* **16**:1 (1978), 1–99.
- [Ben-Dor et al. 1998a] G. Ben-Dor, A. Dubinsky, and T. Elperin, “Effect of air gaps on ballistic resistance of targets for conical impactors”, *Theor. Appl. Fract. Mech.* **30**:3 (1998), 243–249.
- [Ben-Dor et al. 1998b] G. Ben-Dor, A. Dubinsky, and T. Elperin, “On the ballistic resistance of multi-layered targets with air gaps”, *Int. J. Solids Struct.* **35**:23 (1998), 3097–3103.
- [Ben-Dor et al. 1999a] G. Ben-Dor, A. Dubinsky, and T. Elperin, “Effect of air gap and order of plates on ballistic resistance of two layered armor”, *Theor. Appl. Fract. Mech.* **31**:3 (1999), 233–241.
- [Ben-Dor et al. 1999b] G. Ben-Dor, A. Dubinsky, and T. Elperin, “On the order of plates providing the maximum ballistic limit velocity of a layered armor”, *Int. J. Impact Eng.* **22**:8 (1999), 741–755.
- [Ben-Dor et al. 2000] G. Ben-Dor, A. Dubinsky, and T. Elperin, “The optimum arrangement of the plates in a multilayered shield”, *Int. J. Solids Struct.* **37**:4 (2000), 687–696.
- [Ben-Dor et al. 2005] G. Ben-Dor, A. Dubinsky, and T. Elperin, “Ballistic impact: Recent advances in analytical modeling of plate penetration dynamics”, *Appl. Mech. Rev.* **58**:6 (2005), 355–371. A review.
- [Ben-Dor et al. 2006a] G. Ben-Dor, A. Dubinsky, and T. Elperin, *Applied high-speed plate penetration dynamics*, Solid State and its Applications **132**, Springer, Dordrecht, 2006.
- [Ben-Dor et al. 2006b] G. Ben-Dor, A. Dubinsky, and T. Elperin, “Effect of air gaps on ballistic resistance of ductile shields perforated by non-conical impactors”, *J. Mech. Mater. Struct.* **1** (2006), 279–299.
- [Corran et al. 1983a] R. S. J. Corran, C. Ruiz, and P. J. Shadbolt, “Impact loading of plates: An experimental investigation”, *Int. J. Impact Eng.* **1**:1 (1983), 3–22.
- [Corran et al. 1983b] R. S. J. Corran, C. Ruiz, and P. J. Shadbolt, “On the design of containment shield”, *Comput. Struct.* **16**:1–4 (1983), 563–572.
- [Elek et al. 2005] P. Elek, S. Jaramaz, and D. Mickovic, “Modeling of perforation of plates and multi-layered metallic targets”, *Int. J. Solids Struct.* **42**:3–4 (2005), 1209–1224.
- [Gupta and Madhu 1997] N. K. Gupta and V. Madhu, “An experimental study of normal and oblique impact of hard-core projectile on single and layered plates”, *Int. J. Impact Eng.* **19**:5–6 (1997), 395–414.
- [Honda et al. 1930] K. Honda, G. Takamae, and T. Watanabe, “On the measurement of the resistance of shield plates to penetration by a rifle bullet”, *Science Reports of the Tohoku Imperial University* **19** (1930), 703–725.
- [Kamke 1959] E. Kamke, *Differentialgleichungen: Lösungsmethoden und Lösungen; gewöhnliche Differentialgleichungen*, Geest and Portig, Leipzig, 1959.
- [Liang et al. 2005] C. C. Liang, M. F. Yang, P. W. Wu, and T. L. Teng, “Resistant performance of perforation of multi-layered targets using an estimation procedure with marine application”, *Ocean Eng.* **32**:3–4 (2005), 441–468.
- [Madhu et al. 2003] V. Madhu, T. B. Bhat, and N. K. Gupta, “Normal and oblique impacts of hard projectiles on single and layered plates: An experimental study”, *Def. Sci. J.* **53**:2 (2003), 147–156.

- [Marom and Bodner 1979] I. Marom and S. R. Bodner, “Projectile perforation of multi-layered beams”, *Int. J. Mech. Sci.* **21**:8 (1979), 489–504.
- [Nixdorff 1984a] K. Nixdorff, “Application of the penetration theory of J. Awerbuch and S. R. Bodner on multilayered targets”, *Z. Angew. Math. Mech.* **64**:4 (1984), T147–T149.
- [Nixdorff 1984b] K. Nixdorff, “Some applications of the impact theory of J. Awerbuch and S. R. Bodner”, *Trans. Can. Soc. Mech. Eng.* **8**:1 (1984), 16–20.
- [Nixdorff 1987] K. Nixdorff, “Discussion of two theories on the penetration of multilayer metallic targets”, *Trans. Can. Soc. Mech. Eng.* **11**:3 (1987), 161–178.
- [Park et al. 2005] M. Park, J. Yoo, and D. T. Chung, “An optimization of a multi-layered plate under ballistic impact”, *Int. J. Solids Struct.* **42**:1 (2005), 123–137.
- [Radin and Goldsmith 1988] J. Radin and W. Goldsmith, “Normal projectile penetration and perforation of layered targets”, *Int. J. Impact Eng.* **7**:2 (1988), 229–259.
- [Recht 1990] R. F. Recht, “High velocity impact dynamics: Analytical modeling of plate penetration dynamics”, pp. 443–513 in *High velocity impact dynamics*, edited by J. A. Zukas, Wiley and Sons, New York, 1990.
- [Shirai et al. 1997] T. Shirai, A. Kambayashi, O. T., H. Taniguchi, M. Ueda, and N. Ishikawa, “Experiment and numerical simulation of double-layered RC plates under impact loadings”, *Nucl. Eng. Des.* **176**:3 (1997), 195–205.
- [Vitman and Ioffe 1948] F. F. Vitman and B. S. Ioffe, “A simple method of determining the dynamical hardness of metals using a double cone”, *Zavodskaja Laboratorija* **14**:6 (1948), 727–732. in Russian.
- [Vitman and Stepanov 1959] F. F. Vitman and V. A. Stepanov, “Effect of the strain rate on the resistance of metals to deformation at impact velocities of 100–1000 m/s”, pp. 207–221 in *Nekotoryje problemy prochnosti tvjrdogo tela*, USSR Acad. of Sci., Moscow, 1959. In Russian.
- [Weidemaier et al. 1993] P. Weidemaier, H. Senf, H. Rothenhäusler, G. L. Filbey, and W. A. Gooch, “On the ballistic resistance of laminated steel targets: experiments and numerical calculations”, pp. 681–690 in *Fourteenth International Symposium on Ballistics* (Quebec, 1993), 1993.
- [Zaid et al. 1973] A. I. O. Zaid, A. El-Kalai, and F. W. Travis, “An examination of the perforation of mild steel plate by a flat-ended cylindrical projectile”, *Int. J. Mech. Sci.* **15**:2 (1973), 129–143.
- [Zukas 1996] J. A. Zukas, “Effect of lamination and spacing on finite thickness plate perforation”, pp. 103–115 in *Structures under shock and impact, IV*, edited by N. Jones et al., Computational Mechanics Publications, Southampton, U.K., 1996.
- [Zukas and Scheffler 2001] J. A. Zukas and D. R. Scheffler, “Impact effects in multilayered plates”, *Int. J. Solids Struct.* **38**:19 (2001), 3321–3328.

Received 15 Oct 2005. Accepted 20 Dec 2005.

G. BEN-DOR: bendorg@bgu.ac.il

Pearlstone Center for Aeronautical Engineering, Department of Mechanical Engineering, Ben-Gurion University of the Negev, P. O. Box 653, Beer-Sheva, 84105, Israel
<http://www.bgu.ac.il/me/staff/gabi/index.html>

A. DUBINSKY: dubin@bgu.ac.il

Pearlstone Center for Aeronautical Engineering, Department of Mechanical Engineering, Ben-Gurion University of the Negev, P. O. Box 653, Beer-Sheva, 84105, Israel
<http://www.bgu.ac.il/~dubin>

T. ELPERIN: elperin@bgu.ac.il

Pearlstone Center for Aeronautical Engineering, Department of Mechanical Engineering, Ben-Gurion University of the Negev, P. O. Box 653, Beer-Sheva, 84105, Israel
<http://www.bgu.ac.il/me/staff/tov/index.html>

A NUMERICAL INVESTIGATION OF THE EFFECT OF BOUNDARY CONDITIONS AND REPRESENTATIVE VOLUME ELEMENT SIZE FOR POROUS TITANIUM

HUI SHEN AND L. CATHERINE BRINSON

To facilitate the design and application of porous titanium and titanium foam, numerical simulation of their mechanical behavior is essential. The concept of a representative volume element (RVE) is essential to obtain accurate estimates of the properties. Because of the high contrast between the properties of the two phases (pore vs. matrix), it is impractical to obtain a single RVE independent of boundary conditions to provide accurate predictions. We suggest that a set of small domain RVEs can be used instead, as long as the average of the small domains provides a convergent result. Two mixed boundary conditions simulating uniaxial proportional loading were designed and implemented on several 2D and 3D finite element models at different length scales, that is, containing different numbers of pores. The two boundary conditions provide opposite biased responses. Convergence of both the macroscopic and the microscopic elastoplastic responses associated with the boundary conditions is demonstrated here. By this approach, RVEs that are prohibitively large according to Hill's definition are divided into reasonably small ones associated with special boundary conditions, and the error of predictions associated with model size can be estimated.

1. Introduction

Pure titanium and titanium-based alloys exhibit very useful mechanical and biological properties, which make titanium-based foams potential materials for load-bearing sandwich cores and orthopedic implants [Banhart 2001; Spoerke et al. 2005; Wen et al. 2002a; Wen et al. 2002b]. In particular, we observe that as a potential implant material, it is comparable to bone stiffness in that its stiffness as a porous material drops with the square of relative density, and the open porosity allows complete bone ingrowth [Gibson and Ashby 1997; Spoerke et al. 2005]. These properties make porous titanium a promising material to solve the inherent problems of monolithic metallic implants, such as the "stress shielding" effect [Chang et al. 1996; Dunand 2004; Li et al. 2004; Spoerke et al. 2005; Wen et al. 2002a; Wen et al. 2002b]. However, the porous microstructure of the foam leads to the concentration of stress and strain near pores under load-bearing conditions, which results in reduced strength and ductility. Finite element (FE) simulation on a microstructural level is therefore needed to understand and predict the macroscopic and microscopic responses, to better target and optimize the application of these porous materials.

The titanium foam considered here was processed by a solid-state foaming technique in which individual high-pressure argon pores expand at elevated temperature and coalesce to form large pores

The authors acknowledge the financial support of the National Science Foundation through grant number DMR-0108342 and thank Professor Dunand's group for providing titanium foam and images.

Keywords: representative volume element, titanium foam, microstructure, finite element, boundary condition.

[Dunand 2004; Murray and Dunand 2003]. When porosity is less than 25%, pores are mostly rounded, generally equiaxial, and unmerged (see Figure 1 (top)). As higher porosity, small pores coexist with large pores which have a complex, tortuous shape, as shown in Figure 1 (bottom) [Murray and Dunand 2003]. The microstructures are locally heterogeneous, although sufficiently large experimental samples behave homogeneously. For such a heterogeneous material, it is fundamental to determine whether a FE model that simulates a fragment of the heterogeneous microstructure is large enough to be a representative volume element (RVE) to describe the responses of the titanium foam. The determination of the minimum size of an RVE relies on basic definitions, which have been developed for the study of heterogeneous materials. One definition, proposed by [Hill 1963], states that an RVE is “a sample that (a) is structurally entirely typical of the whole mixture on average, and (b) contains a sufficient number of inclusions for the apparent overall moduli to be effectively independent of the surface values of traction and displacement, so long as these values are macroscopically uniform.” Point (a) requires the RVE to include statistically all possible microstructural configurations, and (b) demands that the effective properties obtained from the RVE be independent of the uniform displacement and traction boundary conditions (BCs). Regarding (b), Huet [1990] analytically proved that the effective elastic modulus obtained from an RVE is bounded by the average apparent responses of finite size domains under uniform displacement boundary condition (UDBC) and uniform traction boundary condition (UTBC). This conclusion was extended to a nonlinear elastic heterogeneous material by [Hazanov 1999] and to elastoplastic materials under proportional loading by [Jiang et al. 2001b]. Subsequently, many researchers have shown homogenization convergence such that as the domain size increases to the minimum RVE, the two bounds converge to the effective property [Hollister and Kikuchi 1992; Huet 1990; Jiang et al. 2001a; Ostoja-Starzewski 1998; Pecullan et al. 1999; Terada et al. 2000]. However, the convergence of the two bounds was found to be extremely slow for heterogeneous materials with soft inclusions in a hard matrix, and the higher the contrast between the moduli of matrix and inclusions, the slower the convergence [Bouyge et al. 2002; Jiang et al. 2001a; Ostoja-Starzewski 1998; Pecullan et al. 1999]. Given that zero-modulus pores provide extreme moduli contrast to the titanium matrix for the titanium foam, the minimum RVE according to Hill’s definition becomes too large for FE analyses, especially for three dimensional (3D) FE analyses, due to the limitation of computational power.

A more pragmatic definition of RVE was introduced by [Drugan and Willis 1996], which defines it as “the smallest material volume element of the composite for which the usual spatially constant ‘overall modulus’ macroscopic constitutive representation is a sufficient accurate model to represent mean constitutive response.” Based on this RVE concept, Drugan and Willis [1996] analytically proved that it is possible to obtain relatively accurate estimations of elastic constants with small RVEs for a microstructure with nonoverlapping spherical inclusions. In particular, the effective moduli obtained by a finite size domain over a length of only two sphere diameters can be close to those obtained by a domain of infinite length, within a few percent of error, even in cases of void inclusions. This conclusion contradicts the results obtained according to Hill’s definition. The BC applied on the RVE is the key factor responsible for the difference. Although the RVE should be independent of BCs according to Hill’s definition, the right BC is needed for the RVE defined by [Drugan and Willis 1996]. As pointed out by [Jiang et al. 2001a], the derivation of [Drugan and Willis 1996] for the minimum RVE implied that the RVE should be associated with periodic BC and that the microstructure is actually periodic. They verified the RVE theory of [Drugan and Willis 1996] for unidirectional fiber-matrix composites with the

modulus contrast of inclusion to matrix in a range of 0.001 to 1000. Gusev [1997] numerically verified that the average of elastic constants of many small RVEs is close to the result for large RVEs for 3D microstructures with randomly distributed nonoverlapping spherical inclusions under periodic BC. Their results also indicate that smaller analyzed windows lead to more scattered results.

Following the concept of the RVE defined by [Drugan and Willis 1996] but accounting for the fluctuations of the apparent properties predicted by finite size domains, Kanit et al. [2003] recently proposed a more quantitative definition. Based on their definition, the concept of one single minimum RVE should be abandoned and a sufficient number of small domain RVEs should be used to obtain the average linear properties. While UTBC and UDBC on small domains result in large, oppositely biased errors for the effective property, a periodic BC gives a smaller error for the same window size. However, it should be noted that periodic BC requires the continuity of the inclusions on opposite boundaries to ensure the periodicity of the microstructure. Because such unnatural periodicity is seldom observed in real heterogeneous materials, periodic BCs are not appropriate for FE models developed by cutting out fragments of actual microstructures or by using simulated microstructures based on actual microstructures.

Alternative BCs might be considered which maintain the philosophy of the RVE concept of Kanit et al. [2003], that is, which emphasize the average of the responses of small domains. Hazanov and Huet [1994] proved analytically that the elasticity tensor predicted by a model smaller than Hill's RVE definition submitted to mixed BCs falls between the predictions associated with UTBC and UDBC. They concluded that relatively accurate results can be obtained by using small domains under mixed BCs. Jiang et al. [2001a] numerically verified this conclusion on unidirectional fiber-matrix composites. However, the kind of mixed BCs to associate with RVEs to obtain accurate estimates for porous microstructure is still an open question. Because of the extreme contrast in properties between inclusion and matrix, no satisfactory solution (achievable with reasonable computer power) yet exists for practical RVEs for porous microstructure.

The objective of this paper is to find reliable and practical RVEs for porous titanium using the homogenization convergence concept and obtaining statistical averages by solving the boundary value problems. As discussed above, solutions of finite size domains under mixed BCs approach effective properties much faster than UDBC and UTBC. However, since results from finite size domains under a single mixed BC approach the effective properties from one side, it is difficult to determine the point where the finite size domains are large enough. In addition, such a one-side bias can be eliminated only by increasing the size of analyzed domains. Therefore, we designed two mixed BCs simulating a uniaxial loading condition providing opposite bias and imposed them on the porous models. This enabled us to determine the convergence of RVEs and obtain relatively accurate results with small RVEs by averaging the results associated with the two BCs. By this approach, we trade-off the large RVEs with two mixed BCs and more small domains. In other words, the prohibitively large RVE of Hill's definition were divided into reasonable small ones associated with special BCs. While previous definitions of RVE focused only on macroscopic linear properties, our current study also aims to verify the convergence of both the macroscopic and the microscopic elastoplastic responses. The results of this paper elucidate a method for numerical prediction of the global and local response with small size models for porous materials.

It should be noted that a porosity of 40–50% is generally considered to be an ideal range for orthopedic applications of porous titanium. This porosity provides reduced stiffness for reduced stress-shielding as well as sites for bone ingrowth, while simultaneously maintaining mechanical durability. However, the

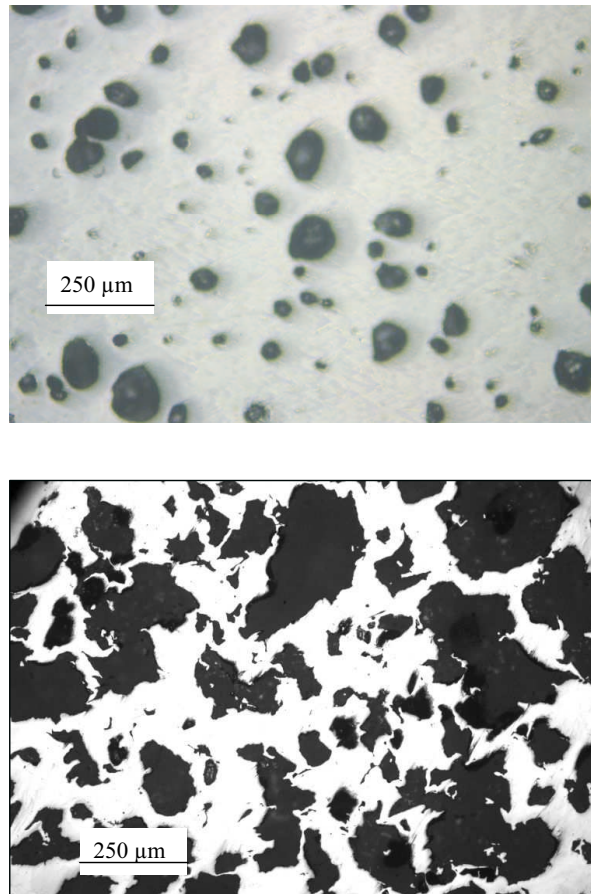


Figure 1. Optical micrograph of metallographic cross-section for titanium foam with 14.7% porosity (top) and 50% porosity (bottom).

microstructure at such high porosity is extremely complex (see, for example, [Figure 1](#) (bottom)). Since we focus on exploring methodology in this current study, we present results for low porosity titanium foam and discuss implications for a 3D model with a higher porosity of 48%. The RVE for higher porosity titanium foams will be considered in our future work.

In next sections, 2D and 3D FE models with different sizes are created based on the simulated microstructure of the experimental material using the methodology presented in our previous work [[Shen et al. 2006](#)]. BCs for the FE simulations are described. Then the uniaxial stress-strain response is simulated based on the FE models associated with the two mixed BCs. Both macroscopic and microscopic responses are demonstrated for the convergence study.

2. Finite element modeling

2.1. Simulated microstructure. We generated a simulated version of the microstructure of the titanium foam at 14.7% porosity using the methodology presented in our previous work [[Shen et al. 2006](#)]. 3D pore size and location distribution information was first derived from 2D sections of a sample at 14.7%

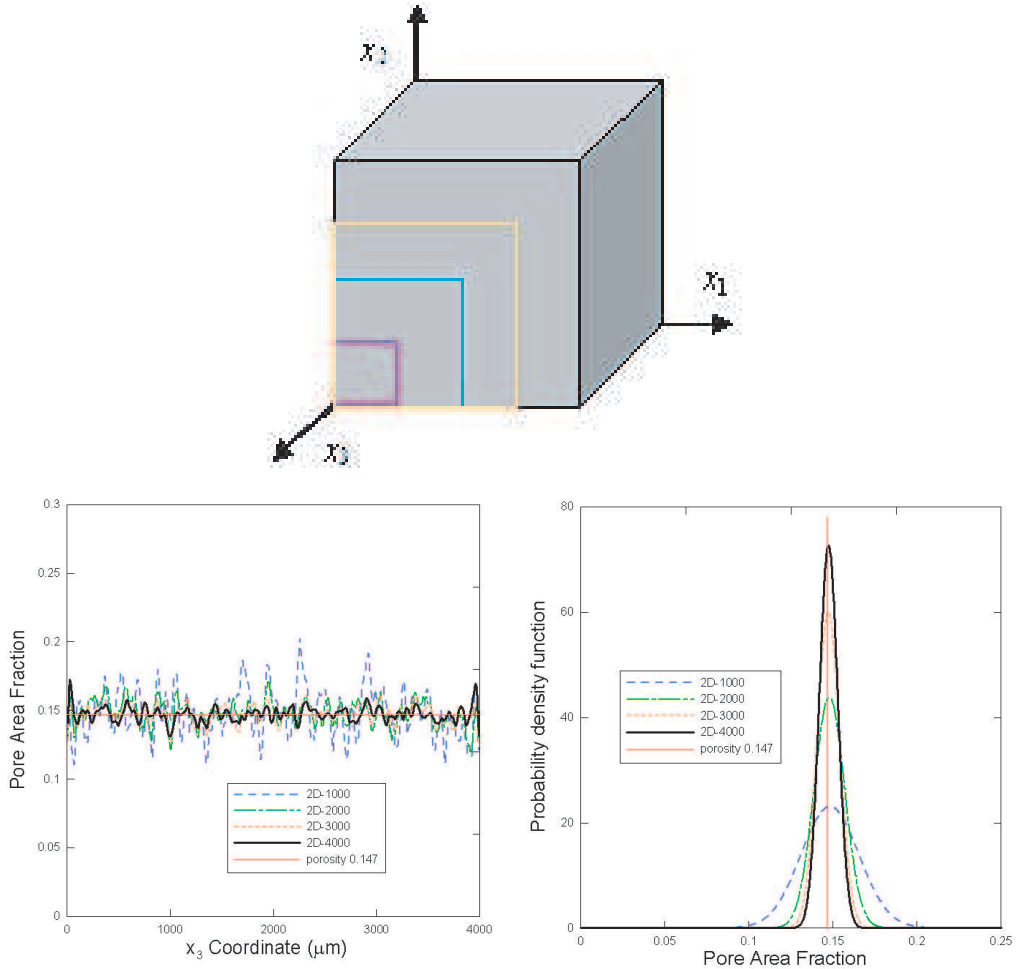


Figure 2. The cubic domain of the 3D-MP-70271 model with side length of 4000 μm and a series of window sizes of 1000 μm , 2000 μm , 3000 μm , and 4000 μm (top). Pore area fraction as a function of the x_3 position for the series of windows (bottom left). Distributions of pore area fraction of each window series (bottom right).

porosity as shown in Figure 1 (top). The location distribution of pores is random. The pore size distribution follows the Weibull distribution [Tobias and Trindade 1995] in which the density function is denoted by

$$f(x) = \frac{m}{x} \left(\frac{x}{c}\right)^m e^{-(x/c)^m},$$

where the parameters, m and c , are shape and scale parameters. We obtained $m = 2.47$ and $c = 64.68$ for the pore sections observed in 2D sectioning planes, observing an average diameter of 63.3 μm . We derived $m = 2.29$ and $c = 60.52$ by stereology study, resulting in 3D average pore diameter of 53.6 μm [Shen et al. 2006]. Based on these data, a 3D simulated microstructure which retains the essential geometry features of the random microstructure was developed. The microstructure of the foam at higher

porosity was determined by a geometric simulation of pore growth and movement during the foaming process.

In the simulated 3D multipore microstructure (3D-MP-70271) at porosity 14.7%, 70,271 spherical pores were randomly located in a $(4000\ \mu\text{m})^3$ cube. No pore impingement was permitted. To simulate the serial sectioning process, a reliable technique for constructing microstructures [Li et al. 1998], sections parallel to the x_1x_2 plane passed through the 3D-MP-70271 model were cut every $10\ \mu\text{m}$ along x_3 axis.

The distribution of pore area fractions in window sizes of $1000\ \mu\text{m}$, $2000\ \mu\text{m}$, $3000\ \mu\text{m}$, and $4000\ \mu\text{m}$ is shown in Figure 2. We see that as the size of the window increases, the range and variation of the area fraction decreases and the area fractions converge to the overall porosity of the microstructure.

The simulated microstructure is comprised of two distinct phases: pores and titanium matrix. To avoid computational difficulties, it was assumed that pores are linear elastic with a very low modulus of 10^{-7} GPa and Poisson's ratio of 0.3. The titanium matrix having elastic modulus of 110 GPa, Poisson's ratio of 0.33, and yield strength of 275 MPa is representative of CP Ti-40 [ASM 2002]. The matrix yield surface follows the Von Mises yield criterion with isotropic hardening. All material properties and simulations are for room temperature.

2.2. 2D and 3D finite element models. 2D and 3D finite element models were created by cutting out the fragments of the simulated microstructure. To study the convergence of responses of various size windows, four groups of 2D sections of side length from $1000\ \mu\text{m}$ to $4000\ \mu\text{m}$ having an area fraction matching the overall porosity of 14.7% were generated based on the simulated microstructure to construct 2D models. The four groups of 2D finite element models with side lengths of $1000\ \mu\text{m}$, $2000\ \mu\text{m}$, $3000\ \mu\text{m}$, and $4000\ \mu\text{m}$ have ratios of model length to the average pore size (L/d) of 15.8, 31.6, 47.4, and 63.2, respectively. Each model group contains eight models and is labeled with the size, that is, side length. For example, 2D-1000 refers to the model group with side length of $1000\ \mu\text{m}$. Examples of these 2D model groups are shown in Figure 3. We see that some pores having a centroid near an edge are truncated. On average, there are 59 pores and 10,930 elements in the 2D-1000 model; 235 pores and 39,010 elements in the 2D-2000 model; 542 pores and 88,385 elements in the 2D-3000 model; 943 pores and 159,768 elements in the 2D-4000 model.

Two 3D model groups with side lengths of $170\ \mu\text{m}$ and $340\ \mu\text{m}$ having porosity of 14.7% were selected from different locations of the 3D-MP-70271 microstructure. Each group contains four 3D models. The ratios of model size to the average pore size (L/d) are 3.17 and 6.34, respectively. Models are labeled with the two sizes as 3D-170 and 3D-340. Examples of the 3D-170 and 3D-340 models are shown in Figure 4. Again, some pores having a centroid near a face are truncated. On average, the 3D-170 model contain 12 pores and 15,439 elements; the 3D-340 model 64 pores and 125,536 elements.

One 3D model with higher porosity of 48% in a $340\ \mu\text{m}$ cube was created by cutting a block of a high porosity microstructure. As shown in Figure 5, pores are connected to form large pores which have a complex, tortuous shape. The model contains 130,552 elements.

All 2D models were meshed with eight-node biquadratic plane strain elements and all 3D models were meshed with ten-node modified tetrahedral elements with hourglass control to prevent volumetric lock during plastic deformation [ABAQUS 2004]. All finite element analyses were performed using ABAQUS software. Mesh convergence was verified based on overall and local stress values. The overall

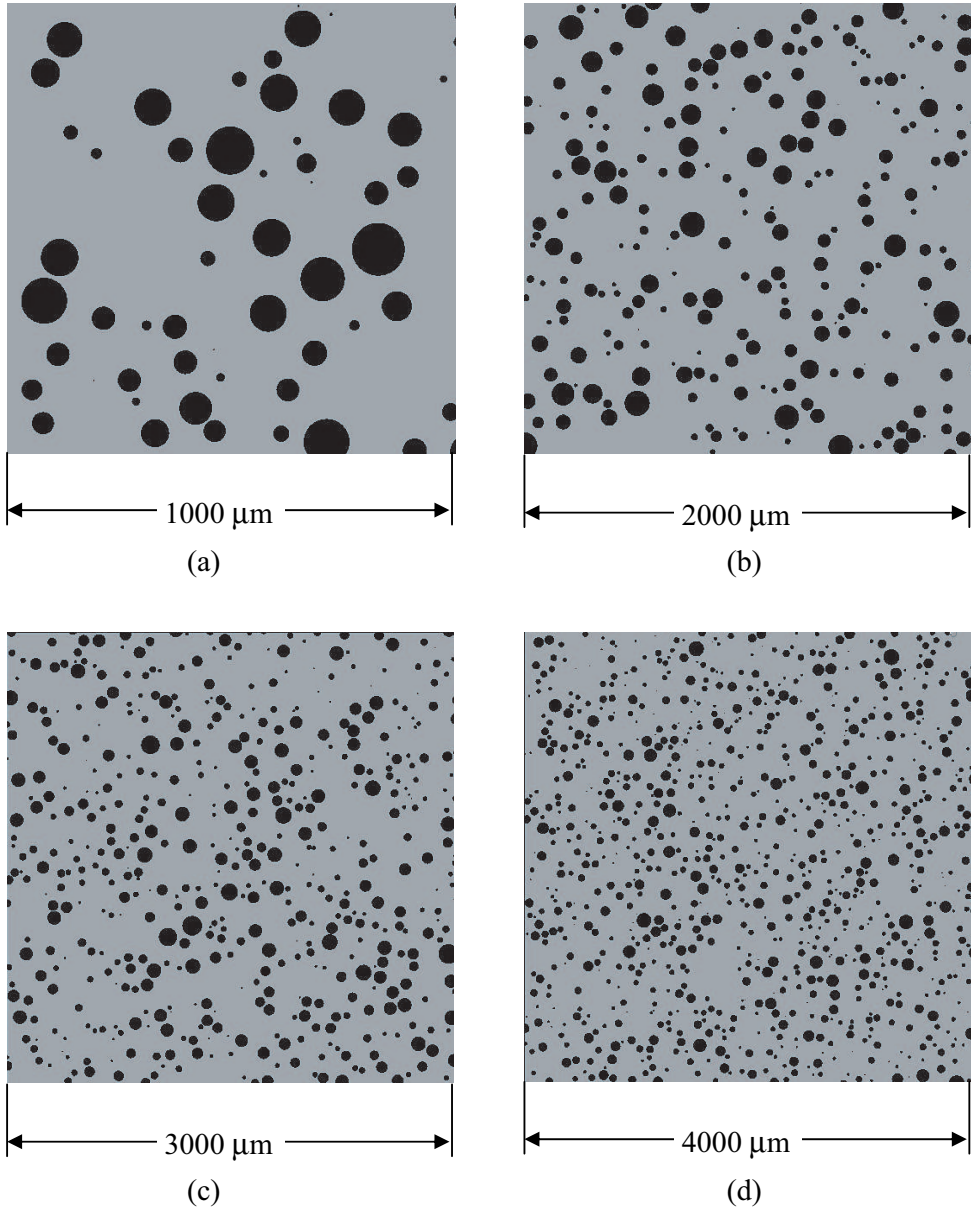


Figure 3. Geometry of the (a) 2D-1000, (b) 2D-2000, (c) 2D-3000, and (d) 2D-4000 models.

strain and stress are calculated by using volume averages

$$\bar{\varepsilon}_{ij} = \frac{1}{V} \int_V \varepsilon_{ij} dV = \frac{1}{\sum_{m=1}^N V^{(m)}} \sum_{m=1}^N \varepsilon_{ij}^{(m)} V^{(m)},$$

$$\bar{\sigma}_{ij} = \frac{1}{V} \int_V \sigma_{ij} dV = \frac{1}{\sum_{m=1}^N V^{(m)}} \sum_{m=1}^N \sigma_{ij}^{(m)} V^{(m)}.$$

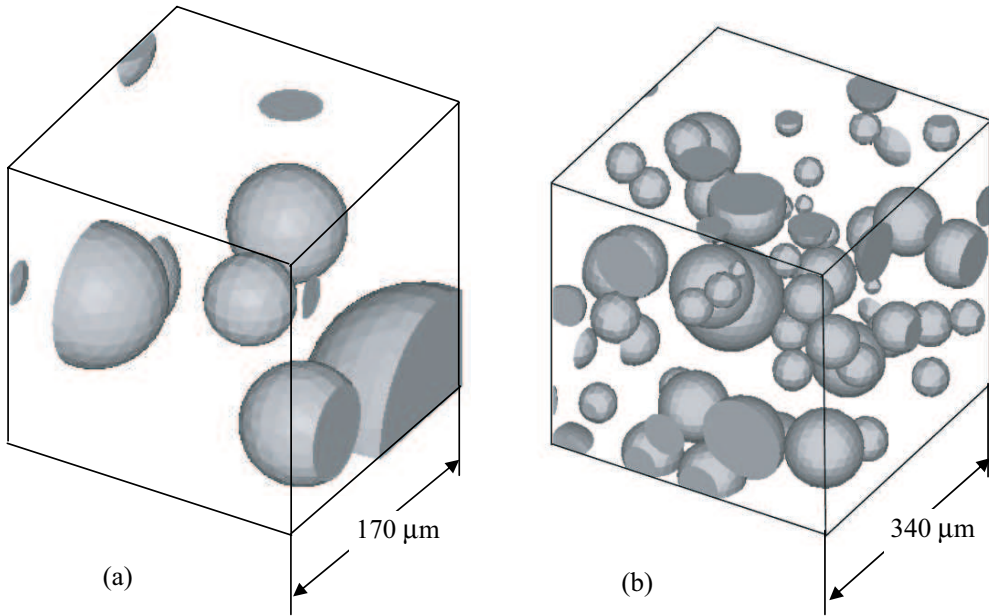


Figure 4. Geometry of the (a) 3D-170 and (b) 3D-340 models.

The standard deviation of the microscopic stress distribution is weighted by the volume of the element as follows:

$$SD = \sqrt{\frac{\sum_{m=1}^N V^{(m)} (\sigma_{ij}^{(m)} - \bar{\sigma}_{ij})^2}{\sum_{m=1}^N V^{(m)}}},$$

where $V^{(m)}$ is the volume of element m , N is the total number of elements, and σ_{ij} is the Cauchy stress tensor. The total strain tensor is decomposed into elastic and plastic components. Note that the stress and strain tensors σ_{ij} and ε_{ij} are obtained at the centroid of each element.

2.3. Boundary conditions. The experimental procedure to obtain macroscopic stress-strain response for porous materials is typically a uniaxial compression test, which has been performed for porous titanium in [Davis et al. 2001] and [Shen et al. 2006]. Our numerical study focuses on the responses of the titanium foam under uniaxial proportional compressive loading. As discussed in Section 1, one can obtain accurate estimates of material properties with relatively small RVEs under mixed BCs [Hazanov and Huet 1994]. Two types of mixed BCs were designed in the numerical simulation as described in Table 1 in which x_2 direction is the loading direction. For boundary condition 1 (BC1), uniform displacements are imposed on the faces perpendicular to the loading direction without friction. Other faces parallel to the loading direction are traction free. This boundary condition is used to simulate the experimental setup in the mechanical test. For boundary condition 2 (BC2), the same conditions are set for the faces perpendicular to the loading direction; however the faces parallel to the loading direction remain straight and parallel during deformation to simulate an interior domain compatible with the surrounding material. Therefore, BC2 is periodic mechanically, but not microstructurally since the pores on opposing edges are not continuous. The boundaries for 2D models are the same as those applied

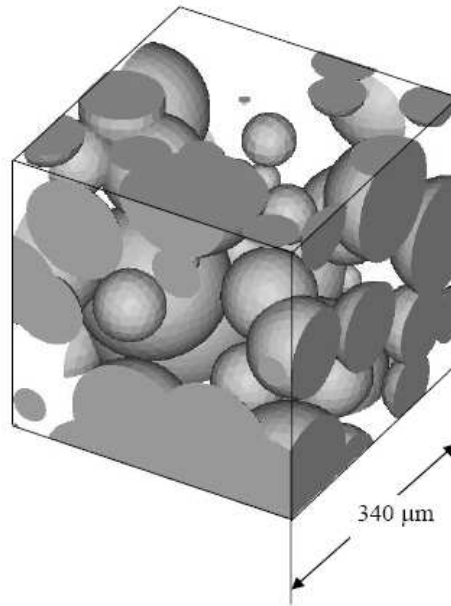


Figure 5. Geometry of the 3D model with porosity of 48% in a 340 μm cube.

to the left, right, top, and bottom faces of the 3D models to impose uniaxial compressive loading. Note that 2D models are restricted to uniaxial and biaxial load cases.

3. Results and discussion

3.1. Macroscopic response. The uniaxial stress-strain responses predicted by the sixteen individual 2D simulations (eight models deformed along x_1 and x_2 directions) of the 2D-1000, 2D-2000, 2D-3000, and 2D-4000 models under the two mixed BCs are shown in Figure 6. These collected results reveal that as 2D window size increases from 1000 μm to 4000 μm, the dispersion of the predicted stress-strain curves for each BC decreases. The range of the two groups of stress-strain curves associated with BC1 and BC2 also become smaller. The average responses of the sixteen individual 2D simulations under the two BCs

Model Face	Boundary Condition 1	Boundary Condition 2
Top ($x_2 = a$)	$u_2 = -0.01a; \quad t_1 = t_3 = 0$	$u_2 = -0.01a; \quad t_1 = t_3 = 0$
Bottom ($x_2 = 0$)	$u_2 = 0; \quad t_1 = t_3 = 0$	$u_2 = 0; \quad t_1 = t_3 = 0$
Left ($x_1 = 0$)	$t_1 = t_2 = t_3 = 0$	$u_1 = -\bar{u}_1; \quad t_2 = t_3 = 0$
Right ($x_1 = a$)	$t_1 = t_2 = t_3 = 0$	$u_1 = \bar{u}_1; \quad t_2 = t_3 = 0$
Front ($x_3 = a$)	$t_1 = t_2 = t_3 = 0$	$u_3 = \bar{u}_3; \quad t_1 = t_2 = 0$
Back ($x_3 = 0$)	$t_1 = t_2 = t_3 = 0$	$u_3 = -\bar{u}_3; \quad t_1 = t_2 = 0$

Table 1. Boundary conditions (\bar{u}_1 and \bar{u}_3 are displacements of the four side faces upon loading on the top).

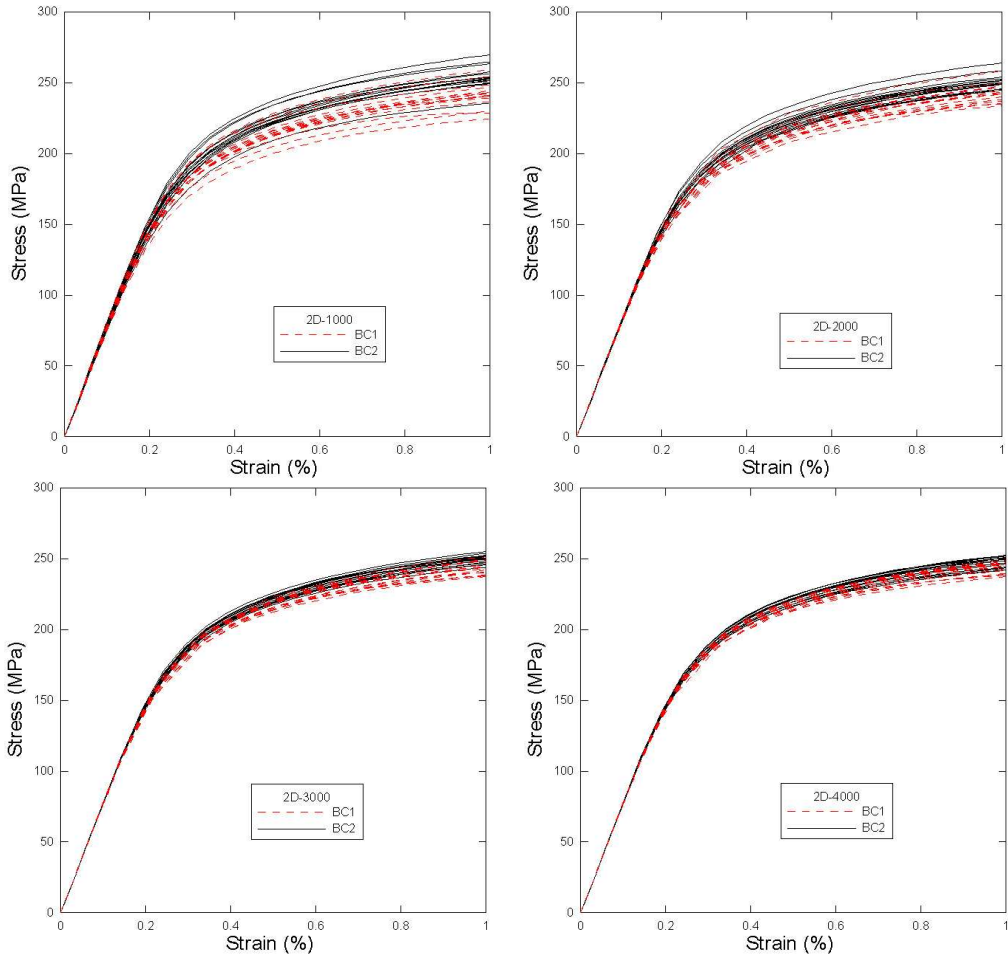


Figure 6. Macroscopic stress-strain responses predicted by the sixteen individual simulations of 2D-1000 (top left), 2D-2000 (top right), 2D-3000 (bottom left), and 2D-4000 models (bottom right) associated with the two mixed boundary conditions.

converge to a common value as the window size increases as shown in [Figure 7](#). The convergence trend of the two BCs suggests BC1 is slightly underrestrictive which is similar to UTBC, and BC2 is slightly overrestrictive, which is similar to UDBC. The asymptotic relationship of the average elastic modulus and overall stress at 1% strain corresponding to the length scale of the window is illustrated in [Figure 8](#). The overall averages of all thirty-two responses (eight models deformed along x_1 and x_2 directions under BC1 and BC2) for each model group are shown in [Figure 9](#), and the curves are nearly indistinguishable.

The observations presented in the figures are confirmed in [Table 2](#), which shows the 2D model predictions for elastic modulus and overall stress at 1% uniaxial strain. We see here that under BC1 and BC2 the standard deviation of elastic modulus decreases from 2.34% and 2.12% for the 2D-1000 models to 0.45% and 0.44% for the 2D-4000 models. The overall stress decreases from 3.69% and 3.0% to 1.55% and 1.44%, respectively. For all thirty-two responses for the two BCs, the standard deviation decreases

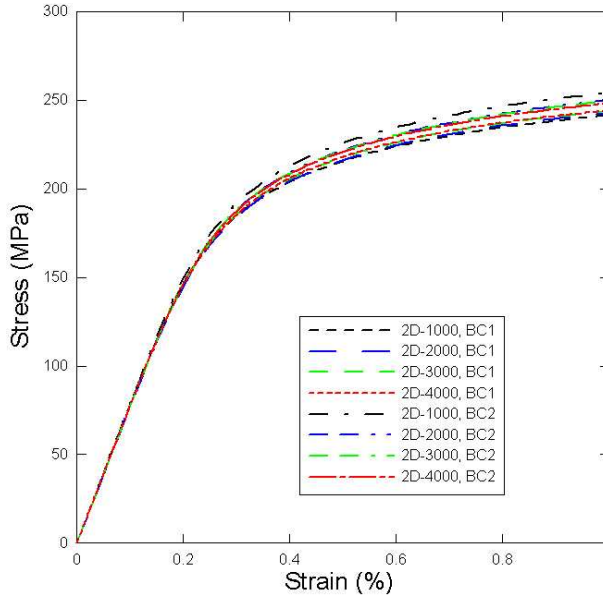


Figure 7. Macroscopic stress-strain responses averaged over the sixteen individual simulations of 2D-1000, 2D-2000, 2D-3000, and 2D-4000 models associated with the two mixed boundary conditions.

		<i>E</i> (GPa)		σ (MPa)	
		AVG.	SD%	AVG.	SD%
2D-1000	BC1	78.06	2.34	241.37	3.69
	BC2	79.08	2.12	254.30	3.00
	<i>BC12avg</i>	78.57	2.29	247.84	4.23
2D-2000	BC1	77.19	0.97	242.59	2.61
	BC2	77.92	0.91	250.1	2.10
	<i>BC12avg</i>	77.56	1.04	246.27	2.79
2D-3000	BC1	77.67	0.54	243.72	1.92
	BC2	78.03	0.51	249.45	1.29
	<i>BC12avg</i>	77.85	0.57	246.59	1.99
2D-4000	BC1	77.69	0.45	244.04	1.55
	BC2	78	0.44	248.15	1.44
	<i>BC12avg</i>	77.85	0.48	246.09	1.7

Table 2. 2D model predictions for elastic modulus and overall stress in loading direction at 1% uniaxial strain.

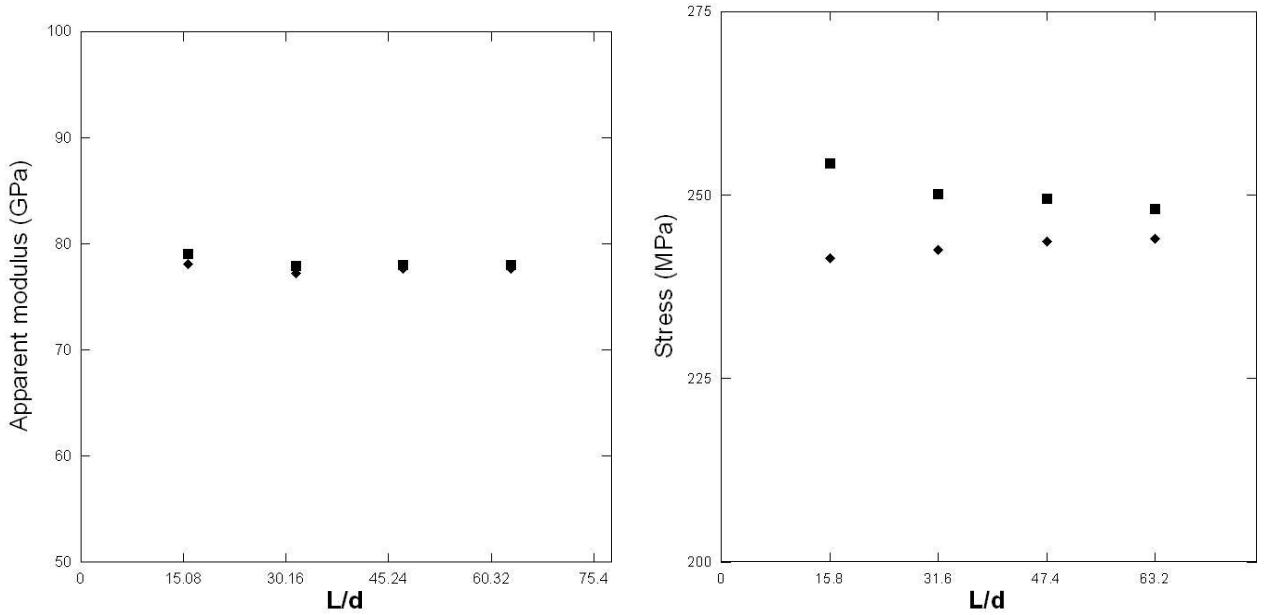


Figure 8. Apparent modulus (left) and overall average stress (right) at 1% far-field strain associated with the two mixed boundary conditions as a function of the ratio of the window size to pore diameter.

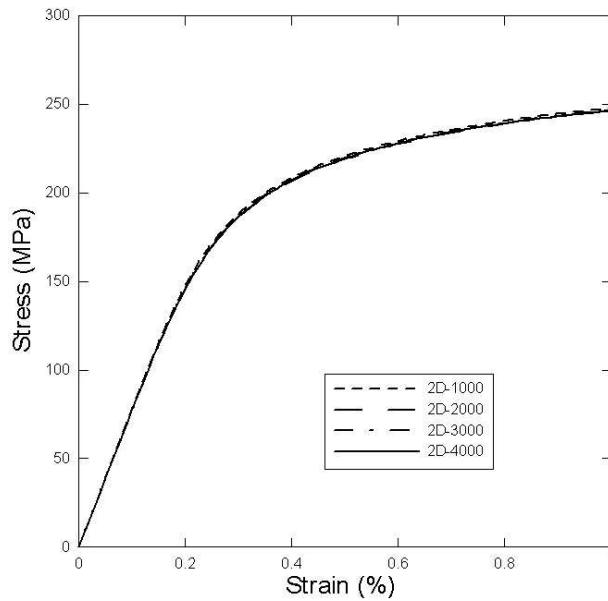


Figure 9. Macroscopic stress-strain responses averaged over the thirty-two individual simulations of 2D-1000, 2D-2000, 2D-3000, and 2D-4000 models.

from 2.29% to 0.48% for elastic modulus and 4.23% to 1.7% for overall stress. As the scatter of the data decreases, the overall averages (BC1.2avgs) of each model group under the two BCs remain almost constant. For example, only 0.71% difference exists between the averages of the overall stresses of the 2D-1000 and 2D-4000 models.

Based on the observations above, we believe that the averages over the individual simulations under the two BCs should be close to an “exact” solution. We derive this hypothesis from the homogenization convergence assumption: estimates under different BCs converge to the effective response as the calculated domain approaches Hill’s RVE for locally heterogeneous but globally homogeneous microstructures [Hazanov and Huet 1994; Hollister and Kikuchi 1992; Huet 1990; Jiang et al. 2001a; Ostoja-Starzewski 1998; Pecullan et al. 1999; Sab 1992; Terada et al. 2000]. Therefore, we conclude that a number of small models can obtain convergent results equivalent to larger models. At the same time, since the averaged stress-strain curves associated with BC1 and BC2 approach the “exact” solution which lies in between, the error of the predicted result of each BC to the effective one can be estimated. For example, since 1.7% difference exists between the average stresses at 1% strain for the 2D-4000 models under the two BCs as shown in Figure 8, the error of the result from each BC to the “exact” solution should be less than 1.7%, and the error of the average of BC1 and BC2 (BC1.2avg in Table 2) less than 0.85%. This method suggests that by selecting a certain number of models associated with two selected slightly underrestrictive and overrestrictive boundary conditions providing opposite bias of the result, both the convergent result and the degree of accuracy can be estimated.

The fast homogenization achieved here occurs because all the models selected are of fixed porosity and are subjected to the two mixed BCs. These conditions are different from the findings in [Kanit et al. 2003]. In their work on the determination of the RVE size, small models have large variance of volume fractions, a fact which leads to large variance in results. They also showed that bias exists for the average of predictions of a number of small domains associated with one periodic BC, and that the bias decreases to zero as the size of analyzed domains reaches a certain level. With this one-sided approach, variance can be eliminated only by increasing domain size.

The study can also be generalized to 3D FE analysis. The uniaxial stress-strain responses predicted by the twelve individual 3D simulations (four models deformed along the three perpendicular directions) of the 3D-170 and 3D-340 models under the two mixed BCs are shown in Figure 10. Similar to the 2D simulations, the scatter of the curves decreases as the size of the 3D models increases. The average stress-strain curves over the individual simulations associated with BC1 and BC2 for 3D-340 models are closer than 3D-170 models as shown in Figure 11. The overall averages of the stress-strain responses for each model group of both the BCs (BC1.2avg) are plotted in Figure 12 and the two curves almost superpose. The results for elastic modulus and overall average stress at 1% uniaxial strain for the 3D models are shown in Table 3. For all twenty-four responses for the two BCs, the standard deviation for modulus decreases from 3.05% for 3D-170 models to 0.97% for 3D-340 models, and from 5.95% to 2.47% for overall average stress. The two mixed BCs offer biased predictions as in the 2D models. Therefore, the discussion and conclusions based on the 2D FE analyses above hold true for the 3D FE study. We presented a detailed comparison between 2D and 3D FE simulations in [Shen and Brinson 2007], and found that the macroscopic responses predicted by the 3D models are in reasonable agreement with the experimental and theoretical results. The macroscopic plastic responses predicted by 2D models are lower than those predicted by 3D models, while the elastic responses are close. 2D models overpredict

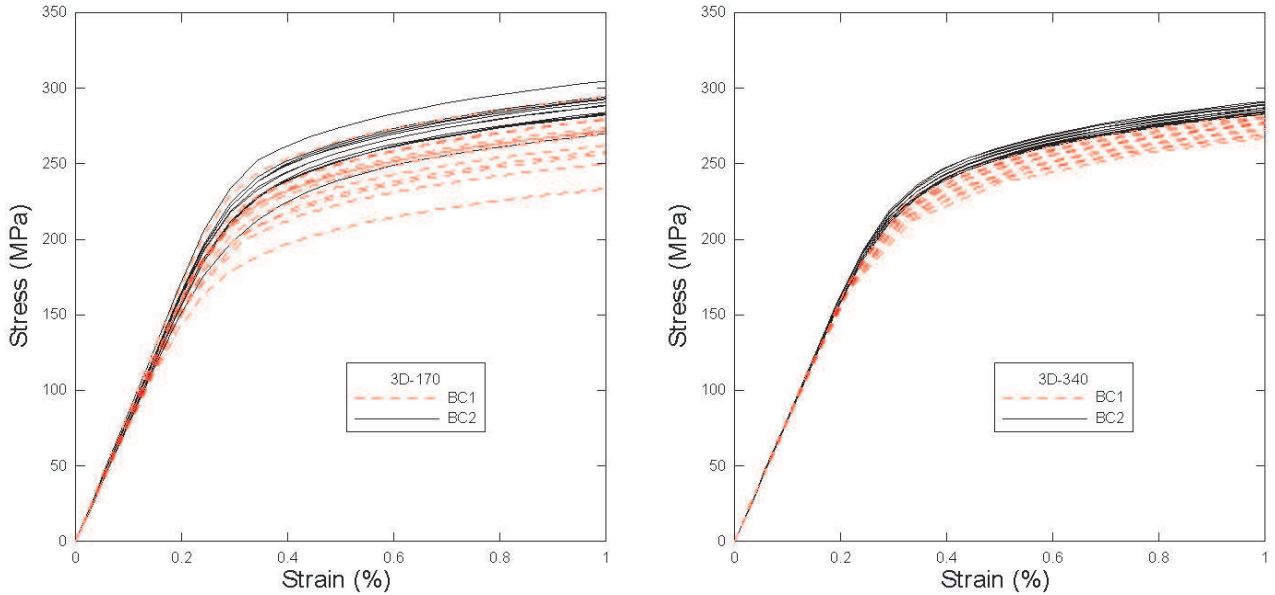


Figure 10. Macroscopic stress-strain responses predicted by the twelve individual simulations of 3D-170 (left) and 3D-340 (right) models associated with the two mixed boundary conditions.

the probability of high Von Mises stress and equivalent plastic strain and therefore overestimate the failure probability for porous materials.

It should be noted that the current BCs for the model groups are only appropriate for the simulation of titanium foam at low porosities (less than 25%) under uniaxial loading conditions. However, this study elucidates a method to find relatively small RVEs for heterogeneous materials, especially for the difficult case of high contrast properties between the phases. As the material is foamed to high porosity, pores are connected to form larger pores complicating the microstructure as shown in [Figure 5](#). The uniaxial stress-strain responses predicted by the 3D model with higher porosity of 48% (the 3D model deformed

		E (GPa)		σ (MPa)	
		AVG.	SD%	AVG.	SD%
3D-170	BC1	80.36	3.26	266.73	5.93
	BC2	81.93	2.62	287.91	2.97
	BC12avg	81.15	3.05	277.32	5.95
3D-340	BC1	80.61	0.91	275.63	1.89
	BC2	81.42	0.78	286.66	0.96
	BC12avg	81.01	0.97	281.14	2.47

Table 3. 3D model predictions for elastic modulus and overall stress in loading direction at 1% uniaxial strain.

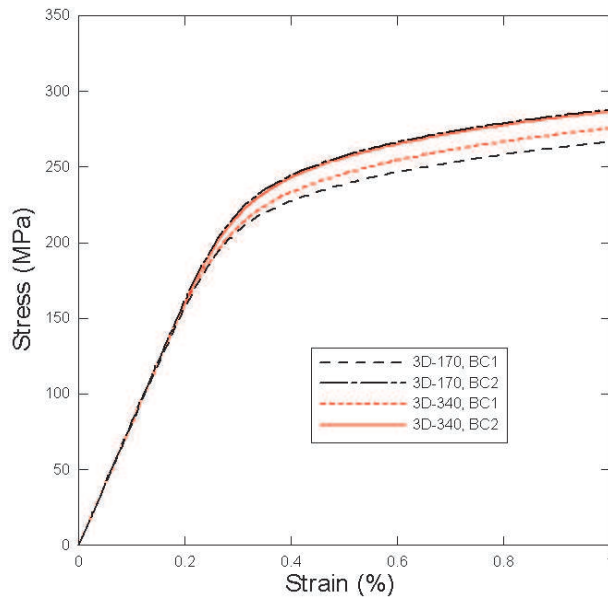


Figure 11. Macroscopic stress-strain responses averaged over the twelve individual simulations of 3D-170 and 3D-340 models associated with the two mixed boundary conditions.

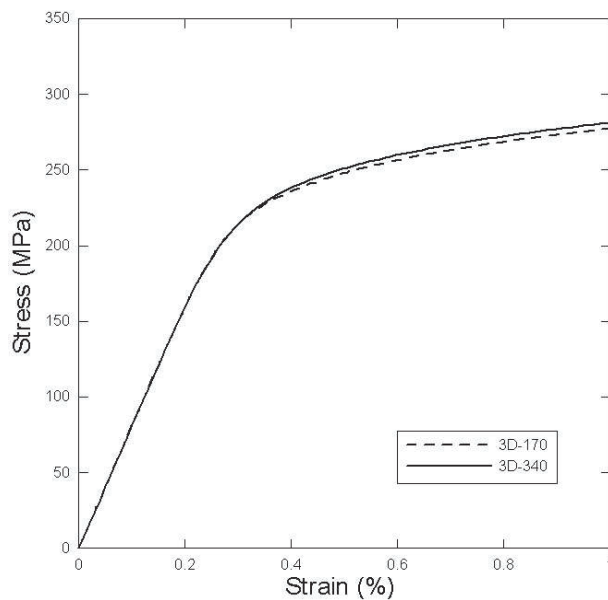


Figure 12. Macroscopic stress-strain responses averaged over the twenty-four individual simulations of 3D-170 and 3D-340 models.

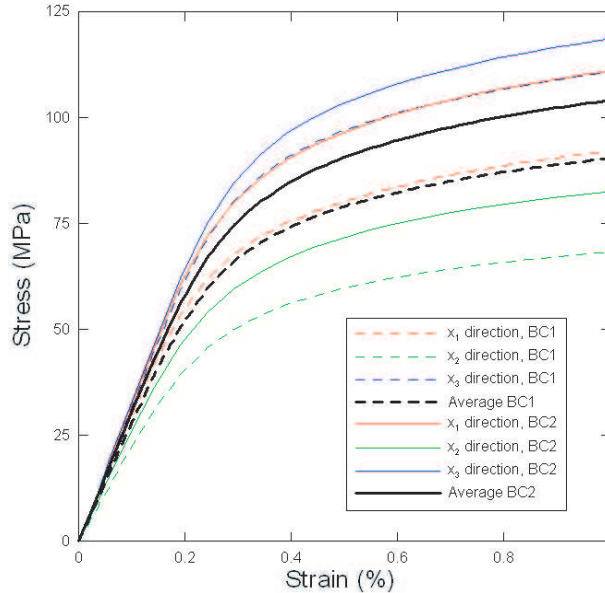


Figure 13. Macroscopic stress-strain responses predicted by the 3D model of 48% porosity associated with the two mixed boundary conditions.

along x_1, x_2 and x_3 directions) under the two mixed BCs are shown in Figure 13. The results indicate a much larger scatter than the 3D-340 models which have the same model size but lower porosity. The convergent response prediction for titanium foam at high porosity is therefore quite challenging and will be the focus of our future work. We can expect that more analyzed domains are needed to obtain a convergent result while using the boundary conditions which provide biased error.

3.2. Microscopic response. Microscopic field variable distributions are very important for failure analysis because failure is a local event rather than a volume averaged event. The Von Mises stress distributions in the matrices of all the 2D models deformed along x_1 and x_2 directions under 1% macroscopic strain are plotted in Figure 14. Since BC1 is less restrictive than BC2, the distributions of Von Mises stress under BC1 are broader than those under BC2. As with macroscopic responses, as model size increases, the curves become less dispersed. Both the mean value and standard deviation of the Von Mises stress distribution converge with increasing model size. For example, the maximum difference of the mean values of Von Mises stress under BC2 is 8.5% for 2D-1000 models and 4.2% for 2D-4000 models. The average distribution curves of the sixteen individual simulations of 2D-1000, 2D-2000, 2D-3000, and 2D-4000 models associated with the two mixed BCs converge to a common mean value and a common standard deviation as shown in Figure 15. The difference between the averaged mean values under BC1 and BC2 for 2D-1000 models is 5.9% and for 2D-4000 models is 1.8%. This common mean value and common standard deviation of the Von Mises stress distribution is clearly seen in Figure 16, in which the overall averages of the total thirty-two distribution curves for all the 2D models are plotted. Although not shown here, the equivalent plastic strain distribution follows a similar convergence trend.

To see the influence of the BCs on the microscopic distributions for models with different sizes, the equivalent plastic strain distributions predicted by one of the 2D-1000 and 2D-4000 models under 1% far

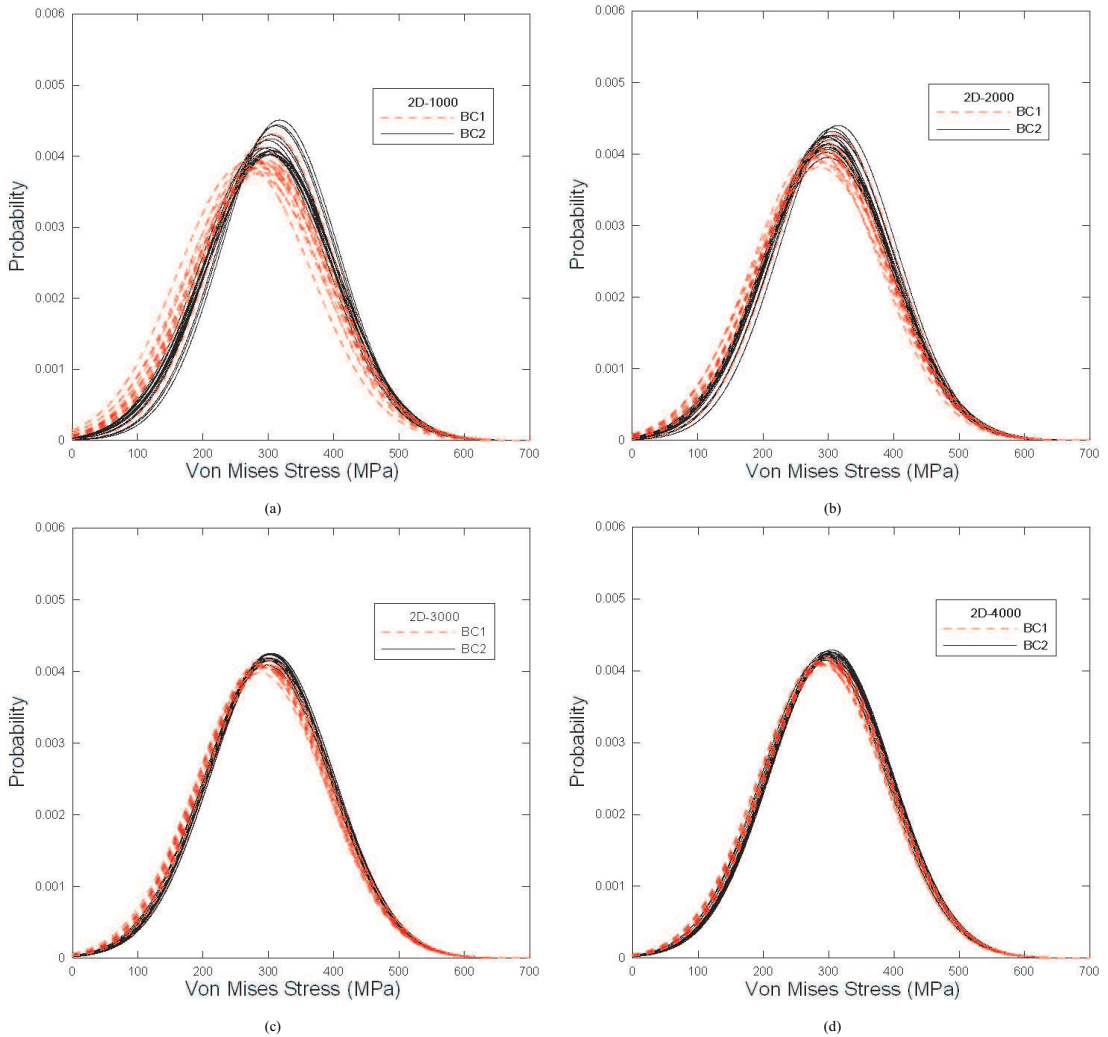


Figure 14. Von Mises stress distributions predicted by the sixteen individual simulations of (a) 2D-1000, (b) 2D-2000, (c) 2D-3000, and (d) 2D-4000 models associated with the two mixed boundary conditions.

field strain were plotted in [Figure 17](#). In the 2D-1000 model, plastic strain distributions are influenced by BCs such that differences exist even in the middle of the analyzed domain. In the 2D-4000 models, differences in the plastic strain distributions away from the boundaries become negligible. However, the deficiency of the individual small 2D models can be compensated by averaging results of more models associated with the two BCs.

The accumulated frequencies of the Von Mises stress of the 2D models are plotted in [Figure 18](#). These values were obtained by calculating the percentage of all the matrix elements exceeding a certain value in each model group. As is evident in [Figure 18](#), the results of the Von Mises stress distribution of the 2D models under BC1 and BC2 also converge in the same manner as the macroscopic stress-strain responses.

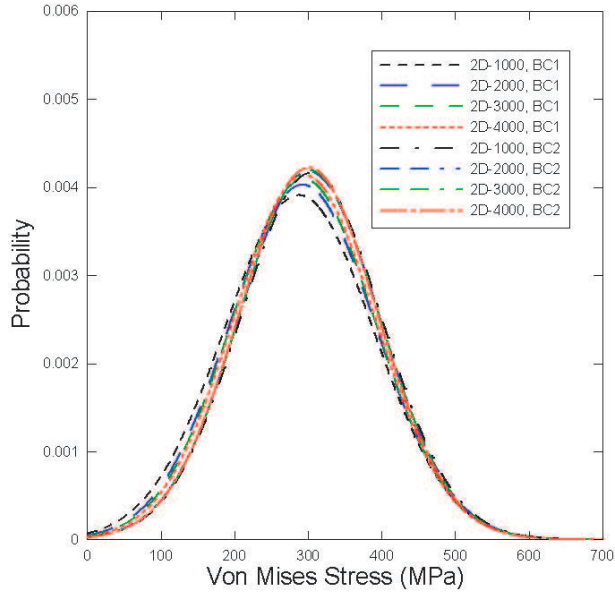


Figure 15. Von Mises stress distributions averaged over the sixteen individual simulations of 2D-1000, 2D-2000, 2D-3000, and 2D-4000 models associated with the two mixed boundary conditions.

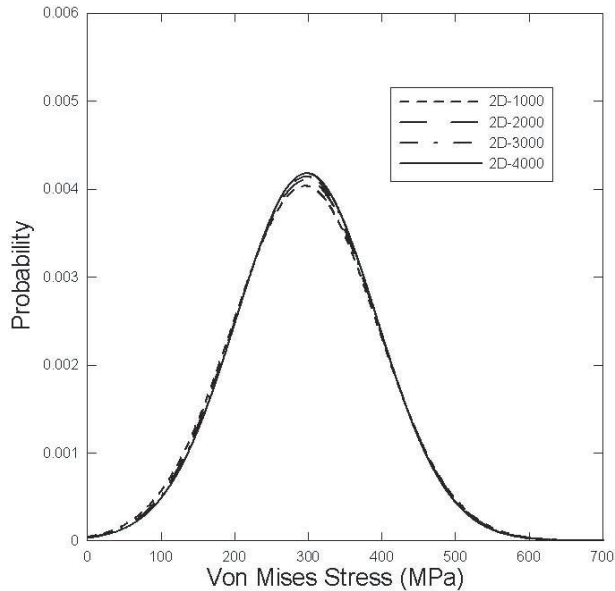


Figure 16. Von Mises stress distributions averaged over the thirty-two individual simulations of 2D-1000, 2D-2000, 2D-3000, and 2D-4000 models.

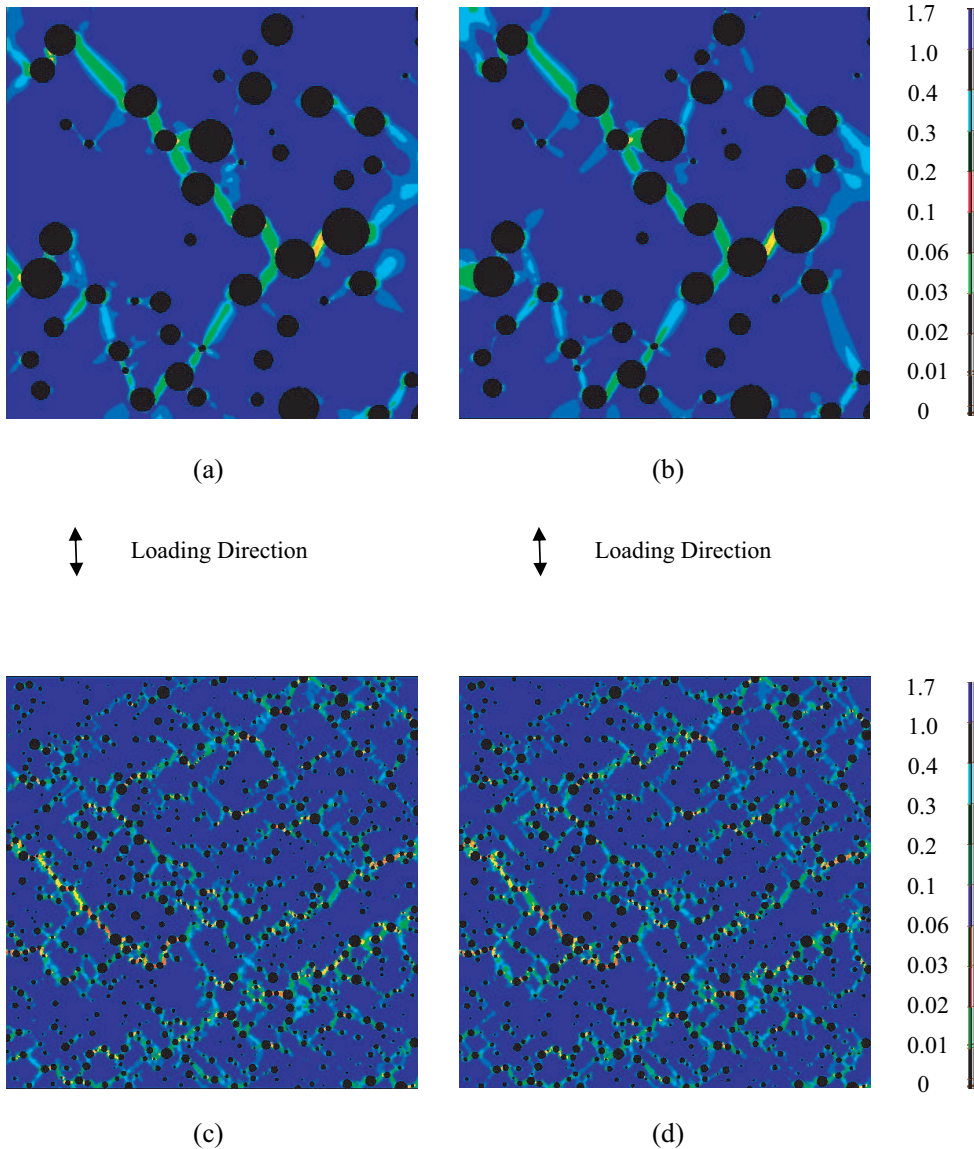


Figure 17. Equivalent plastic strain distribution predicted by (a) one of 2D-1000 model under BC1, (b) the 2D-1000 model under BC2, (c) one of 2D-4000 model under BC1, and (d) the 2D-4000 model under BC2.

With this frequency averaged over all the 2D simulations under the two BCs, a relatively accurate result can be obtained by the 2D-1000 model, one which is very close to the prediction of 2D-4000 models as shown in Figure 19. Therefore the convergence discussion on the macroscopic responses should be still valid for the microscopic variable statistic distributions.

To generalize the microscopic study to 3D FE analysis, the corresponding results of Von Mises stress predicted by the twelve individual 3D simulations (four models deformed along the three perpendicular

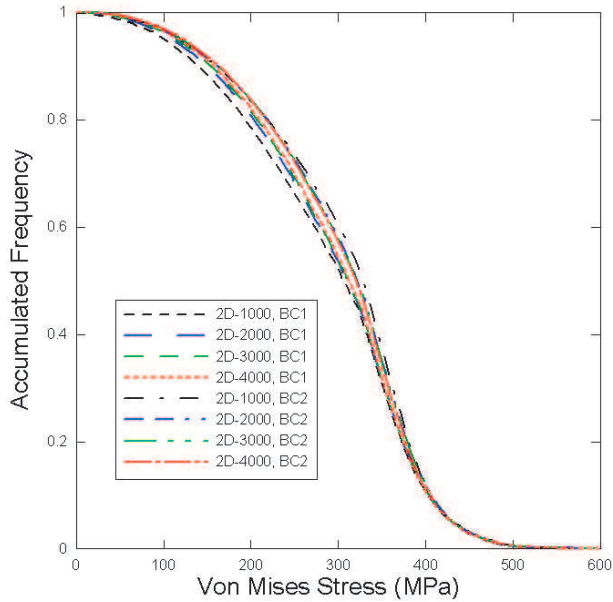


Figure 18. Accumulative frequency of Von Mises stress exceeding a certain value predicted by 2D-1000, 2D-2000, 2D-3000, and 2D-4000 models associated with the two mixed boundary conditions.

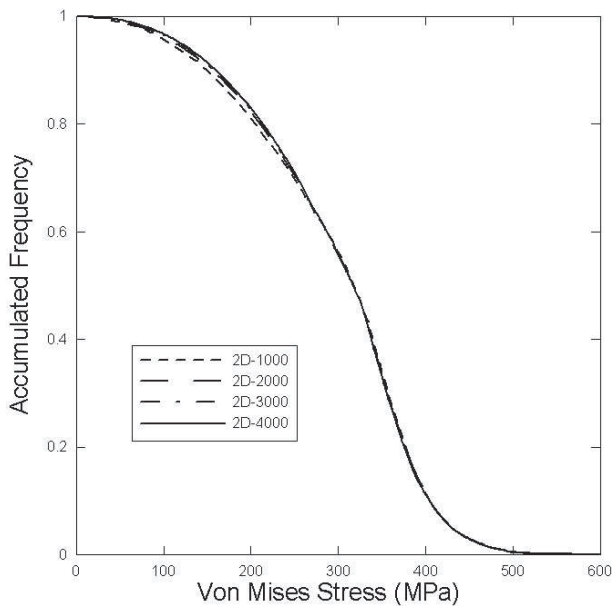


Figure 19. Accumulative frequency of Von Mises stress exceeding a certain value, averaged over the two mixed boundary conditions predicted by 2D-1000, 2D-2000, 2D-3000, and 2D-4000 models.

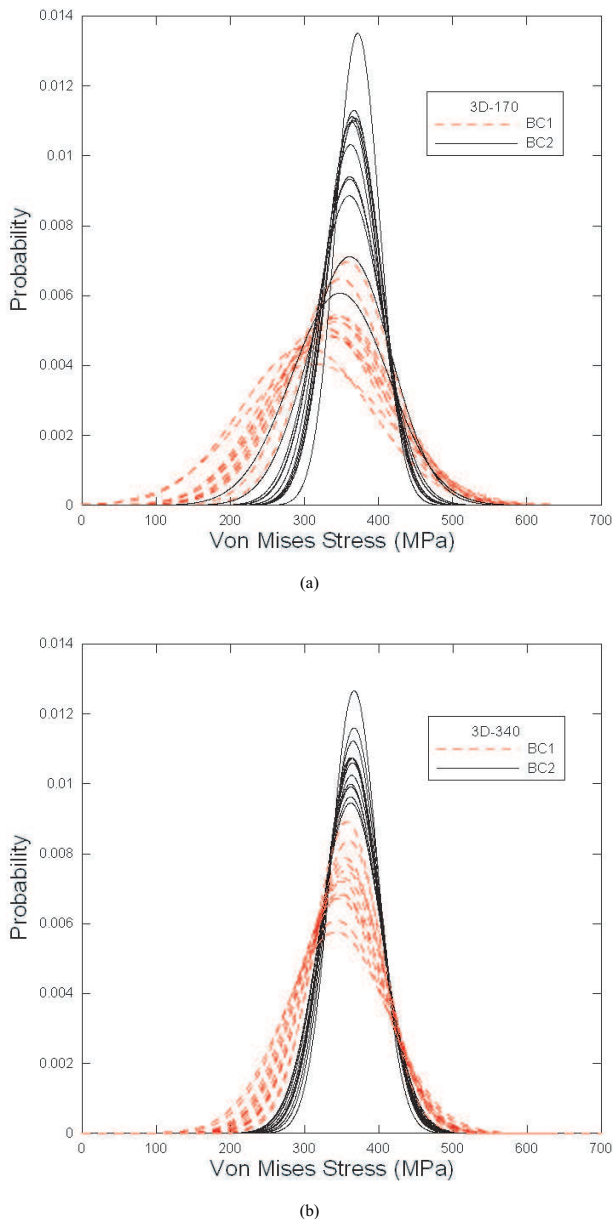


Figure 20. Von Mises stress distribution predicted by the twelve individual simulations of (a) 3D-170 and (b) 3D-340 models associated with the two mixed boundary conditions.

directions) of the 3D-170 and 3D-340 models under the two mixed BCs are shown in Figure 20. Similar convergence trend can be observed as the size of the 3D models increases. The average responses over the individual simulations associated with the two BCs are shown in Figure 21. The difference between the mean Von Mises stress at 1% strain under BC 1 and BC 2 for the 3D-170 models is 8.5% and for

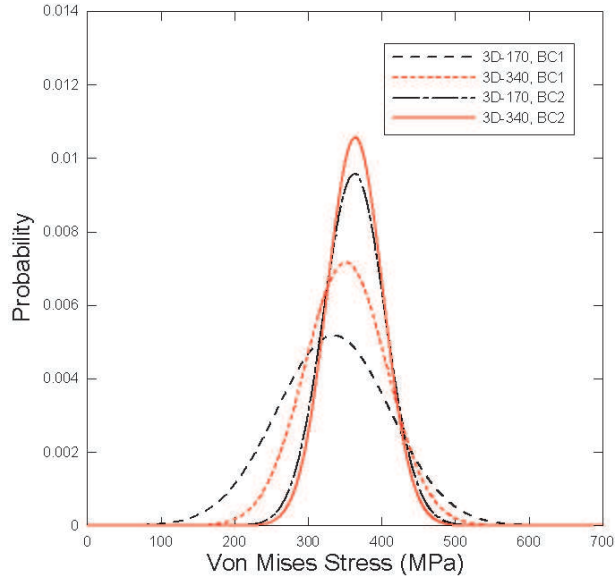


Figure 21. Von Mises stress distributions averaged over the twelve individual simulations of 3D-170 and 3D-340 models associated with the two mixed boundary conditions.

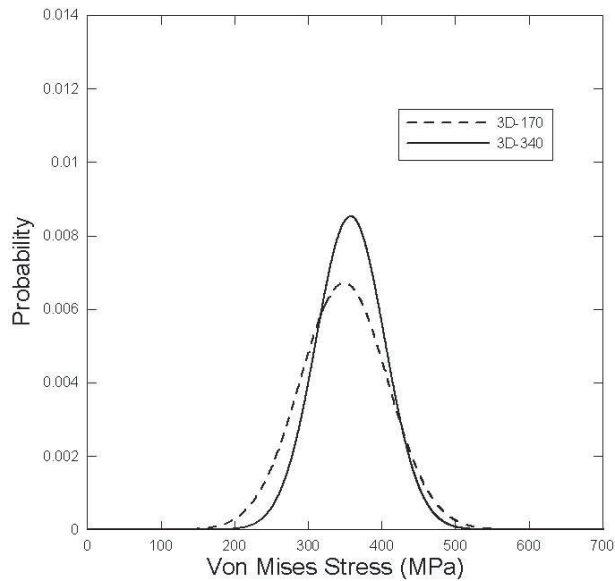


Figure 22. Von Mises stress distributions averaged over the twenty-four individual simulations of 3D-170 and 3D-340 models.

3D-340 models is 3.6%. The overall averages of the total responses for each 3D model group are shown in [Figure 22](#). Although the curves are not as close as 2D models, the convergence trend is similar to the 2D study. The accumulated frequencies of the Von Mises stress of the 3D models are plotted in [Figure](#)

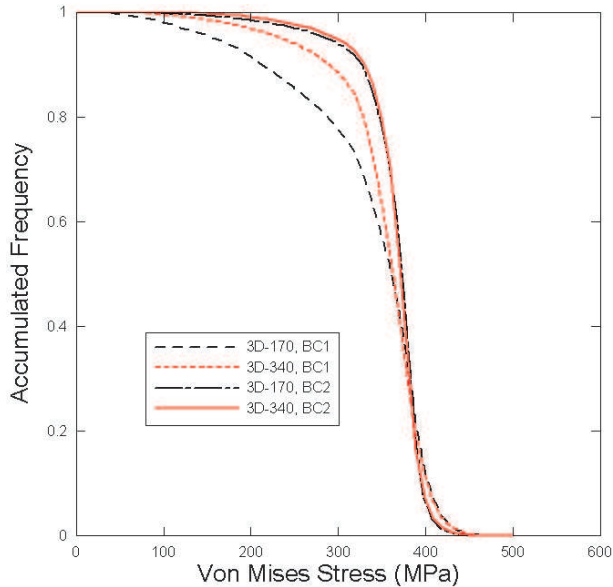


Figure 23. Accumulative frequency of Von Mises stress exceeding a certain value predicted by 3D-170 and 3D-340 models associated with the two mixed boundary conditions.

23. The frequency averaged over all the 3D simulations under the two BCs is shown in Figure 24. A similar convergence trend can also be observed. We expect that as the 3D models increase to $640 \mu\text{m}$, the individual stress and strain curves would become more convergent. However, due to computational limitations, it is not practical to analyze the model with a $640 \mu\text{m}$ side length. Since the two BCs are bounds for the properties, the “exact” effective response should lie in between. In other words, since the difference between the mean Von Mises stress at 1% strain for the 3D-340 models under BC1 and BC2 is 3.6%, the average should be within 1.8% of the exact solution.

We find that for microscopic response, the 3D models predict higher mean Von Mises stress than 2D models, but relatively uniform distributions with smaller standard deviation. For example, the distribution of the Von Mises stress is $357.7 \pm 46.7 \text{ MPa}$ for 3D-340 models and $298 \pm 95.5 \text{ MPa}$ for 2D-4000 models. Our companion work [Shen and Brinson 2007] gives an extensive comparison between the stress and strain distribution.

4. Conclusions

In this study, we present an approach to determine RVEs of porous titanium. The method adopts the RVE concept of [Kanit et al. 2003] according to which the RVEs can be small domains as long as the average of the small domains provides an unbiased result. Since the estimates associated with uniform traction and displacement BCs provide the lower and higher bounds for the effective properties providing the largest bias, two mixed boundary conditions are therefore designed to obtain results with a smaller bias. Four groups of 2D models and two groups of 3D models with various sizes and fixed porosity were constructed based on a simulated microstructure of an experimental material. As the length scale

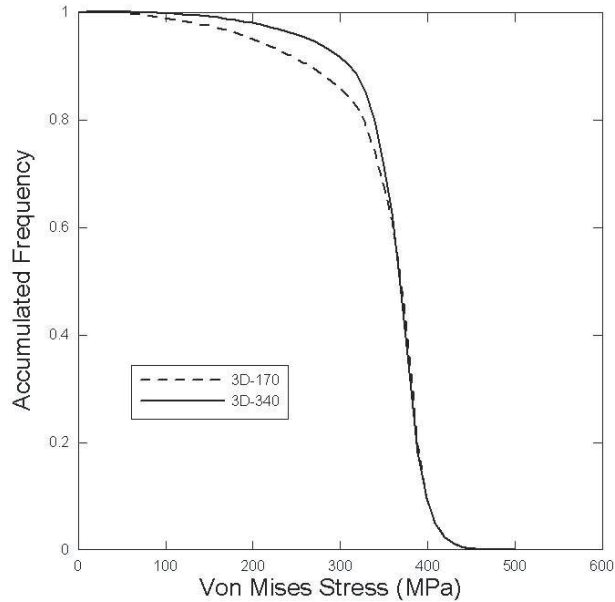


Figure 24. Accumulative frequency of Von Mises stress exceeding a certain value, averaged over the two mixed boundary conditions predicted by 3D-170 and 3D-340 models.

of the model increases, the individual responses of models become less dispersed. At the same time, the averages of the estimates associated with the two mixed BCs show opposite bias and converge to a common value. The error can be estimated and a convergent result can be obtained from relatively small models by averaging the responses associated with the two mixed BCs. The method developed here can be used to simulate microstructures of real materials. Although we have studied only a special case for titanium foam at low porosity under uniaxial loading, this method elucidates an approach for studying other heterogeneous materials, including those with a higher volume fraction of pores to inclusions. By choosing appropriate boundary conditions, a convergent result can be achieved by averaging the results of a number of small analyzed domains. The number of the domains needed will depend on the nature of the microstructure, the designed boundary, and the domain size.

References

- [ABAQUS 2004] *ABAQUS standard user's manual*, version 6.4, Hibbitt Karlsson Sorensen Inc., Pawtucket, RI, 2004.
- [ASM 2002] *Atlas of stress-strain curves*, 2nd ed., ASM International, Materials Park, OH, 2002.
- [Banhart 2001] J. Banhart, "Manufacture, characterisation and application of cellular metals and metal foams", *Prog. Mater. Sci.* **46**:6 (2001), 559–632.
- [Bouyge et al. 2002] F. Bouyge, I. Jasiuk, S. Boccara, and M. Ostoja-Starzewski, "A micromechanically based couple-stress model of an elastic orthotropic two-phase composite", *Eur. J. Mech. A: Solids* **21**:3 (2002), 465–481.

- [Chang et al. 1996] Y. S. Chang, M. Oka, M. Kobayashi, H. O. Gu, Z. L. Li, T. Nakamura, and Y. Ikada, “Significance of interstitial bone ingrowth under load-bearing conditions: a comparison between solid and porous implant materials”, *Biomaterials* **17**:11 (1996), 1141–1148.
- [Davis et al. 2001] N. G. Davis, J. Teisen, C. Schuh, and D. C. Dunand, “Solid-state foaming of titanium by superplastic expansion of argon-filled pores”, *J. Mater. Res.* **16**:5 (2001), 1508–1519.
- [Drugan and Willis 1996] W. J. Drugan and J. R. Willis, “A micromechanics-based nonlocal constitutive equation and estimates of representative volume element size for elastic composites”, *J. Mech. Phys. Solids* **44**:4 (1996), 497–524.
- [Dunand 2004] D. C. Dunand, “Processing of titanium foams”, *Adv. Eng. Mater.* **6**:6 (2004), 369–376.
- [Gibson and Ashby 1997] L. Gibson and M. Ashby, *Cellular solids: Structure and properties*, 2nd ed., Cambridge University Press, New York, 1997.
- [Gusev 1997] A. A. Gusev, “Representative volume element size for elastic composites: A numerical study”, *J. Mech. Phys. Solids* **45**:9 (1997), 1449–1459.
- [Hazanov 1999] S. Hazanov, “On apparent properties of nonlinear heterogeneous bodies smaller than the representative volume”, *Acta Mech.* **134**:3–4 (1999), 123–134.
- [Hazanov and Huet 1994] S. Hazanov and C. Huet, “Order relationships for boundary conditions effect in heterogeneous bodies smaller than the representative volume”, *J. Mech. Phys. Solids* **42**:12 (1994), 1995–2011.
- [Hill 1963] R. Hill, “Elastic properties of reinforced solids: Some theoretical principles”, *J. Mech. Phys. Solids* **11**:5 (1963), 357–372.
- [Hollister and Kikuchi 1992] S. J. Hollister and N. Kikuchi, “A comparison of homogenization and standard mechanics analyses for periodic porous composites”, *Comput. Mech.* **10**:2 (1992), 73–95.
- [Huet 1990] C. Huet, “Application of variational concepts to size effects in elastic heterogeneous bodies”, *J. Mech. Phys. Solids* **38**:6 (1990), 813–841.
- [Jiang et al. 2001a] M. Jiang, K. Alzebdeh, I. Jasiuk, and M. Ostoja-Starzewski, “Scale and boundary conditions effects in elastic properties of random composites”, *Acta Mech.* **148** (2001), 63–78.
- [Jiang et al. 2001b] M. Jiang, M. Ostoja-Starzewski, and I. Jasiuk, “Scale-dependent bounds on effective elastoplastic response of random composites”, *J. Mech. Phys. Solids* **49**:3 (2001), 655–673.
- [Kanit et al. 2003] T. Kanit, S. Forest, I. Galliet, V. Mounoury, and D. Jeulin, “Determination of the size of the representative volume element for random composites: statistical and numerical approach”, *Int. J. Solids Struct.* **40**:13–14 (2003), 3647–3679.
- [Li et al. 1998] M. Li, S. Ghosh, T. N. Rouns, H. Weiland, O. Richmond, and W. Hunt, “Serial sectioning method in the construction of 3-D microstructures for particle-reinforced MMCs”, *Mater. Charact.* **41**:2–3 (1998), 81–95.
- [Li et al. 2004] H. Li, S. M. Oppenheimer, S. I. Stupp, D. C. Dunand, and L. C. Brinson, “Effects of pore morphology and bone ingrowth on mechanical properties of microporous titanium as an orthopaedic implant material”, *Mater. Trans.* **45**:4 (2004), 1124–1131.
- [Murray and Dunand 2003] N. G. D. Murray and D. C. Dunand, “Microstructure evolution during solid-state foaming of titanium”, *Compos. Sci. Technol.* **63**:16 (2003), 2311–2316.
- [Ostoj-Starzewski 1998] M. Ostoj-Starzewski, “Random field models of heterogeneous materials”, *Int. J. Solids Struct.* **35**:19 (1998), 2429–2455.
- [Pecullan et al. 1999] S. Pecullan, L. V. Gibiansky, and S. Torquato, “Scale effects on the elastic behavior of periodic and hierarchical two-dimensional composites”, *J. Mech. Phys. Solids* **47**:7 (1999), 1509–1542.
- [Sab 1992] K. Sab, “On the homogenization and the simulation of random materials”, *Eur. J. Mech. A: Solids* **11**:5 (1992), 585–607.
- [Shen and Brinson 2007] H. Shen and L. C. Brinson, “Finite element modeling of titanium foam”, *Int. J. Solids Struct.* **44**:1 (2007), 320–335.
- [Shen et al. 2006] H. Shen, S. M. Oppenheimer, D. C. Dunand, and L. C. Brinson, “Numerical modeling of pore size and distribution in foamed titanium”, *Mech. Mater.* **38**:8–10 (2006), 933–944.

- [Spoerke et al. 2005] E. D. Spoerke, N. G. Murray, H. Li, L. C. Brinson, D. C. Dunand, and S. I. Stupp, “A bioactive titanium foam scaffold for bone repair”, *Acta Biomater.* **1**:5 (2005), 523–533.
- [Terada et al. 2000] K. Terada, M. Horib, T. Kyoyac, and N. Kikuchi, “Simulation of the multi-scale convergence in computational homogenization approaches”, *Int. J. Solids Struct.* **37**:16 (2000), 2285–2311.
- [Tobias and Trindade 1995] P. A. Tobias and D. C. Trindade, *Applied reliability*, Van Nostrand Reinhold, New York, 1995.
- [Wen et al. 2002a] C. E. Wen, Y. Yamada, K. Shimojima, Y. Chino, T. Asahina, and M. Mabuchi, “Processing and mechanical properties of autogenous titanium implant materials”, *J. Mater. Sci.: Mater. Med.* **13**:4 (2002), 397–401.
- [Wen et al. 2002b] C. E. Wen, Y. Yamada, K. Shimojima, Y. Chino, T. Hosokawa, and M. Mabuchi, “Novel titanium foam for bone tissue engineering”, *J. Mater. Res.* **17**:10 (2002), 2633–2639.

Received 11 Jan 2006. Accepted 12 May 2006.

HUI SHEN: h-shen@onu.edu

Mechanical Engineering Department, Ohio Northern University, Ada, OH 45810, United States

<http://www2.onu.edu/%7Ehshen/>

L. CATHERINE BRINSON: cbrinson@northwestern.edu

Mechanical Engineering Department, Northwestern University, Technological Institute B224, 2145 Sheridan Road, Evanston, IL 60208, United States

<http://www.mech.northwestern.edu/web/people/faculty/brinson.htm>

DAMAGE IN DOMAINS AND INTERFACES: A COUPLED PREDICTIVE THEORY

FRANCESCO FREDDI AND MICHEL FRÉMOND

In this study, we propose a model coupling damage of domains and damage of interfaces. A predictive theory of continuum damage mechanics is developed within the framework of the principle of virtual power. Because damage results from microscopic motions, the power of these microscopic motions is included in the power of the internal forces. The power of the internal forces we choose depends on the damage velocity and on its gradient to take into account local interactions. An interaction between the domain damage and the damage along the interface is introduced. To overcome the insensitivity of the local interface model to elongation, nonlocal elongation has been considered as a source of damage. Representative numerical examples confirm that our proposed model can be used to describe various damage phenomena in agreement with experiments.

1. Introduction

Mechanical degradation of quasibrittle materials is usually traced back to development of micro-cracking and microvoids. Continuum damage mechanics based upon general principles which govern the evolution of the variables representative of the material state is an effective tool for analysis of these behaviors, [Lemaitre 1992; Stumpf and Hackl 2003; Mosconi 2006]. In particular, isotropic damage formulations are extensively employed in the literature because of their simplicity, efficiency and adequacy for many practical applications [Voyaiadjis et al. 1998; Lemaitre and Desmorat 2005]. Damage theory has been used successfully to describe adhesion of solids [Borino and Failla 2005; Alfano and Crisfield 2001; Zou et al. 2003]. In fact, the interface regions between materials fundamentally governs the strength and stability of structural elements [Truong Dinh Tien 1990]. Moreover, structural collapse in composite structures is often caused by the appearance and evolution of different damage phenomena in a narrow region near the interface [Yao et al. 2005; Aimi et al. 2007; Freddi and Savoia 2006; Gonzalez et al. 2005].

The practical problem is to determine whether the design of a future structure forbids any failure by surface or volume damage under service loads. Predictive theories must account for these physical results, including short-term behaviour.

The present work deals with the structural response of quasibrittle domains, for instance pieces of concrete glued on one another. We take into account both volume and interface damaging behaviors and their interactions. As a starting point, we used two damage models proposed in [Frémond and Nedjar 1996; Frémond 2001] for the description of domain and interface behaviour. These models are based on adaptation of the principle of virtual power. In particular, we assume that damage results from microscopic motions, and include the power of these motions in the principle of virtual power. This power contribution is assumed to depend on the strain rate (displacement discontinuity for the interface), the

Keywords: principle of virtual power, domain damage, interface damage, elongation, damage of glued concrete structures.

rate of damage and the damage gradient (damage discontinuity for the interface). The damage gradient is introduced to account for the local interaction of the damage at a material point on the damage of its neighborhood. Correspondingly, we also introduce two new quantities: the internal work of damage and the flux vector of internal work of damage (adhesion energy and energy flux vector of the contact surface).

On the contact surface there are local damage interactions between damage at a point and damage in its neighborhood. Thus there is interaction within the glue as well as interaction between the glue and the two concrete pieces. These interactions are defined such that their virtual power involves appropriate kinematic quantities. For instance, experiments show that elongation may have damaging effects. In this setting, an elongation is a variation of the distance between two distinct points belonging to the contact surface. This is a nonlocal quantity which introduces nonlocal contributions in the theory.

The principle of virtual power leads to three sets of equations of motion; the first is the classical equation of motion and the other two are nonstandard fields representative of the domains and evolution of interface damage.

The constitutive laws we adopt permit us to control the energy dissipated during degradation and separation of solids so as to avoid stiffness recovery and cohesive state restoration. Suitable free energies let us express nonstandard internal forces conjugated to the damage rate and the gradient damage rate. We then introduce pseudo-potentials of dissipation to characterize the damage evolution. The internal constraints on the values of damage quantities and on their velocities are taken into account explicitly in the expressions of the free energy and of the pseudo-potential.

The domain model derived from this formulation is not affected by mesh sensitivity. In fact, the damage model for the domains overcomes the well-known problem of mesh dependence: a boundary value problem that governs the evolution of the damage variable instead of the usual local constitutive law. Moreover, impenetrability between domains is included in the constitutive laws, thus avoiding the introduction of interface parameters for penalty stiffness, parameters which can create numerical problems, such as spurious traction oscillations [Alfano and Crisfield 2001]. Numerical simulations are proposed which correctly determine whether the zone affected by damage is the interface or a narrow region inside the domains. Specific cases of two concrete elements glued together are considered and a FRP-concrete delamination test is performed. In some cases, we compare the experimental results quantitatively and qualitatively to computations.

Several studies have considered the two models separately. For the domain model the behaviour of concrete structures is correctly predicted in [Frémond and Nedjar 1996] and [Frémond 2001]. Recently, an extension to elastoplastic-damage model was proposed in [Nedjar 2001] and numerical aspects were investigated in [Nedjar 2002] and [Ireman 2005].

Moreover, some mathematical results are reported in [Frémond et al. 1998]. Dynamic processes of adhesive contact with a deformable foundation are considered in [Truong Dinh Tien 1990; Chau et al. 2004], where the rate of bonding field is assumed to be reversible and irreversible. [Bonetti et al. 2005] obtained the global existence and uniqueness results for two solids glued together and results for local existence for a damage model in elastic materials were reported in [Bonetti and Schimperna 2004; Bonetti et al. 2006]. In addition, a model coupling adhesion, friction and unilateral contact is considered in [Raous et al. 1999] and [Raous and Monerie 2002].

2. Physical capacities, potentialities and limits of the model

Gluing of structural elements, an attractive assembly method in civil engineering, must always be evaluated with respect to both short- and long-term behavior. In the short term, we must answer the question: Is the structure designed so that the glued connections and the mechanical elements are strong enough to support the service loads? Over the long term the question becomes: is the operating structure still solid, or must it be strengthened?

The predictive theory we present answers the first question by determining the service load. Once the service load is known, it is possible to predict if the design is such that the future structure will be free of volume or surface damage which would lead to immediate collapse. The examples of [Section 7](#) clearly show that the computer program resulting from our model is efficient and versatile enough to deal with very different structures made of glued parts. Beyond the damage of glued connections, the theory also predicts coupling with the volume damage which can also endanger structures.

The theory is sparing of parameters (three for each material): a cohesion parameter, an extension parameter and a viscosity parameter. We think this is the minimum number of parameters to correctly describe damaging phenomena and answer questions about the damage, such as:

- (a) Does damage appear (cohesion parameter)?
- (b) Does the damage extend or remain concentrated in thin zones (extension parameter)?
- (c) Does the damage evolve slowly or rapidly (viscosity parameter)?

For the glue, we have used the three parameters above and three more extension parameters to describe nonlocal interactions within the glue and the interaction of the glue with its neighboring materials

For short-term behavior, we have established the capabilities of the predictive theory. Its limitations are mainly mechanical and are due to the elastic-damaging constitutive law. Let us also note that for the surface, the constitutive laws which involve nonlocal actions are much richer than needed for some practical applications.

For long-term behavior, aging theory must be added together with rules to determine the related parameters. The predictive theory seems a good starting point, and some results are already available [[Bruneaux 2004](#)].

3. State quantities and quantities describing the evolution

In this section we introduce the state quantities E , and the quantities δE describing the evolution or development of damage. Let us consider a system made of two domains Ω_i , $i = 1, 2$, in the undistorted natural reference configuration subjected to mixed boundary conditions and connected by an adhesive interface $\Gamma_s = \partial\Omega_1 \cap \partial\Omega_2$. An example is a system of two pieces of concrete glued on one another.

For the sake of simplicity, we neglect the thermal effects, do not take the temperature into account, and limit our analysis to small perturbation theory. Note that the equations of motion reported in [Section 4](#) are valid without this restriction.

For each domain Ω_i , the state quantities are the macroscopic damage quantity $\beta_i(\vec{x}, t)$, its gradient $\text{grad } \beta_i(\vec{x}, t)$ and deformation $\varepsilon_i(\vec{x}, t)$. The values of $\beta_i(\vec{x}, t)$ are between 0 and 1, where 1 represents the undamaged state and 0 the completely damaged one. Damage quantity β_i may be understood as the volume fraction of active links or of undamaged material. The gradient of $\beta_i(\vec{x}, t)$ accounts for local

interactions of the damage at a point on damage of its neighbourhood. Recall that the deformation $\varepsilon_i(\vec{x}, t)$ accounts for the local interaction of the displacement at a point on displacement of its neighborhood.

The quantities which describe the evolution in each domain Ω_i are the velocities of the state quantities. The velocities $d\beta/dt$ account for the microscopic velocities at the macroscopic level.

The state quantities on the contact surface $\partial\Omega_1 \cap \partial\Omega_2$ involve quantities which describe the evolution of the surface, and quantities which describe the macroscopic and microscopic interactions between domains and surface. The quantities which describe the surface evolution, for instance the glue evolution, are the surface or glue damage quantity, and its surface gradient, $\beta_s(\vec{x}, t)$, and $\text{grad}_s \beta_s(\vec{x}, t)$ taking into account the local damage interaction in the surface or in the glue. The macroscopic interactions are described by the gap as is usual in contact mechanics, and also by the elongation, a new nonlocal state quantity which describes the variation of the distance of two different points of the surface. Microscopic interactions are also described by the traces of the domain damage quantities.

The gap $\vec{u}_2(\vec{x}) - \vec{u}_1(\vec{x})$ is the difference between two small displacements \vec{u}_i at the same point \vec{x} of the surface. Note that even if the gap is 0, the displacements which are not equal at two different points of the surface would produce a notable damaging action. To account for this property, we introduce the elongation

$$g(\vec{x}, \vec{y}) = 2(\vec{y} - \vec{x}) \cdot (\vec{u}_2(\vec{y}) - \vec{u}_1(\vec{x})).$$

It describes the evolution of the distance between two different points, \vec{x} and \vec{y} , and it may be different from 0 if the gap is 0.

The quantities describing the evolution of the contact surface are the velocities of the state quantities. The velocity of the elongation is

$$D_{1,2}(\vec{U}_1, \vec{U}_2)(\vec{x}, \vec{y}) = 2(\vec{y} - \vec{x}) \cdot (\vec{U}_2(\vec{y}) - \vec{U}_1(\vec{x})).$$

where $\vec{U}_i = d\vec{u}_i/dt$ are the macroscopic velocities.

Let us note that this velocity is 0 in any rigid system velocity, that is, a set of velocities which do not change the form of the system. It is easy to check that rigid system velocities satisfy

$$\begin{aligned} \vec{U}_1(\vec{x}) &= \vec{A} + \vec{B} \times \vec{x}, \\ \vec{U}_2(\vec{x}) &= \vec{A} + \vec{B} \times \vec{x}, \\ \frac{d\beta_1}{dt} &= \frac{d\beta_2}{dt} = \frac{d\beta_s}{dt} = 0. \end{aligned}$$

These rigid velocities do not change the form of the system because the gap does not change on the contact surface. Moreover, since the damage velocities are 0, the microscopic velocities which are responsible for their evolutions are 0.

Remark 1. The velocity of the elongation is the time derivative of the square of the distance of two points

$$D_{1,2}(\vec{U}_1, \vec{U}_2)(\vec{x}, \vec{y}) = 2(\vec{y} - \vec{x}) \cdot (\vec{U}_2(\vec{y}) - \vec{U}_1(\vec{x})) = \frac{d}{dt}(\vec{y} - \vec{x})^2.$$

We find that within the small deformation assumption, the elongation $g(\vec{y}, \vec{x})$ is the variation of the square of the distance of the two points. The physical properties of the internal force associated with the elongation may be understood with this property.

To sum up, the state quantities E and the quantities describing the evolution are, in Ω_1 and in Ω_2 ,

$$E_1 = \{\varepsilon_1, \beta_1, \text{grad } \beta_1\}, \quad \delta E_1 = \left\{ \frac{d\varepsilon_1}{dt}, \frac{d\beta_1}{dt}, \text{grad } \frac{d\beta_1}{dt} \right\},$$

$$E_2 = \{\varepsilon_2, \beta_2, \text{grad } \beta_2\}, \quad \delta E_2 = \left\{ \frac{d\varepsilon_2}{dt}, \frac{d\beta_2}{dt}, \text{grad } \frac{d\beta_2}{dt} \right\},$$

where $d\varepsilon_i/dt$ are the classical strain rates.

On the contact surface $\partial\Omega_1 \cap \partial\Omega_2$

$$E_s = \{\vec{u}_2 - \vec{u}_1, \beta_s, \text{grad}_s \beta_s, \beta_1 - \beta_s, \beta_2 - \beta_s\},$$

$$E_{s,1,2} = \{g(\vec{x}, \vec{y}) = 2(\vec{y} - \vec{x}) \cdot (\vec{u}_2(\vec{y}) - \vec{u}_1(\vec{x})), \beta_s(\vec{x}), \beta_s(\vec{y})\},$$

$$\delta E_s = \left\{ \vec{U}_2 - \vec{U}_1, \frac{d\beta_s}{dt}, \text{grad}_s \frac{d\beta_s}{dt}, \frac{d\beta_1}{dt} - \frac{d\beta_s}{dt}, \frac{d\beta_2}{dt} - \frac{d\beta_s}{dt} \right\},$$

$$\delta E_{s,1,2}(\vec{x}, \vec{y}) = \left\{ D_{1,2}(\vec{U}_1, \vec{U}_2)(\vec{x}, \vec{y}), \frac{d\beta_s}{dt}(\vec{x}), \frac{d\beta_s}{dt}(\vec{y}) \right\},$$

where $\beta_i - \beta_s$ is the discrete analog of the gradient.

4. Equations of motion

The equations of motion result from the principle of virtual power which involves the powers of the internal forces, the exterior forces, and the acceleration forces and which yield the introduction of new internal forces which describe the evolution and interaction of damage variables.

4.1. Virtual power of the internal forces. Both volume damage and surface damage result from microscopic motions whose power is taken into account in the power of the internal forces. We have chosen the velocities $d\beta/dt$ to account for the microscopic velocities at the macroscopic level. Assuming $\vec{V} = (\vec{V}_1, \vec{V}_2)$ and $\gamma = (\gamma_1, \gamma_2, \gamma_s)$ to be macroscopic and microscopic virtual velocities, the virtual power of the internal forces, which is a linear function of the virtual velocities, is chosen to be

$$\begin{aligned} \mathcal{P}_{int} = & - \int_{\Omega_1} \sigma_1 : D(\vec{V}_1) d\Omega - \int_{\Omega_1} B_1 \gamma_1 + \vec{H}_1 \cdot \text{grad } \gamma_1 d\Omega \\ & - \int_{\Omega_2} \sigma_2 : D(\vec{V}_2) d\Omega - \int_{\Omega_2} B_2 \gamma_2 + \vec{H}_2 \cdot \text{grad } \gamma_2 d\Omega \\ & - \int_{\partial\Omega_1 \cap \partial\Omega_2} \vec{R}(\vec{V}_2 - \vec{V}_1) d\Gamma - \int_{\partial\Omega_1 \cap \partial\Omega_2} B_s \gamma_s + \vec{H}_s \cdot \text{grad}_s \gamma_s + B_{1,s}(\gamma_1 - \gamma_s) + B_{2,s}(\gamma_2 - \gamma_s) d\Gamma \\ & + \int_{\partial\Omega_1 \cap \partial\Omega_2} \int_{\partial\Omega_1 \cap \partial\Omega_2} M(\vec{x}, \vec{y}) D_{1,2}(\vec{V}_1, \vec{V}_2)(\vec{x}, \vec{y}) d\Gamma(\vec{x}) d\Gamma(\vec{y}) \\ & + \int_{\partial\Omega_1 \cap \partial\Omega_2} \int_{\partial\Omega_1 \cap \partial\Omega_2} B_{s,1}(\vec{x}, \vec{y}) \gamma_s(\vec{x}) + B_{s,2}(\vec{x}, \vec{y}) \gamma_s(\vec{y}) d\Gamma(\vec{x}) d\Gamma(\vec{y}), \end{aligned}$$

where

$$(D(\vec{V}))_{i,j} = \frac{1}{2} \left(\frac{\partial V_i}{\partial x_j} + \frac{\partial V_j}{\partial x_i} \right) = \frac{1}{2} (V_{i,j} + V_{j,i})$$

are the classical strain rates. The different quantities which contribute to the power of the internal forces are products of kinematic quantities by internal forces. Kinematic quantities are those which intervene in the motion we intend to describe. Their choice is of paramount importance to the predictive capability of the theory. They are chosen following the experimental phenomena of volume and surface deformations together with volume and surface damage, that is, microvoiding and microcracking. Thus the model includes quantities with surface and volume densities which depend on the quantities we have chosen to describe the evolutions or the deformations of the system. Some are classical and others are new. Also, most are local but a few are nonlocal because there is a nonlocal kinematic quantity. Let us comment on the different power densities:

- The usual strain rate D introduces the stress σ .
- The damage velocity, $d\beta/dt$ is a scalar, thus the associated internal force is also a scalar, B . It is a mechanical work, specifically, the internal damage work which is responsible for the evolution of the damage in the volume and in the surface.
- The gradient of the damage velocity, $\text{grad}(d\beta/dt)$ is a vector, thus the internal force is a vector, \vec{H} . It is a work flux vector which is responsible for the interaction of the damage at a point on the damage of its neighborhood. Its physical meaning is to be given by the boundary condition of the equation of motion just as the physical meaning of the stress is given by the boundary condition of the equation of motion.
- The gap velocity $\vec{U}_2 - \vec{U}_1$ on the contact surface introduces the classical macroscopic interaction force \vec{R} .
- The difference between the damage velocities $d\beta_i/dt - d\beta_s/dt$ introduces a damage work flux on the surface $B_{i,s}$, which describes the influence of the volume damage on the surface damage.
- The nonlocal elongation velocity, $D_{1,2}(\vec{U}_1, \vec{U}_2)(\vec{x}, \vec{y})$ introduces a nonlocal scalar $M(\vec{x}, \vec{y})$ internal force. It describes the effects of the elongation, and results in the equations of motion as a classical force. The interaction macroscopic mechanical force has a nonlocal part and a classical local part, the force \vec{R} (see Equation (5)). Since we are going to assume the internal force $M(\vec{x}, \vec{y})$ depending on the surface damage β_s , it is wise to add an extra nonlocal power depending on damage velocity $d\beta_s/dt$. It describes the effect of damage at point \vec{x} on damage at point \vec{y} . The internal forces $B_{s,i}(\vec{x}, \vec{y})$ have the same effect than M : they introduce a nonlocal internal source of damage work. The microscopic mechanical force has a nonlocal part and three local parts, B_s due to the glue and the two $B_{i,s}$ due to the interactions which the volumes (see Equation (7) below).

Note that even if the internal forces are numerous and some are unusual, they are all simple and precisely chosen to take into account a particular aspect of the coupling of volume and surface, and of the microscopic and macroscopic evolution of the system.

4.2. Virtual power of the exterior forces. We assume no exterior microscopic surfacic or volumic source of damage, such as radiative, electrical or chemical damaging actions. Thus the power does not depend

on γ , and we have

$$\mathcal{P}_{ext} = \int_{\Omega_1} \vec{f}_1 \vec{V}_1 d\Omega + \int_{\partial\Omega_1 \setminus (\partial\Omega_1 \cap \partial\Omega_2)} \vec{g}_1 \vec{V}_1 d\Gamma + \int_{\Omega_2} \vec{f}_2 \vec{V}_2 d\Omega + \int_{\partial\Omega_2 \setminus (\partial\Omega_1 \cap \partial\Omega_2)} \vec{g}_2 \vec{V}_2 d\Gamma,$$

where the \vec{f} and \vec{g} are the body and surface exterior forces.

4.3. Virtual power of the acceleration forces. For the sake of simplicity, we assume a quasistatic problem. Thus

$$\mathcal{P}_{acc} = 0.$$

4.4. The principle of virtual power and the equations of motion. The principle of virtual power

$$\mathcal{P}_{acc} = \mathcal{P}_{int} + \mathcal{P}_{ext}, \quad \text{for all } \vec{V}_1, \vec{V}_2, \gamma_1, \gamma_2, \gamma_s,$$

gives three sets of equations of motion. By choosing convenient virtual velocities, we obtain

$$\operatorname{div} \sigma_i + \vec{f}_i = 0, \quad \text{in } \Omega_i, \tag{1}$$

$$-B_i + \operatorname{div} \vec{H}_i = 0, \quad \text{in } \Omega_i, \tag{2}$$

$$\sigma_i \vec{N}_i = \vec{g}_i, \quad \text{in } \partial\Omega_i \setminus (\partial\Omega_1 \cap \partial\Omega_2), \tag{3}$$

$$\vec{H}_i \vec{N}_i = 0, \quad \text{in } \partial\Omega_i \setminus (\partial\Omega_1 \cap \partial\Omega_2), \tag{4}$$

where the \vec{N}_i are the outward normal to the Ω_i . Equations (1)–(4) are the volume equations of motion accounting for macroscopic and microscopic effects. The equation of motion (3) gives the physical meaning of the stress tensor. In the same way, the equation of motion (4) gives the physical meaning of vector \vec{H} : its scalar product with vector \vec{N} is the amount of work which is provided to the domain with exterior normal \vec{N} by microscopic motions. These microscopic motions may be due either to macroscopic deformations (as in the examples given below), or to radiative, electrical, chemical, and optical actions.

On surface $\partial\Omega_1 \cap \partial\Omega_2$, the boundary conditions for the volume equations of motion (1) and (2), as well as the surface equation of motion, involve nonlocal forces. For the volume equations of motion (1), the boundary conditions are

$$\begin{aligned} \sigma_1 \vec{N}_1(\vec{x}) &= \vec{R}(\vec{x}) + \int_{\partial\Omega_1 \cap \partial\Omega_2} 2(\vec{x} - \vec{y}) M(\vec{x}, \vec{y}) d\Gamma(\vec{y}), \quad \vec{x} \in \partial\Omega_1 \cap \partial\Omega_2, \\ \sigma_2 \vec{N}_2(\vec{y}) &= -\vec{R}(\vec{y}) + \int_{\partial\Omega_1 \cap \partial\Omega_2} 2(\vec{y} - \vec{x}) M(\vec{x}, \vec{y}) d\Gamma(\vec{x}), \quad \vec{y} \in \partial\Omega_1 \cap \partial\Omega_2. \end{aligned} \tag{5}$$

As already mentioned, the stress $\sigma_i \vec{N}_i$ on the contact surface has a local part \vec{R} and a nonlocal part

$$\int_{\partial\Omega_1 \cap \partial\Omega_2} (-1)^i 2(\vec{y} - \vec{x}) M(\vec{x}, \vec{y}) d\Gamma(\vec{x}).$$

The boundary conditions for the equation of motions (2) in $\partial\Omega_1 \cap \partial\Omega_2$ are

$$\vec{H}_1 \vec{N}_1 = -B_{1,s}, \quad \vec{H}_2 \vec{N}_2 = -B_{2,s}, \tag{6}$$

and a surface equation of motion with a boundary condition on the boundary of the contact surface $\partial(\partial\Omega_1 \cap \partial\Omega_2)$,

$$\begin{aligned}
 -B_s(\vec{x}) + \operatorname{div}_s \vec{H}_s(\vec{x}) + B_{1,s}(\vec{x}) + B_{2,s}(\vec{x}) - \int_{\partial\Omega_1 \cap \partial\Omega_2} B_{s,1}(\vec{x}, \vec{y}) + B_{s,2}(\vec{y}, \vec{x}) d\Gamma(\vec{y}) &= 0, \quad \text{in } \partial\Omega_1 \cap \partial\Omega_2, \\
 \vec{H}_s \vec{n}_s &= 0, \quad \text{in } \partial(\partial\Omega_1 \cap \partial\Omega_2),
 \end{aligned} \tag{7}$$

where div_s is the surface divergence and \vec{n}_s is normal vector to the boundary $\partial(\partial\Omega_1 \cap \partial\Omega_2)$. As already mentioned, the internal source of damage on the contact surface has three local parts $-B_s(\vec{x})$ due to the glue and $B_{1,s}(\vec{x})$, $B_{2,s}(\vec{x})$ due to the two neighboring volumes, and a nonlocal part

$$\int_{\partial\Omega_1 \cap \partial\Omega_2} B_{s,1}(\vec{x}, \vec{y}) + B_{s,2}(\vec{y}, \vec{x}) d\Gamma(\vec{y}).$$

Of course, the opposite of the damage work $B_{1,s}(\vec{x})$ and $B_{2,s}(\vec{x})$ which are provided to the glue by the two neighboring volumes, are provided by the glue to the volumes by Equations (6) and (7).

Constitutive laws are needed for the numerous interior forces. As usual, we choose to define them with free energies Ψ depending on state quantities E and pseudo-potential of dissipation Φ depending on velocities δE .

5. The constitutive laws

Since the thermal phenomena are not taken into account, the second law of thermodynamics for the domains and the interface are [Frémond 2001]

$$\frac{d\Psi_i}{dt}(E_i) \leq \sigma_i D(\vec{U}_1) + B_i \frac{d\beta_i}{dt} + \vec{H}_i \operatorname{grad} \frac{d\beta_i}{dt}, \quad \text{in } \Omega_i, \tag{8}$$

$$\begin{aligned}
 \frac{d\Psi_s}{dt}(E_s) \leq \vec{R}(\vec{U}_2 - \vec{U}_1) + B_s \frac{d\beta_s}{dt} + \vec{H}_s \operatorname{grad}_s \frac{d\beta_s}{dt} \\
 + B_{1,s} \left(\frac{d\beta_1}{dt} - \frac{d\beta_s}{dt} \right) + B_{2,s} \left(\frac{d\beta_2}{dt} - \frac{d\beta_s}{dt} \right), \quad \text{in } \partial\Omega_1 \cap \partial\Omega_2, \tag{9}
 \end{aligned}$$

$$\begin{aligned}
 \frac{d\Psi_{s,1,2}}{dt}(E_{s,1,2})(\vec{x}, \vec{y}) \leq -M(\vec{x}, \vec{y}) D_{1,2}(\vec{U}_1, \vec{U}_2)(\vec{x}, \vec{y}), \\
 - B_{1,s}(\vec{x}, \vec{y}) \frac{d\beta_s}{dt}(\vec{x}) - B_{2,s}(\vec{x}, \vec{y}) \frac{d\beta_s}{dt}(\vec{y}), \quad \text{in } (\partial\Omega_1 \cap \partial\Omega_2) \times (\partial\Omega_1 \cap \partial\Omega_2). \tag{10}
 \end{aligned}$$

We use Equations (8)–(10) to define the constitutive laws with pseudo-potential of dissipation. The + or – sign appearing in the constitutive laws results from the + or – sign in the right sides of the inequalities, and right sides are the opposite of the densities of the virtual powers.

The free energy and pseudo-potential of dissipation of the domains are, respectively,

$$\Psi_i(E_i) = \Psi_i(\varepsilon_i, \beta_i, \text{grad } \beta_i) \in w_i(1 - \beta_i) + \frac{k_i}{2} (\text{grad } \beta_i)^2 + I(\beta_i) + \frac{\beta_i}{2} \{ \lambda_i (\text{tr } \varepsilon_i)^2 + 2\mu_i \varepsilon_i : \varepsilon_i \},$$

$$\Phi_i(\delta E_i) = \Phi_i\left(\frac{d\beta_i}{dt}\right) = \frac{c_i}{2} \left(\frac{d\beta_i}{dt}\right)^2 + I_-\left(\frac{d\beta_i}{dt}\right),$$

where λ_i and μ_i are the Lamé parameters. The quantities w_i are initial damage thresholds expressed in terms of volumetric energies. They are equivalent to the initial thresholds expressed in terms of damage forces or stresses [Lemaitre 1992; Voyaiadjis et al. 1998; Lemaitre and Desmorat 2005]. The quantities c_i are the viscosity parameters of damage and k_i measure the local influences of a material point on its neighborhood. The c_i quantities control the velocity of the phenomena. If they are large, damage evolution is slow and if they are small, damage evolution is very fast. The values of c_i can be measured with experiments performed at different velocities. The extension parameters k_i control the size of the transition zone between sound material and damaged material. If the k_i are large, damage is diffuse and spread in the whole domain. If the k_i are small, the damage is concentrated in thin zones which may represent fractures. The values of k_i can be measured with structure experiments, but not with sample experiments where the state quantities are homogeneous.

The functions I and I_- are the indicator functions of the intervals $[0, 1]$, ($I(\gamma) = 0$, if $0 \leq \gamma \leq 1$, and $I(\gamma) = +\infty$, if $\gamma \notin [0, 1]$), and of $[-\infty, 0] = \mathbb{R}^-$, ($I_-(\gamma) = 0$, if $\gamma \leq 0$ and $I_-(\gamma) = +\infty$, if $\gamma > 0$) (see [Moreau 1966]).

The free energies and pseudo-potentials are the most simple energies coupling elasticity and damage. They give the constitutive laws

$$\sigma_i = \frac{\partial \Psi_i}{\partial \varepsilon_i} = \beta_i \{ \lambda_i \text{tr } \varepsilon_i \mathbf{1} + 2\mu_i \varepsilon_i \},$$

$$B_i = \frac{\partial \Psi_i}{\partial \beta_i} + \frac{\partial \Phi_i}{\partial (d\beta_i/dt)}$$

$$\in -w_i + \frac{1}{2} \{ \lambda_i (\text{tr } \varepsilon_i)^2 + 2\mu_i \varepsilon_i : \varepsilon_i \} + \partial I(\beta_i) + c_i \left(\frac{d\beta_i}{dt}\right) + \partial I_-\left(\frac{d\beta_i}{dt}\right),$$

$$\vec{H}_i = \frac{\partial \Psi_i}{\partial (\text{grad } \beta_i)} = k_i \text{grad } \beta_i.$$

where $\mathbf{1}$ is the identity matrix.

In the previous formula, ∂I and ∂I_- are the subdifferential sets or the sets of the generalized derivatives of the indicator functions I , ($\partial I(\beta) = \{0\}$, if $0 < \beta < 1$; $\partial I(0) = \mathbb{R}^-$; $\partial I(1) = \mathbb{R}^+ = [0, +\infty[$; $\partial I(\beta) = \emptyset$, if $\beta \notin [0, 1]$) and I_- , ($\partial I_-(x) = \{0\}$, if $x < 0$ and $\partial I_-(0) = [0, +\infty[$). These generalized derivatives are the reactions to the internal constraints $0 \leq \beta_i \leq 1$ and $d\beta_i/dt \leq 0$. The latter internal constraint accounts for the irreversibility of damage. The reactions are different from 0 only for the extreme values of the inequalities.

The free energy and pseudo-potential of the glued contact surface are

$$\begin{aligned}\Psi_s(E_s) &= \Psi_s(\vec{u}_2 - \vec{u}_1, \beta_s, \text{grad}_s \beta_s, \beta_1 - \beta_s, \beta_2 - \beta_s) \\ &= w_s(1 - \beta_s) + \frac{k_s}{2} (\text{grad}_s \beta_s)^2 + I(\beta_s) + I_- \left((\vec{u}_2 - \vec{u}_1) \cdot \vec{N}_2 \right) \\ &\quad + \frac{\beta_s \hat{k}_s}{2} (\vec{u}_2 - \vec{u}_1)^2 + \frac{k_{s,1}}{2} (\beta_1 - \beta_s)^2 + \frac{k_{s,2}}{2} (\beta_2 - \beta_s)^2, \\ \Phi_s(\delta E_s) &= \Phi_s \left(\frac{d\beta_s}{dt} \right) = \frac{c_s}{2} \left(\frac{d\beta_s}{dt} \right)^2 + I_- \left(\frac{d\beta_s}{dt} \right),\end{aligned}$$

where k_s is the local surface extension or interaction coefficient, w_s the Dupré's energy accounting for the glue cohesion, c_s the viscosity of the adhesive evolution, $k_{s,1}$ and $k_{s,2}$ are the surface-volume interaction parameters, and \hat{k}_s represents the rigidity of the bonds between the two solids. The function $I_-((\vec{u}_2 - \vec{u}_1) \cdot \vec{N}_2)$ takes into account the impenetrability of the two domains on their contact surface and function $I_-(d\beta_s/dt)$ implies irreversibility of damage.

The expressions of the free energy and pseudo-potential of dissipation are the simplest to give a model where damage is coupled with elasticity. They account for elastic, viscous and damage properties. The resulting constitutive laws are

$$\begin{aligned}\vec{R} &= \frac{\partial \Psi_s}{\partial (\vec{u}_2 - \vec{u}_1)} \in \beta_s \hat{k}_s (\vec{u}_2 - \vec{u}_1) + \partial I_- \left((\vec{u}_2 - \vec{u}_1) \cdot \vec{N}_2 \right) \vec{N}_2, \\ B_s &= \frac{\partial \Psi_s}{\partial \beta_s} + \frac{\partial \Phi_s}{\partial (d\beta_s/dt)} \in -w_s + \frac{\hat{k}_s}{2} (\vec{u}_2 - \vec{u}_1)^2 + \partial I(\beta_s) + c_s \frac{d\beta_s}{dt} + \partial I_- \left(\frac{d\beta_s}{dt} \right), \\ \vec{H}_s &= \frac{\partial \Psi_s}{\partial (\text{grad}_s \beta_s)} = k_s \text{grad}_s \beta_s, \\ B_{1,s} &= \frac{\partial \Psi_s}{\partial (\beta_1 - \beta_s)} = k_{s,1} (\beta_1 - \beta_s), \\ B_{2,s} &= \frac{\partial \Psi_s}{\partial (\beta_2 - \beta_s)} = k_{s,2} (\beta_2 - \beta_s).\end{aligned}$$

The force $\partial I_-((\vec{u}_2 - \vec{u}_1) \cdot \vec{N}_2) \vec{N}_2$ is the impenetrability reaction. Note that it is active only when there is actually contact, that is, when $(\vec{u}_2 - \vec{u}_1) \cdot \vec{N}_2 = 0$.

The nonlocal free energy on the glued contact surface is

$$\Psi_{s,1,2}(E_{s,1,2}(\vec{x}, \vec{y})) = \frac{k_{s,1,2}}{2} g^2(\vec{x}, \vec{y}) (\beta_s(\vec{x})\beta_s(\vec{y})) \exp\left(-\frac{|\vec{x} - \vec{y}|^2}{d^2}\right),$$

with

$$g(\vec{x}, \vec{y}) = 2(\vec{y} - \vec{x}) \cdot (\vec{u}_2(\vec{y}) - \vec{u}_1(\vec{x})).$$

The exponential function with distance d , describes the attenuation of nonlocal actions with distance $|\vec{x} - \vec{y}|$ between points \vec{x} and \vec{y} . Assuming no dissipation with respect to $\delta E_{s,1,2}(\vec{x}, \vec{y})$, we have the

constitutive law

$$\begin{aligned} -B_{s,1}(\vec{x}, \vec{y}) &= \frac{\partial \Psi_{s,1,2}(E_{s,1,2}(\vec{x}, \vec{y}))}{\partial \beta_s(\vec{x})} = \frac{k_{s,1,2}}{2} g^2(\vec{x}, \vec{y}) \beta_s(\vec{y}) \exp\left(-\frac{|\vec{x} - \vec{y}|^2}{d^2}\right), \\ -B_{s,2}(\vec{x}, \vec{y}) &= \frac{\partial \Psi_{s,1,2}(E_{s,1,2}(\vec{x}, \vec{y}))}{\partial \beta_s(\vec{y})} = \frac{k_{s,1,2}}{2} g^2(\vec{x}, \vec{y}) \beta_s(\vec{x}) \exp\left(-\frac{|\vec{x} - \vec{y}|^2}{d^2}\right), \\ -M(\vec{x}, \vec{y}) &= \frac{\partial \Psi_{s,1,2}(E_{s,1,2}(\vec{x}, \vec{y}))}{\partial g(\vec{x}, \vec{y})} = k_{s,1,2} g(\vec{x}, \vec{y}) (\beta_s(\vec{x}) \beta_s(\vec{y})) \exp\left(-\frac{|\vec{x} - \vec{y}|^2}{d^2}\right). \end{aligned}$$

The state quantities we use have dimension. The time and length scales related to the classical quantities are those of solids mechanics, in particular, of civil engineering. The new length scales are related to the gradient of damage, which corresponds to the size of the influence zone of damage (a few centimeters in our examples), and to the effect of damage elongation (on the order of millimeters in our examples). The first length scale is already known. To measure it, structure experiments have to be performed; in our case we used four point bending experiments. The second length scale has also been estimated with the four point bending experiments. Systematic research is under way at the Laboratoire Central des Ponts et Chaussées to estimate the amplitude of the variations of these parameters related to the durability of glued structures. Moreover, the parameters c_i may be seen as the characteristic times of the processes. They can be identified by performing experiments at different loading velocities, specifically, small velocities to remain in a quasistatic situation.

Let us note that all the constitutive laws involve the reactions to the internal constraints when needed, which are clearly non linear relationships, and linear relationships between the forces and the state quantities and velocities. Thus they are simple and we think that they have to account for the main phenomena: non linear constitutive laws are to be chosen only to make the results more adapted but the linear relationships have to be sufficient in a first step to capture the basic physical features. More complicated constitutive law has been considered in [Nedjar 2001; 2002]. For the sake of simplicity, we assume the simplest case of dissipation that is, only the dissipation with respect to the $d\beta/dt$'s and not the dissipation with respect to the gradient of the $d\beta/dt$'s. This assumption minimizes the number of the parameters of the predictive theory, and it is sufficient to ensure both mechanical and mathematical coherency [Bonetti et al. 2006; Bonetti and Schimperna 2004; Bonetti et al. 2005; Frémond and Nedjar 1996].

6. The equations

The principle of virtual power and a proper use of the constitutive laws leads to three sets of equations of motion; the first one is the classical equation of motion and the others are nonstandard partial differential equations describing domains and interface damage evolution.

6.1. In the domains. The equations of the evolution of damage for the domains obtained by using the constitutive laws and equilibrium equations are

$$\operatorname{div}(\beta_i \{\lambda_i \operatorname{tr} \varepsilon_i(\vec{u}_i) \mathbf{1} + 2\mu_i \varepsilon_i(\vec{u}_i)\}) + \vec{f}_i = 0, \quad (11)$$

$$c_i \frac{d\beta_i}{dt} - k_i \Delta \beta_i + \partial I(\beta_i) + \partial I_-\left(\frac{d\beta_i}{dt}\right) \ni w_i - \frac{1}{2} \left\{ \lambda_i (\text{tr} \varepsilon_i)^2 + 2\mu_i \varepsilon_i : \varepsilon_i \right\}, \quad (12)$$

with initial conditions

$$\begin{aligned} \beta_i(x, 0) &= \beta_i^0(x), & \text{in } \Omega_i, \\ \beta_s(x, 0) &= \beta_s^0(x), & \text{in } \partial\Omega_1 \cap \partial\Omega_2, \end{aligned}$$

and boundary conditions

$$\begin{aligned} \sigma_i \vec{N}_i &= \vec{g}_i, & \text{in } \partial\Omega_i \setminus (\partial\Omega_1 \cap \partial\Omega_2), \\ k_i \frac{\partial \beta_i}{\partial N_i} &= 0, & \text{in } \partial\Omega_i \setminus (\partial\Omega_1 \cap \partial\Omega_2), \end{aligned}$$

where the \vec{f}_i and \vec{g}_i are the exterior body forces and surface traction.

The elements $\partial I(\beta_i)$ and $\partial I_-(\partial\beta_i/\partial t)$ contain reactions which forces β_i to remain between 0 and 1 and $\partial\beta_i/\partial t$ to be negative, to account for the irreversibility of damage. The source of damage in the right-hand side of (12) is a deformation energy that well agrees with experimental results. This model is sufficient to describe the damage phenomena during multi-axial loading and unloading without changing the sign of exterior actions. In case the exterior actions change sign, a slightly more sophisticated theory is to be used following [Frémond and Nedjar 1996; Frémond 2001]. It involves the positive and negative parts of the deformations. The positive and negative part of a tensor are obtained after diagonalization (see [Frémond and Nedjar 1996] for details), implying the evaluation of the principal deformations. This is a linear algebra result which holds for symmetric matrices. In particular, considering the positive (or negative) part of the strain tensor leads to an elastic-damage model that exhibits dissymmetric behaviors between tension and compression. The threshold of damage in compression is greater than the one in tension due to a different source term in Equation (12) (see [Frémond and Nedjar 1996]).

6.2. On the contact surface. With the previous constitutive laws, the damage evolution law for the cohesive interface reads, [Freddi and Frémond 2005]

$$\begin{aligned} c_s \frac{d\beta_s}{dt} - k_s \Delta_s \beta_s + \partial I(\beta_s) + \partial I_-\left(\frac{d\beta_s}{dt}\right) \ni w_s - \frac{\hat{k}_s}{2} (\vec{u}_2 - \vec{u}_1)^2 - k_{s,1} (\beta_s - \beta_1) - k_{s,2} (\beta_s - \beta_2) \\ - \int_{\partial\Omega_1 \cap \partial\Omega_2} \frac{k_{s,1,2}}{2} (g^2(\vec{x}, \vec{y}) + g^2(\vec{y}, \vec{x})) \beta_s(\vec{y}) \exp\left(-\frac{|\vec{x} - \vec{y}|^2}{d^2}\right) d\Gamma(\vec{y}), \quad (13) \end{aligned}$$

where Δ_s is the surface Laplace operator. The last term is not 0 when $\vec{u}_2 = \vec{u}_1$, and is responsible for the damage resulting from elongation. The glue damage source in the right hand side results from the gap between the two solids, from the elongation (the nonlocal effect) and from the flux of damaging work coming from the concrete. This flux is proportional to the difference of damage between the concrete and the glue (see Figure 1). Thus it is more difficult to damage the glue when the concrete is not damaged. In this case, Equation (13) may be interpreted with a glue threshold equal to $w_s + k_{s,1} + k_{s,2}$, whereas it is w_s when the concrete is completely damaged. Indeed, in some experiments intended to separate two adhering pieces, damage of the pieces is produced to facilitate surface damage. The contact boundary

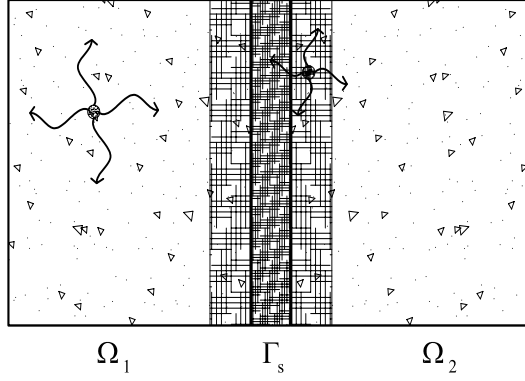


Figure 1. Local interaction between the damage at a material point on the damage on its neighborhood (arrows in the domain), and the damage interaction between domain and interface (arrows in the interphase).

conditions on the glued contact surface $\partial\Omega_1 \cap \partial\Omega_2$ are

$$\sigma_1 \vec{N}_1(\vec{x}) \in \beta_s \hat{k}_s (\vec{u}_2 - \vec{u}_1) + \partial I_-((\vec{u}_2 - \vec{u}_1) \cdot \vec{N}_2) \vec{N}_2 - \int_{\partial\Omega_1 \cap \partial\Omega_2} 2(\vec{x} - \vec{y}) k_{s,1,2} g(\vec{x}, \vec{y}) (\beta_s(\vec{x}) \beta_s(\vec{y})) \exp\left(-\frac{|\vec{x} - \vec{y}|^2}{d^2}\right) d\Gamma(\vec{y}) \quad (14)$$

for $\vec{x} \in \partial\Omega_1 \cap \partial\Omega_2$,

$$\sigma_2 \vec{N}_2(\vec{y}) \in -\beta_s \hat{k}_s (\vec{u}_2 - \vec{u}_1) - \partial I_-((\vec{u}_2 - \vec{u}_1) \cdot \vec{N}_2) \vec{N}_2 - \int_{\partial\Omega_1 \cap \partial\Omega_2} 2(\vec{y} - \vec{x}) k_{s,1,2} g(\vec{x}, \vec{y}) (\beta_s(\vec{x}) \beta_s(\vec{y})) \exp\left(-\frac{|\vec{x} - \vec{y}|^2}{d^2}\right) d\Gamma(\vec{x}) \quad (15)$$

for $\vec{y} \in \partial\Omega_1 \cap \partial\Omega_2$,

$$k_1 \frac{\partial \beta_1}{\partial N_1} = k_{s,1} (\beta_s - \beta_1), \quad k_2 \frac{\partial \beta_2}{\partial N_2} = k_{s,2} (\beta_s - \beta_2), \quad k_s \frac{\partial \beta_s}{\partial N_s} = 0 \in \partial(\partial\Omega_1 \cap \partial\Omega_2). \quad (16)$$

For the sake of simplicity, we neglect in the numerical simulations the nonlocal mechanical effect in surface stresses (14) and (15) because it is negligible compared to the local effect. The values of parameters $\hat{k}_s \gg k_{s,1,2}$ of the constitutive laws we choose in the sequel agree with this assumption (see Table 1). Thus the stress on the interface Γ_s becomes the sum of the reaction to the noninterpenetration condition $(\vec{u}_2 - \vec{u}_1) \cdot \vec{N}_2 \leq 0$ and of the elastic interaction $\beta_s \hat{k}_s (\vec{u}_2 - \vec{u}_1)$, with rigidity proportional to β_s , the fraction of undamaged bonds between the two solids.

Boundary condition (16) means that the damaging energy flux in the concrete is proportional to the difference of damage between the glue and the concrete. Parameter $k_{s,i}$ quantifies the importance of the interaction of the volume and surface damages. When $k_{s,1} = 0$ there is no influence of the volume damage on the surface damage. The damage equations are uncoupled and the interface acts as a damage barrier (see the four point bending test in Section 7).

L (mm)	400	\hat{k}_s^{\parallel} (MPa · mm ⁻¹)	1.9×10^3
l (mm)	300	\hat{k}_s^{\perp} (MPa · mm ⁻¹)	1.9×10^3
h (mm)	50	c_s (MPa · mm · s)	7.2×10^{-2}
d (mm)	100	k_s (MPa · mm ²)	0.1
t (mm)	100	w_s (MPa · mm)	1.1×10^{-2}
E (MPa)	38000	$k_{s,1}$ (MPa · mm)	0.1
ν	0.2	$k_{s,2}$ (MPa · mm)	0.1
c (MPa · s)	2×10^{-3}	d (mm)	10
k (mm)	0.3	$k_{s,1,2}$ (MPa/mm)	20
w (MPa)	2×10^{-5}		
P_{\max}^{one} (kN)	14.3		
P_{\max}^{two} (kN)	18.2		

Table 1. Left: Geometrical, mechanical parameters of the two concrete pieces and maximum loads for four-point bending tests of Figure 2. Right: Glue parameters for the same tests.

In the classical interface problem (that is, one without damaging materials) it is possible to obtain a bilateral connection simply by imposing $\hat{k}_s \cong \infty$. However, in the case we consider — the damaging phenomena of the two materials — a perfect interface is obtained by imposing not only $\hat{k}_s \cong \infty$ but also $k_{s,1} \cong \infty$ and $c_s = w_s = k_s \cong 0$, in order to have the continuity of damage and of its flux across the interface.

As a test to underline the physical meaning of the damage interaction parameters, we consider two square pieces of concrete $[0, 0.05 \text{ m}]^2$ connected by a cohesive interface in a pure traction test, that is, where opposite vertical tractions are applied along the horizontal sides of the two bodies. We suppose that the interface is very strong such that no damage appears along the contact surface. Normally, with the two bodies subjected to nearly uniform traction, a diffused damage should involve the whole domains.

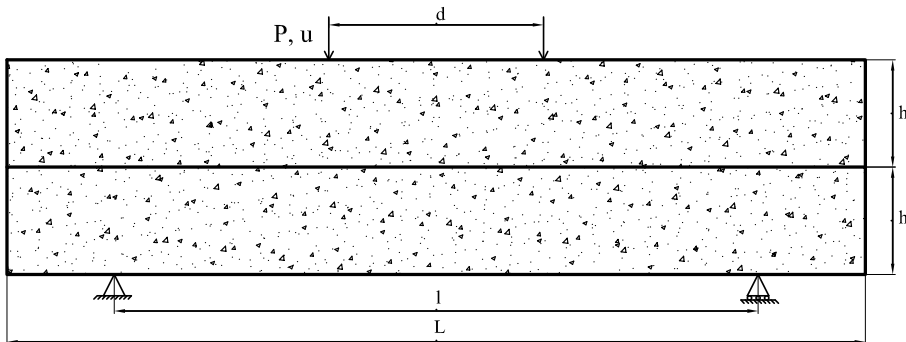


Figure 2. Four point bending test for sample of thickness t . See Table 1 for parameter values for numerical and experimental results.

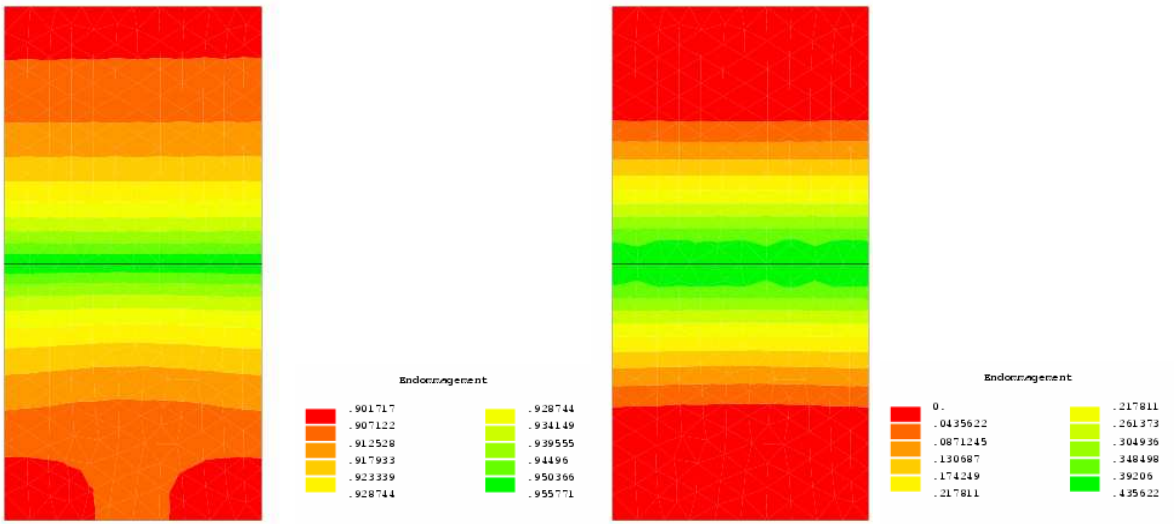


Figure 3. Damage evolution in pure-traction test: $k_{s,1} = k_{s,2} = 0.05$. Note the (green) less damaged zone due to the strong glue connecting the two specimen. The left figure represents an initial damaged state while the right figure shows the complete damaged state. The glue acts as a reinforcement for the material.

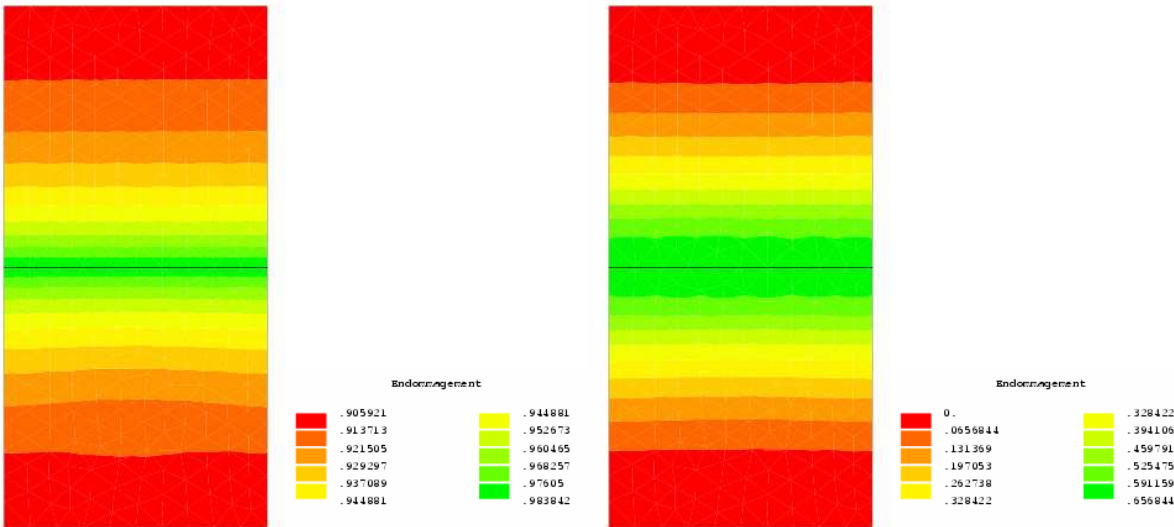


Figure 4. Damage evolution in pure-traction test: $k_{s,1} = k_{s,2} = 0.2$. The left figure represents an initial damaged state while the right figure shows the complete damaged state. The (green) less damaged zone is more important when the interaction parameters $k_{s,i}$ are large. The glue acts like a reinforcement for the material, but is stronger than the case shown in Figure 3.

Instead, as shown in the Figures 3 and 4, the interaction between the glue and the materials determines the presence of more resistant zones next to the interface. Particularly, the zone is larger and the phenomenon more pronounced for higher $k_{s,1}$ and $k_{s,2}$ values.

In view of the examples and experiments investigated in the sequel, we define three models which differ by their surface properties:

- Model a: uncoupled without elongation effects where $k_{s,1} = 0$, $k_{s,2} = 0$, $k_{s,1,2} = 0$;
- Model b: coupled without elongation effects where $k_{s,1,2} = 0$;
- Model c: coupled with elongation effects, that is, the complete model with every physical action.

All other quantities are not zero in any of the models.

7. Numerical simulations and some experimental results

The proposed model has been implemented in the finite element code CESAR-LCPC, [Humbert et al. 2005]. The coupled damage-mechanics model is solved in a semicoupled fashion. Given a time increment, the motion equation (11) is solved first assuming that the damage variables are constants. This equation is solved with a quasi-Newton method. Moreover, in order to deal with the unilateral boundary conditions an ad hoc Uzawa algorithm has been implemented. Afterwards, the damage equations (12) and (13) are solved via a Crank-Nicholson scheme, and boundary conditions (16) are included explicitly.

Actually, mathematical results concerning the existence of the solution, the proof that the problem is well posed, and numerical verification will appear in a forthcoming paper [Bonetti et al. 2006].

In the following simulations the loads applied are always monotonic and do not change in sign. In particular, all the analysis have been carried out under displacement control. An explicit linear relationship between the time and the imposed displacement is introduced. Moreover, plain strain hypothesis is assumed. Finally, the interface stiffness matrix \hat{k}_s is composed by normal \hat{k}_s^\perp and tangential component \hat{k}_s^\parallel with respect to the surface orientation. It should be mentioned that the damage scale in each iso-value picture is always represented by green-to-red variation, but it is representative of different damage values and the deformation scale for horizontal and vertical displacement is adapted to numerical results.

7.1. Four-point bending test. The goal of this analysis is to validate the model and to evaluate the influence of the enhancements to it that we introduced: the coupling between the damage in the domains and the damage in the interface and the nonlocal elongation contribution to interface damage evolution. In particular, this test shows the importance of the interaction parameters $k_{s,1}$ and $k_{s,2}$ which couple the damages of solids 1 and 2. When solid 1 becomes damaged in the neighborhood of solid 2, solid 2 also becomes damaged. Also the test shows that it is more difficult to damage the glue when the concrete is not damaged than when the concrete is damaged. As already noted, the glue cohesion or threshold is $w_s + k_{s,1} + k_{s,2}$ when the concrete is not damaged whereas it is w_s when concrete is completely damaged in the two solids.

7.1.1. Test setup and experimental results. Figure 2 on page 1217 shows a classical four-point bending test. Experimental tests performed by Thaveau [2005] have been considered. We used two different test configurations: one concrete specimen, and two concrete specimens connected with via epoxy glue. The maximum loads obtained, the geometrical and mechanical properties of the specimens are reported in

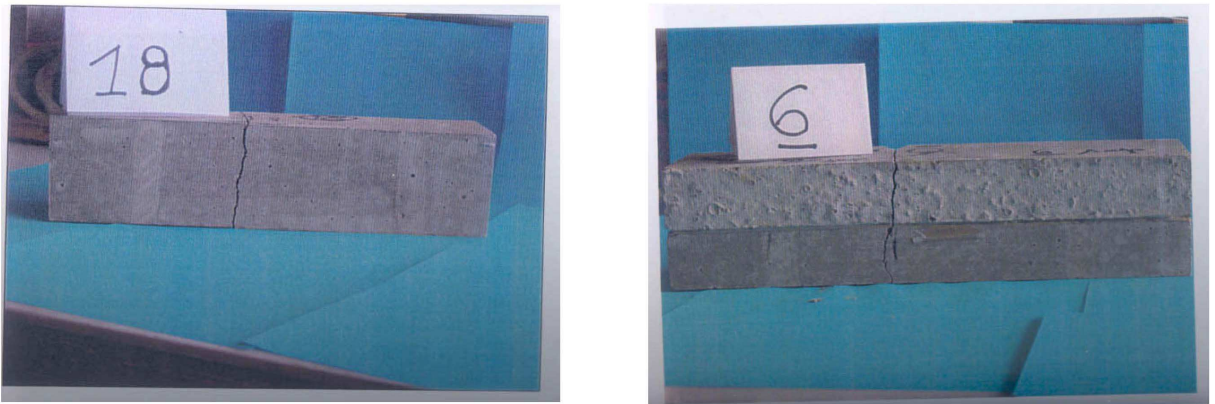


Figure 5. Experimental tests: one specimen on the left; two glued specimens on the right [Thaveau 2005].

Table 1. It should be noted that the maximum load is greater for the glued concrete specimen. **Figure 5** show clearly the failure mechanism for the two configurations. In both cases, a vertical fracture in the middle of the specimens appears which propagates from the bottom to the upper face of the beam.

7.1.2. Numerical results. The load versus displacement curves obtained from the numerical simulations for single and double specimens are shown in **Figure 6**. In particular, the case of the uncoupled model

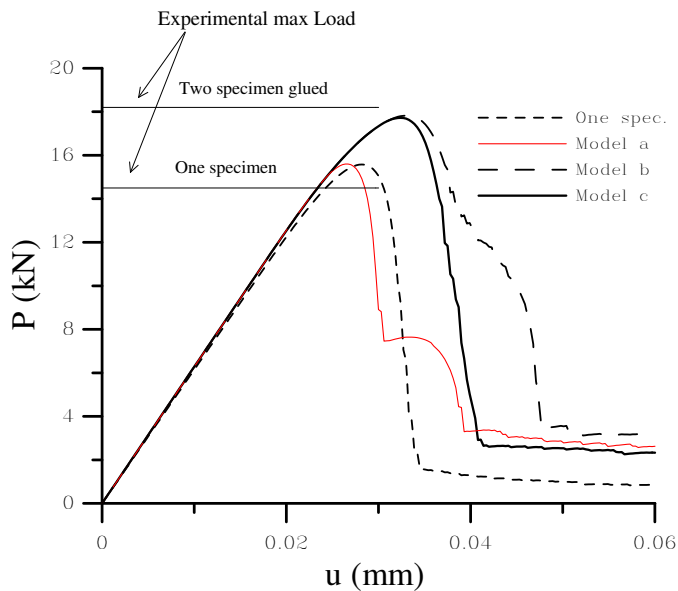


Figure 6. Load versus displacement curves for single and double glued specimens in four point bending tests. The short dashed line is the curve for one specimen, while the red line, the long dashed line, and the straight line are the load versus displacement curves for two glued pieces of concrete obtained with models a, b and c, respectively.

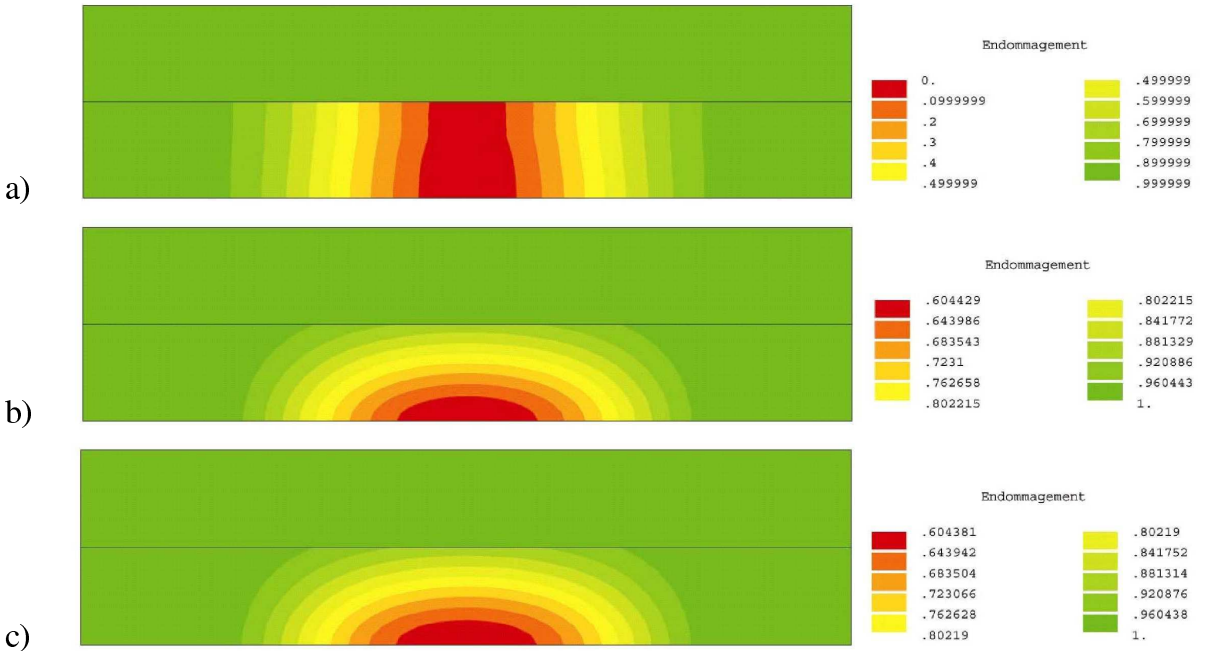


Figure 7. Four point bending test. Damage field at displacement $u = 0.03$ mm for model a (uncoupled damage without elongation effect), model b (coupled damage model for concrete and glue without elongation effect), and model c (coupled damage model for concrete and glue with elongation effect). At the beginning, the contact surface acts as a damage barrier.

presents a very strange hill in the softening branch. This unrealistic behavior completely vanishes when we consider model c with both enhancements, and it is less pronounced in the coupled model b where the nonlocal elongation effect is neglected. The horizontal paths in load versus displacement curves represent structural effects and interplay between surface and volume damage. A similar effect is exhibited in experiments [Gonzalez et al. 2005]. Moreover, for large displacement values the hypothesis of small deformation is no longer sufficient fully to completely describe the failure phenomena [Nedjar 2002].

The damage fields of the two concrete domains for the damage models uncoupled (model a), coupled (model b) and coupled with the nonlocal elongation contribution (model c) are shown in Figures 7–8 for different displacement values: 0.03, 0.045, 0.06 mm. These figures clearly show the inability of the uncoupled model to describe correctly the physical failure phenomenon. In fact, the interface acts as a barrier to the damage propagation, causing the entire damaging of the inferior specimen. On the contrary, the coupling between damages allows correct description of the damage evolution inside the domains. Additional comments are reported in captions. The interface damage evolutions for models b and c are reported in Figure 9.

For model b, the damage of the interface is almost incomplete (that is, $\beta_s \neq 0$) even if the fracture has already crossed the glue thickness. To capture the correct behavior, in the coupled model it is necessary to introduce also the nonlocal elongation contribution. In this test, model a presents no glue damage at

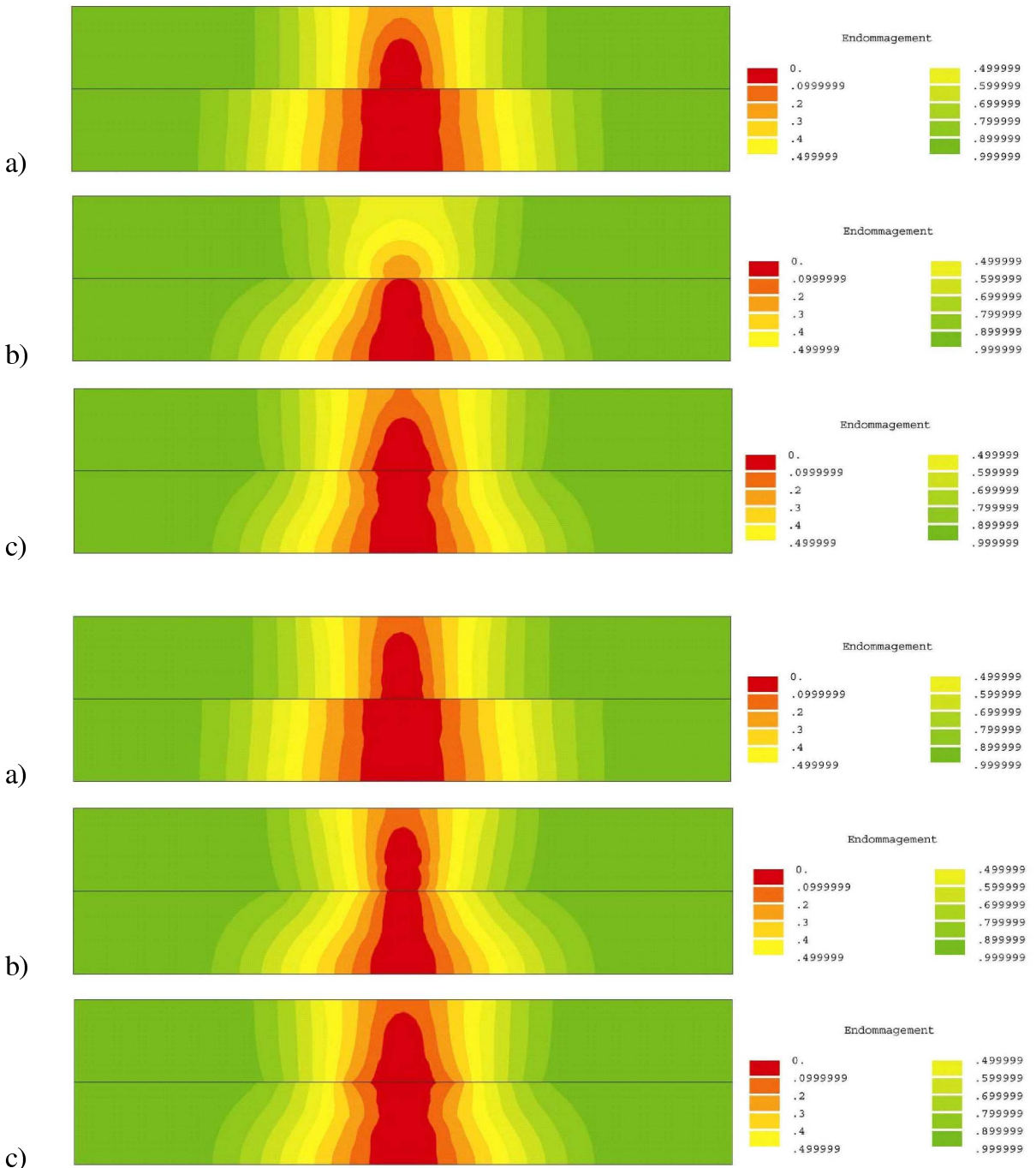


Figure 8. Four point bending test. Damage field at displacement $u = 0.045$ mm (top) and $u = 0.06$ mm (bottom) for model a (uncoupled damage without elongation effect), model b (coupled damage model for concrete and glue without elongation effect), and model c (coupled damage model for concrete and glue with elongation effect).

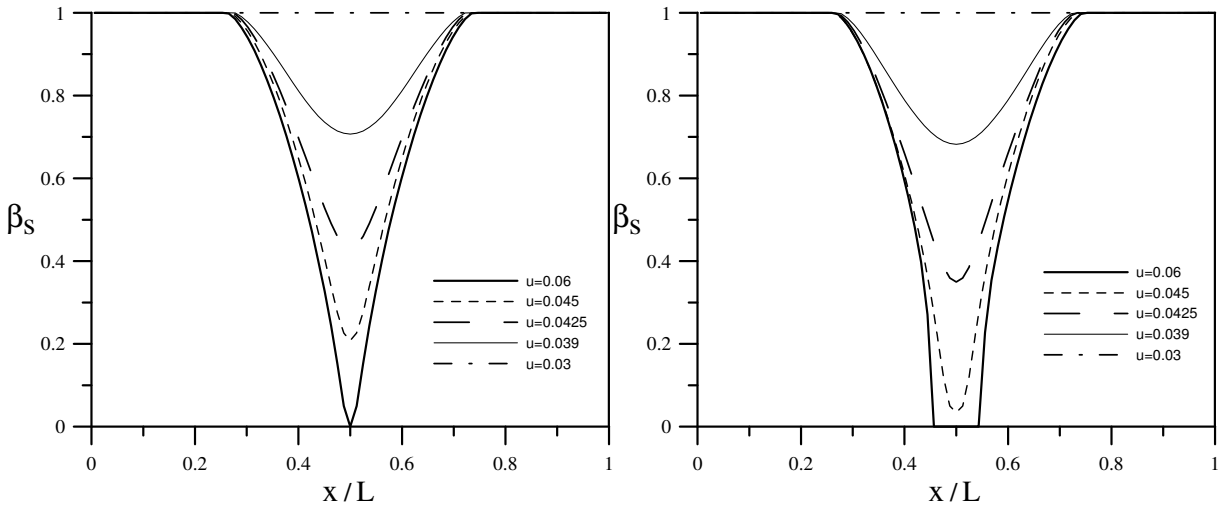


Figure 9. Four point bending test. Left: Surface damage field β_s along the interface for model b (coupled damage model for concrete and glue without elongation). Right: Surface damage field β_s along the interface for model c (coupled damage model for concrete and glue with elongation). The effect of the elongation is to enlarge the damage zone of the glue, which is completely broken in the middle of the specimen.

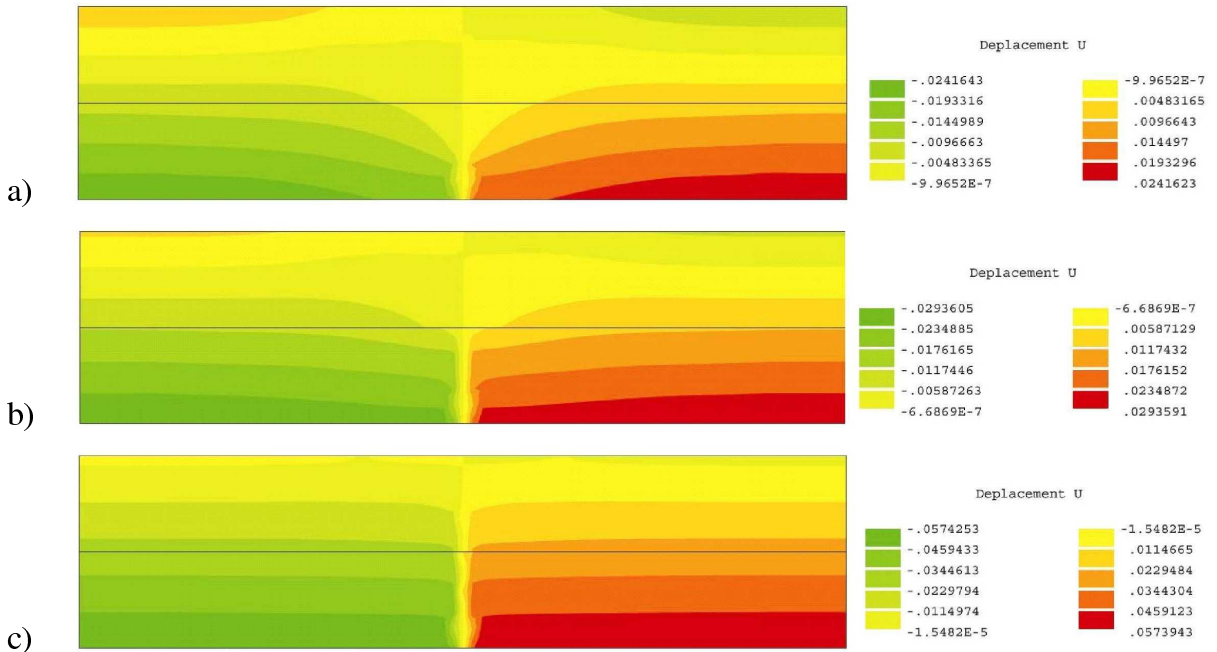


Figure 10. Four point bending test. Horizontal displacement field evaluated at different equilibrium points ($\bar{u} = 0.03, 0.045, 0.06$ mm) for model c. The displacement discontinuity of the horizontal displacement accounts for the fracture in the middle of the sample (see experimental results of Figure 5).

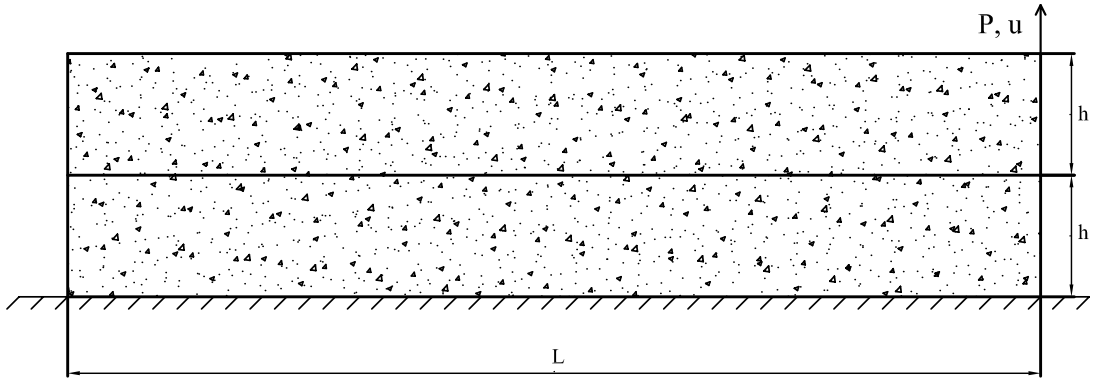


Figure 11. Pull test. The load P is applied on the right and produces displacement u .

L (mm)	400	\hat{k}_s^{\parallel} (MPa · mm ⁻¹)	$2. \times 10^2$
h (mm)	50	\hat{k}_s^{\perp} (MPa · mm ⁻¹)	$5. \times 10^2$
E^{up} (MPa)	40000	c_s (MPa · mm · s)	7.2×10^{-3}
E^{dw} (MPa)	35000	k_s (MPa · mm ²)	0.1
ν	0.2	w_s^{strong} (MPa · mm)	10.3×10^{-3}
c (MPa · s)	2×10^{-3}	w_s^{weak} (MPa · mm)	5.15×10^{-3}
k (mm)	0.3	$k_{s,1}$ (MPa · mm)	0.1
w^{up} (MPa)	2×10^{-3}	$k_{s,2}$ (MPa · mm)	0.1
w^{dw} (MPa)	2×10^{-5}	d (mm)	5
		$k_{s,1,2}$ (MPa/mm)	10

Table 2. Left: Geometrical, mechanical parameters of the two concrete pieces in Figure 11. Right: Glue parameters for the two pull tests in the same.

all because $\vec{u}_1 - \vec{u}_2 \cong 0$. Horizontal displacement fields are shown in Figure 10 for different values of applied vertical displacement $\bar{u} = 0.03, 0.045, 0.06$ mm. The discontinuity of the displacement clearly shows the fracture propagation in the middle of the specimen.

7.2. Pull test. A vertical force is applied to the free right corner of the upper piece of concrete, Figure 11. The relative stiffness of the concrete and of the glue governs the behavior of the structure. The geometrical and mechanical properties of the specimens of two tests are reported in Table 2. If the glue is strong and the concrete is weak, damage occurs in concrete just under the contact surface (Figure 12), in full agreement with experimental results [Theillout 1983]. On the other hand, if the glue is weak and the concrete is solid, separation of the two pieces occurs on the contact surface and the concrete is not damaged (Figure 13). Interface damage evolution is reported in Figure 14. Observe that even if the global structural response for the two simulations is very similar (see Figure 15) the failure mechanisms are completely different.

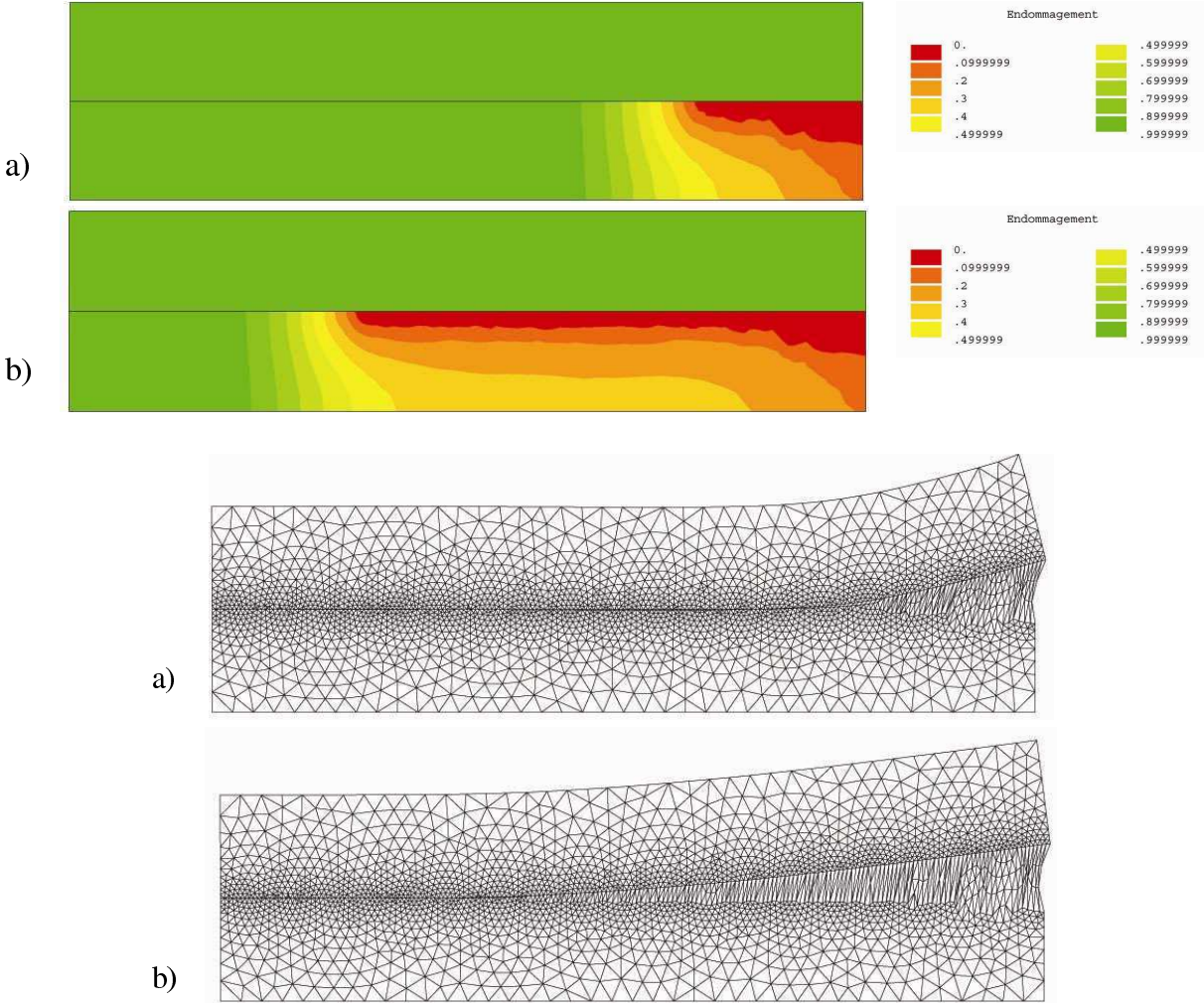


Figure 12. Delamination with strong glue. Top: Damage field at displacement (a) $u = 0.0625$ mm, and (b) $u = 0.3$ mm. A thin damaged zone appears under the interface. Bottom: Deformed configurations at displacement (a) $u = 0.0625$ mm and (b) $u = 0.3$ mm. The concrete breaks just under the contact surface while the glue remains intact. In this simulation no damage appears in the interface, so $\beta_s = 1$.

7.3. FRP-concrete delamination test. External bonding of fiber-reinforced polymer (FRP) plates or sheets has recently emerged as a popular method for strengthening reinforced concrete (RC structures). The behavior of such FRP-strengthened RC structures is often controlled by the behavior of the interface between FRP and concrete, which is commonly studied through a pull test in which an FRP sheet or plate is bonded to a concrete prism and is subjected to tension. Figure 16 shows a typical configuration for a pull-pull delamination test, [Point and Sacco 1996]. Left and bottom sides of the specimen have been fixed in order to have no displacements in the direction normal to the surface and free displacements

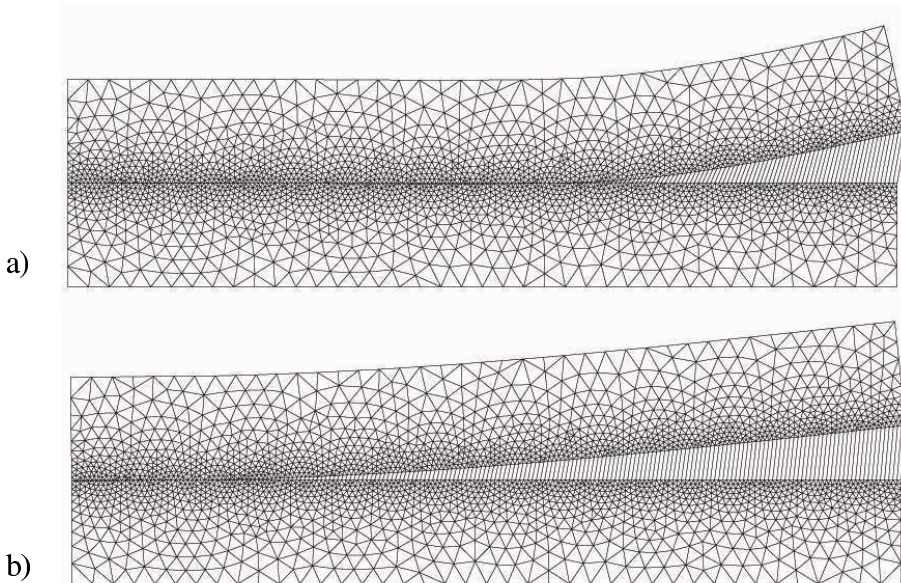


Figure 13. Delamination with weak glue. Top: Deformed configurations at displacement (a) $u = 0.0625$ mm and (b) $u = 0.3$ mm. The glue breaks progressively and there is almost no damage within the concrete. The straight lines connecting the two pieces of concrete represent the gap. $\vec{u}_2 - \vec{u}_1$.

tangent to it. Existing studies reported in [Yao et al. 2005] suggest that the main failure mode of FRP-to-concrete bonded joints in pull tests is concrete failure under shear which occurs generally at a few millimeters from the adhesive layer as shown in Figure 17 (see [Ferracuti et al. 2006]).

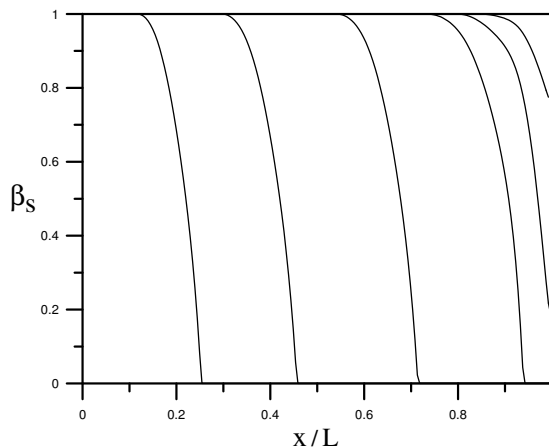


Figure 14. Delamination with weak glue. Damage interface evolution of the glue. The damage field $\beta_s(x/l, t)$ is plotted at different times t .

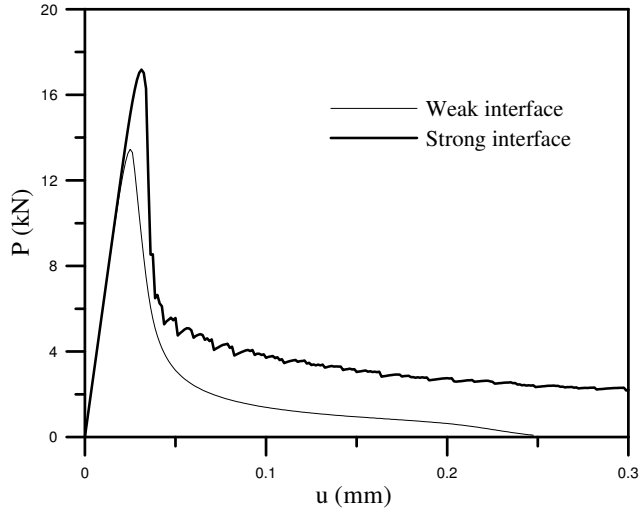


Figure 15. Pull test. Load versus displacement curves obtained for different stiffness values. It is important to observe that even if the global structural response for the two simulations is very similar, the failure mechanisms are completely different, as outlined from the previous Figures 12, 13, and 14.

The geometrical and mechanical properties of the specimens are reported in Table 3. The numerical simulation (Figures 18 and 19) clearly shows a thin damaged zone in the concrete as well as large displacements. The damaged zone corresponds to a small layer of concrete which remains glued on the FRP in the experiments.

L (mm)	100
d (mm)	100
h (mm)	50
E (MPa)	33640
ν	0.2
c (MPa · s)	2×10^{-3}
k (mm)	0.2
w (MPa)	4×10^{-5}

t (mm)	1.016
E (MPa)	230000
ν	0.3
c (MPa · s)	2×10^{-3}
k (mm)	0.1
w (MPa)	2×10^{-2}

\hat{k}_s^{\parallel} (MPa · mm ⁻¹)	$5. \times 10^2$
\hat{k}_s^{\perp} (MPa · mm ⁻¹)	$1. \times 10^3$
c_s (MPa · mm · s)	7.2×10^{-2}
k_s (MPa · mm ²)	0.1
w_s (MPa · mm)	10.3×10^{-4}
$k_{s,1}$ (MPa · mm)	0.1
$k_{s,2}$ (MPa · mm)	0.2
d (mm)	5
$k_{s,1,2}$ (MPa/mm)	20

Table 3. Geometrical, mechanical parameters of the concrete for the pull-pull test (left), the FRP (middle), and the FRP-concrete pull-pull test (right).

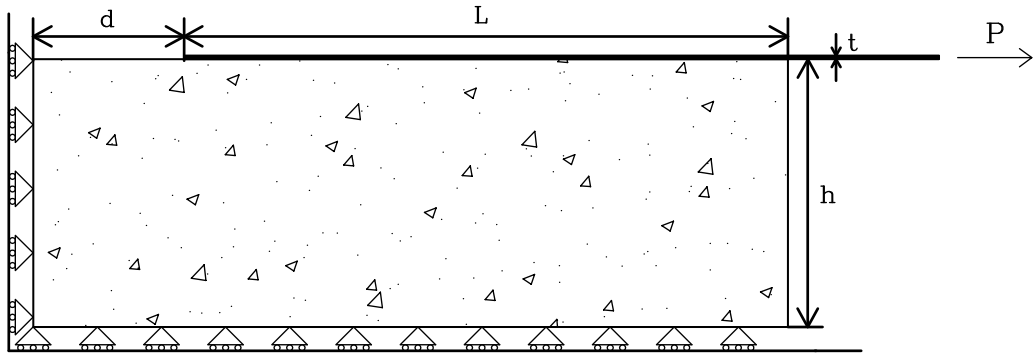


Figure 16. FRP-concrete pull-pull delamination test [Freddi and Savoia 2006].



Figure 17. FRP-concrete pull-pull delamination test: experimental failure mode [Yao et al. 2005].

8. Conclusions

The predictive model which has been derived with the continuum mechanics theory involves only macroscopic quantities. The few parameters of the model can be measured with sample and structure experiments. The numerous results concerning different structures and experiments show the ability of the model to deal with engineering problems and predict failure modes. As outlined in the examples, once the damage is diffused and very low load bearing capacity remains, large displacement values may

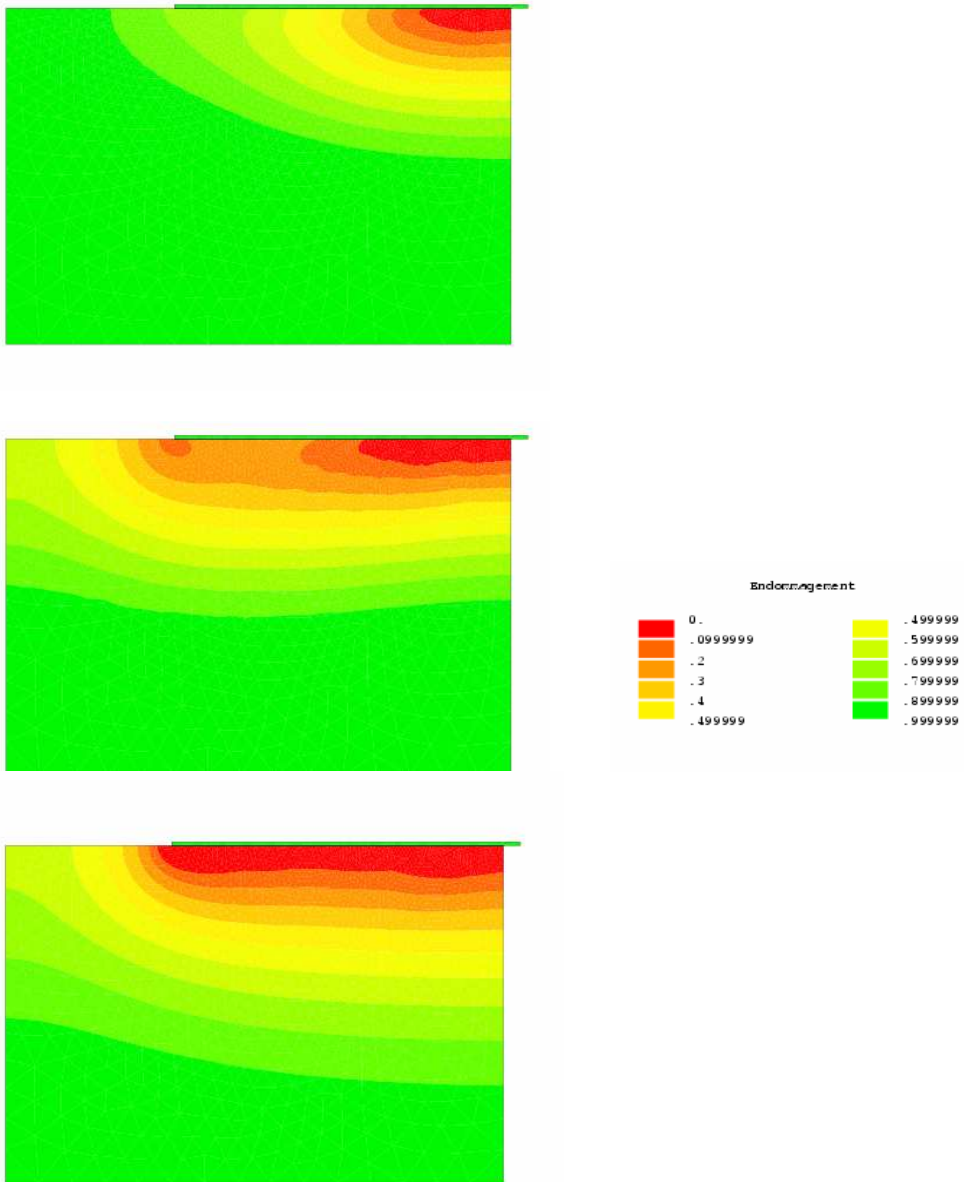


Figure 18. FRP-concrete pull-pull delamination test. Damage evolution. A thin zone is damaged under the reinforcement.

appear such that the hypothesis of small deformations may no longer be sufficient to describe the failure phenomena completely [Nedjar 2002]. In this case, large deformation theory should be considered.

Finally, this model is applicable to the design of concrete structures as well as other composite structures.

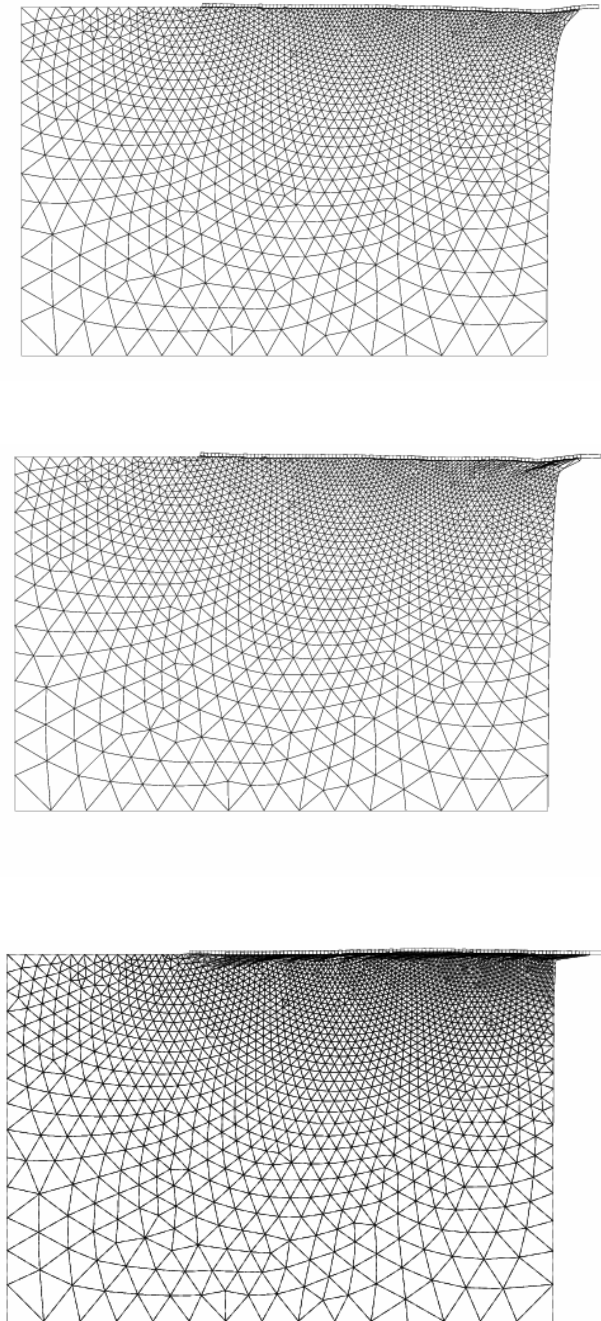


Figure 19. FRP-concrete pull-pull delamination test. Deformed configurations. The thin damaged zone under the reinforcement results in large deformation. The displacement scale is different in each deformed mesh.

References

- [Aimi et al. 2007] A. Aimi, M. Diligenti, and F. Freddi, “Numerical aspects in the SGBEM solution of softening cohesive interface problems”, *J. Comput. Appl. Math.* (2007). In press.
- [Alfano and Crisfield 2001] G. Alfano and M. Crisfield, “Finite element interface models for the delamination analysis of laminated composites: Mechanical and computational issues”, *Int. J. Numer. Methods Eng.* **50**:7 (2001), 1701–1736.
- [Bonetti and Schimperna 2004] E. Bonetti and G. Schimperna, “Local existence to Frémond’s model for damaging in elastic materials”, *Continuum Mech. Therm.* **16** (2004), 319–335.
- [Bonetti et al. 2005] E. Bonetti, G. Bonfanti, and R. Rossi, “Global existence for a contact problem with adhesion”, Preprint 16, Università di Brescia, Italy, 2005, Available at <http://www.dmf.unicatt.it/cgi-bin/preprintserv/semmat/Quad2005n16.pdf>.
- [Bonetti et al. 2006] E. Bonetti, F. Freddi, and M. Frémond, “Coupled volume and surface damage: An existence theory”, 2006. Preprint.
- [Borino and Failla 2005] G. Borino and B. Failla, “An elastic interface model with nonlocal integral damaging effects”, in *Atti del XVII Congresso dell’Associazione Italiana di Meccanica Teorica e Applicata* (Florence), September 2005. Available on CD.
- [Bruneaux 2004] M. A. Bruneaux, *Durabilité des assemblages collés: Développement d’un modèle mécanique prédictif avec prise en compte des caractéristiques physico-chimiques de l’adhésif*, Ph.D. thesis, Ecole National des Ponts et Chaussées, Paris, and University Tor Vergata, Rome, 2004.
- [Chau et al. 2004] O. Chau, M. Shillor, and M. Sofonea, “Dynamic frictionless contact with adhesion”, *Z. Angew. Math. Phys.* **55**:1 (2004), 32–47.
- [Ferracuti et al. 2006] B. Ferracuti, M. Savoia, and C. Mazzotti, “A numerical model for FRP-concrete delamination”, *Compos. B Eng.* **37**:4–5 (2006), 356–364.
- [Freddi and Frémond 2005] F. Freddi and M. Frémond, “A damage model for domains and interfaces problem”, in *Atti del XVII Congresso dell’Associazione Italiana di Meccanica Teorica e Applicata* (Florence), September 2005. Available on CD.
- [Freddi and Savoia 2006] F. Freddi and M. Savoia, “Analysis of FRP-concrete delamination via boundary integral equations”, *Eng. Fract. Mech.* (2006). In press.
- [Frémond 2001] M. Frémond, *Non-smooth thermomechanics*, Springer, Heidelberg, 2001.
- [Frémond and Nedjar 1996] M. Frémond and B. Nedjar, “Damage, gradient of damage and principle of virtual power”, *Int. J. Solids Struct.* **33**:8 (1996), 1083–1103.
- [Frémond et al. 1998] M. Frémond, K. L. Klutter, B. Nedjar, and M. Shillor, “One-dimensional damage model”, *Adv. Math. Sci. Appl.* **8**:2 (1998), 541–570.
- [Gonzalez et al. 2005] D. Gonzalez, K. Benzarti, L. Gonon, and H. De Baynast, “Durability of the concrete epoxy/adhesive bond: Micro- and macro-scale investigations”, pp. 413–420 in *Third International Conference on Composites in Construction* (Lyon), edited by P. Hamelin et al., July 2005.
- [Humbert et al. 2005] P. Humbert, G. Fezans, A. Dubouchet, and D. Remaud, “CESAR-LCPC, un progiciel de calcul dédié au génie civil”, *Bull. Lab. Ponts Chaussées* **256–257** (2005), 7–37.
- [Ireman 2005] B. Ireman, “Algorithm for gradient damage models based on semi-smooth Newton method”, *Comput. Methods Appl. Mech. Eng.* **194**:6–8 (2005), 727–741.
- [Lemaitre 1992] J. Lemaitre, *A course on damage mechanics*, Springer, Berlin, 1992.
- [Lemaitre and Desmorat 2005] J. Lemaitre and R. Desmorat, *Engineering damage mechanics: Ductile, creep, fatigue and brittle failures*, Springer, Berlin, 2005.
- [Moreau 1966] J. J. Moreau, “Fonctionnelles convexes: Séminaire sur les équations aux dérivées partielles”, Lecture notes, Collège de France, Paris, 1966. Reprinted Istituto Poligrafico e Zecca dello Stato, University Tor Vergata, Rome 2003.
- [Mosconi 2006] M. Mosconi, “Uniqueness and minimum theorems for a multifield model of brittle solids”, *Int. J. Solids Struct.* **43**:11–12 (2006), 3428–3443.
- [Nedjar 2001] B. Nedjar, “Elastoplastic-damage modelling including the gradient of damage: Formulation and computational aspects”, *Int. J. Solids Struct.* **38**:30–31 (2001), 5421–5451.

- [Nedjar 2002] B. Nedjar, “A theoretical and computational setting for a geometrically nonlinear gradient damage modelling framework”, *Comput. Mech* **30**:1 (2002), 65–80.
- [Point and Sacco 1996] N. Point and E. Sacco, “A delamination model for laminated composites”, *Int. J. Solids Struct.* **33**:4 (1996), 483–509.
- [Raous and Monerie 2002] M. Raous and Y. Monerie, “Unilateral contact, friction and adhesion: 3D cracks in composite materials”, pp. 333–343 in *Contact Mechanics: Proceedings of the Third Contact Mechanics International* (Peniche), Kluwer, 2002.
- [Raous et al. 1999] M. Raous, L. Cangémi, and M. Cocu, “A consistent model coupling adhesion, friction, and unilateral contact”, *Comput. Methods Appl. Mech. Eng.* **177**:3–4 (1999), 383–399.
- [Stumpf and Hackl 2003] H. Stumpf and K. Hackl, “Micromechanical concept for the analysis of damage evolution in thermo-viscoelastic and quasi-brittle materials”, *Int. J. Solids Struct.* **40**:6 (2003), 1567–1584.
- [Thaveau 2005] M. P. Thaveau, “Flexion quatre points de prismes en béton collés”, 2005. Laboratoires des Ponts et Chaussées, Internal report.
- [Theillout 1983] J. N. Theillout, *Renforcement et réparation des ouvrages d’art par la technique des tôles collées*, Ph.D. thesis, Ecole National des Ponts et Chaussées, Paris, 1983.
- [Truong Dinh Tien 1990] J. M. Truong Dinh Tien, *Contact avec adhérence*, Ph.D. thesis, Université Pierre et Marie Curie, Paris, 1990.
- [Voyaiadjis et al. 1998] G. Z. Voyaiadjis, J. J. W. Woody, and J. L. Chaboche, *Damage mechanics in engineering materials*, Elsevier, 1998.
- [Yao et al. 2005] J. Yao, J. G. Teng, and J. F. Chen, “Experimental study on FRP-to-concrete bonded joints”, *Compos. B Eng.* **36**:2 (2005), 99–113.
- [Zou et al. 2003] Z. Zou, S. Reid, and S. Li, “A continuum damage model for delamination in laminated composites”, *J. Mech. Phys. Solids* **51**:2 (2003), 333–356.

Received 6 Feb 2006. Revised 20 Apr 2006. Accepted 6 Jun 2006.

FRANCESCO FREDDI: francesco.freddi@unipr.it

Department of Civil Engineering & Architecture, University of Parma, Viale Usberti 181/A, 43100 Parma, Italy

MICHEL FRÉMOND: fremond@cmla.ens-cachan.fr

Laboratoire Lagrange, Laboratoire Central des Ponts et Chaussées - LCPC, 58 Boulevard Lefebvre, 75732 Paris Cedex 15, France

ELASTIC FLEXURAL-TORSIONAL BUCKLING OF CIRCULAR ARCHES UNDER UNIFORM COMPRESSION AND EFFECTS OF LOAD HEIGHT

MARK ANDREW BRADFORD AND YONG-LIN PI

A circular arch with in-plane radial loads uniformly distributed around the arch axis is primarily subjected to uniform compression. Under this action, the arch may suddenly deflect laterally and twist out of the plane of loading and fail in a flexural-torsional buckling mode. In most studies of the elastic flexural-torsional buckling of arches under uniform compression, the directions of the uniformly distributed loads are assumed to be unchanged and parallel to their initial directions during buckling. In practice, arches may be subjected to hydrostatic or to uniformly distributed directed radial loads. Hydrostatic loads always remain normal to the tangent of the deformed arch axis, while uniformly distributed directed radial loads always remain directed toward a specific point during buckling. These uniform radial loads may act at a load height, such as at the top surface of the cross-section. In this case, the radial loads produce an additional torsional moment during buckling which affects the flexural-torsional buckling of the arch. This paper uses both virtual work and static equilibrium approaches to study the elastic flexural-torsional buckling, effects of the load height on the buckling of circular arches under uniform compression (that is, produced by uniformly distributed dead or by directed radial loads), and closed form solutions for the buckling loads are developed.

1. Introduction

An arch with in-plane radial loads q at a load height y_q , uniformly distributed around the axis of a circular arch, is primarily subjected to a uniform compression force $Q = q(R - y_q)$, as shown in [Figure 1a](#), where R is the radius of the initial curvature of the arch and Θ is the included angle of the arch. Under this action, the arch may suddenly deflect laterally and twist out of its plane of loading and fail in a flexural-torsional buckling mode ([Figure 1b](#)). The elastic flexural-torsional buckling of arches under uniform compression has been studied by a number of researchers. The static equilibrium approach was used by Vlasov [1961], while an energy approach was used by other researchers [Timoshenko and Gere 1961; Yoo 1982; Papangelis and Trahair 1987; Yang and Kuo 1987; Rajasekaran and Padmanabhan 1989; Kang and Yoo 1994; Bradford and Pi 2002]. With the exception of [Vlasov 1961], these studies conventionally assumed that the directions of the uniformly distributed radial loads do not change and remain parallel to their initial directions during buckling ([Figure 1b \(i\)](#)); this load case is called *radial dead loads* in this study for convenience. In addition to the radial dead loads, the uniform compression in a circular arch may also be assumed to be produced by hydrostatic or uniformly distributed directed radial loads, for example in the case of submerged arches. In the case of hydrostatic loads ([Figure 1b \(ii\)](#)), the loads always remain

This work has been supported by a Federation Fellowship, an Australian Professorial Fellowship, and a Discovery Project awarded to the first author by the Australian Research Council.

Keywords: buckling, circular arch, directed radial loads, flexural-torsional, hydrostatic loads, effect of load height, uniform compression.

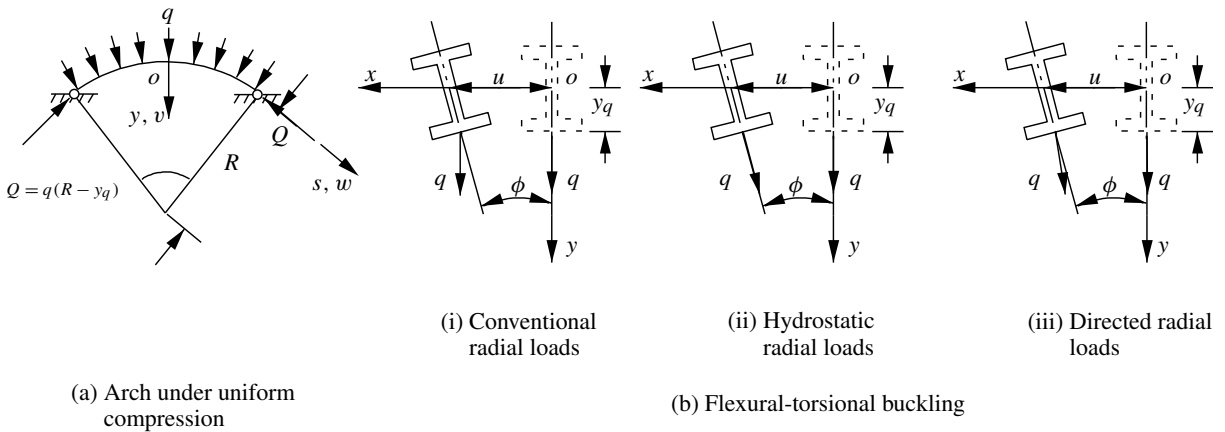


Figure 1. Flexural-torsional buckling of arches under uniform compression.

normal to the tangent of the deformed arch axis during buckling. As proved by Bolotin [1963], when both normal and tangential displacements at the boundaries vanish, hydrostatic loads are conservative because they have potentials. Hence, hydrostatic loads acting on pin-ended or fixed arches, whose radial and axial displacements vanish, are conservative. Timoshenko and Gere [1961] analyzed the in-plane buckling of circular ring and arches under the hydrostatic loads, while Vlasov [1961] studied the flexural-torsional buckling of circular arches under the hydrostatic loads. It is worth pointing out that Vlasov's result has been referenced by a number of researchers as being the result for uniformly distributed radial dead loads [Yoo 1982; Papangelis and Trahair 1987; Yang and Kuo 1987; Rajasekaran and Padmanabhan 1989; Kang and Yoo 1994; Bradford and Pi 2002]. In the case of uniformly distributed directed radial loads (Figure 1b (iii)), the loads are always directed to a specific point, such as the center of the initial curvature of the arch during buckling. A load directed to a certain point during deformation has also been proved to be conservative [Timoshenko and Gere 1961; Simites 1976; Ings and Trahair 1987] because it also has a potential. Ings and Trahair [1987] investigated the stability of beams and columns under directed loading. Simites [1976] and Simites and Hodges [2006] studied the in-plane buckling of arches that are subjected to uniformly distributed radial dead loads, uniformly distributed loads always directed to the arch curvature center, and to hydrostatic loads. Simites and Hodges [2006] also studied the flexural-torsional buckling for end-loaded cases. Timoshenko and Gere [1961] investigated the flexural-torsional buckling of arches with a narrow rectangular cross-section under the radial loads directed to the center of the initial curvature of the arch. In the buckled configuration, hydrostatic loads and uniformly distributed loads that are directed to the initial arch curvature center have lateral components in the opposite direction to that of the lateral buckling displacements. These lateral components increase the resistance of the arch to flexural-torsional buckling, and thus their effects on the flexural-torsional buckling of the arch have to be considered in the buckling analysis. The uniform radial loads that produce uniform axial compression in an arch do not necessarily act at the centroid, and they may act at a load height such as at the top surface of the cross-section. In this case, the radial loads produce an additional torsional moment during buckling which affects the flexural-torsional buckling behavior of the arch, and so the effects of the load height on the flexural-torsional buckling of arches under uniform compression warrant investigation.

Trahair and Papangelis [1987] and Trahair [1993] investigated effects of the load height on the flexural-torsional buckling of arches under uniform compression produced by uniformly distributed radial dead loads. However, comprehensive studies of the elastic flexural-torsional buckling of arches under uniform compression produced by dead or directed uniformly distributed radial loads or by hydrostatic loads, and of the effects of the load height on the flexural-torsional buckling, do not appear to have been reported.

The purpose of this paper is to use both virtual work and static equilibrium approaches to study the elastic flexural-torsional buckling and the effects of the load height on the buckling of circular arches under uniform compression produced by dead, or directed uniformly distributed radial loads, or by hydrostatic loads, and to derive the buckling loads in closed form. The principle of virtual work will lead to the equilibrium equations in weak form, while the static equilibrium approach will lead to the differential equilibrium equations directly.

2. Curvatures and strains

2.1. Rotations and curvatures. The basic assumptions used in this investigation are:

- (1) Euler–Bernoulli bending theory and Vlasov’s torsion theory are used, so the cross-sections are assumed to remain rigid in their plane (that is, not to distort during deformation), and local buckling and/or effects of distortion of the cross-section are excluded;
- (2) the arches are circular and of doubly symmetric uniform cross-section, so the centroid of the cross-section coincides with its shear center;
- (3) the height D of the cross-section is much smaller than both the length S and the radius R of the initial curvature of the arch, that is, $D/S \ll 1$ and $D/R \ll 1$.

A body-attached curvilinear orthogonal axis system $oxys$ is defined as follows. The axis os passes through the locus of the centroids of the cross-section of the undeformed arch, and the axes ox and oy coincide with the principal axes of the cross-section, as shown in Figures 1 and 2. In the undeformed configuration, the axis oy is toward the center of the arch. After the deformation, the origin o displaces laterally u , radially v , and axially w to o_1 and the cross-section rotates through an angle ϕ , and so the body-attached curvilinear orthogonal axis system $oxys$ moves and rotates to a new position $o_1x_1y_1s_1$, as shown in Figures 2 and 3. In the axis system $oxys$, the initial curvature κ_{x0} of the centroidal axis os of a circular arch about the major principal axis ox is defined as positive (that is, in the direction of the minor principal axis oy of the cross-section), and so $\kappa_{x0} = -1/R$ for arches with the upward rise as shown in Figure 1. This definition for the initial curvature is consistent with the definition of the curvature after deformation.

A unit vector \mathbf{p}_s in the tangent direction of the axis os , and unit vectors \mathbf{p}_x and \mathbf{p}_y in the direction of the axes ox and oy (Figures 2 and 3) are used as the fixed reference basis. They do not change with the deformation, but their directions change from point to point along the arch axis os . In the deformed configuration, a unit vector \mathbf{q}_s is defined in the tangent direction of the axis o_1s_1 of the axis system $o_1x_1y_1s_1$, and unit vectors \mathbf{q}_x and \mathbf{q}_y are defined in the principal axes o_1x_1 , o_1y_1 of the rotated cross-section at o_1 , as shown in Figure 2. The unit vectors \mathbf{q}_x , \mathbf{q}_y , \mathbf{q}_s are attached to the arch and move with it during the deformation with the vector \mathbf{q}_s , being normal to the cross-section at all times.

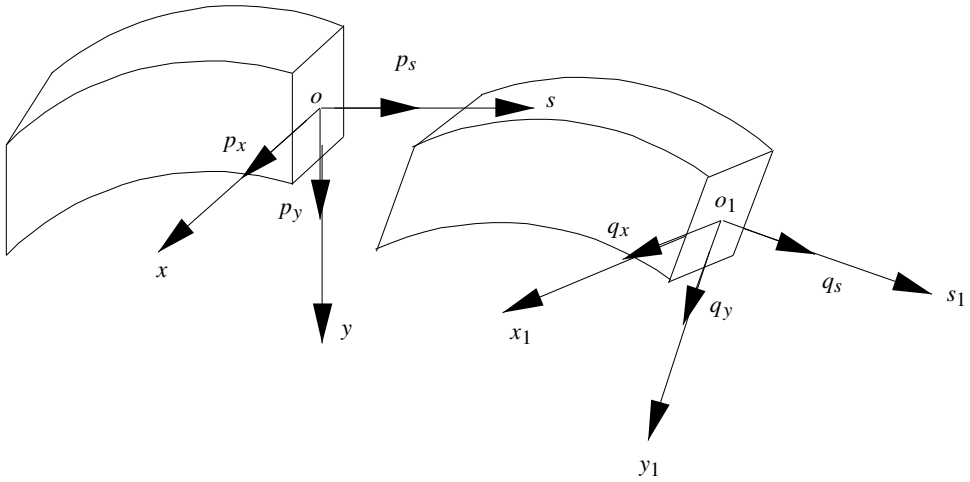


Figure 2. Kinematics during buckling.

The rotation from the basis vectors $\mathbf{p}_x, \mathbf{p}_y, \mathbf{p}_s$ in the undeformed configuration to the basis vectors $\mathbf{q}_x, \mathbf{q}_y, \mathbf{q}_s$ in the deformed configuration (Figures 2 and 3) can be expressed [Pi and Bradford 2004] using a rotation matrix \mathbf{R} as

$$\begin{bmatrix} \mathbf{q}_x \\ \mathbf{q}_y \\ \mathbf{q}_s \end{bmatrix} = \begin{bmatrix} R_{xx} & R_{xy} & R_{xs} \\ R_{yx} & R_{yy} & R_{ys} \\ R_{sx} & R_{sy} & R_{ss} \end{bmatrix} \begin{bmatrix} \mathbf{p}_x \\ \mathbf{p}_y \\ \mathbf{p}_s \end{bmatrix}, \tag{1}$$

where

$$\begin{aligned} R_{xx} &= (1 - \lambda \hat{u}'^2)C - \lambda \hat{u}' \hat{v}' S, & R_{xy} &= -(1 - \lambda \hat{u}'^2)S - \lambda \hat{u}' \hat{v}' C, & R_{xs} &= \hat{u}', \\ R_{yx} &= (1 - \lambda \hat{v}'^2)S - \lambda \hat{u}' \hat{v}' C, & R_{yy} &= (1 - \lambda \hat{v}'^2)C + \lambda \hat{u}' \hat{v}' S, & R_{ys} &= \hat{v}', \\ R_{sx} &= -\hat{u}' C - \hat{v}' S, & R_{sy} &= \hat{u}' S - \hat{v}' C, & R_{ss} &= \hat{w}', \end{aligned}$$

in which $C \equiv \cos \phi$, $S \equiv \sin \phi$, $\hat{u}' = u'/(1 + \epsilon)$, $\hat{v}' = \tilde{v}'/(1 + \epsilon)$, $\hat{w}' = (1 + \tilde{w}')/(1 + \epsilon)$, $\tilde{v}' = v' - w\kappa_{x0}$, $\tilde{w}' = w' + v\kappa_{x0}$, $(\cdot)' \equiv d(\cdot)/ds$, $(1 + \epsilon) = \sqrt{(u')^2 + (\tilde{v}')^2 + (1 + \tilde{w}')^2}$, $\lambda = 1/(1 + \hat{w}')$.

The rotation matrix \mathbf{R} in Equation (1) belongs to a special orthogonal rotation group denoted $SO(3)$ because it satisfies the orthogonality and unimodular conditions that $\mathbf{R}\mathbf{R}^T = \mathbf{R}^T\mathbf{R} = \mathbf{I}$ and $\det \mathbf{R} = +1$ [Burn 1985].

It can be shown [Pi and Bradford 2004] that the material curvatures in the deformed configuration can be obtained from the rotation matrix \mathbf{R} as

$$(1 + \epsilon)\mathbf{K} = \mathbf{R}^T \frac{d\mathbf{R}}{ds} + \mathbf{R}^T \mathbf{K}_0 \mathbf{R}, \tag{2}$$

where

$$\mathbf{K}_0 = \begin{bmatrix} 0 & 0 & 0 \\ 0 & 0 & -\kappa_{x0} \\ 0 & \kappa_{x0} & 0 \end{bmatrix} = \frac{1}{R} \begin{bmatrix} 0 & 0 & 0 \\ 0 & 0 & 1 \\ 0 & -1 & 0 \end{bmatrix} \quad \text{and} \quad \mathbf{K} = \begin{bmatrix} 0 & -\kappa_s & \kappa_y \\ \kappa_s & 0 & -\kappa_x \\ -\kappa_y & \kappa_x & 0 \end{bmatrix}, \quad (3)$$

in which κ_x and κ_y are the material curvatures about the unit vectors \mathbf{q}_x and \mathbf{q}_y , that is, about the positive direction of the axes o_1x_1 and o_1y_1 , and κ_s is the material twist per unit length about the unit vector \mathbf{q}_s , that is, about the positive direction of the o_1s_1 axis in the deformed configuration.

Substituting Equation (1) and the first equation of Equation (3) into Equation (2) leads to the curvatures κ_x and κ_y and the twist κ_s , expressed explicitly as

$$\begin{aligned} \kappa_x &= \{ \hat{u}''S - \hat{v}''C - \lambda\hat{w}''(\hat{u}'S - \hat{v}'C) + [\lambda(1 - \hat{u}'^2 - \hat{w}'^2)C - \lambda\hat{u}'\hat{v}'S + \hat{w}'C] \kappa_{x0} \} (1 + \epsilon)^{-1}, \\ \kappa_y &= \{ \hat{u}''C + \hat{v}''S - \lambda\hat{w}''(\hat{u}'C + \hat{v}'S) - [\lambda(1 - \hat{u}'^2 - \hat{w}'^2)S + \lambda\hat{u}'\hat{v}'C + \hat{w}'S] \kappa_{x0} \} (1 + \epsilon)^{-1}, \\ \kappa_s &= [\phi' + \lambda(\hat{u}''\hat{v}' - \hat{u}'\hat{v}'') + \hat{u}'\kappa_{x0}] (1 + \epsilon)^{-1}. \end{aligned}$$

2.2. Strains and displacements of load points. The position vector \mathbf{a}_0 of an arbitrary point $P(x, y)$ on the cross-section in the undeformed configuration can be expressed as $\mathbf{a}_0 = \mathbf{r}_0 + x\mathbf{p}_x + y\mathbf{p}_y$ (see Figure 3), where \mathbf{r}_0 is the position vector of the centroid o , related to the unit vector \mathbf{p}_s by $\mathbf{p}_s = d\mathbf{r}_0/ds$, and the

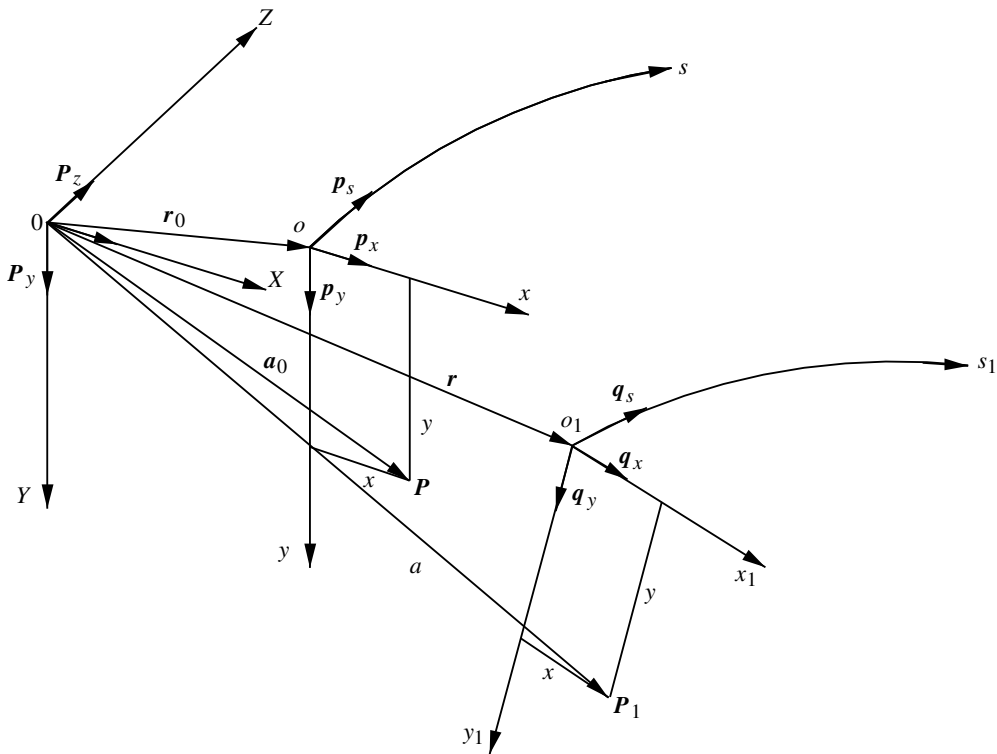


Figure 3. Position vectors.

initial gradient tensor \mathbf{F}_0 in the undeformed configuration can be expressed as

$$\mathbf{F}_0 = \left(\frac{\partial \mathbf{a}_0}{\partial x}, \frac{\partial \mathbf{a}_0}{\partial y}, \frac{\partial \mathbf{a}_0}{\partial s} \right). \quad (4)$$

The position of the point $P(x, y)$ in the deformed configuration is determined based on the assumption that the total displacement of a point P results from two successive motions: translation and rotation of the cross-section, and a superimposed warping displacement along the unit vector \mathbf{q}_s in the deformed configuration. The position vector \mathbf{a} of the point P in the deformed configuration can be expressed as $\mathbf{a} = \mathbf{r} + x\mathbf{q}_x + y\mathbf{q}_y - \omega(x, y)\kappa_s\mathbf{q}_s$ (see Figure 3), in which $\omega(x, y)$ is the warping function and \mathbf{r} is the position vector of the centroid o_1 in the deformed configuration and is given by $\mathbf{r} = \mathbf{r}_0 + u\mathbf{p}_x + v\mathbf{p}_y + w\mathbf{p}_s$.

The deformation gradient tensor \mathbf{F} can then be expressed as

$$\mathbf{F} = \left(\frac{\partial \mathbf{a}}{\partial x}, \frac{\partial \mathbf{a}}{\partial y}, \frac{\partial \mathbf{a}}{\partial s} \right) = \left(\frac{\partial \mathbf{a}}{\partial x}, \frac{\partial \mathbf{a}}{\partial y}, (1 + \epsilon) \frac{\partial \mathbf{a}}{\partial s_1} \right), \quad (5)$$

and so the strain tensor can be expressed in terms of the initial and deformation gradient tensors as

$$\begin{bmatrix} \epsilon_{xx} & \frac{1}{2}\gamma_{xy} & \frac{1}{2}\gamma_{xs} \\ \frac{1}{2}\gamma_{yx} & \epsilon_{yy} & \frac{1}{2}\gamma_{ys} \\ \frac{1}{2}\gamma_{sx} & \frac{1}{2}\gamma_{sy} & \epsilon_{ss} \end{bmatrix} = \frac{1}{2}(\mathbf{F}^T \mathbf{F} - \mathbf{F}_0^T \mathbf{F}_0). \quad (6)$$

Substituting Equations (4) and (5) into Equation (6) yields

$$\epsilon_{xx} = \epsilon_{yy} = \gamma_{xy} = 0, \quad (7)$$

$$\begin{aligned} \epsilon_{ss} = & \tilde{w}' + \frac{1}{2}u'^2 + \frac{1}{2}\tilde{v}'^2 - x\kappa_y + y\kappa_x - \omega\kappa_s' + \frac{1}{2}(x^2 + y^2)\kappa_s^2 = \tilde{w}' + \frac{1}{2}u'^2 + \frac{1}{2}\tilde{v}'^2 \\ & - x(u'' \cos \phi + \tilde{v}'' \sin \phi - \kappa_{x0} \sin \phi) + y(u'' \sin \phi - \tilde{v}'' \cos \phi + (\cos \phi - 1 - \frac{1}{2}u'^2)\kappa_{x0}) \\ & - \omega(\phi'' + u''\kappa_{x0}) + \frac{1}{2}(x^2 + y^2)(\phi' + u'\kappa_{x0})^2, \end{aligned} \quad (8)$$

$$\gamma_{sx} = -\left(y + \frac{\partial \omega}{\partial x}\right)\kappa_s = -\left(y + \frac{\partial \omega}{\partial x}\right)(\phi' + u'\kappa_{x0}), \quad (9)$$

$$\gamma_{sy} = \left(x - \frac{\partial \omega}{\partial y}\right)\kappa_s = \left(x - \frac{\partial \omega}{\partial y}\right)(\phi' + u'\kappa_{x0}), \quad (10)$$

where ϵ_{ss} is the longitudinal normal strain and γ_{sx} and γ_{sy} are the uniform torsional shear strains at an arbitrary point $P(x, y)$ on the cross-section.

It is assumed that the uniform radial loads q are acting at a load position $(0, y_q)$, where y_q is the radial coordinate of the point of application load q . The displacements of the load point at the position $(0, y_q)$ are given by

$$\begin{bmatrix} u_q \\ v_q \\ w_q \end{bmatrix} = \begin{bmatrix} u \\ v \\ w \end{bmatrix} + \mathbf{R} \begin{bmatrix} 0 \\ y_q \\ 0 \end{bmatrix} - \begin{bmatrix} 0 \\ -y_q \\ 0 \end{bmatrix} \approx \begin{bmatrix} u - y_q(\phi - \frac{1}{2}u'\tilde{v}') \\ v - \frac{1}{2}y_q(\phi^2 - \tilde{v}'^2) \\ \tilde{w} + y_q\tilde{v}' \end{bmatrix}, \quad (11)$$

where the third and higher-order terms have been ignored.

3. Virtual work approach

3.1. Virtual work and equilibrium equations. Because all three load cases are conservative, the problem can be treated using energy methods such as the minimum potential energy method or virtual work method [Simitse 1976; Guran 2000; Simitse and Hodges 2006]. The principle of virtual work is used in this paper. When the uniform radial load q acts at a load height y_q , the principle of virtual work for the equilibrium of the arch in the buckled configuration can then be stated as

$$\delta \Pi = \int_V (E \epsilon_{ss} \delta \epsilon_{ss} + G \gamma_{sx} \delta \gamma_{sx} + G \gamma_{sy} \delta \gamma_{sy}) dV - \int_0^S (q_{ex} \delta u_q + q_{ey} \delta v_q) \frac{R - y_q}{R} ds = 0, \quad (12)$$

for all kinematically admissible sets of infinitesimal virtual displacements $\{\delta u, \delta v, \delta w, \delta \phi\}$, where the compatible strains ϵ_{ss} , γ_{sx} and γ_{sy} are given by Equations (8)–(10) and the compatible displacements u_q and v_q of the load point are given by Equation (11), and where V indicates the volume of the arch, E and G are the Young’s and shear moduli of elasticity, q_{ex} and q_{ey} are the lateral and radial components of the uniform load q , as shown in Figure 4, and $\delta(\cdot)$ denotes the Lagrange operator of simultaneous variations.

During flexural-torsional buckling, the in-plane deformations are constant and thus the variations of the in-plane deformations vanish, so that $\delta v = \delta v' = \delta v'' = \delta w = \delta w' = \delta w'' = 0$. By substituting Equations (7)–(11) into Equation (12), and considering that the initial curvature $\kappa_{x0} = -1/R$, that the bending moment $M = 0$ under uniform compression, and that the axial stress resultant $N = \int_A E \epsilon_{ss} dA = -Q = -q(R - y_q)$, the statement for the principle of virtual work given by Equation (12) can be expressed

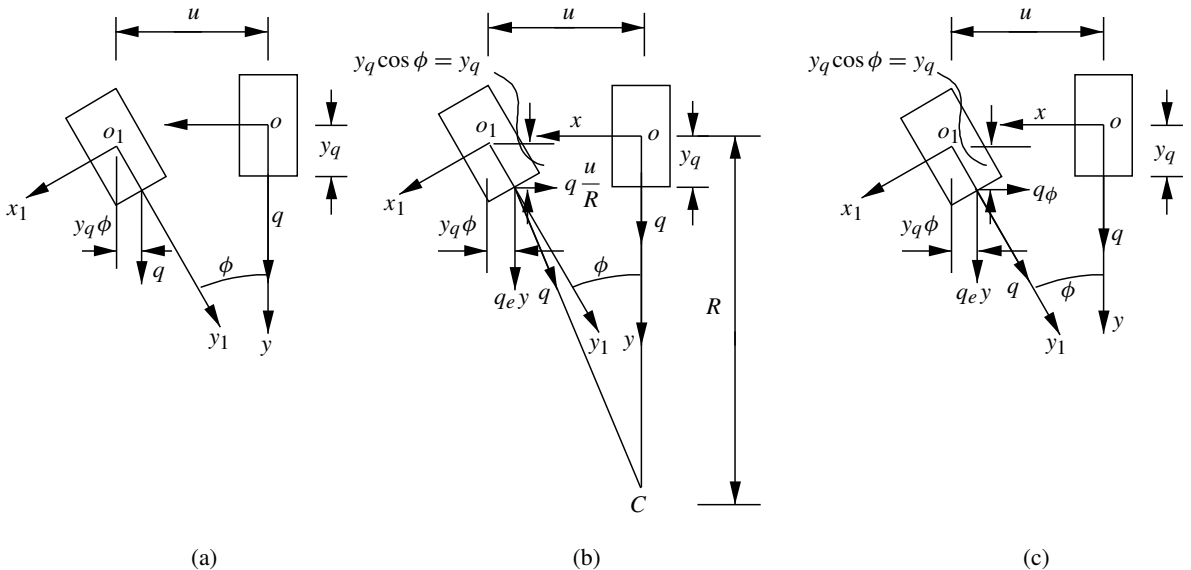


Figure 4. Lateral and radial components of uniform loads. (a) Radial dead loads (load case I); (b) radial loads directed toward arch center (load case II); (c) hydrostatic radial loads (load case III).

as

$$\delta \Pi = \int_0^S \left(EI_y \left(u'' + \frac{\phi}{R} \right) \left(\delta u'' + \frac{\delta \phi}{R} \right) + GJ \left(\phi' - \frac{u'}{R} \right) \left(\delta \phi' - \frac{\delta u'}{R} \right) + EI_w \left(\phi'' - \frac{u''}{R} \right) \left(\delta \phi'' - \frac{\delta u''}{R} \right) - Q \left(u' \delta u' + r_0^2 \left(\phi' - \frac{u'}{R} \right) \left(\delta \phi' - \frac{\delta u'}{R} \right) \right) + (q_{ey}y_q \phi \delta \phi - q_{ex}(\delta u - y_q \delta \phi)) \frac{R - y_q}{R} \right) ds = 0, \quad (13)$$

where I_y is the second moment of area of the cross-section about its minor principal axis, J is the Saint-Venant torsion constant, I_w is the warping constant of the cross-section, and the term

$$\left(-Qr_0^2 \left(\phi' - \frac{u'}{R} \right) \left(\delta \phi' - \frac{\delta u'}{R} \right) \right),$$

represents the virtual work due to Wagner effects [Hodges 2006] with the cross-sectional radius of gyration r_0 being defined by $r_0 = \sqrt{(I_x + I_y)/A}$.

Integrating Equation (13) by parts leads to the differential equilibrium equations for the flexural-torsional buckling

$$\left(EI_y \left(u'' + \frac{\phi}{R} \right) \right)' + \left(GJ \left(\phi' - \frac{u'}{R} \right) \frac{1}{R} \right)' - \left(EI_w \left(\phi'' - \frac{u''}{R} \right) \frac{1}{R} \right)'' + \left(Q \left(u' - r_0^2 \left(\phi' - \frac{u'}{R} \right) \frac{1}{R} \right) \right)' - q_{ex} \frac{R - y_q}{R} = 0, \quad (14)$$

$$EI_y \left(u'' + \frac{\phi}{R} \right) \frac{1}{R} - \left(GJ \left(\phi' - \frac{u'}{R} \right) \right)' + \left(EI_w \left(\phi'' - \frac{u''}{R} \right) \right)'' + \left(r_0^2 Q \left(\phi' - \frac{u'}{R} \right) \right)' + (q_{ey}y_q \phi + q_{ex}y_q) \frac{R - y_q}{R} = 0, \quad (15)$$

and to the static boundary conditions at both ends of the arch ($s = 0$ and $s = S$)

$$\left(\left(EI_y \left(u'' + \frac{\phi}{R} \right) \right)' + \left(GJ \left(\phi' - \frac{u'}{R} \right) \frac{1}{R} \right) - \left(EI_w \left(\phi'' - \frac{u''}{R} \right) \frac{1}{R} \right)' + Qu' - Q \left(\phi' - \frac{u'}{R} \right) \frac{r_0^2}{R} \right) \delta u = 0, \quad (16)$$

$$\left(\left(EI_y \left(u'' + \frac{\phi}{R} \right) \right) - \left(EI_w \left(\phi'' - \frac{u''}{R} \right) \frac{1}{R} \right) \right) \delta u' = 0, \quad (17)$$

$$\left(GJ \left(\phi' - \frac{u'}{R} \right) - \left(EI_w \left(\phi'' - \frac{u''}{R} \right) \right)' - Qr_0^2 \left(\phi' - \frac{u'}{R} \right) \right) \delta \phi = 0, \quad (18)$$

$$EI_w \left(\phi'' - \frac{u''}{R} \right) \delta \phi' = 0. \quad (19)$$

In addition, the kinematic boundary conditions for pin-ended arches, such that

$$u = \phi = 0 \quad \text{at} \quad s = 0 \quad \text{and} \quad s = S, \quad (20)$$

also need to be satisfied. For a laterally pin-ended arch, the buckling deformations $u'' = \phi'' = 0$ at its boundaries and the variations $\delta u = \delta \phi = 0$, so that the static boundary conditions given by Equations (16)–(19) are satisfied.

Three cases of the uniformly distributed loads q are considered. In the case of radial dead loads (load case I), it is assumed that the directions of the loads do not change during buckling and that the loads remain parallel to their initial directions, as shown in Figure 4a. In this case, the loads q have lateral and radial components, q_{ey} and q_{ex} , given by

$$q_{ex} = 0, \quad q_{ey} = q = \frac{Q}{R - y_q}. \quad (21)$$

This case has been studied by a number of researchers [Timoshenko and Gere 1961; Yoo 1982; Papangelis and Trahair 1987; Yang and Kuo 1987; Rajasekaran and Padmanabhan 1989; Kang and Yoo 1994; Bradford and Pi 2002].

In the case of directed radial loads (load case II), the loads q are assumed to be always directed toward the center of the initial curvature of the arch as shown in Figure 4b during buckling. In this case, the loads q have lateral and radial components, q_{ey} and q_{ex} , given by

$$q_{ex} \approx -\frac{qu}{R} = -\frac{Qu}{R(R - y_q)}, \quad q_{ey} \approx q = \frac{Q}{R - y_q}. \quad (22)$$

In the case of hydrostatic loads (load case III), the loads q are assumed to be mechanically hydrostatic, that is, the loads q change their directions slightly but always remain normal to the tangent of the deformed arch axis (that is, remain in the direction of the axis o_1y_1 of the cross-section) during buckling, as shown in Figure 4c. In this case, the hydrostatic loads q have the lateral and radial components, q_{ex} and q_{ey} , given by

$$q_{ex} = -q \sin \phi \approx -q\phi = -\frac{Q\phi}{R - y_q}, \quad q_{ey} = q \cos \phi \approx q = \frac{Q}{R - y_q}, \quad (23)$$

where $\sin \phi \approx \phi$ and $\cos \phi \approx 1$, since the buckling displacements ϕ are infinitesimally small.

It can be seen from Figure 4 and from Equations (22) and (23) that during buckling, the lateral components q_{ex} of directed radial loads and of hydrostatic loads acting on an arch are in opposite directions to the lateral buckling displacements. The lateral components q_{ex} are expected to produce combined torsion and lateral bending actions that oppose the flexural-torsional buckling, so the flexural-torsional buckling loads of the arch will increase.

3.2. Solutions for flexural-torsional buckling loads. The n -th mode buckled shapes of a laterally pin-ended arch can be assumed to be given by

$$\frac{u}{u_m} = \frac{\phi}{\phi_m} = \sin \frac{n\pi s}{S}, \quad (24)$$

which satisfies the kinematic boundary conditions given by Equation (20), and where u_m and ϕ_m are the maximum lateral displacement of the centroid and the twist angle of the cross-section during buckling, and n is the number of buckled half waves. Substituting Equations (21), (22) or (23), and Equation (24)

into Equations (14) and (15) leads to

$$\begin{bmatrix} k_{11} & k_{12} \\ k_{21} & k_{22} \end{bmatrix} \begin{bmatrix} u_m \\ \phi_m \end{bmatrix} = \begin{bmatrix} 0 \\ 0 \end{bmatrix}, \tag{25}$$

where the coefficients k_{11} , k_{12} , k_{21} , and k_{22} are given by

$$k_{11} = \begin{cases} \left(1 + a_n^2 b_n^2 - (1 + a_n^2 b_n^2 \frac{P_{yn}}{P_{sn}}) \frac{Q}{P_{yn}}\right) P_{yn}, & \text{for load case I,} \\ \left(1 + a_n^2 b_n^2 - (1 - a_n^2 + a_n^2 b_n^2 \frac{P_{yn}}{P_{sn}}) \frac{Q}{P_{yn}}\right) P_{yn}, & \text{for load case II,} \\ \left(1 + a_n^2 b_n^2 - (1 + a_n^2 b_n^2 \frac{P_{yn}}{P_{sn}}) \frac{Q}{P_{yn}}\right) P_{yn}, & \text{for load case III,} \end{cases} \tag{26}$$

$$k_{12} = \begin{cases} -\left(\frac{a_n}{b_n} + a_n b_n - a_n b_n \frac{P_{yn}}{P_{sn}} \frac{Q}{P_{yn}}\right) M_{ysn}, & \text{for load case I,} \\ -\left(\frac{a_n}{b_n} + a_n b_n - a_n b_n \frac{P_{yn}}{P_{sn}} \frac{Q}{P_{yn}}\right) M_{ysn}, & \text{for load case II,} \\ -\left(\frac{a_n}{b_n} + a_n b_n - \left(\frac{a_n}{b_n} + a_n b_n \frac{P_{yn}}{P_{sn}}\right) \frac{Q}{P_{yn}}\right) M_{ysn}, & \text{for load case III,} \end{cases} \tag{27}$$

$$k_{21} = \begin{cases} -\left(\frac{a_n}{b_n} + a_n b_n - a_n b_n \frac{P_{yn}}{P_{sn}} \frac{Q}{P_{yn}}\right) M_{ysn}, & \text{for load case I,} \\ -\left(\frac{a_n}{b_n} + a_n b_n - \left(a_n b_n \frac{P_{yn}}{P_{sn}} - \frac{a_n}{b_n} \frac{y_q}{R}\right) \frac{Q}{P_{yn}}\right) M_{ysn}, & \text{for load case II,} \\ -\left(\frac{a_n}{b_n} + a_n b_n - a_n b_n \frac{P_{yn}}{P_{sn}} \frac{Q}{P_{yn}}\right) M_{ysn}, & \text{for load case III,} \end{cases} \tag{28}$$

$$k_{22} = \begin{cases} \left(1 + \frac{a_n^2}{b_n^2} - \left(\frac{P_{yn}}{P_{sn}} - \frac{y_q}{R b_n^2}\right) \frac{Q}{P_{yn}}\right) r_0^2 P_{sn}, & \text{for load case I,} \\ \left(1 + \frac{a_n^2}{b_n^2} - \left(\frac{P_{yn}}{P_{sn}} - \frac{y_q}{R b_n^2}\right) \frac{Q}{P_{yn}}\right) r_0^2 P_{sn}, & \text{for load case II,} \\ \left(1 + \frac{a_n^2}{b_n^2} - \frac{P_{yn}}{P_{sn}} \frac{Q}{P_{yn}}\right) r_0^2 P_{sn}, & \text{for load case III.} \end{cases} \tag{29}$$

In Equations (26)–(29), P_{yn} is the n -th mode elastic flexural buckling load of a pin-ended column of length S under uniform compression about the minor principal axis of its cross-section, P_{sn} is the n -th mode elastic torsional buckling load of a pin-ended column of length S under uniform compression, and M_{ysn} is the n -th mode elastic flexural-torsional buckling moment of a simply supported beam of length S under uniform bending. It is well known that P_{yn} , P_{sn} and M_{ysn} are given by [Trahair 1993; Trahair and Bradford 1998]

$$P_{yn} = \frac{(n\pi)^2 E I_y}{S^2}, \quad P_{sn} = \frac{1}{r_0^2} \left(G J + \frac{(n\pi)^2 E I_w}{S^2} \right), \quad M_{ysn} = \sqrt{r_0^2 P_{yn} P_{sn}}, \quad r_0^2 = \frac{I_x + I_y}{A}.$$

The parameters a_n and b_n are defined as

$$a_n = \frac{S}{n\pi R}, \quad b_n = \frac{n\pi M_{ysn}}{P_{yn} S}.$$

Equation (25) has nontrivial solutions for u_m and ϕ_m when the determinant of its coefficient matrix vanishes, that is, when $k_{11}k_{22} - k_{12}k_{21} = 0$, which leads to the generic equation for the elastic flexural-torsional buckling load of a pin-ended arch under uniform compression produced by uniformly distributed

radial loads,

$$A_1 \left(\frac{Q}{P_{yn}} \right)^2 + B_1 \frac{Q}{P_{yn}} + C_1 = 0, \quad (30)$$

where the coefficients for load cases I, II, and III are, respectively,

$$\begin{aligned} A_1 &= \frac{P_{yn}}{P_{sn}} - \left(1 + a_n^2 b_n^2 \frac{P_{yn}}{P_{sn}} \right) \frac{y_q}{R b_n^2}, \\ B_1 &= - \left(\left(1 + \frac{a_n^2}{b_n^2} \right) + \left(1 - a_n^2 \right)^2 \frac{P_{yn}}{P_{sn}} - \left(1 + a_n^2 b_n^2 \right) \frac{y_q}{R b_n^2} \right), \\ C_1 &= (1 - a_n^2)^2; \end{aligned} \quad (31)$$

$$\begin{aligned} A_1 &= \frac{P_{yn}}{P_{sn}} - \frac{y_q}{R b_n^2}, \\ B_1 &= - \left(1 + \frac{a_n^2}{b_n^2} + (1 - a_n^2)^2 \frac{P_{yn}}{P_{sn}} - \frac{y_q}{R b_n^2} \right), \\ C_1 &= 1 - a_n^2; \end{aligned} \quad (32)$$

$$\begin{aligned} A_1 &= 1, \\ B_1 &= - \left(\frac{P_{sn}}{P_{yn}} + (1 - a_n^2) \right), \\ C_1 &= (1 - a_n^2) \frac{P_{sn}}{P_{yn}}. \end{aligned} \quad (33)$$

It can be seen from Equations (31) and (32) that the load height y_q affects the flexural-torsional buckling of an arch in the cases of dead or directed uniformly distributed radial loads (load cases I and II). However, Equation (33) indicates that the load height y_q of hydrostatic loads (load case III) has no effect on the flexural-torsional buckling of an arch. When the radial loads act at the centroid ($y_q = 0$), it can be demonstrated that for the same arch, the buckling load for load case III given by Equations (30) and (33) is the highest, while the buckling load for load case I given by Equations (30) and (31) is the lowest.

4. Static equilibrium approach

A static equilibrium approach is used in this section to investigate the flexural-torsional buckling and the effects of the load height on the buckling of arches under uniform compression, and to verify the solutions obtained by the virtual work approach in the previous section. In the buckled configuration, the axial compressive force Q in the axis os has an axial compressive component $Q_{es} \approx Q$ in the axis o_1s_1 (see Figure 5a) which produces a torsional moment action M_{es} given by

$$M_{es} = r_0^2 Q_{es} \kappa_s = r_0^2 Q_{es} \left(\phi' - \frac{u'}{R} \right) = r_0^2 Q \left(\phi' - \frac{u'}{R} \right).$$

The uniform torsional resistance M_{iu} about the axis o_1s_1 and the bimoment resistance B_i of the cross-section are given by

$$M_{iu} = GJ\kappa_s = GJ\left(\phi' - \frac{u'}{R}\right), \quad B_i = -EI_w\kappa'_s = -EI_w\left(\phi'' - \frac{u''}{R}\right).$$

It is well known that the bimoment resistance B_i induces a warping torsional resistance M_{iw} as $M_{iw} = dB_i/ds$ [Vlasov 1961; Trahair and Bradford 1998]. The total torsional resistance M_{is} can be obtained by combining the uniform and warping torsional resistances M_{iu} and M_{iw} as

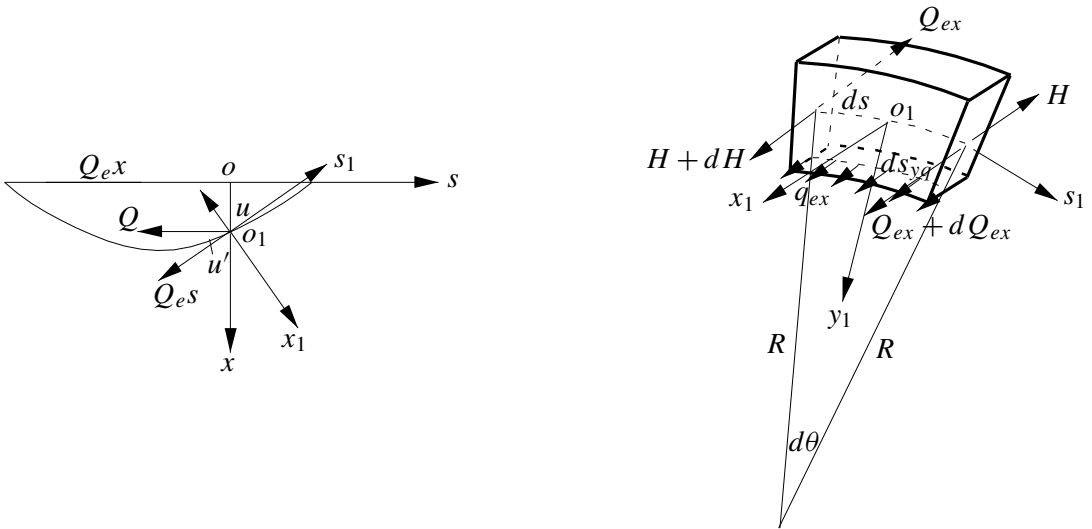
$$M_{is} = M_{iu} + M_{iw} = GJ\left(\phi' - \frac{u'}{R}\right) - EI_w\left(\phi''' - \frac{u'''}{R}\right).$$

In a straight member, the torsional action is in equilibrium with the torsional resistance. However, in an arch, the torsional action couples with the lateral bending action while the torsional resistance also couples with the lateral bending resistance. Hence, the resultant of the torsional action and resistance at a cross-section of an arch does not vanish. The resultant torsional moment at the cross-section is then

$$M_s = M_{es} - M_{is} = r_0^2 Q\left(\phi' - \frac{u'}{R}\right) - GJ\left(\phi' - \frac{u'}{R}\right) + EI_w\left(\phi''' - \frac{u'''}{R}\right), \quad (34)$$

where the first term is historically called the trapeze effect, the bifilar effect, Wagner’s term, or Buckley’s term; the second term is St. Venant torsion moment; and the third term is the warping torsion moment (Vlasov’s term) [Hodges 2006].

In the buckled configuration, the axial compressive force Q in the axis os also has a lateral component Q_{ex} in the axis o_1x_1 given by $Q_{ex} = -Qu'$ (see Figure 5a). The resultant lateral bending moment at the cross-section is then equal to the lateral bending resistance M_{iy} of the cross-section about the axis o_1y_1



(a) components of compressive force

(b) lateral force equilibrium

Figure 5. Lateral force equilibrium.

and is given by

$$M_y = M_{iy} = -EI_y \left(u'' + \frac{\phi}{R} \right). \tag{35}$$

The differential equilibrium equations in the buckled configuration can be established by considering the lateral and torsional equilibrium of a free body of a differential element ds of the arch, as shown in Figures 5 and 6. For lateral force equilibrium, it can be shown from Figure 5b that

$$H + dH - H + Q_{ex} + dQ_{ex} - Q_{ex} + q_{ex} ds_{sq} = 0, \tag{36}$$

where $ds_{sq} = [(R - y_q)/R] ds$ and H is the internal lateral shear force. From Equation (36),

$$\frac{dH}{ds} = -\frac{dQ_{ex}}{ds} - q_{ex} \frac{R - y_q}{R}. \tag{37}$$

For lateral moment equilibrium, it can be shown from Figure 6 that

$$(M_y + dM_y) - M_y + 2M_s \sin \frac{d\theta}{2} + Q_x ds = dM_y + \frac{M_s}{R} ds - H ds = 0, \tag{38}$$

from which

$$H = \frac{dM_y}{ds} + \frac{M_s}{R}. \tag{39}$$

Substituting Equation (39) into Equation (37) yields the differential equilibrium equation for the lateral buckling deformation

$$\frac{d^2 M_y}{ds^2} + \frac{dM_s}{ds} \frac{1}{R} + \frac{dQ_{ex}}{ds} + q_{ex} \frac{R - y_q}{R} = 0. \tag{40}$$

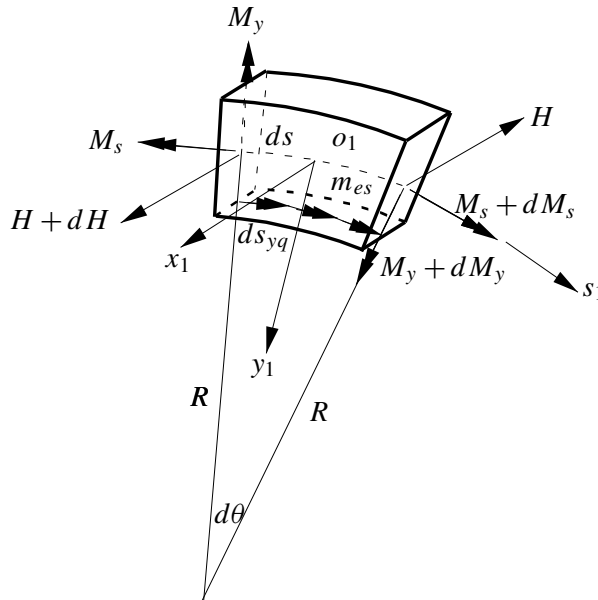


Figure 6. Lateral and torsional moment equilibrium.

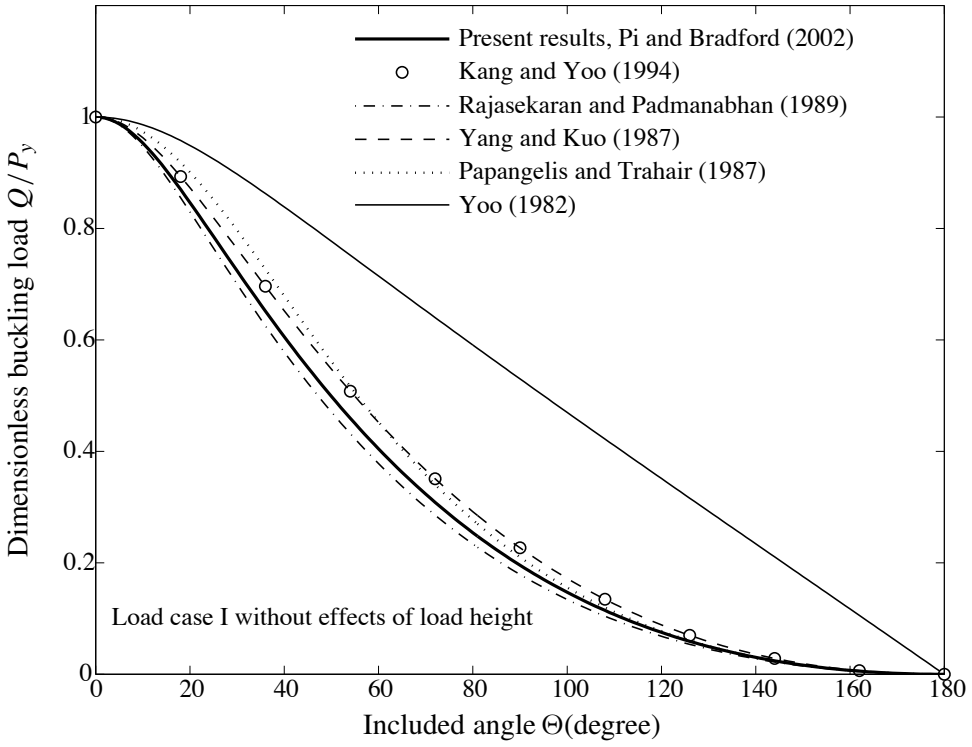


Figure 7. Comparison of buckling loads for load case I without effects of load height with the results of other researchers.

For torsional moment equilibrium, it can be shown from [Figure 6](#) that

$$(M_s + dM_s) - M_s - 2M_y \sin \frac{d\theta}{2} + m_s ds_{sq} = dM_s - \frac{M_y}{R} ds + m_{es} \frac{R - y_q}{R} ds = 0,$$

which gives the differential equilibrium equation for the torsional buckling deformation

$$\frac{dM_s}{ds} - \frac{M_y}{R} + m_{es} \frac{R - y_q}{R} = 0. \tag{41}$$

Here the distributed torques m_{es} produced by the lateral and radial components q_{ex} and q_{ey} of the loads q at the load height y_q are given by

$$m_{es} = q_{ey}y_q\phi + q_{ex}y_q. \tag{42}$$

Substituting the expressions for Q_{ex} , M_s , M_y , and m_{es} given by Equations (34)–(35) and (42) into Equations (40) and (41) leads to the same differential equilibrium equations as those given by Equations (14) and (15).

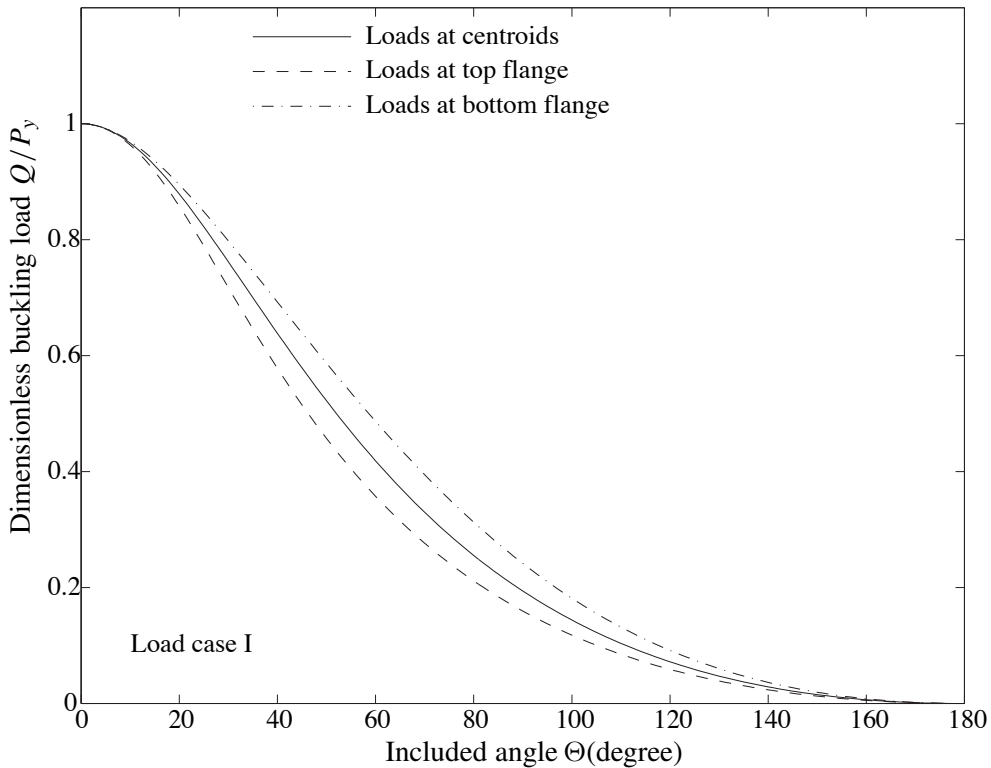


Figure 8. Effects of load height on buckling loads for load case I.

5. Numerical examples and comparisons

5.1. Comparison with solutions by other researchers for load case I. A number of researchers [Yoo 1982; Papangelis and Trahair 1987; Yang and Kuo 1987; Rajasekaran and Padmanabhan 1989; Kang and Yoo 1994; Bradford and Pi 2002] have obtained closed form solutions for the flexural-torsional buckling load for arches under uniform compression when the uniformly distributed radial dead loads act at the centroid (the load case I). In this case, the load height $y_q = 0$ and the solution for the buckling load given by Equations (30) and (31) become

$$\left(\frac{Q}{P_{yn}}\right)^2 - \left(\left(1 + \frac{a_n^2}{b_n^2}\right)\frac{P_{sn}}{P_{yn}} + (1 - a_n^2)^2\right)\frac{Q}{P_{yn}} + (1 - a_n^2)^2\frac{P_{sn}}{P_{yn}} = 0, \quad (43)$$

the same results as those obtained by Bradford and Pi [2002].

Solutions for the first mode flexural-torsional buckling load of arches under uniform compression given by Equation (43) are compared with the solutions by other researchers in Figure 7 for arches with an Australian I-section 1200WB249 ($A = 31700 \text{ mm}^2$, $I_x = 6380 \times 10^6 \text{ mm}^4$, $I_y = 87 \times 10^6 \text{ mm}^4$, $J = 4310 \times 10^3 \text{ mm}^4$, $I_w = 28500 \times 10^9 \text{ mm}^6$, $E = 200,000 \text{ MPa}$, $\nu = 0.3$) [BHP 2000] and with the length $S = 5000 \text{ mm}$. Because the length S is constant, the curvature $1/R$ increases with an increase of the included angle Θ . It can be seen that there are some differences between the results. In particular, the result of Yoo [1982] (based on the method of a forced analogy of curved members

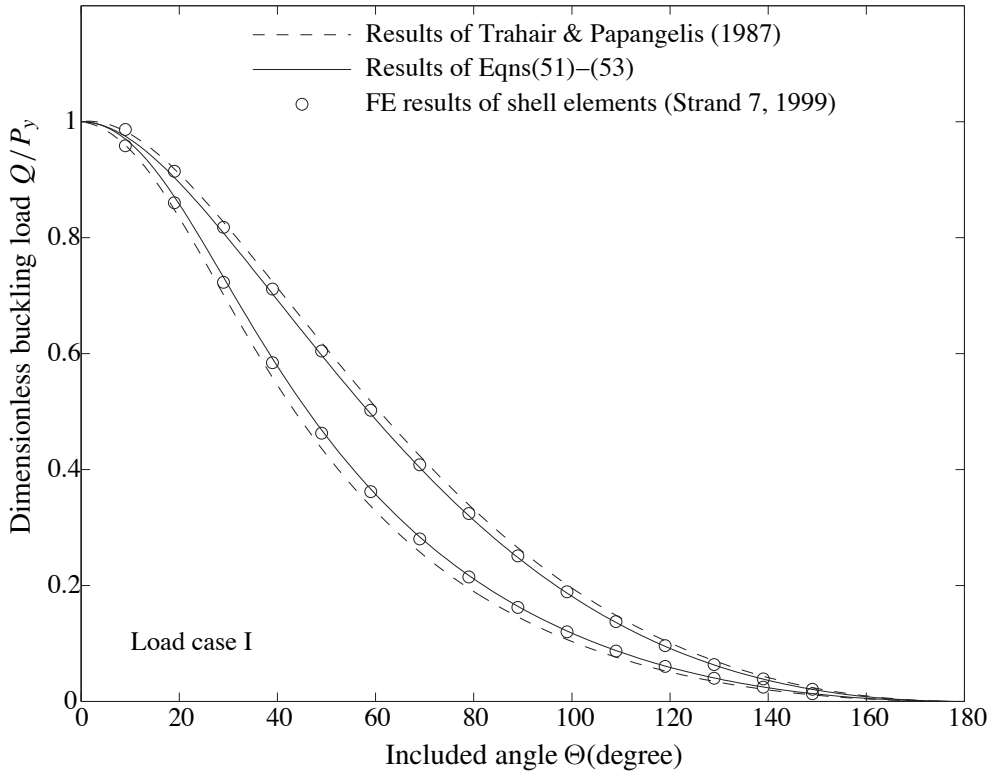


Figure 9. Comparison of effects of load height on buckling loads with results of FE and other results for load case I.

to straight members) diverges substantially from those of the others. It is worth pointing out that the solution methods used by most of these researchers [Papangelis and Trahair 1987; Yang and Kuo 1987; Rajasekaran and Padmanabhan 1989; Kang and Yoo 1994; Bradford and Pi 2002] are correct. The minor discrepancies between the results are due to the fact that some small differences in the terms of the strain-displacement relationship were obtained when different methods of derivation were used. Researchers such as [Papangelis and Trahair 1987; Yang and Kuo 1987; Rajasekaran and Padmanabhan 1989; Kang and Yoo 1994; Bradford and Pi 2002] have also presented comparisons and analyses of these discrepancies.

5.2. Effects of load height. Solutions for the first mode flexural-torsional buckling loads of arches subjected to radial dead loads (load case I) and acting at the top, the centroid, and the bottom of the cross-section are compared in Figure 8. These arches have an Australian steel I-section 250UB25 ($A = 3270 \text{ mm}^2$, $I_x = 35.4 \times 10^6 \text{ mm}^4$, $I_y = 2.55 \times 10^6 \text{ mm}^4$, $J = 67.4 \times 10^3 \text{ mm}^4$, $I_w = 36.7 \times 10^9 \text{ mm}^6$, $E = 200,000 \text{ MPa}$ and Poisson's ratio $\nu = 0.3$) [BHP 2000] and the length $S = 2000 \text{ mm}$. It can be seen that when the radial loads act at the centroid, the buckling load is lower than when the radial loads act at the bottom of the cross-section, but it is higher than when the radial loads act at the top of the cross-section. The difference between these buckling loads increases with an increase of the included angle of the arch, and then decreases with a further increase of the included angle of the arch.

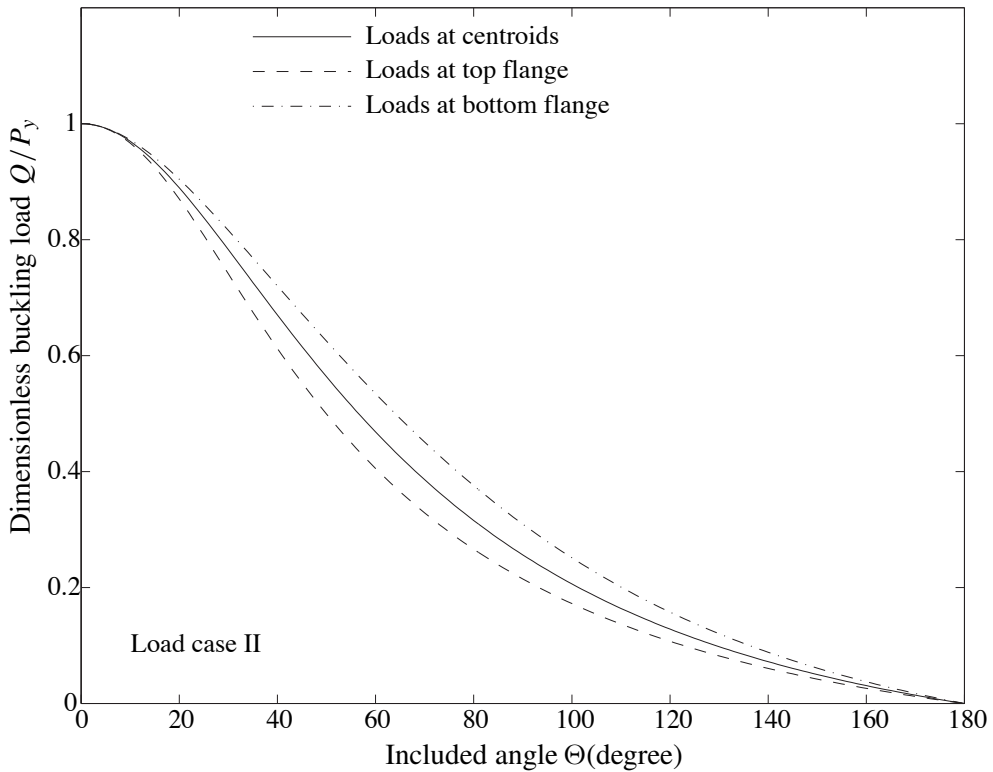


Figure 10. Effects of load height on buckling loads for load case II.

Trahair and Papangelis [1987] and Trahair [1993] studied the effects of load height on the flexural-torsional buckling of arches under uniform compression for case I. Trahair [1993] used diagrams to show the effects without giving analytical solutions, while Trahair and Papangelis [1987] obtained an analytical solution. The solutions of Equations (30)–(31) for load case I are compared with their solutions in Figure 9. Also shown in Figure 9 are results which were obtained by an eigenvalue analysis using the 8-noded shell elements of the FE package [Strand7 1999] to verify the solutions Equations (30)–(31). The FE results agree with the solutions of Equations (30)–(31) very well. Trahair and Papangelis [1987] ignored the small term r_y^2/R^2 , and their results are slightly lower than the FE results, while for bottom flange loading, their results are slightly higher than the FE results. However, the differences between them are very small and so the solutions of [Trahair and Papangelis 1987] are also accurate.

Figure 10 compares solutions for the first mode flexural-torsional buckling loads of arches subjected to radial loads that are always directed towards the arch center during buckling (the load case II) and are acting at the top, at the centroid, and at the bottom of the cross-section for arches with an I-section 250UB25 and length $S = 2000$ mm. It can be seen that when the radial loads act at the centroid, the buckling load is lower than that when they act at the bottom of the cross-section, but it is higher than when the radial loads act at the top of the cross-section. The difference between these buckling loads increases with an increase of the included angle of the arch, and then decreases with a further increase of the included angle of the arch.

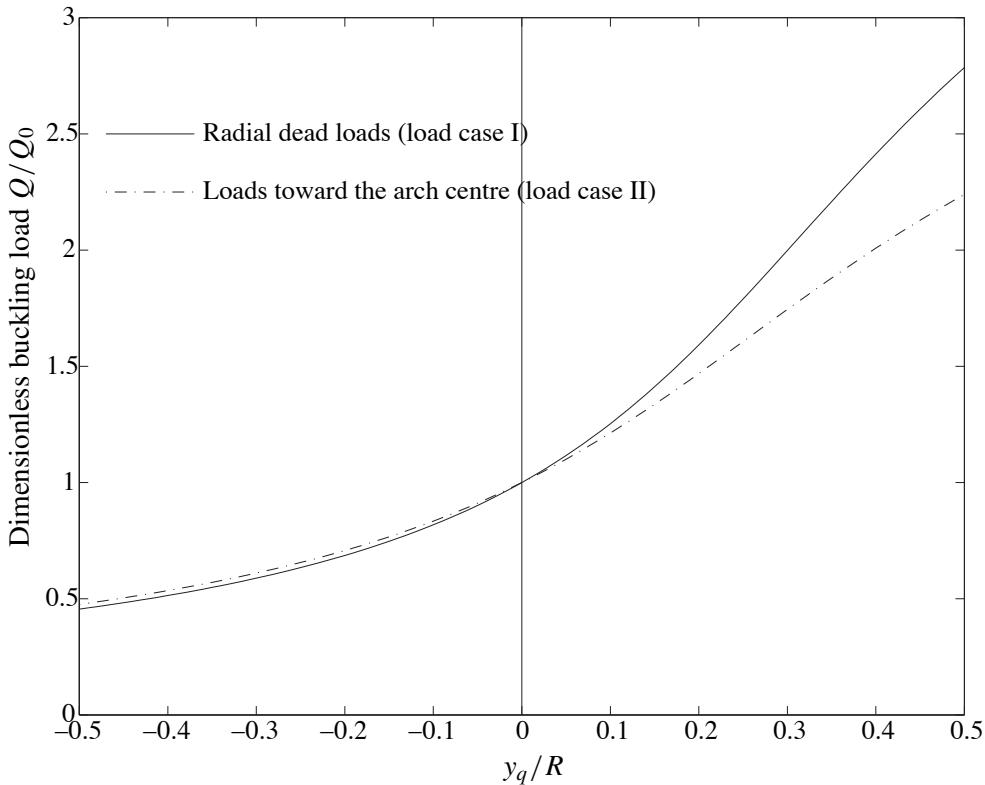


Figure 11. Comparison of effects of load height on buckling loads for load cases I and II.

Figure 11 compares the effects of the load height on the buckling loads of arches subjected to radial loads always directed to the arch center (load case II), given by Equations (30) and (32), with those for arches subjected to radial dead loads (load case I), given by Equations (30) and (31); in the figure, Q_0 is the buckling load when the loads act at the centroid. It can be seen that the effects of load height on the buckling loads only differ in a visible way when the loads act below the centroid (that is, y_q is positive as shown in Figures 1 and 4). In this case, the arches subjected to uniformly distributed radial dead loads experience higher buckling load increases, particularly for larger y_q values.

5.3. Comparison with Vlasov's solution for load case III. Solutions for the first mode of flexural-torsional buckling load of arches with an I-section 250UB25 and length $S = 2000$ mm under hydrostatic loads given by Equations (30) and (33) are compared in Figure 12 with the solution of [Vlasov 1961].

It can be seen from Figure 12 that the solution of [Vlasov 1961] is slightly lower than the present results, because he did not consider the coupling term contributed by the torsional moment M_{es} to the differential equilibrium equation for lateral deformations.

5.4. Arches with a narrow rectangular cross-section. Timoshenko and Gere [1961] investigated the flexural-torsional buckling of an arch with a narrow rectangular cross-section for the load cases I and II, but without considering the Wagner effects and warping. In this case, the virtual work

$$(-Qr_0^2(\phi' - u'/R)(\delta\phi' - \delta u'/R)),$$

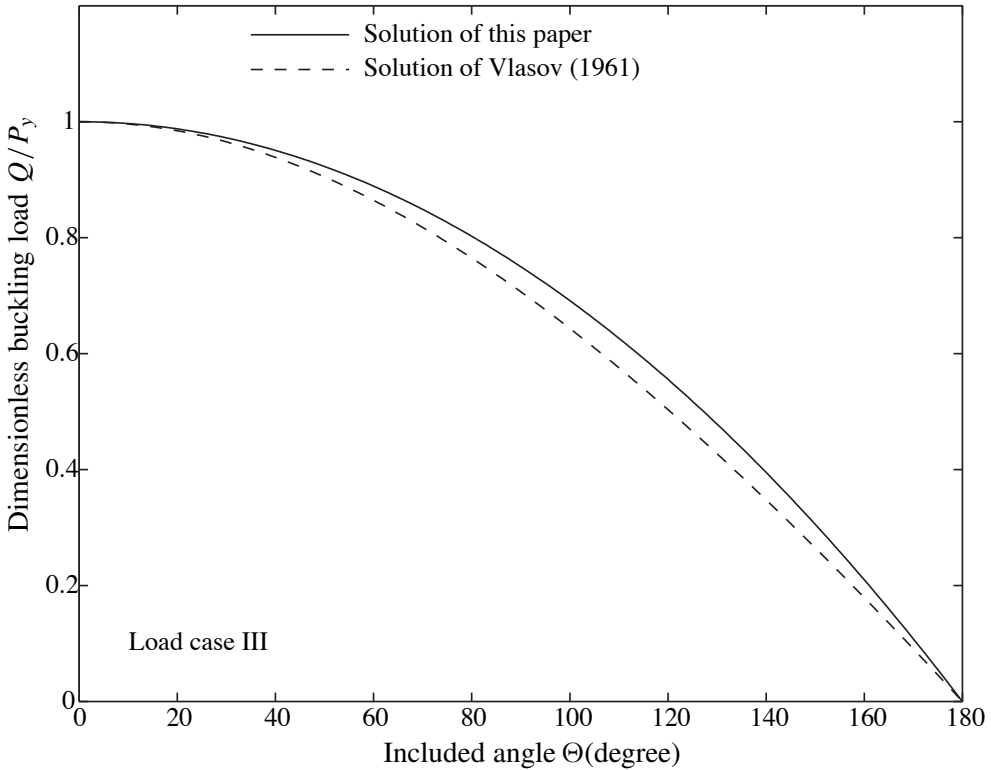


Figure 12. Comparison with Vlasov’s solution for load case III.

due to Wagner effects, and

$$EI_w (\phi'' - u''/R) (\delta\phi'' - \delta u''/R),$$

due to warping in the virtual work statement given by Equation (13), are equal to zero, and accordingly the Wagner terms and warping torsion moments (Vlasov terms) in the differential equilibrium equations (14) and (15) vanish. The flexural-torsional buckling load for an arch with a narrow rectangular section can then be obtained from Equations (14) and (15), by considering the components of q_{ex} and q_{ey} of the load q being given by Equations (21)–(23) respectively, as

$$\frac{Q}{P_{yn}} = \begin{cases} \frac{(1-a_n^2)^2}{1+a_n^2/b_n^2}, & \text{for the case of radial dead loads,} \\ \frac{1-a_n^2}{1+a_n^2/b_n^2}, & \text{for the case of directed radial loads,} \\ 1 - a_n^2, & \text{for the case of hydrostatic loads.} \end{cases} \quad (44)$$

The solutions given by Equation (44) are the same as those of [Timoshenko and Gere 1961].

6. Conclusions

This paper has used both virtual work and equilibrium approaches to investigate the elastic flexural-torsional buckling of circular arches under uniform compression produced by uniformly distributed radial

dead loads, by hydrostatic loads or by uniformly distributed directed radial loads. The effects of the load height on the buckling loads have also been studied, and solutions for the buckling loads for these loading cases, including the effects of the load height, have been obtained in closed form. It was found that the buckling load under hydrostatic loading is highest while the buckling load under uniform radial dead loading is the lowest. The lateral components of the uniformly distributed radial loads that are always directed toward the center of the initial curvature of the arch and those of the hydrostatic loads, too, increase the flexural-torsional buckling resistance of an arch under uniform compression. The buckling load increases as the load height below the centroid of the cross-section increases, while the buckling load decreases as the load height above the centroid of the cross-section increases.

References

- [BHP 2000] BHP, *Hot rolled and structural steel products*, BHP, Melbourne, 2000.
- [Bolotin 1963] V. V. Bolotin, *Nonconservative problems of theory of elastic stability*, Pergamon, Oxford, 1963.
- [Bradford and Pi 2002] M. A. Bradford and Y. L. Pi, “Elastic flexural-torsional buckling of discretely restrained arches”, *J. Struct. Eng. (ASCE)* **128**:6 (2002), 719–729.
- [Burn 1985] R. P. Burn, *Groups: A path to geometry*, Cambridge University Press, Cambridge, 1985.
- [Guran 2000] A. Guran, *Theory of elasticity for scientists and engineers*, Birkhauser, Boston, MA, 2000.
- [Hodges 2006] D. H. Hodges, *Nonlinear composite beam theory*, AIAA, Reston, VA, 2006.
- [Ings and Trahair 1987] N. L. Ings and N. S. Trahair, “Beam and column buckling under directed loading”, *J. Struct. Eng. (ASCE)* **113**:6 (1987), 1251–1263.
- [Kang and Yoo 1994] Y. J. Kang and C. H. Yoo, “Thin-walled curved beams, II: Analytical solutions for buckling of arches”, *J. Eng. Mech. (ASCE)* **120**:10 (1994), 2102–2125.
- [Papangelis and Trahair 1987] J. P. Papangelis and N. S. Trahair, “Flexural-torsional buckling of arches”, *J. Struct. Eng. (ASCE)* **113**:4 (1987), 889–906.
- [Pi and Bradford 2004] Y. L. Pi and M. A. Bradford, “Effects of prebuckling deformations on the elastic flexural-torsional buckling of laterally fixed arches”, *Int. J. Mech. Sci.* **46**:2 (2004), 321–342.
- [Rajasekaran and Padmanabhan 1989] S. Rajasekaran and S. Padmanabhan, “Equations of curved beams”, *J. Eng. Mech. (ASCE)* **115**:5 (1989), 1094–1111.
- [Simitses 1976] G. J. Simitses, *An introduction to the elastic stability of structures*, Prentice-Hall, Englewood Cliffs, NJ, 1976.
- [Simitses and Hodges 2006] G. J. Simitses and D. H. Hodges, *Fundamentals of structural stability of structures*, Elsevier, Boston, MA, 2006.
- [Strand7 1999] *Using Strand7: Introduction to the Strand 7 finite element analysis system*, G+D Computing, Sydney, 1999, Available at <http://www.strand7.com/Downloads/Using%20Strand7%20Manual.zip>.
- [Timoshenko and Gere 1961] S. P. Timoshenko and J. M. Gere, *Theory of elastic stability*, 2nd ed., McGraw-Hill, New York, 1961.
- [Trahair 1993] N. S. Trahair, *Flexural-torsional buckling of structures*, E&FN Spon, London, 1993.
- [Trahair and Bradford 1998] N. S. Trahair and M. A. Bradford, *The behaviour and design of steel structures to AS4100*, E&FN Spon, London, 1998.
- [Trahair and Papangelis 1987] N. S. Trahair and J. P. Papangelis, “Flexural-torsional buckling of monosymmetric arches”, *J. Struct. Eng. (ASCE)* **113**:10 (1987), 2271–2288.
- [Vlasov 1961] V. Z. Vlasov, *Thin-walled elastic beams*, 2nd ed., Israel Program for Scientific Translation, Jerusalem, 1961.
- [Yang and Kuo 1987] Y. B. Yang and S. R. Kuo, “Effects of curvature on stability of curved beams”, *J. Struct. Eng. (ASCE)* **113**:6 (1987), 821–841.
- [Yoo 1982] C. H. Yoo, “Flexural-torsional stability of curved beams”, *J. Eng. Mech. Div. (ASCE)* **108**:6 (1982), 1351–1369.

Received 11 Dec 2005. Revised 22 Mar 2006. Accepted 3 Apr 2006.

MARK ANDREW BRADFORD: m.bradford@unsw.edu.au

School of Civil and Environmental Engineering, The University of New South Wales, Sydney, NSW 2052, Australia

YONG-LIN PI: y.pi@unsw.edu.au

School of Civil and Environmental Engineering, The University of New South Wales, Sydney, NSW 2052, Australia

TRANSIENT ANALYSIS OF A SUDDENLY-OPENING CRACK IN A COUPLED THERMOELASTIC SOLID WITH THERMAL RELAXATION

LOUIS MILTON BROCK AND MARK TODD HANSON

For a semiinfinite crack that opens in an unbounded thermoelastic solid initially at rest under uniform plane-strain tension at uniform temperature, the governing equations contain as special cases the Fourier model, and two thermal relaxation models with, respectively, one and two relaxation times. Integral transforms reduce the initial/mixed boundary value problem to a Wiener–Hopf equation. Its solution produces analytical expressions for temporal transforms of normal stress and temperature change near the crack edge. For 4340 steel, numerical inversions allow comparisons of the crack edge stress for the three thermoelastic models with the isothermal result, and temperature change at the crack edge for the two thermal relaxation models with the Fourier model result. Calculations indicate that thermoelasticity has a mild relaxation effect on the stress, and that temperature changes for the thermal relaxation model are much larger than those that arise for the Fourier model just after the crack opens. After a time interval in the order of a nanosecond, however, the Fourier changes are larger, although the deviation is minuscule.

Introduction

Thermal waves appear as a feature of heat conduction when thermal relaxation times are introduced into the classical Fourier law [Joseph and Preziosi 1989]. The modified heat equation is in turn incorporated in the coupled equations of thermoelasticity [Chandrasekharia 1986; Sharma and Sharma 2002] in a fashion similar to that used for the Fourier model [Chadwick 1960].

Fracture analysis, however, is often based on the Fourier model with partial or complete uncoupling of the heat and momentum balance equations, for example, [Rice and Levy 1969; Sumi and Katayama 1980; Noda et al. 1989; Rizk and Radwan 1993]. Such models can be justified on various grounds, as follows:

- For equilibrium or slow-moving cracks under thermal loading only or static mechanical loading, inertial effects may well be negligible.
- Heat production near a crack edge is controlled by plastic energy when yield occurs [Freund and Hutchinson 1985].
- The Fourier law is adequate for describing temperature fields measured near a crack edge [Mason and Rosakis 1993].
- Calculations for fluids [Fan and Lu 2002] suggest that thermal relaxation effects are highly transient.

Keywords: transient analysis, thermoplastic crack, thermal relaxation, dynamic stress intensity.

- Asymptotic analyses of dynamic steady-state fracture [Brock 2004; 2006] show that, even for high crack speeds, solution behavior can be described by the Fourier model, except very near the crack edge.

For more insight into thermal effects in dynamic fracture, in this paper we consider the canonical situation of a semiinfinite crack that opens suddenly in an unbounded solid. The solid is initially at rest at a uniform temperature in a uniform plane-strain tension field, and plastic yield is ignored. To ascertain the importance of thermal relaxation effects, we investigated a general form [Sharma and Sharma 2002] of the coupled thermoelastic equations which contains as special cases thermal relaxation models with one [Lord and Shulman 1967] and two [Green and Lindsay 1972] relaxation times, as well as the Fourier model [Chadwick 1960].

We use multiple integral transforms and a Wiener–Hopf technique, and analytically obtain the temporal transforms of normal stress and temperature change in the crack plane. By numerical inversion we then obtain calculations for 4340 steel that allow us to gauge thermal effects on stress at the crack edge and thermal relaxation effects on temperature change at the crack edge.

Governing equations

Consider governing equations for an isotropic, homogeneous linear coupled thermoelastic solid initially at uniform (absolute) temperature T_0 of the form

$$\nabla^2 \mathbf{u} + m \nabla \Delta - \mathbf{u}_{ss} - \alpha_v \nabla D_2 \theta = 0, \tag{1a}$$

$$h \nabla^2 \theta - \frac{\varepsilon}{\alpha_v} D \Delta_s - D_1 \theta_s = 0, \tag{1b}$$

$$\frac{1}{\mu} \mathbf{S} = [(m - 1) \Delta - \alpha_v D_2 \theta] \mathbf{I} + \nabla \mathbf{u} + \mathbf{u} \nabla, \tag{1c}$$

where $(\mathbf{u}, \Delta, \theta, \mathbf{S}, \mathbf{I})$ are, respectively, the displacement vector, dilatation, temperature change, and stress and identity tensors. In terms of $(\Delta, \theta, \mathbf{r})$, decomposition of Equation (1a) gives

$$a \nabla^2 \Delta - \Delta_{ss} - \alpha_v D_2 \nabla^2 \theta = 0, \quad \nabla^2 \mathbf{r} - \mathbf{r}_{ss} = 0, \tag{2}$$

where (∇^2, ∇) are, respectively, the Laplacian and gradient operators, where \mathbf{r} is the rotation tensor.

For the single- and double-relaxation time model 1 [Lord and Shulman 1967] and 2 [Green and Lindsay 1972], and Fourier model F [Chadwick 1960], respectively, it is understood that

$$(1) : D_2 = 1, \quad D = D_1 \quad (2) : D = D_2 \quad (F) : D = D_1 = D_2 = 1, \tag{3}$$

where the thermal relaxation operators are

$$D_1 = 1 + h_1(\cdot)_s \quad D_2 = 1 + h_2(\cdot)_s. \tag{4}$$

The operator $(\cdot)_s$ signifies differentiation with respect to temporal variable $s = v_r \times (\text{time})$. Note that the additional relaxation time in model 2 serves to introduce thermal relaxation explicitly into constitutive

Equation (1c). In (1)–(4) dimensionless parameters are defined as

$$m = \frac{1}{1-2\nu}, \quad a = 2\left(\frac{1-\nu}{1-2\nu}\right), \quad \varepsilon = \frac{\mu T_0}{\rho c_v} \alpha_v^2, \tag{5}$$

and thermoelastic characteristic lengths (h, h_1, h_2) and rotational wave speed v_r are defined as

$$h = \frac{K}{c_v \sqrt{\mu \rho}}, \quad h_1 = v_r t_1, \quad h_2 = v_r t_2, \quad v_r = \sqrt{\frac{\mu}{\rho}}, \tag{6}$$

where material constants $t_1 > t_2 \geq 0$ are thermal relaxation times, and ($\nu, \mu, \rho, \alpha_v, c_v, K$) are, respectively, Poisson’s ratio, shear modulus, mass density, coefficient of volumetric thermal expansion, specific heat at constant volume, and thermal conductivity.

For many materials [Chadwick 1960; Achenbach 1973; Sharma and Sharma 2002]

$$v_r \approx O(10^3) \text{ m/s}, \quad m \geq 2, \quad \varepsilon \approx O(10^{-2}), \tag{7a}$$

$$h \approx O(10^{-9}) \text{ m}, \quad (t_1, t_2), \approx O(10^{-13}) \text{ s}. \tag{7b}$$

In view of (6), these values suggest that $h \gg h_1 > h_2$.

Crack problem

When at $s = 0$ a semiinfinite crack ($y = 0, x < 0$) forms, an unbounded solid is motionless at uniform temperature T_0 in a state of plane strain generated by the biaxial tension field

$$(\sigma_x^0, \sigma_{xy}^0, \sigma_{yz}^0, \sigma_{zx}^0) = 0, \quad (\sigma_y^0, \sigma_z^0) = (\sigma, \nu\sigma), \tag{8}$$

where (x, y, z) are Cartesian coordinates and σ is a positive constant. We invoke symmetry to study the crack problem in half-space $y > 0$ as the superposition

$$\mathbf{u} = \mathbf{u}^C + \mathbf{u}^0, \quad \theta = \theta^C, \tag{9}$$

where \mathbf{u}^0 corresponds to (8) and $(\mathbf{u}^C, \mathbf{S}^C, \theta^C)$ are governed by (1)–(6) in the plane-strain limit, that is,

$$\mathbf{u}^C = \mathbf{u}^C(x, y, s) = (u_x^C, u_y^C), \quad \mathbf{S}^C = \mathbf{S}^C(x, y, s) = (\sigma_x^C, \sigma_y^C, \sigma_z^C, \sigma_{xy}^C), \quad \theta^C = \theta^C(x, y, s).$$

In addition, for $y > 0$ initial conditions are

$$s \leq 0 : (\mathbf{u}^C, \mathbf{S}^C, \theta^C) \equiv 0. \tag{10}$$

For $s > 0$, boundary conditions are

$$y = 0 : \sigma_y^C = -\sigma \ (x < 0), \quad u_y^C = 0 \ (x > 0), \quad \left(\sigma_{xy}^C, \frac{\partial \theta^C}{\partial y} \right) = 0. \tag{11}$$

For $y > 0$ and finite $s \geq 0$, $(\mathbf{u}^C, \mathbf{S}^C, \theta^C)$ must also be bounded above as $\sqrt{x^2 + y^2} \rightarrow \infty$. The condition on θ^C in (11) means that no heat is assumed to flow across the crack plane.

Initial/mixed boundary value problem

We adopt a Wiener–Hopf technique [Noble 1958] whereby the mixed conditions in (11) are replaced for $s > 0$ by the unmixed set

$$y = 0 : \sigma_y^C = -\sigma H(-x) + \Sigma_+(x, s)H(x), \quad u_y^C = V_-(x, s)H(-x), \tag{12}$$

where $H()$ is the Heaviside function, (Σ_+) is the the unknown traction ahead of the crack edge, and (V_-) is the unknown crack opening displacement. The function $\Sigma_+(x, s)$ must be integrable for $x \geq 0$ and bounded and continuous for $x > 0$, while $V_-(x, s)$ must be bounded and continuous for $x < 0$, and vanish as $x \rightarrow 0$.

Unilateral [Sneddon 1972] and bilateral [Van der Pol and Bremmer 1950] Laplace transforms over temporal and spatial variables (s, x) are defined, respectively, as

$$\hat{f}(x) = \int_0^\infty f(x, s)e^{-ps} ds, \quad \tilde{f} = \int_{-\infty}^\infty \hat{f}(x)e^{-pqx} dx, \tag{13}$$

where the transform variables (p, q) are real and imaginary, respectively, with $p > 0$. Application of (13) to (1)–(6) in view of the boundary conditions in (10), (12), the unmixed conditions in (11), the boundedness of (Σ_+, V_-) and $(\mathbf{u}^C, \mathbf{S}^C, \theta^C)$ produces a coupled set of linear ordinary differential equations. For $y > 0$, these yield the transforms

$$\begin{bmatrix} \tilde{u}_x^C \\ \tilde{u}_y^C \\ \frac{ap}{\alpha_v d_2} \tilde{\theta}^C \end{bmatrix} = \begin{bmatrix} q & q & B \\ -A_+ & -A_- & q \\ k_0^2 - k_+^2 & k_0^2 - k_-^2 & 0 \end{bmatrix} \begin{bmatrix} U_+ e^{-pA_+ y} \\ U_- e^{-pA_- y} \\ U_B e^{-pBy} \end{bmatrix}, \tag{14a}$$

$$\begin{bmatrix} \tilde{\sigma}_x^C \\ \tilde{\sigma}_y^C \\ \tilde{\sigma}_z^C \\ \tilde{\sigma}_{xy}^C \end{bmatrix} = \mu p \begin{bmatrix} 1 - 2A_+^2 & 1 - 2A_-^2 & 2qB \\ T & T & -2qB \\ T - 2A_+^2 & T - 2A_-^2 & 0 \\ -2qA_+ & -2qA_- & -T \end{bmatrix} \begin{bmatrix} U_+ e^{-pA_+ y} \\ U_- e^{-pA_- y} \\ U_B e^{-pBy} \end{bmatrix}, \tag{14b}$$

where U_\pm and U_B are arbitrary functions of (p, q) , and

$$A_\pm = \sqrt{k_\pm^2 - q^2}, \quad B = \sqrt{1 - q^2}, \quad T = 1 - 2q^2 \tag{15a}$$

$$k_\pm = \frac{k_0}{2\sqrt{hp}} \left(\sqrt{(\sqrt{hp} + \sqrt{ad_1})^2 + \varepsilon d} \pm \sqrt{(\sqrt{hp} - \sqrt{ad_1})^2 + \varepsilon d} \right), \quad k_0 = \frac{1}{\sqrt{a}}, \tag{15b}$$

$$(1) : d = d_1, \quad (2) : d = d_2, \quad (F) : d = d_1 = 1. \tag{15c}$$

The thermal relaxation factors (d_1, d_2) in (15c) are defined by

$$(k_0^2 - k_+^2)(k_0^2 - k_-^2) = -k_0^4 \frac{\varepsilon d}{hp}, \quad d_1 = 1 + h_1 p, \quad d_2 = 1 + h_2 p. \tag{16}$$

For positive real p , (14a) and (14b) are bounded above for $y \rightarrow \infty$ only when branches $\text{Im}(q) = 0$, $|\text{Re}(q)| > (k_{\pm}, 1)$ are introduced, so that $\text{Re}(A_{\pm}, B) \geq 0$ in the corresponding cut planes. For positive real p ,

$$k_+ > k_0 > k_-, \quad k_- < 1 \tag{17a}$$

$$hp \leq \frac{m + \varepsilon}{m(1 - l_1) - \varepsilon l} : k_+ \geq 1 \tag{17b}$$

$$hp \geq \frac{m + \varepsilon}{m(1 - l_1) - \varepsilon l} : k_+ \leq 1 \tag{17c}$$

$$(1) : l = l_1 = \frac{h_1}{h} \quad (2) : l = \frac{h_2}{h}, \quad l_1 = \frac{h_1}{h} \quad (F) : l = l_1 = 1. \tag{17d}$$

Thus, the value of positive real p defines the relative position of the branch points of (A_+, B) . Using (12) and the unmixed conditions in (11) in view of (14a) and (14b) gives

$$(U_+, U_-) = \frac{T}{\mu R} (A_-, -A_+) \left(\tilde{\Sigma}_+ - \frac{\sigma}{p^2 q} \right), \tag{18a}$$

$$U_B = \frac{2q A_+ A_-}{\mu R} (k_- - k_+) \left(\tilde{\Sigma}_+ - \frac{\sigma}{p^2 q} \right), \tag{18b}$$

$$R = (k_0^2 - k_-^2) A_- R_+ - (k_0^2 - k_+^2) A_+ R_-, \quad R_{\pm} = 4q^2 A_{\pm} B^2 + T^2, \tag{18c}$$

subject to the constraint

$$\frac{A_+ A_-}{\mu p R} (k_-^2 - k_+^2) \left(\tilde{\Sigma}_+ - \frac{\sigma}{p^2 q} \right) = \tilde{V}_-. \tag{19}$$

We solve Equation (19), which is of the Wiener–Hopf type, using (13) such that transforms $(\tilde{\Sigma}_+, \tilde{V}_-)$ are analytic in the overlapping regions $\text{Re}(q) > 0-$ and $\text{Re}(q) < 0+$, respectively, of the q -plane for positive real p .

Wiener–Hopf solution

In light of (15a) and (17), the term $A_+ A_-$ can be written as the product of factors $\sqrt{k_+ + q} \sqrt{k_- + q}$ and $\sqrt{k_+ - q} \sqrt{k_- - q}$ that are analytic for positive real p in the overlapping regions $\text{Re}(q) > -k_-$ and $\text{Re}(q) < k_-$. Equation (18c) gives a Rayleigh function that for positive real p has branch cuts $\text{Im}(q) = 0$, $|\text{Re}(q)| > k_-$ and isolated real roots at $q = \pm k_R$ ($0 < k_R < k_-$), and is given as

$$\frac{R}{q^2 A_-} \approx 2(k_+^2 - k_-^2)(k_0^2 - 1) (|q| \rightarrow \infty). \tag{20}$$

It follows that the function

$$G = \frac{R}{2(k_+^2 - k_-^2)(k_0^2 - 1) A_- (q^2 - k_R^2)} \tag{21}$$

has branch cuts $\text{Im}(q) = 0$, $k_- < |\text{Re}(q)| < \max(1, k_+)$ but no isolated roots or poles, is integrable at $q = \pm k_-$, and approaches unity for $|q| \rightarrow \infty$. It can therefore be written as the product $G_+ G_-$, where

G_{\pm} are analytic in overlapping regions $\text{Re}(q) > -k_-$ and $\text{Re}(q) < k_-$, respectively. For positive real p , we apply a standard technique [Noble 1958] for case (17b) and (17c) of the form, respectively,

$$\begin{aligned} \ln G_{\pm}(q) &= -\frac{1}{\pi} \int_{k_-}^1 \frac{\psi_b dt}{t \pm q} + \frac{1}{\pi} \int_1^{k_+} \frac{\psi dt}{t \pm q}, \\ \ln G_{\pm}(q) &= -\frac{1}{\pi} \int_1^{k_-} \frac{\psi_c dt}{t \pm q} + \frac{1}{\pi} \int_{k_-}^{k_+} \frac{\psi dt}{t \pm q}, \end{aligned} \tag{22}$$

where

$$\begin{aligned} \psi_b &= \tan^{-1} \frac{\sqrt{t^2 - k_-^2}}{(k_+^2 - k_0^2)T^2} \left(4(k_+^2 - k_-^2)t^2 B + (k_0^2 - k_-^2) \frac{T^2}{A_+} \right), \\ \psi_c &= \tan^{-1} \frac{4(k_+^2 - k_-^2)t^2 A_+ A_- \sqrt{t^2 - 1}}{T^2[(k_0^2 - k_-^2)A_- - (k_0^2 - k_+^2)A_+]}, \\ \psi &= \tan^{-1} \frac{T^2 (k_0^2 - k_-^2) \sqrt{t^2 - k_-^2}}{A_+ 4(k_+^2 - k_-^2) \sqrt{t^2 - 1} \sqrt{t^2 - k_-^2} + (k_0^2 - k_+^2)T^2 A_+}. \end{aligned} \tag{23}$$

Because (G_{\pm}, G) are all analytic at $q = 0$, (21) and (22) also yield the Rayleigh root as

$$k_R = \frac{1}{G_0} \sqrt{\frac{k_+^2 + k_-^2 + k_+ k_- - k_0^2}{2k_-(k_+ + k_-)(1 - k_0^2)}}, \quad G_0 = G_+(0) = G_-(0) \tag{24}$$

We can perform multiplication of (19) and rearrange terms to produce an equation whose sides are single-valued in overlapping regions $\text{Re}(q) > 0-$ and $\text{Re}(q) < 0+$. We then render the sides analytic in their respective regions by appropriate addition and subtraction of the residues of poles at $q = (0+, -\sqrt{k_R})$ that remain after multiplication and factorization. The result is

$$\begin{aligned} 2(k_0^2 - 1)G_-(q) \frac{q - k_R}{\sqrt{k_+ - q}} \tilde{V}_- + \frac{\sigma}{\mu p^3} \frac{\sqrt{k_+}}{k_R G_+(0)q} \\ = \frac{\sigma}{\mu p^3 q} \left(\frac{\sqrt{k_+}}{k_R G_+(0)} - \frac{\sqrt{k_+ + q}}{G_+(q)(q + k_R)} \right) - \frac{\tilde{\Sigma}_+}{\mu p} \frac{\sqrt{k_+ + q}}{G_+(q)(q + k_R)}. \end{aligned} \tag{25}$$

Here the left and right sides are analytic for $\text{Re}(q) < 0+$ and $\text{Re}(q) > 0-$, respectively, and must be analytic continuations of a bounded entire function in the q -plane. That V_- must vanish continuously as $x \rightarrow 0-$ implies, in light of (13), that

$$pq \tilde{V}_- \rightarrow 0 \quad (|q| \rightarrow \infty). \tag{26}$$

Thus, the left-hand side of (25) vanishes as $|q| \rightarrow \infty$, such that the entire function vanishes, and Equation (25) becomes

$$\tilde{\Sigma}_+ = \frac{\sigma}{p^2 q} \left(\frac{\sqrt{k_+} G_+(q)}{G_+(0) \sqrt{k_+ + q}} \frac{q + k_R}{k_R} - 1 \right) \tag{27a}$$

$$\tilde{V}_- = \frac{\sigma}{2\mu(1 - k_0^2)p^3} \frac{\sqrt{k_+} \sqrt{k_+ - q}}{G_+(0) G_-(q) k_R (q - k_R) q}. \tag{27b}$$

We then combine Equation (14a), (18) and (27) to obtain the temperature change transform

$$\tilde{\theta}^C = \frac{-\varepsilon \sigma}{2\mu \alpha_v m} \frac{d}{hp^3 d_2} \left(\frac{1}{A_+} - \frac{1}{A_-} \right) \frac{\sqrt{k_+} \sqrt{k_+ - q}}{G_+(0) G_-(q) k_R (q - k_R)} \frac{1}{(k_+^2 - k_-^2) q}, \tag{28a}$$

$$(1) : d = d_1, d_2 = 1, \quad (2) : d = d_2, \quad (F) : d = d_2 = 1, \tag{28b}$$

for $y = 0$, where (18) holds.

Transient response ahead of a crack

In view of (14a) and (14b), (18) and (27) we can construct an exact transform solution for \mathbf{u}^C . The dynamic stress intensity factor for the total field \mathbf{u} , however, can be studied directly using (27a). The bilateral Laplace transform [Van der Pol and Bremmer 1950] has the inverse

$$\hat{f}(x) = \frac{p}{2\pi i} \int \tilde{f} e^{pqx} dq, \tag{29}$$

where p is real and positive, and for $\tilde{\Sigma}_+$ integration can be along the positive real side of the entire $\text{Im}(q)$ axis. However the first and second terms in (27a) exhibit, respectively, only the branch cut $\text{Im}(q) = 0, \text{Re}(q) < -\sqrt{k_+}$ and the pole $q = 0$. The integrand in (29) decays exponentially as $|q| \rightarrow 0$ for $x > 0$ in the same region, so that residue theory can be used to give the temporal transform

$$\hat{\Sigma}_+ = -\frac{\sigma}{p} + \frac{\sigma}{\pi p^2} \sqrt{2(1 - k_0^2)} \sqrt{\frac{k_+ k_- (k_+ + k_-)}{k_+^2 + k_-^2 + k_+ k_- - k_0^2}} \int_{k_+}^{\infty} \frac{G_-(u) (k_R - u)}{u \sqrt{u - k_+}} e^{-pux} du. \tag{30}$$

Integrating over positive real u , and using (24), we eliminate the product $k_R G_+(0)$. For $x \rightarrow 0+$ we find an asymptotic form for the integral in (30) analytically. Then, in view of (8), (9), (13), (15), (16) and (28) the temporal transform of the normal traction ahead of the crack edge ($y = 0, x \approx 0+$) is

$$\hat{\sigma}_y = \sqrt{\frac{2(1 - k_0^2)}{\pi x}} \frac{\sigma}{p^{3/2}} \sqrt{\frac{k_+ k_- (k_+ + k_-)}{k_+^2 + k_-^2 + k_+ k_- - k_0^2}} + O(x). \tag{31}$$

Study of (28) shows that we can find a similar analytic solution for positive real p in the q -plane. Thus, for $y = 0, x \approx 0+$, and using (9) and (29),

$$\hat{\theta} = \frac{-\varepsilon\sigma}{\mu\alpha_v} \frac{k_0^2 d}{hp^3 d_2} \frac{k_+ k_-}{k_+ - k_-} \frac{1}{k_+^2 + k_-^2 + k_+ k_- - k_0^2} + \frac{\varepsilon\sigma}{\mu\alpha_v} \frac{d}{hd_2(k_+ - k_-)p^{3/2}} \sqrt{\frac{k_+ k_-}{(k_+^2 + k_-^2 + k_+ k_- - k_0^2)(k_+ + k_-)}} \frac{1}{\sqrt{\pi(1 - k_0^2)x}} + O(x). \tag{32}$$

In light of (22) and (23), (31) and (32) are insensitive to any formal distinction between cases (17b), and (17c). Equations (16) and (28b) again govern parameters (d, d_2). The isothermal result corresponding to (31) is extracted from work by Achenbach [1973] and inverted to give

$$\sigma_y^i = 2\sigma \sqrt{\frac{2(1 - k_0^2)}{\pi\sqrt{a}}} \sqrt{\frac{s}{x}} + O(x) \quad (y = 0, x \approx 0+). \tag{33}$$

We can compare transient isothermal and thermoelastic crack edge stresses by examining the dimensionless ratio of the transform inversions of the singular terms in (31) with those in (33), that is,

$$\frac{\sigma_y}{\sigma_y^i} \Big|_{(y=0, x \approx 0+)} = \left(\frac{K_1}{K_i}, \frac{K_2}{K_i}, \frac{K_F}{K_i} \right), \tag{34}$$

where $K_i, K_1, K_2,$ and K_F are coefficients of the dynamic stress intensity factors for respectively, the isothermal model, the thermal relaxation models 1 and 2, and the Fourier model. The coefficient for the isothermal model is defined as

$$K_i = \frac{2}{a^{1/4}} \sqrt{\frac{s}{\pi}}. \tag{35}$$

By (15) the temporal transforms for $K_1, K_2,$ and K_F are

$$\begin{aligned} \hat{K}_1 &= \frac{((\sqrt{hp} + \sqrt{ad_1})^2 + \varepsilon d_1)^{1/4}}{p^{3/2} \sqrt{a_\varepsilon \sqrt{d_1} + \sqrt{ahp}}}, \quad a_\varepsilon = a + \varepsilon, \\ \hat{K}_2 &= \frac{d_1^{1/4} ((\sqrt{hp} + \sqrt{ad_1})^2 + \varepsilon d_2)^{1/4}}{p^{3/2} \sqrt{ad_1 + \varepsilon d_2 + \sqrt{ahpd_1}}}, \\ \hat{K}_F &= \frac{((\sqrt{a} + \sqrt{hp})^2 + \varepsilon)^{1/4}}{p^{3/2} \sqrt{a_\varepsilon + \sqrt{ahp}}}. \end{aligned} \tag{36}$$

Similarly, transient temperature changes at the crack edge for the thermal relaxation and Fourier models can be compared in terms of the dimensionless ratios

$$\frac{\theta}{\theta_F} \Big|_{(y=0, x \approx 0+)} = \left(\frac{K_1^T}{K_F^T}, \frac{K_2^T}{K_F^T} \right), \tag{37}$$

where K_1^T , K_2^T and K_F^T are coefficients of the singular terms in (32). Their temporal transforms are

$$\hat{K}_1^T = \frac{d_1}{p^{3/2}[(\sqrt{hp} + \sqrt{ad_1})^2 + \varepsilon d_1]^{1/4}} \frac{1}{\sqrt{(\sqrt{hp} - \sqrt{ad_1})^2 + \varepsilon d_1} \sqrt{a_\varepsilon \sqrt{d_1} + \sqrt{ahp}}}, \tag{38a}$$

$$\hat{K}_2^T = \frac{d_1^{1/4}}{p^{3/2}[(\sqrt{hp} + \sqrt{ad_1})^2 + \varepsilon d_2]^{1/4}} \frac{1}{\sqrt{(\sqrt{hp} - \sqrt{ad_1})^2 + \varepsilon d_2} \sqrt{ad_1 + \varepsilon d_2 + \sqrt{ahpd_1}}}, \tag{38b}$$

$$\hat{K}_F^T = \frac{1}{p^{3/2}[(\sqrt{hp} + \sqrt{a})^2 + \varepsilon]^{1/4}} \frac{1}{\sqrt{(\sqrt{hp} - \sqrt{a})^2 + \varepsilon} \sqrt{a_\varepsilon + \sqrt{ahp}}}. \tag{38c}$$

Some numerical results

To demonstrate the behavior of (34) and (37), consider 4340 steel initially at rest at room temperature (294 K) with elastic properties [Brock 2006]

$$v = \frac{1}{3}, \quad \rho = 7834 \text{ kg/m}^3, \quad \mu = 75 \text{ GPa},$$

and thermal properties

$$c_v = 448 \text{ J/kgK}, \quad \alpha_v = 88.2(10^{-6}) \text{ 1/K}, \quad K = 34.6 \text{ W/mK},$$

$$t_1 = 0.75(10^{-13}) \text{ s}, \quad t_2 = 0.5(10^{-13}) \text{ s}.$$

The ratios in (36) and (38) are actually functions of dimensionless parameter s/h . In light of (6), the following correspondence holds:

$$\frac{s}{h} = 1.0: \quad 1.233(10^{-12}) \text{ s}. \tag{39}$$

we use a standard procedure [Weeks 1966] to carry out numerical inversion of (36) and (38).

For fluids, thermal relaxation effects may be most prominent near a disturbance (here, the crack edge) for extremely short times after the disturbance arises [Fan and Lu 2002]. Therefore, our calculations of (34) and (37) are given in Table 1 for values $s/h \ll 1$ and $s/h \gg 1$ that correspond to the nano-second range.

For the stress field ratios of Equation (34), all three thermoelastic models serve to relax the isothermal crack edge stress, but by margins of less than 1%. For $s/h \ll 1$ some variation exists between the thermoelastic models. The result of the Fourier model is closer to the isothermal model than either of the thermal relaxation models. In addition, for $s/h \ll 1$ the differences between results of the isothermal and thermoelastic models decrease with time. For $s/h \gg 1$, however, all three thermoelastic models produce essentially the same constant deviation from the isothermal result.

For transient temperature changes at the crack edge of (37), much more transient behavior is seen for $s/h \ll 1$. Crack edge temperature changes for models 1 and 2 exceed the Fourier model change. For model 1 the deviation is orders of magnitude larger, but for both relaxation models, the deviations themselves diminish with s/h . This domination by model 1 can be predicted by noting that transforms

(38a), (38b) are proportional to $(d_1, d_1^{1/4})$, respectively. In light of (16)

$$\frac{\hat{K}_1^T}{\hat{K}_2^T} \approx O(p^{3/4}) \quad (p \rightarrow \infty). \quad (40)$$

Therefore it is not surprising that an asymptotic analysis gives

$$\frac{K_1^T}{K_2^T} \approx O\left(\frac{h}{s}\right), \quad \left(\frac{s}{h} \rightarrow 0\right). \quad (41)$$

For $s/h \gg 1$ the crack edge temperature changes for models 1 and 2 are essentially identical. They fall below the Fourier model change, but the deviation is almost negligible and decreases with s/h . In view of (39) it is less than 0.1% at times after crack opening of nano-second order.

Discussion and conclusions

In this article we treat the transient problem of a semiinfinite crack that opens instantaneously in an isotropic, homogeneous solid that is initially at rest at uniform temperature in a state of uniform plane strain. The coupled thermoelastic governing equations for the solid included as special cases thermal models with one [Lord and Shulman 1967] and two [Green and Lindsay 1972] relaxation times, as well as the classical Fourier model [Chadwick 1960].

To solve the initial/mixed boundary value problem, we used integral transforms and a Wiener–Hopf technique. We obtained exact expressions for the temporal transforms of the normal stress and temperature change near the crack edge. Numerical inversion for 4340 steel gave dimensionless ratios of crack edge stress for the three thermoelastic models with the isothermal result, and temperature change at the crack edge for the two thermal relaxation models with the Fourier model.

Calculations for crack edge stress showed that all three thermoelastic models relaxed the isothermal crack edge stress, but by less than 1%. Moreover, within time intervals on the order of a nanosecond after a crack opens, the deviations of the three thermoelastic models were essentially the same, and constant.

Calculations for temperature change at the crack edge showed pronounced transient behavior within a time interval of orders magnitude less than a nanosecond after a crack opens. Then, temperature changes at the crack edge for both thermal relaxation models exceeded values for the Fourier model. Indeed, deviation for the single-relaxation time model was by orders of magnitude. The deviation of both models did decrease with time. Within times on the order of a nanosecond, thermal relaxation changes were essentially identical, with values less than the Fourier results. However, the deviation was by a fraction of 1% in both cases. This behavior indicates that explicit inclusion of thermal relaxation in the constitutive equation [Green and Lindsay 1972] can serve to moderate short-time temperature change.

In summary, our results indicate that thermoelasticity may have a small effect on crack edge stress, and one that quickly becomes time-invariant and insensitive to thermal relaxation. Temperature changes at the crack edge, however, are highly transient early on, at which time thermal relaxation effects are dominant. By times of nano-second order, the Fourier model gives the larger changes, but the deviation is both negligible and decreasing.

$\frac{s}{h} \ll 1$	$\frac{K_1}{K_i}$	$\frac{K_2}{K_i}$	$\frac{K_F}{K_i}$	$\frac{K_1^T}{K_F^T}$	$\frac{K_2^T}{K_F^T}$
0.0001	0.9982	0.9988	0.9998	1522	1.416
0.001	0.99818	0.99875	0.9993	151	1.401
0.01	0.99813	0.99867	0.9978	13.739	1.258
$\frac{s}{h} \gg 1$					
100	0.99687	0.99687	0.9532	0.9915	0.9915
1000	0.99688	0.99687	0.9831	0.9968	0.9968
10,000	0.9969	0.9969	0.9969	0.9989	0.9989
100,000	0.9969	0.9969	0.9969	0.9996	0.9996

Table 1. Dimensionless ratios of crack edge stress and temperature change versus dimensionless time ($s/h = 1 : 1.233(10^{-12}) s$).

As a dynamic fracture model, the canonical problem treated here is especially idealized because plastic yield is neglected, and the crack opens instantaneously along its entire length. Nevertheless, both the relative insensitivity of crack edge stress to thermoelasticity, and the highly transient temperature changes at the crack edge, which are sensitive to thermal relaxation seen here, may be worth noting when considering a less idealized situation.

References

- [Achenbach 1973] J. D. Achenbach, *Wave propagation in elastic solids*, North-Holland, Amsterdam, 1973.
- [Brock 2004] L. M. Brock, “Dynamic contact and fracture: Some results for transversely isotropic solids”, pp. 50–60 in *Proceedings of the Seventh National Congress on Mechanics*, Technical University of Crete, Chania, 2004.
- [Brock 2006] L. M. Brock, “[Debonding of a thermoelastic material from a rigid substrate at any constant speed: Thermal relaxation effects](#)”, *Acta Mech.* **184**:1–4 (2006), 171–188.
- [Chadwick 1960] P. Chadwick, “Thermoelasticity: The dynamical theory”, pp. 263–328 in *Progress in solid mechanics*, vol. 1, edited by I. N. Sneddon and R. Hill, North-Holland, Amsterdam, 1960.
- [Chandrasekharia 1986] D. S. Chandrasekharia, “Thermoelasticity with second sound”, *Appl. Mech. Rev.* **39** (1986), 355–376.
- [Fan and Lu 2002] Q. M. Fan and W. Q. Lu, “[A new numerical method to simulate the non-Fourier heat conduction in a single-phase medium](#)”, *Int. J. Heat Mass Transf.* **45**:13 (2002), 2815–2821.
- [Freund and Hutchinson 1985] L. B. Freund and J. Hutchinson, “[High strain-rate growth in rate-dependent plastic solids](#)”, *J. Mech. Phys. Solids* **33**:2 (1985), 169–191.
- [Green and Lindsay 1972] A. E. Green and K. A. Lindsay, “[Thermoelasticity](#)”, *J. Elasticity* **2**:1 (1972), 1–7.
- [Joseph and Preziosi 1989] D. D. Joseph and L. Preziosi, “[Heat waves](#)”, *Rev. Mod. Phys.* **61**:1 (1989), 41–73.
- [Lord and Shulman 1967] H. W. Lord and Y. Shulman, “[A generalized dynamical theory of thermoelasticity](#)”, *J. Mech. Phys. Solids* **15**:5 (1967), 299–309.
- [Mason and Rosakis 1993] J. J. Mason and A. J. Rosakis, “[The effects of hyperbolic heat conduction around a dynamically propagating crack tip](#)”, *Mech. Mater.* **15**:4 (1993), 263–278.

- [Noble 1958] B. Noble, *Methods based on the Wiener–Hopf technique*, Pergamon, New York, 1958.
- [Noda et al. 1989] N. Noda, Y. Matsunaga, T. Tsuji, and H. Nyuko, “Thermal shock problems of elastic bodies with cracks”, *J. Therm. Stresses* **12** (1989), 369–384.
- [Van der Pol and Bremmer 1950] B. Van der Pol and H. Bremmer, *Operational calculus based on the two-sided Laplace integral*, Cambridge University Press, London, 1950.
- [Rice and Levy 1969] J. R. Rice and N. Levy, “Local heating by plastic deformation of a crack tip”, pp. 277–293 in *Physics of strength and plasticity*, edited by A. S. Argon, MIT Press, Cambridge, MA, 1969.
- [Rizk and Radwan 1993] A. A. Rizk and S. F. Radwan, “Fracture of a plate under transient thermal stress”, *J. Therm. Stresses* **16** (1993), 79–102.
- [Sharma and Sharma 2002] J. N. Sharma and P. K. Sharma, “Free vibrations of homogeneous transversely isotropic thermo-elastic cylindrical panel”, *J. Therm. Stresses* **25**:2 (2002), 169–182.
- [Sneddon 1972] I. N. Sneddon, *The use of integral transforms*, McGraw-Hill, New York, 1972.
- [Sumi and Katayama 1980] N. Sumi and T. Katayama, “Thermal stress singularities at tips of a Griffith crack in a finite rectangular plate”, *Nucl. Eng. Des.* **60**:3 (1980), 389–394.
- [Weeks 1966] W. T. Weeks, “Numerical inversion of Laplace transforms using Laguerre functions”, *J. ACM* **13**:3 (1966), 419–429.

Received 5 Mar 2006. Accepted 12 May 2006.

LOUIS MILTON BROCK: brock@engr.uky.edu

265 RGAN, Mechanical Engineering, University of Kentucky, Lexington, KY 40506-0503, United States

MARK TODD HANSON: hanson@engr.uky.edu

286 RGAN, Mechanical Engineering, University of Kentucky, Lexington, KY 40506-0503, United States

3D GREEN'S FUNCTIONS FOR A STEADY POINT HEAT SOURCE INTERACTING WITH A HOMOGENEOUS IMPERFECT INTERFACE

X. WANG AND L. J. SUDAK

The image method is applied to derive the three-dimensional temperature field induced by a steady point heat source interacting with a homogeneous imperfect interface. Our approach is a straightforward extension of that of Sommerfeld who addressed the half-space Green's function for a steady point heat source at the beginning of the last century. Both weakly and highly conducting type imperfect interface conditions are considered. It is found that the temperature field for both types of imperfect interface is only dependent on the two-phase conductivity parameter and another parameter measuring the interface "rigidity". As an application, we discuss the Coulomb force on a static point electric charge due to its interaction with the imperfect interface. It is possible to find an equilibrium position for the electric charge interacting with an imperfect interface. In addition, the equilibrium position is stable provided the interface is weakly conducting whereas the equilibrium position is unstable if the interface is highly conducting.

1. Introduction

Recently, Ang et al. [2004] calculated the steady state two-dimensional temperature field in a thermally isotropic bimaterial with a homogeneous imperfect interface. They derived a special Green's function for a steady line heat source in two bonded half-planes with an imperfect interface so as to devise a boundary element method (BEM) which does not require the interface to be discretized. As discussed in [Ang et al. 2004], the problem is two-dimensional, in that the temperature is independent of a certain coordinate (say, the z -coordinate) and the imperfect interface is a weakly conducting one. The weakly conducting interface is based on the assumption that the normal component of heat flux is continuous but that the temperature across the interface is discontinuous. More precisely, the jump in temperature is proportional to the normal component of heat flux. Discussions on weakly conducting interface can also be found in the works of [Benveniste and Miloh 1986; Ru and Schiavone 1997; Chen 2001], among others. For a highly conducting interface, the temperature is continuous across the interface, whereas the normal component of the heat flux has a discontinuity across the interface which is proportional to a certain differential expression of the temperature (see [Miloh and Benveniste 1999; Chen 2001; Benveniste 2006] among others).

At the beginning of the last century, [Sommerfeld 1926; 1978] derived the half-space Green's function for a steady point heat source by using the image method. As stated by Ochmann [2004], "Sommerfeld [1978] treated the half-space problem by writing the total thermal field as a superposition of an original

This work is supported by the Natural Sciences and Engineering Research Council of Canada through NSERC Grant No. 249516.

Keywords: imperfect interface, point heat source, image method.

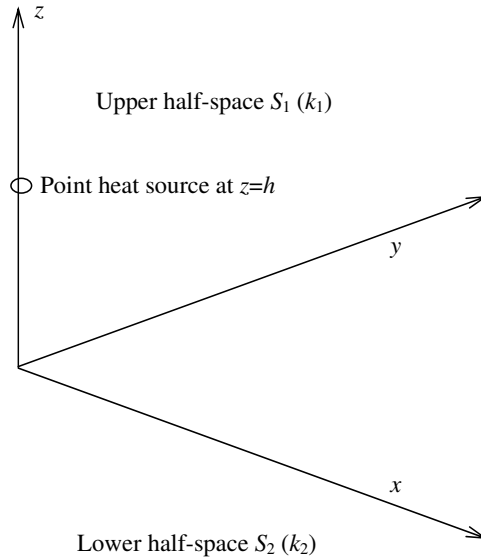


Figure 1. A steady point heat source in two imperfectly bonded half-spaces.

heat source, a mirror source and a line integral combined of single thermal sources placed at the z -axis below the mirror source”. We note that Sommerfeld’s technique has been recently extended to address the sound field caused by a monopole source above an impedance plane by means of the complex image method [Ochmann 2004; Taraldsen 2005b; Taraldsen 2005a]. Sommerfeld’s method can guide us on the matter of how to conceive the Green’s functions for a steady heat source in two imperfectly bonded half-spaces. Here we write the total temperature field in the upper half-space, in which the heat source is located at $(0, 0, h)$, ($h > 0$), as a superposition of the original heat source, a mirror source, and a line integral combined of single thermal sources placed at the z -axis below the mirror source. On the other hand, we write the temperature field in the lower half-space as a line integral combined of single thermal sources placed at the z -axis above the location of the original heat source. We find that by using this method, we can arrive at the Green’s function for both a weakly conducting interface and a highly conducting one.

The objective of the present work is to seek the possibility of deriving the corresponding three-dimensional Green’s functions for a steady point heat source in two bonded half-spaces with a weakly or highly conducting interface. The expressions of the derived Green’s functions should be as simple as possible in order to conveniently incorporate them in BEM.

2. Preliminaries

In a fixed Cartesian coordinate system (x, y, z) , we consider the upper and the lower half-spaces, $S_1 : z \geq 0$ and $S_2 : z \leq 0$, in which the conductivity of each phase is denoted by k_1 and k_2 , as shown in Figure 1.

The two half-spaces are separated by the imperfect interface $z = 0$. Let T be the temperature field and the heat fluxes are given by $q_x = -kT_{,x}$, $q_y = -kT_{,y}$, $q_z = -kT_{,z}$. A steady point heat source of strength H is located at the point $(0, 0, h)$, ($h > 0$) in the upper half-space. Under steady state conditions, the temperature obeys the three-dimensional inhomogeneous Laplace equation

$$\frac{\partial^2 T}{\partial x^2} + \frac{\partial^2 T}{\partial y^2} + \frac{\partial^2 T}{\partial z^2} = -\frac{H}{k_1} \delta(x) \delta(y) \delta(z - h), \quad \text{in } S_1 \text{ and } S_2, \quad (1)$$

where $\delta(*)$ is the Dirac delta function.

For a weakly conducting interface, the normal heat flux is continuous, whereas the temperature field undergoes a discontinuity which is proportional to the normal heat flux as

$$k_1 \frac{\partial T_1}{\partial z} = k_2 \frac{\partial T_2}{\partial z} = \alpha(T_1 - T_2), \quad (z = 0), \quad (2)$$

where the nonnegative interface parameter α is defined by

$$\alpha = \lim_{\substack{t \rightarrow 0 \\ k_0 \rightarrow 0}} \frac{k_0}{t}, \quad (3)$$

and where k_0 and t are respectively the interphase conductivity and its thickness. The case where $\alpha \rightarrow \infty$ corresponds to a perfectly bonded interface whereas $\alpha = 0$ stands for adiabatic contact. In this work we assume that α is constant (that is, the imperfection is uniformly distributed over the interface).

For a highly conducting interface, the temperature field is continuous whereas the normal heat flux undergoes a discontinuity of the type

$$T_1 = T_2, \quad k_2 \frac{\partial T_2}{\partial z} - k_1 \frac{\partial T_1}{\partial z} = \beta \Delta_s T_1 = \beta \Delta_s T_2, \quad (z = 0), \quad (4)$$

where

$$\Delta_s T_1 = \frac{\partial^2 T_1}{\partial x^2} + \frac{\partial^2 T_1}{\partial y^2}$$

is the operator of the surface Laplacian and the nonnegative interface parameter β is defined by

$$\beta = \lim_{\substack{t \rightarrow 0 \\ k_0 \rightarrow \infty}} k_0 t. \quad (5)$$

The case where $\beta = 0$ corresponds to a perfectly bonded interface, whereas $\beta \rightarrow \infty$ describes contact with a medium of infinite conductivity. In writing Equation (4), it has been assumed that β is a constant.

Following the idea of [Sommerfeld 1978] who treated half-space problems of heat conduction, let us write the total temperature field in the upper half-space as a superposition of the original heat source at $(0, 0, h)$, a mirror source at $(0, 0, -h)$ and a line integral combined of single thermal sources placed at the z -axis below the mirror source. By contrast, let us write the temperature field in the lower half-space as a line integral combined of single thermal sources placed at the z -axis above the location of the original heat source. Thus, the distribution of temperature in the upper and lower half-spaces can be expressed

as

$$T_1 = \frac{H}{4\pi k_1} \left(\frac{1}{\sqrt{x^2 + y^2 + (z-h)^2}} + \frac{A}{\sqrt{x^2 + y^2 + (z+h)^2}} - B \int_0^{+\infty} \frac{\exp(-\gamma\eta)}{\sqrt{x^2 + y^2 + (z+h+\eta)^2}} d\eta \right), \quad (z \geq 0), \quad (6)$$

$$T_2 = \frac{HC}{4\pi k_1} \int_0^{+\infty} \frac{\exp(-\gamma\eta)}{\sqrt{x^2 + y^2 + (z-h-\eta)^2}} d\eta, \quad (z \leq 0), \quad (7)$$

where A , B , C and γ are unknowns to be determined.

3. A point heat source interacting with weakly conducting interface

Let us first consider a point heat source interacting with a weakly conducting interface described by Equation (2). Inserting Equations (6) and (7) into the interface condition (2) for a weakly conducting interface and using the following relations

$$\int_0^{+\infty} \frac{\exp(-\gamma\eta)}{\sqrt{x^2 + y^2 + (z+h+\eta)^2}} d\eta = \exp[\gamma(z+h)] \int_{z+h}^{+\infty} \frac{\exp(-\gamma q)}{\sqrt{x^2 + y^2 + q^2}} dq, \quad (8)$$

$$\int_0^{+\infty} \frac{\exp(-\gamma\eta)}{\sqrt{x^2 + y^2 + (z-h-\eta)^2}} d\eta = -\exp[-\gamma(z-h)] \int_{z-h}^{-\infty} \frac{\exp(\gamma q)}{\sqrt{x^2 + y^2 + q^2}} dq,$$

we arrive at the following set of linear algebraic equations

$$\begin{aligned} A &= 1, \\ k_1 B &= k_2 C, \\ k_1 B &= 2\alpha, \\ k_1 B \gamma &= \alpha(B + C). \end{aligned} \quad (9)$$

Consequently, the unknowns A , B , C and γ can be uniquely determined and given by

$$\begin{aligned} A &= 1, \\ B &= \frac{2\alpha}{k_1}, \\ C &= \frac{2\alpha}{k_2}, \\ \gamma &= \alpha \frac{k_1 + k_2}{k_1 k_2}. \end{aligned} \quad (10)$$

Thus, the explicit expressions for the temperature field in the two half-spaces are

$$T_1 = \frac{H}{4\pi k_1} \left(\frac{1}{\sqrt{x^2 + y^2 + (z-h)^2}} + \frac{1}{\sqrt{x^2 + y^2 + (z+h)^2}} - \frac{2\alpha}{k_1} \int_0^{+\infty} \frac{\exp(-\alpha \frac{k_1+k_2}{k_1 k_2} \eta)}{\sqrt{x^2 + y^2 + (z+h+\eta)^2}} d\eta \right), \quad (z \geq 0), \quad (11)$$

$$T_2 = \frac{\alpha H}{2\pi k_1 k_2} \int_0^{+\infty} \frac{\exp(-\alpha \frac{k_1+k_2}{k_1 k_2} \eta)}{\sqrt{x^2 + y^2 + (z-h-\eta)^2}} d\eta, \quad (z \leq 0). \quad (12)$$

Here it should be mentioned that the line integrals in Equations (11) and (12) are convergent due to the fact that

$$\gamma = \alpha \frac{k_1 + k_2}{k_1 k_2} > 0.$$

The distribution of temperature along the z -axis can be concisely given as

$$\tilde{T} = \begin{cases} \frac{1}{|\tilde{z}-1|} + \frac{1}{\tilde{z}+1} - \frac{2-\Gamma}{\tilde{z}+1} f\left(\lambda_1 \frac{\tilde{z}+1}{2}\right), & (\tilde{z} \geq 0), \\ \frac{\Gamma}{1-\tilde{z}} f\left(\lambda_1 \frac{1-\tilde{z}}{2}\right), & (\tilde{z} \leq 0), \end{cases} \quad (13)$$

where

$$\begin{aligned} \tilde{T} &= \frac{4\pi h k_1}{H} T, \\ \tilde{z} &= \frac{z}{h}, \\ \Gamma &= \frac{2k_1}{k_1 + k_2}, \\ \lambda_1 &= \alpha h \frac{k_1 + k_2}{k_1 k_2}, \end{aligned} \quad (14)$$

and $f(\lambda)$, which falls in the range between 0 and 1, is defined by [Fan and Wang 2003]

$$f(\lambda) = 2\lambda \exp(2\lambda) E_1(2\lambda), \quad (15)$$

with $E_1(2\lambda)$ being the exponential integral function defined as follows [Abramovitz and Stegun 1972]:

$$E_1(2\lambda) = \int_{2\lambda}^{\infty} \frac{\exp(-t)}{t} dt. \quad (16)$$

Expression (13) indicates that the distribution of temperature along the z -axis is totally reliant on the two-phase conductivity parameter Γ , ($0 \leq \Gamma \leq 2$) and λ_1 , which measures the interface ‘‘rigidity’’ [Fan and Wang 2003]. Figure 2 demonstrates the distribution of temperature along the z -axis for a weakly conducting interface under various values of λ_1 with $\Gamma = 1.2$. It is observed that temperature is continuous across the interface $z = 0$ only when $\lambda_1 = \infty$ for a perfect interface, otherwise the temperature will be discontinuous across the weakly conducting interface. The influence of the interface imperfections on the temperature distribution is especially apparent for those points very close to the interface. The

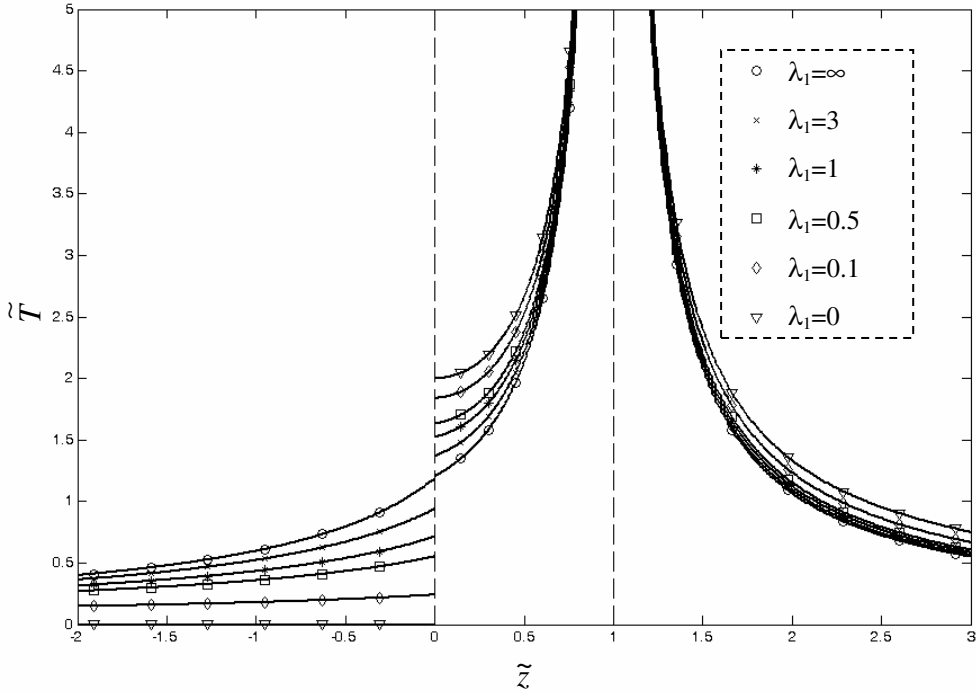


Figure 2. Distribution of the temperature along the z -axis for a weakly conducting interface with $\Gamma = 1.2$.

temperature in the positive z -axis is always higher than the corresponding one for a perfect interface, while the temperature in the negative z -axis is always lower than the corresponding one for a perfect interface.

4. A point heat source interacting with highly conducting interface

In this section, let us consider a point heat source interacting with a highly conducting interface, as described by Equation (4). Because the temperature field satisfies Laplace’s Equation (2), the interface conditions for a highly conducting interface can be equivalently expressed as

$$T_1 = T_2, \quad k_1 \frac{\partial T_1}{\partial z} - k_2 \frac{\partial T_2}{\partial z} = \beta \frac{\partial^2 T_1}{\partial z^2} = \beta \frac{\partial^2 T_2}{\partial z^2}, \quad (z = 0). \tag{17}$$

Inserting Equations (6) and (7) into the above interface conditions and using Equation (8), we arrive at the following set of linear algebraic equations

$$\begin{aligned} A &= -1, \\ B + C &= 0, \\ 2k_1 &= -\beta B, \\ k_1 + k_2 &= \beta\gamma. \end{aligned} \tag{18}$$

Consequently, the unknowns A, B, C and γ can be uniquely determined and given by

$$A = -1, \quad B = -\frac{2k_1}{\beta}, \quad C = \frac{2k_1}{\beta}, \quad \gamma = \frac{k_1 + k_2}{\beta}. \tag{19}$$

Thus, the explicit expressions for the temperature field in the two half-spaces are

$$T_1 = \frac{H}{4\pi k_1} \left(\frac{1}{\sqrt{x^2 + y^2 + (z - h)^2}} - \frac{1}{\sqrt{x^2 + y^2 + (z + h)^2}} + \frac{2k_1}{\beta} \int_0^{+\infty} \frac{\exp\left(-\frac{k_1+k_2}{\beta}\eta\right)}{\sqrt{x^2 + y^2 + (z + h + \eta)^2}} d\eta \right), \quad (z \geq 0), \tag{20}$$

$$T_2 = \frac{H}{2\pi\beta} \int_0^{+\infty} \frac{\exp\left(-\frac{k_1+k_2}{\beta}\eta\right)}{\sqrt{x^2 + y^2 + (z - h - \eta)^2}} d\eta, \quad (z \leq 0). \tag{21}$$

Here it should be mentioned that the line integrals in Equations (20) and (21) are convergent due to the fact that

$$\gamma = \frac{k_1 + k_2}{\beta} > 0.$$

The distribution of temperature along the z -axis can also be concisely given by

$$\tilde{T} = \begin{cases} \frac{1}{|\tilde{z}-1|} - \frac{1}{\tilde{z}+1} + \frac{\Gamma}{\tilde{z}+1} f\left(\lambda_2 \frac{\tilde{z}+1}{2}\right), & (\tilde{z} \geq 0), \\ \frac{\Gamma}{1-\tilde{z}} f\left(\lambda_2 \frac{1-\tilde{z}}{2}\right), & (\tilde{z} \leq 0), \end{cases} \tag{22}$$

where $\tilde{T}, \tilde{z}, \Gamma$ have been defined by Equation (14) and

$$\lambda_2 = \frac{h(k_1 + k_2)}{\beta}. \tag{23}$$

Expression (22) indicates that the distribution of temperature along the z -axis is totally reliant on Γ and λ_2 which also measures the interface “rigidity” as λ_1 . Figure 3 illustrates the distribution of temperature along the z -axis for a highly conducting interface under various values of λ_2 with $\Gamma = 1.2$. It is observed that temperature is always continuous across the highly conducting interface $z = 0$. The temperature along the total z -axis is always lower than the corresponding one for a perfect interface. By comparing Figures 2 and 3 we observe that the distributions of the temperature in the negative z -axis ($z \leq 0$) are the same for the two kinds of imperfect interface conditions when $\lambda_1 = \lambda_2$. In fact, by comparing Equation (12) with Equation (21), we find that the distribution of the temperature in the lower half-space is always

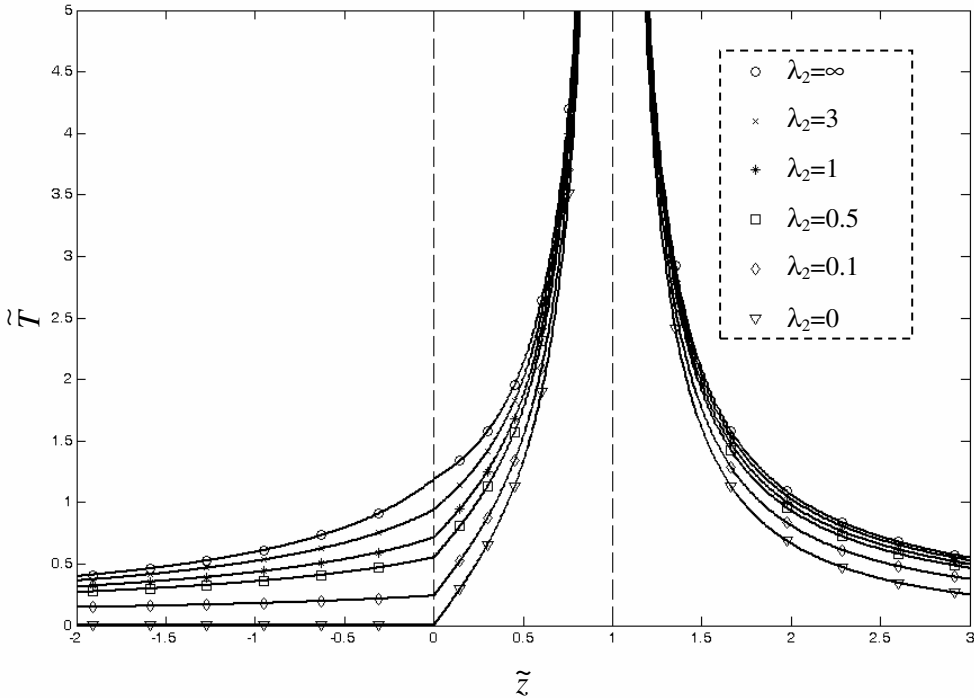


Figure 3. Distribution of the temperature along the z -axis for a highly conducting interface with $\Gamma = 1.2$.

exactly the same for the two types of imperfect interface conditions when $\lambda_1 = \lambda_2$, or equivalently when $\alpha\beta = k_1k_2$.

5. An application

Besides the incorporation of the present solution in BEM which does not require the discretization of the imperfect interface, another interesting application is that of a static point electric charge Q located at $(0, 0, h)$, ($h > 0$) in two imperfectly bonded half-spaces with dielectric constants ϵ_1 and ϵ_2 . (Since the differential equations for the electrostatic problem and for the heat conduction problem are identical, the results for the heat conduction problem obtained in the previous two sections can be applied directly to the electrostatic problem considered in this section). The Coulomb force F on the electric charge due to its interaction with a weakly conducting interface is

$$F = \frac{Q^2 \left(1 - 2\lambda_1(2 - \Gamma)(1 - f(\lambda_1)) \right)}{16\pi\epsilon_1 h^2}, \tag{24}$$

where

$$\Gamma = \frac{2\epsilon_1}{\epsilon_1 + \epsilon_2} \quad \text{and} \quad \lambda_1 = \alpha h \frac{\epsilon_1 + \epsilon_2}{\epsilon_1 \epsilon_2}.$$

Here the boundary conditions on the weakly conducting interface are

$$\epsilon_1 \frac{\partial \phi_1}{\partial z} = \epsilon_2 \frac{\partial \phi_2}{\partial z} = \alpha(\phi_1 - \phi_2), \quad (z = 0), \quad (25)$$

where ϕ is the electric potential, α is a nonnegative constant interface parameter.

Similarly, the Coulomb force F on the electric charge due to its interaction with a highly conducting interface is

$$F = \frac{Q^2 \left(2\lambda_2 \Gamma (1 - f(\lambda_2)) - 1 \right)}{16\pi \epsilon_1 h^2}, \quad (26)$$

where

$$\lambda_2 = \frac{h(\epsilon_1 + \epsilon_2)}{\beta}.$$

Here the boundary conditions on the highly conducting interface are

$$\phi_1 = \phi_2, \quad \epsilon_2 \frac{\partial \phi_2}{\partial z} - \epsilon_1 \frac{\partial \phi_1}{\partial z} = \beta \Delta_s \phi_1 = \beta \Delta_s \phi_2, \quad (z = 0), \quad (27)$$

where β is a nonnegative constant interface parameter.

In Equations (24) and (26) the Coulomb force F is in the z -direction due to the fact that all the image charges are distributed at the z -axis. A positive value of the force means that the electric charge is repelled from the interface whereas a negative value means that the electric charge is attracted to the interface. By applying the following asymptotic expansion

$$1 - f(\eta) \cong \frac{1}{2\eta} - \frac{1}{2\eta^2} + o\left(\frac{1}{\eta^3}\right), \quad \text{when } \eta \rightarrow \infty, \quad (28)$$

the Coulomb force F on the electric charge due to its interaction with a perfect interface ($\lambda_1, \lambda_2 \rightarrow \infty$) is

$$F = \frac{(\Gamma - 1)Q^2}{16\pi \epsilon_1 h^2}. \quad (29)$$

The above indicates that the electric charge will be repelled from the perfect interface when $\Gamma > 1$ and it will be attracted to the perfect interface when $\Gamma < 1$. The situation in which $F = 0$ occurs only when $\Gamma = 1$ or $\epsilon_1 = \epsilon_2$. In other words, there is no equilibrium position, $F = 0$, for an electric charge interacting with a perfect interface separating two half-spaces with different dielectric properties.

On the other hand, it follows from Equation (24) that it is possible to find a situation in which the Coulomb force F on the electric charge due to its interaction with a weakly conducting interface is zero, if the following condition is satisfied

$$f(\lambda_1) = 1 - \frac{1}{2\lambda_1(2 - \Gamma)}. \quad (30)$$

It can be easily observed from (24) that

$$F = \frac{Q^2}{16\pi \epsilon_1 h^2} > 0,$$

Γ	λ_1	Γ	λ_2
0	0.7798	2	0.7798
0.1	0.8788	1.9	0.8788
0.2	1.004	1.8	1.004
0.3	1.1671	1.7	1.1671
0.4	1.3873	1.6	1.3873
0.5	1.6999	1.5	1.6999
0.6	2.1754	1.4	2.1754
0.7	2.9792	1.3	2.9792
0.8	4.6095	1.2	4.6095
0.9	9.563	1.1	9.563
0.95	19.534	1.05	19.534
1	∞	1	∞

Table 1. The pairs of Γ and λ_1 (left side) that satisfy Equation (30). The pairs of Γ and λ_2 (right side) that satisfy Equation (31).

if $h \rightarrow 0$ (or equivalently $\lambda_1 \rightarrow 0$) and

$$F = \frac{Q^2(\Gamma - 1)}{16\pi\epsilon_1 h^2} < 0,$$

if $h \rightarrow \infty$ (or equivalently $\lambda_1 \rightarrow \infty$) and $\Gamma < 1$. Consequently, the equilibrium position determined by Equation (30) is a stable one. Table 1 (left side) presents the pairs of Γ and λ_1 that satisfy (30). We find that only when $\Gamma < 1$ (or equivalently $\epsilon_1 < \epsilon_2$, when the upper half-space is less conducting than the lower half-space) does an equilibrium position for the electric charge exist.

Similarly, it follows from Equation (26) that it is possible to find a situation in which the Coulomb force F on the electric charge due to its interaction with a highly conducting interface is zero if the following condition is satisfied

$$f(\lambda_2) = 1 - \frac{1}{2\lambda_2\Gamma}. \tag{31}$$

It can also be easily observed from Equation (26) that

$$F = -\frac{Q^2}{16\pi\epsilon_1 h^2} < 0,$$

if $h \rightarrow 0$ (or equivalently $\lambda_2 \rightarrow 0$) and

$$F = \frac{Q^2(\Gamma - 1)}{16\pi\epsilon_1 h^2} > 0,$$

if $h \rightarrow \infty$ (or equivalently $\lambda_2 \rightarrow \infty$) and $\Gamma > 1$. Consequently, the equilibrium position determined by Equation (31) is an unstable one. Table 1 (right side) presents the pairs of Γ and λ_2 that satisfy (31). We find that only when $\Gamma > 1$ (or equivalently $\epsilon_1 > \epsilon_2$, the upper half-space is more conducting than the lower half-space) does an equilibrium position for the electric charge exist.

The physical implication of the phenomenon of the existence of an equilibrium position for the electric charge interacting with the imperfect interface is that a properly chosen imperfect interface “shields” the charge located in the upper half-space from the interference of the lower half-space which has a different dielectric constant than the one in which it is embedded. The shielding is achieved by a compensation effect that the imperfect interface introduces. This, in a sense, is similar to the so-called neutral inhomogeneities which may be rendered “invisible” through some properly chosen imperfect interface (see [Benveniste and Miloh 1999], and [Milton 2003, Section 7.11]). In the present case, the lower half-space is the neutral inhomogeneity. In other words, as far as the point charge is concerned, its effect has been made neutral through the presence of a suitably chosen imperfect interface.

6. Conclusions

We have presented in Equations (11) and (12) the Green's function for a steady heat source interacting with a weakly conducting interface. Similarly, Equations (20) and (21) present the Green's function for a steady heat source interacting with a highly conducting interface. In particular, the temperature along the z -axis for both kinds of imperfect interface conditions can be concisely expressed in terms of the exponential integral function. We have also tried to derive the Green's function for a steady point heat source interacting with the following interface model of [Bövik 1994]

$$T_1 - T_2 = \frac{t}{2} \left(\frac{k_1}{k_0} - 1 \right) \frac{\partial T_1}{\partial z} + \frac{t}{2} \left(\frac{k_2}{k_0} - 1 \right) \frac{\partial T_2}{\partial z}, \quad (z = 0), \quad (32)$$

$$k_2 \frac{\partial T_2}{\partial z} - k_1 \frac{\partial T_1}{\partial z} = \frac{t}{2} (k_0 - k_1) \Delta_s T_1 + \frac{t}{2} (k_0 - k_2) \Delta_s T_2,$$

which can reduce to a weakly conducting interface, Equation (2), by letting $t \rightarrow 0$ and $k_0 \rightarrow 0$. Also (32) can be reduced to a highly conducting one, (4), by letting $t \rightarrow 0$ and $k_0 \rightarrow \infty$. Unfortunately, the image method adopted here is invalid in treating this more general kind of imperfect interface. More specifically, the assumption of Equation (6) and (7) with four undetermined constants A , B , C and γ for the temperature field in the two half-spaces is not sufficient to satisfy Equation (32).

Acknowledgments

The reviewers' comments on revising the manuscript are greatly appreciated.

References

- [Abramovitz and Stegun 1972] M. Abramovitz and I. A. Stegun, *Handbook of mathematical functions with formulas, graphs, and mathematical tables*, Dover, New York, 1972.
- [Ang et al. 2004] W. T. Ang, K. K. Choo, and H. Fan, “A Green's function for steady-state two-dimensional heat conduction across a homogeneously imperfect interface”, *Commun. Numer. Methods Eng.* **20**:5 (2004), 391–399.
- [Benveniste 2006] Y. Benveniste, “A general interface model for a three-dimensional curved thin anisotropic interphase between two anisotropic media”, *J. Mech. Phys. Solids* **54**:4 (2006), 708–734.
- [Benveniste and Miloh 1986] Y. Benveniste and T. Miloh, “The effective conductivity of composite with imperfect contact at constituent interfaces”, *Int. J. Eng. Sci.* **24**:9 (1986), 1537–1552.

- [Benveniste and Miloh 1999] Y. Benveniste and T. Miloh, “Neutral inhomogeneities in conduction phenomena”, *J. Mech. Phys. Solids* **47**:9 (1999), 1873–1892.
- [Bövik 1994] P. Bövik, “On the modelling of thin interface layers in elastic and acoustic scattering problems”, *Q. J. Mech. Appl. Math.* **47**:1 (1994), 17–42.
- [Chen 2001] T. Chen, “Thermal conduction of a circular inclusion with variable interface parameter”, *Int. J. Solids Struct.* **38**:17 (2001), 3081–3097.
- [Fan and Wang 2003] H. Fan and G. F. Wang, “Screw dislocation interacting with imperfect interface”, *Mech. Mater.* **35**:10 (2003), 943–953.
- [Miloh and Benveniste 1999] T. Miloh and Y. Benveniste, “On the effective conductivity of composites with ellipsoidal inhomogeneities and highly conducting interface”, *Proc. R. Soc. Lon. Ser. A* **455**:1987 (1999), 2687–2706.
- [Milton 2003] G. W. Milton, *The theory of composites*, Cambridge University Press, 2003.
- [Ochmann 2004] M. Ochmann, “The complex equivalent source method for sound propagation over an impedance plane”, *J. Acoust. Soc. Am.* **116**:6 (2004), 3304–3311.
- [Ru and Schiavone 1997] C. Q. Ru and P. Schiavone, “A circular inclusion with circumferentially inhomogeneous interface in antiplane shear”, *Proc. R. Soc. Lon. Ser. A* **453**:1967 (1997), 2551–2572.
- [Sommerfeld 1926] A. Sommerfeld, “Über die Ausbreitung der Wellen in der drahtlosen Telegraphie”, *Ann. Physik* **386** (1926), 1135–1153.
- [Sommerfeld 1978] A. Sommerfeld, *Partielle Differentialgleichungen der Physik*, Harri Deutsch, Thun, 1978.
- [Taraldsen 2005a] G. Taraldsen, “The complex image method”, *Wave Motion* **43**:1 (2005), 91–97.
- [Taraldsen 2005b] G. Taraldsen, “A note on reflection of spherical waves”, *J. Acoust. Soc. Am.* **117**:6 (2005), 3389–3392.

Received 18 May 2006. Accepted 1 Jul 2006.

X. WANG: xuwang_sun@hotmail.com

Department of Civil Engineering, University of Akron, Akron, Ohio 44325-3905, United States

L. J. SUDAK: lsudak@ucalgary.ca

Department of Mechanical and Manufacturing Engineering, University of Calgary, 2500 University Dr. NW, Calgary, Alberta, T2N 1N4, Canada

THE SHEAR RESPONSE OF METALLIC SQUARE HONEYCOMBS

FRANÇOIS COTE, VIKRAM S. DESHPANDE AND NORMAN A. FLECK

Stainless steel square honeycombs have been manufactured by slotting together steel sheets and then brazing the assembly. Their out-of-plane shear response is measured as a function of the relative density of the honeycomb and of the direction of shearing with respect to the material axes of the square honeycomb. The response is nearly isotropic with the shear strength and reasonably insensitive to the loading direction. In contrast to the out-of-plane compressive response, the shear response is monotonically hardening and the shear strength scales linearly with relative density. A simple analytical model based upon uniform deformation of the cell walls is in good agreement with the measured shear behavior at low shear strains, and predicts the onset of wrinkling of the cell walls to reasonable accuracy. Finite element (FE) calculations are accurate up to large values of shear strain, and reveal that the shear strength of the square honeycombs is relatively insensitive to the ratio of honeycomb height to cell size. The shear strength of square honeycombs compares favorably with other competing sandwich core topologies such as pyramidal and corrugated truss cores.

1. Introduction

The development of metallic micro-architected materials for application as the cores of sandwich structures is of current academic and industrial interest. Three classes of core architecture have been proposed: prismatic cores, 3D trusses, and honeycombs. The most suitable choice of sandwich core architecture depends upon the specific application. For example, trusses with their open celled architecture are ideal for multifunctional applications involving heat transfer in addition to load carrying capacity [Evans et al. 2001]. On the other hand, these sandwich cores have a low in-plane stretching strength. Thus, for load-bearing, honeycomb cores are superior to the truss cores. Traditionally, hexagonal honeycombs have been extensively employed in sandwich construction [Gibson and Ashby 1997]. Similar to the truss cores, these hexagonal honeycombs suffer from the drawback of low in-plane stretching strength. Square honeycombs overcome this drawback, at least for loadings along the directions of the cell walls, and thereby have promise for sandwich construction. The out-of-plane shear properties of stainless steel square honeycombs are the focus of this study. The out-of-plane loading direction is of particular importance in sandwich beams and plates since the core functions by carrying shear loads while the face sheets carry bending loads.

The authors are grateful to ONR for their financial support through US-ONR IFO grant number N00014-03-1-0283 on The Science and Design of Blast Resistant Sandwich Structures. FC acknowledges support from the Cambridge Commonwealth Trust and the Fonds Québécois de la Recherche sur la Nature et les Technologies.

Keywords: honeycombs, wrinkling, shear strength, sandwich panels.

Honeycombs usually comprise hexagonal cells and are manufactured by either an expansion or corrugation process. For example, see the Hexcel Composites¹ honeycomb data sheet [Hexcel 1999]. Hexagonal honeycombs are routinely employed as the cores for lightweight sandwich panels and as energy absorbers. They are typically manufactured from aluminum (Al) alloys and have a relative density $\bar{\rho}$ (that is, the ratio of the density of the honeycomb treated as a homogeneous continuum to the density of the solid) of less than 3%. Experiments and simple analyses have shown that their out-of-plane elastic properties scale linearly with the relative density $\bar{\rho}$ [Kelsey et al. 1958; Zhang and Ashby 1992]. In out-of-plane crushing, these honeycombs exhibit a stress peak followed by large stress oscillations associated with the formation of a succession of plastic folds in each cell. Similarly the out-of-plane peak shear strength is governed by cell wall buckling [Werren and Norris 1950; Zhang and Ashby 1992]. Once the wrinkles have formed, the shear stress drops and subsequently remains approximately constant until failure occurs by the fracture of the cell walls. Experimental studies illustrating this behavior have been presented by [Doyoyo and Mohr 2003; Mohr and Doyoyo 2004b] and the corresponding numerical simulations of the shear response of Al hexagonal honeycombs by [Mohr and Doyoyo 2004a]. Most experimental studies are restricted to relative densities $\bar{\rho} < 0.08$, since debonding of the honeycombs from the plates of the single-lap shear fixture has been observed for both metallic [Hexcel 1999] and nonmetallic honeycombs [Werren and Norris 1950; Zhang and Ashby 1992] at higher relative densities.

Recent studies [Fleck and Deshpande 2004; Xue and Hutchinson 2004] suggest that square honeycomb cores having a high relative density ($\bar{\rho} > 0.05$) are preferable for high-severity loadings such as blasts and shocks because of their high out-of-plane crushing resistance and high in-plane stretching strength. We expect enhanced performance of square honeycombs constructed from solids of high strain hardening, such as stainless steels. An experimental investigation into the out-of-plane compressive response of stainless square honeycombs by [Côté et al. 2004] over a relative density range $0.03 < \bar{\rho} < 0.2$ confirmed that the honeycombs exploit the strain hardening behavior of the stainless steel. Peak compressive strength is set by the axial torsional plastic buckling of the square honeycomb cells. In fact, no progressive folding of the cell walls was observed by [Côté et al. 2004]. This difference in compressive response between aluminum and stainless steel honeycombs is attributed to differences in the strain hardening response of the parent materials.

The objectives of the present study are to investigate the effects of the relative density $\bar{\rho}$, shear loading direction, and cell aspect ratio (that is, the ratio of cell height-to-cell size) on the out-of-plane shear response of stainless steel square honeycombs. First, we describe the procedure used to manufacture stainless steel square honeycomb and our test protocol. Second, we report the observed the out-of-plane shear behavior, including the effects of relative density and loading direction. We compare these experimental measurements with a simple analytical model and 3D finite element simulations. Finally, we compare the shear response of the square honeycombs with that for commercially available aluminum hexagonal honeycombs, as well as three other alternative core topologies.

2. Experimental method

2.1. Specimen manufacture and test protocol. Since metallic square-honeycombs are not yet commercially manufactured, we manufactured them by electro-discharge machining and brazing as described

¹Hexcel Composites, Duxford, Cambridge, CB2 4QD, United Kingdom.

below. Square honeycombs were manufactured from AISI type 304 stainless steel sheets of thickness $t = 0.30$ mm, using the slotting technique of [Côté et al. 2004; Côté et al. 2006]. The sheets were cropped into long strips of height H . Cross-slots of width 0.305 mm and spacing l in the range 6 to 17.5 mm were cut by electro-discharge machining (EDM). To first order in t/l , the relative density $\bar{\rho}$ of the square honeycomb is $\bar{\rho} = 2t/l$. Four relative densities of square honeycomb specimens were manufactured and tested by varying the cell size l .

The square honeycombs were assembled by slotting together the sheets as shown in Figure 1a. A clearance of $5 \mu\text{m}$ between sheet and slot facilitated assembly while providing a sufficiently tight fit to

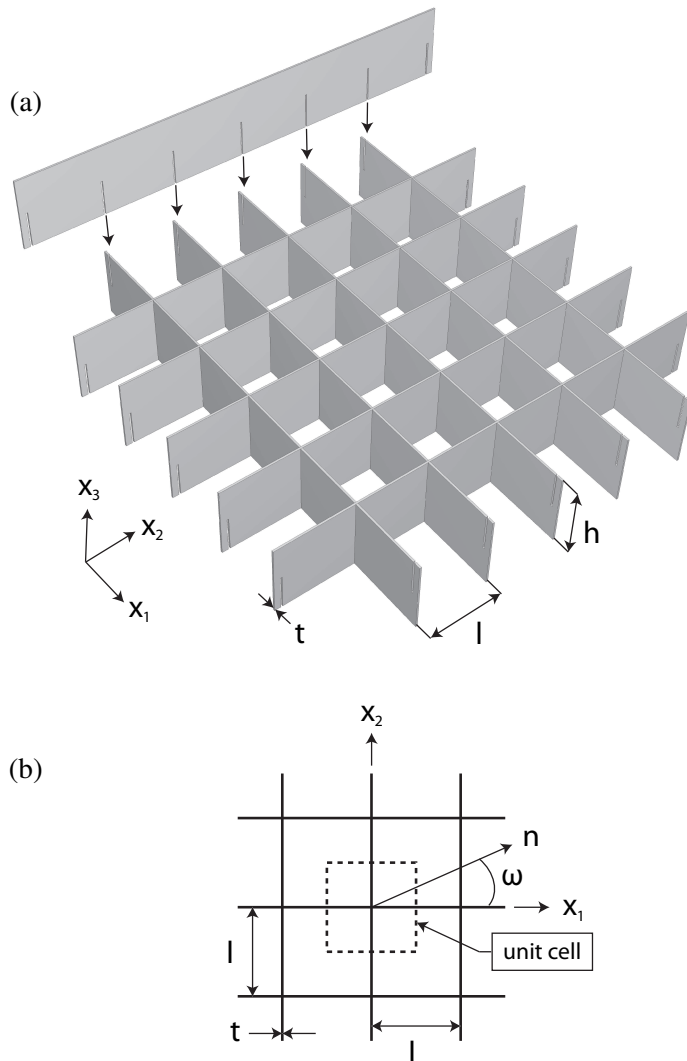


Figure 1. (a) Sketch of the square honeycomb manufacturing technique. (b) Schematic of the unit cell employed in the finite element analysis, including the coordinate system adopted and the loading direction n .

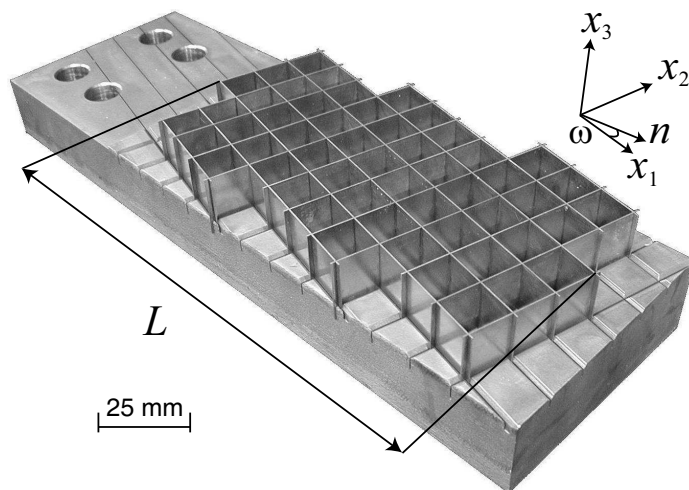


Figure 2. Photograph of $a\bar{\rho} = 0.05$ square honeycomb specimen slotted into one of the faces of the single-lap shear test fixture. This specimen is loaded in the $\omega = \tan^{-1}(1/4)$ direction.

assure stability. To ensure good bonding between the square honeycomb specimens and the shear test fixture, slots of width 0.31 mm and depth 4 mm were electro-discharge machined into 25 mm thick steel sheets. These steel sheets served as the test fixtures. The cross-slotted square honeycomb specimens were then assembled onto the test fixtures as shown in Figure 2. Consequently, the net height of the honeycomb was $h = H - 8$ mm.

After assembly of the honeycomb core into the single-lap shear test fixture, the braze alloy Ni-Cr 25-P10 (wt.%) was applied uniformly over the sheets of the square honeycombs and the inner surfaces of the test fixture. The whole assembly was then brazed together in a vacuum furnace at 1075° C in a dry argon atmosphere at 3–10 Pa. Capillarity forces were sufficient to draw the braze into the joints, resulting in an excellent bond. After brazing, the wall thickness was measured to be $t = 0.32$ mm. In all tests performed in this study the cell aspect ratio of the square honeycomb specimens was $h/l = 1$.

The quality of the braze joints was assessed by optical microscopy and SEM/EDX dot mapping techniques. The surface of a typical square-honeycomb joint was prepared by successive grinding steps and a final polish with 1 μm diamond paste. The polished surface was then etched using a solution comprising 74% hydrochloric acid and 1.3% hydrogen peroxide. An optical photograph of a polished and etched brazed joint is shown in Figure 3 and confirms the good overall bonding at the joints. A closer inspection however reveals the presence of two phases in the joint. The composition of those phases was obtained by EDX dot mapping analysis. The first phase has approximately the composition of stainless steel, that is, Fe, Ni, and Cr, while the second phase contains phosphides and are expected to decrease the ductility of the joint [Zhuang and Eagar 1997].

We defined x_3 as the out-of-plane direction, and n as the unit vector in the $x_1 - x_2$ plane at an angle ω to the x_1 -direction, as sketched in Figure 1b. Then, the out-of-plane shear response $\tau_{3n} - \gamma_{3n}$ was measured using the single-lap shear set-up, with selected values of ω . All tests were performed in accordance

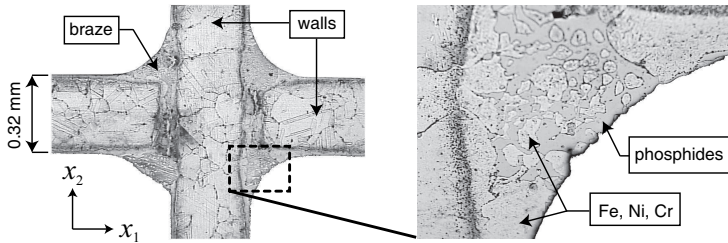


Figure 3. Photograph of a polished braze joint showing the effect of diffusion bonding on the microstructure of the joint. The zoom area reveals the presence of two phases in the joint.

with [ASTM 2000] for shear tests on sandwich cores. The standard demands a specimen aspect ratio of $L/h \geq 12$, where L is the length of the specimen. The example shown in Figure 2 is for a $\bar{\rho} = 0.05$ square honeycomb specimen, loaded in the $\omega = \tan^{-1}(1/4)$ direction.

The shear tests were performed on a 150 kN screw driven test machine at an applied macroscopic nominal shear strain-rate of 10^{-4} s^{-1} . The load was measured by the load cell of the test machine and was used to define the nominal shear stress. A clip gauge mounted on the single-lap shear test fixture was employed to measure the relative displacement between the two faces of the square honeycomb specimens, thereby giving the applied shear strain. A photograph of the overall single-lap shear test

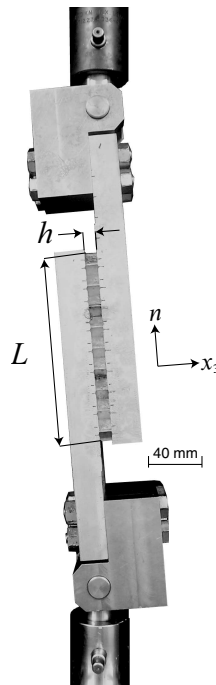


Figure 4. Photograph of the single-lap shear test fixture, with $a\bar{\rho} = 0.05$ square honeycomb specimen loaded in the $\omega = \pi/4$ direction.

fixture with a $\bar{\rho} = 0.05$ square honeycomb specimen loaded in the $\omega = 45^\circ$ direction is shown in Figure 4. For sake of clarity, the clip gauge is not shown on the Figure 4 but was mounted during the experiments using a standard arrangement for a single-lap shear test [Kelsey et al. 1958].

2.2. Properties of the parent material. Tensile specimens of dog-bone geometry were cut from the 304 stainless steel sheets and subjected to the same brazing cycle as that used to manufacture the square honeycombs. The measured true tensile stress versus logarithmic strain response, shown in Figure 5, can be approximated as elastic, linearly hardening with a Young's modulus $E = 210$ GPa, yield strength $\sigma_y = 210$ MPa and post-yield tangent modulus $E_y = 2.1$ GPa.

3. Shear response of square honeycombs

3.1. Measurements. The measured transverse shear stress τ_{31} versus shear strain γ_{31} ($\omega = 0^\circ$) response of four selected relative densities of the square honeycomb are plotted in Figure 6. In all cases, the shear stress versus strain response displays a hardening character with no stress drop.

A montage of photographs of the $\bar{\rho} = 0.04$ specimen at selected levels of applied shear strain γ_{31} is given in Figure 7. The deformation of the cell walls is essentially uniform for shear strains $\gamma_{31} < 0.02$. Wrinkling of the cell walls is observed at larger strains, with typically two folds in each cell wall. Visual observations on the four tests plotted in Figure 6 indicate that wrinkling commenced at $\gamma_{31} = 0.02, 0.04, 0.8$ and 0.11 for $\bar{\rho} = 0.04, 0.05, 0.08$ and 0.11 , respectively. The observed onset of wrinkling is marked by solid circles in Figure 6.

The effect of the loading angle ω on the shear stress τ_{3n} versus γ_{3n} response of the square honeycombs is shown in Figure 8. The shear strength increases with ω for $0 \leq \omega \leq \pi/4$. Note that half of the cell walls carry nearly no load when $\omega = 0^\circ$ while all cell walls are equally loaded when $\omega = \pi/4$. The increase in shear strength also occurs because wrinkling of the cell walls is delayed for loading with $\omega > 0^\circ$. Visual observations suggest that wrinkling of the cell wall parallel to the x_1 commences at $\gamma_{3n} = 0.04, 0.05, 0.06$

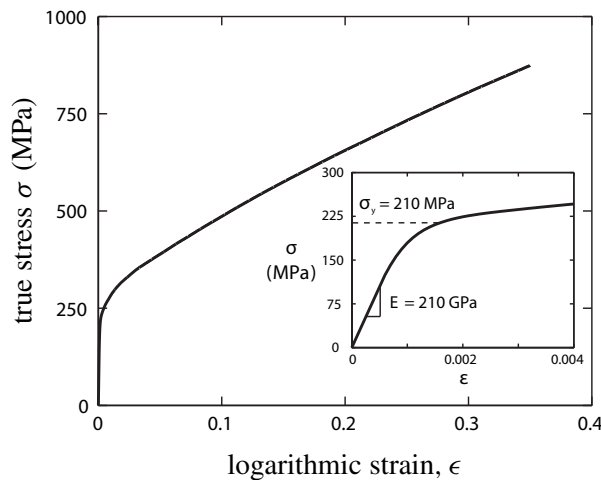


Figure 5. The measured tensile stress versus strain curve of the as-brazed 304 stainless steel. Tensile response was measured at an applied strain rate of 10^{-4} s^{-1} .

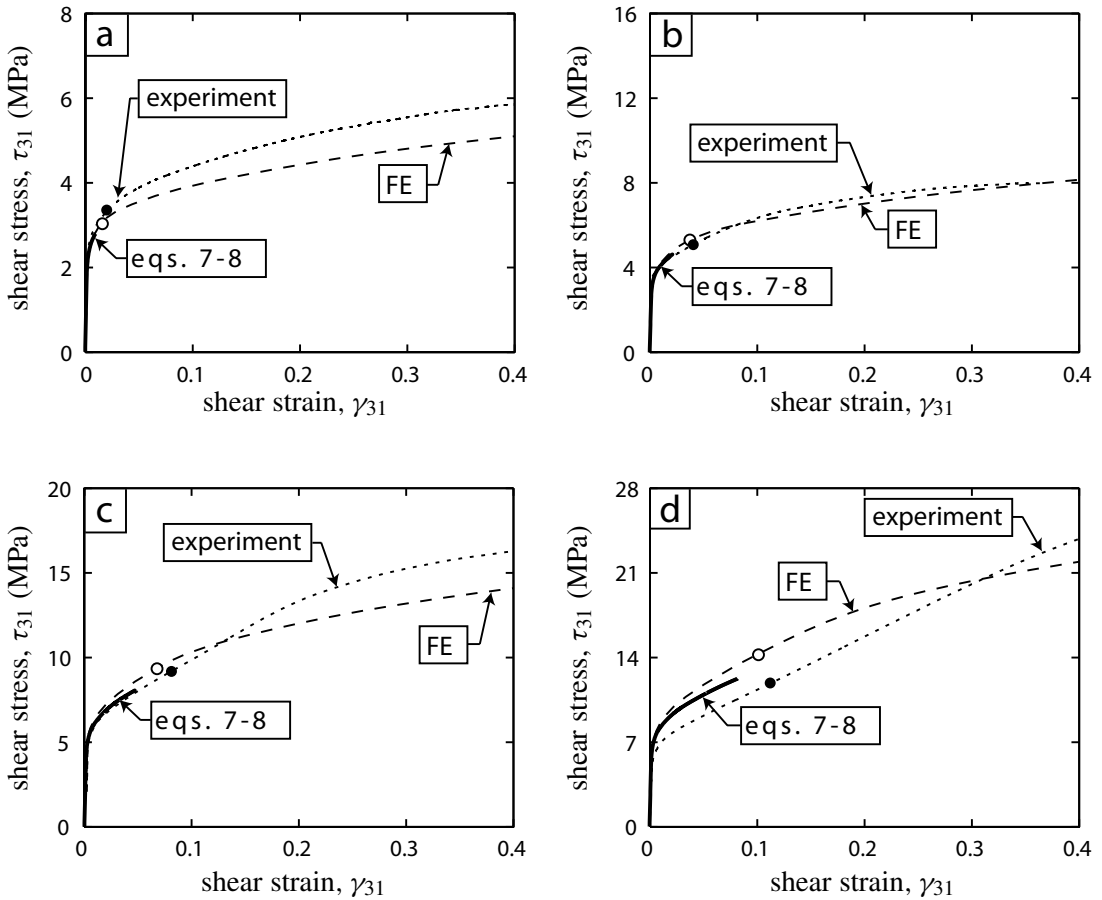


Figure 6. The measured response, and the FE and analytical predictions of the shear stress τ_{31} versus shear strain γ_{31} response for square honeycomb specimens of differing relative density $\bar{\rho}$ with $\omega = 0^\circ$ of (a) $\bar{\rho} = 0.04$, (b) $\bar{\rho} = 0.05$, (c) $\bar{\rho} = 0.08$ and (d) $\bar{\rho} = 0.11$. The onset of wrinkling, as observed in the experiments, and as predicted by the FE calculations, are marked as filled and open circles, respectively.

and 0.07 for loading along $\omega = 0^\circ$, $\tan^{-1}(1/4)$, $\tan^{-1}(1/2)$ and $\pi/4$, respectively. Again, the observed onset of wrinkling is marked by the solid circles in Figure 8.

Note that the shear test fixture applies a prescribed shear strain γ_{3n} , and the measured shear traction is the component along the n -direction. For $\omega \neq 0^\circ$ or 45° the straining direction is not aligned with symmetry axes of the honeycomb, and a finite shear traction perpendicular to the n -direction is also generated. This component of shear traction has not been measured in the current study.

3.2. Analytical predictions. Assuming uniform straining of the cell walls of the square honeycombs, the applied shear strain γ_{3n} is related to the shear strains γ_1^w and γ_2^w in the cell walls parallel to the x_1 and x_2 axis, respectively via

$$\gamma_1^w = \gamma_{3n} \cos \omega, \tag{1a}$$

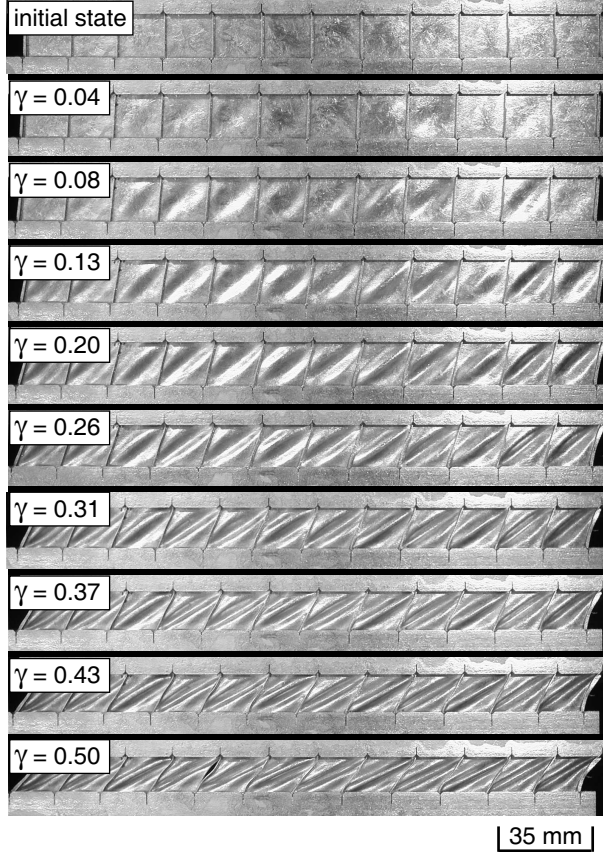


Figure 7. Photographs showing the deformation mode of the $\bar{\rho} = 0.04$ square honeycomb specimen loaded in the $\omega = 0^\circ$ direction.

$$\gamma_2^w = \gamma_{3n} \sin \omega. \tag{1b}$$

The honeycomb responds with a shear traction τ_1^w in the cell wall parallel to the x_1 -direction and with a shear traction τ_2^w parallel to the x_2 -direction. The measured shear stress τ_{3n} , for $0 \leq \omega \leq \pi/4$, is

$$\tau_{3n} = (\tau_1^w \cos \omega + \tau_2^w \sin \omega) \frac{\bar{\rho}}{2}. \tag{2}$$

In general, the traction $(\tau_2^w \cos \omega - \tau_1^w \sin \omega) \bar{\rho}/2$ transverse to the shearing direction does not vanish.

Consider first the elastic response of the honeycomb. For an applied shear strain γ_{3n} , the wall stresses are

$$\tau_1^w = G \gamma_{3n} \cos \omega, \tag{3a}$$

$$\tau_2^w = G \gamma_{3n} \sin \omega, \tag{3b}$$

where G is shear modulus of the cell wall material. The out-of-plane shear modulus G_{3n} of the square honeycombs is isotropic, due to its 4-fold symmetry about the x_3 axis. Combining Equation (2) and

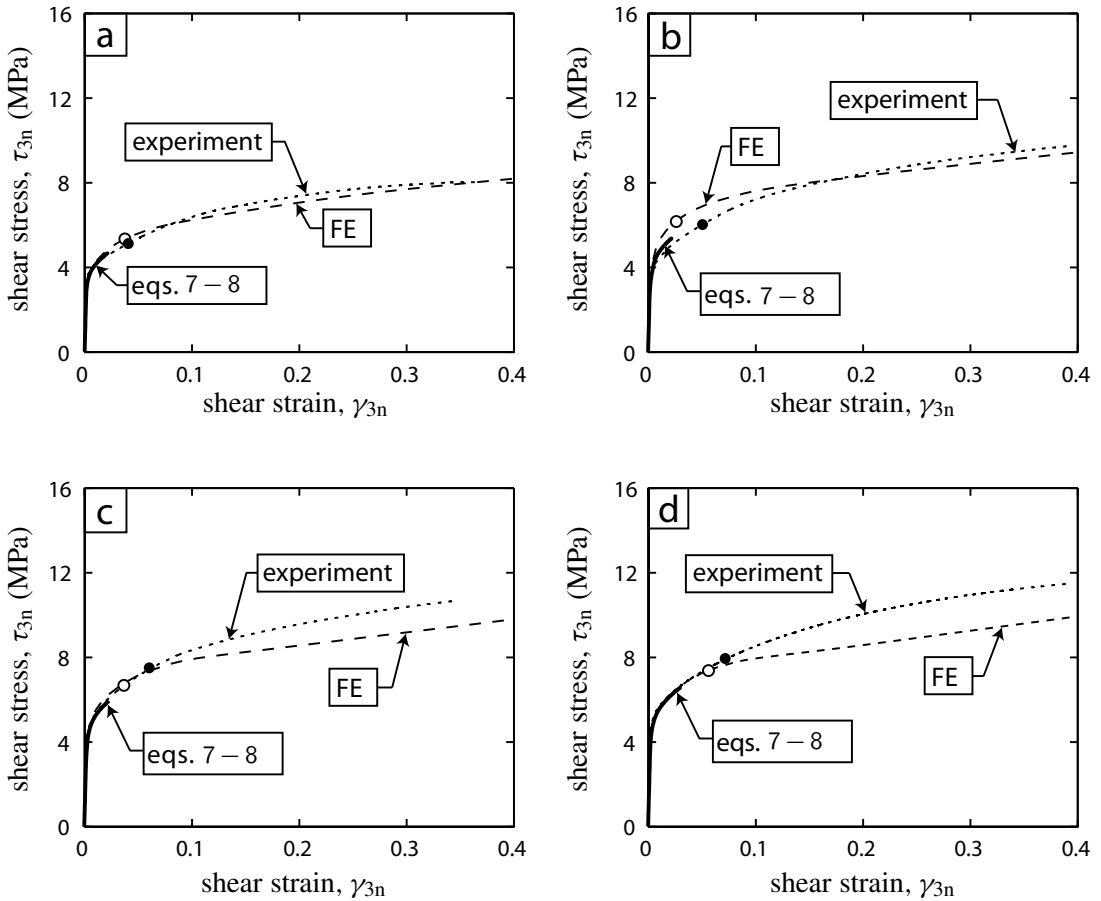


Figure 8. The measured response and the FE and analytical predictions of the shear stress τ_{3n} versus shear strain γ_{3n} response of the $\bar{\rho} = 0.05$ square honeycombs specimens loaded in the (a) $\omega = 0^\circ$, (b) $\omega = \tan^{-1}(1/4)$, (c) $\omega = \tan^{-1}(1/2)$ and (d) $\omega = \pi/4$ directions. The onset of wrinkling as observed in the experiments and predicted by the FE calculations are marked as filled and open circles, respectively.

Equations (3a) and (3b), the shear modulus G_{3n} of the square honeycombs becomes

$$G_{3n} = \frac{E}{4(1 + \nu)} \bar{\rho},$$

where E and ν are the Young’s modulus and Poisson ratio of the isotropic solid parent material, respectively. Moreover, isotropy of elastic response dictates that the shear traction $(\tau_2^w \cos \omega - \tau_1^w \sin \omega) \bar{\rho} / 2$ transverse to the shearing direction vanishes.

We proceed to develop an analytical model for the shear strength τ_{3n}^p of the square honeycombs made from an elastic, ideally plastic material with a Young’s modulus E , Poisson’s ratio ν and yield strength σ_y . With the cell walls modeled as thin clamped plates under shear loading, the maximum allowable shear stress of the square honeycomb is set by either elastic buckling or plastic yielding of cell walls.

The elastic shear buckling strength of a clamped plate is given by [Timoshenko and Gere 1963] as

$$\tau_c = \frac{k\pi^2 E}{12(1-\nu^2)} \left(\frac{t}{l}\right)^2, \tag{4}$$

where k varies from 8.99 to 12.28 [Timoshenko and Gere 1963], depending on the aspect ratio h/l . Note that for a honeycomb with aspect ratio $h/l = 1$ and clamped edges along $x_3 = 0$ and $x_3 = h$, $k = 12.28$. For elastic behavior, Equation (3) dictates that the wall stresses are related by

$$\tau_2^w = \tau_1^w \tan \omega \tag{5}$$

and consequently, with τ_1^w set equal to τ_c the elastic buckling stress of the square honeycomb is

$$\tau_{3n}^p = \begin{cases} \frac{k\pi^2 E}{96 \cos \omega (1-\nu^2)} \bar{\rho}^3, & \text{if } \omega \leq 45^\circ, \\ \frac{k\pi^2 E}{96 \sin \omega (1-\nu^2)} \bar{\rho}^3, & 45^\circ < \omega \leq 90^\circ. \end{cases}$$

In contrast, when the cell walls undergo plastic deformation, Equation (5) is no longer valid. With both the cell walls assumed to be at a state of shear yield, the plastic shear strength of the square honeycomb is obtained by substituting $\tau_2^w = \tau_1^w = \sigma_y/\sqrt{3}$ into Equation (2). Here we assume that the tensile yield strength of the solid is related to its shear yield strength via the usual von Mises relation.) Thus, the maximum allowable shear stress of the square honeycomb made from an elastic, ideally plastic solid follows as

$$\tau_{3n}^p = \begin{cases} \frac{k\pi^2 E}{96 \cos \omega (1-\nu^2)} \bar{\rho}^3, & \text{if } \bar{\rho} < \sqrt{\frac{48(1-\nu^2)\sigma_y \cos \omega}{\sqrt{3}k\pi^2 E (\cos \omega + \sin \omega)}} \\ \frac{\sigma_y}{2\sqrt{3}} \bar{\rho} (\cos \omega + \sin \omega), & \text{otherwise,} \end{cases} \tag{6}$$

for $0 \leq \omega \leq 45^\circ$. The corresponding strength for loading in the $45^\circ < \omega \leq 90^\circ$ direction follows by interchanging $\sin \omega$ and $\cos \omega$ in Equation (6).

Alternatively, consider parent material response for rigid strain hardening. Here we develop an analytical expression for the shear stress versus strain response of the square honeycomb prior to the development of wrinkles (that is, when the constituent sheets are in a uniform state). We assume uniform deformation of the cell walls, and write the uniaxial tensile stress versus plastic strain response of the cell wall material as $\sigma(\varepsilon)$. With the macroscopic shear strain γ_{3n} related to the shear strains in the cell walls via Equations (1a) and (1b), the shear stress versus strain response (τ_{3n} versus γ_{3n}) of the honeycombs follows as

$$\tau_{3n} = \left[\sigma(\varepsilon_1^{\text{ref}}) \cos \omega + \sigma(\varepsilon_2^{\text{ref}}) \sin \omega \right] \frac{\bar{\rho}}{2\sqrt{3}}, \tag{7}$$

where $\varepsilon_1^{\text{ref}} \equiv \gamma_{3n} \cos \omega / \sqrt{3}$ and $\varepsilon_2^{\text{ref}} \equiv \gamma_{3n} \sin \omega / \sqrt{3}$.

Experimental measurements by [Gerard 1948] on the shear of clamped plates suggest that employing the secant shear modulus $G_s \equiv \tau/\gamma$ in Equation (4) gives good agreement with measured results. Thus, we estimate the plastic shear buckling stress of clamped plates as

$$\tau_c^p = \frac{k\pi^2 G_s}{6(1-\nu)} \left(\frac{t}{l}\right)^2.$$

Here, $G_s \equiv \tau/\gamma = \sigma/3\varepsilon$ is the shear secant modulus derived from the true tensile stress versus logarithmic strain curve of the parent material and evaluated at $\sigma = \sqrt{3}\tau_c^p$. Assuming collapse of the square honeycomb when either the wall parallel to the x_1 axis or x_2 axis plastically buckles, the shear strength of the square honeycomb is

$$\tau_{3n}^p = \begin{cases} \left(\sqrt{3}\tau_c^p \cos \omega + \sigma(\varepsilon^{\text{ref}} \tan \omega) \sin \omega \right) \frac{\bar{\rho}}{2\sqrt{3}}, & \text{if } \omega \leq 45^\circ, \\ \left(\sigma(\varepsilon^{\text{ref}} \cot \omega) \cos \omega + \sqrt{3}\tau_c^p \sin \omega \right) \frac{\bar{\rho}}{2\sqrt{3}}, & 45^\circ < \omega \leq 90^\circ, \end{cases} \quad (8)$$

where ε^{ref} is the tensile strain of the solid material at a tensile stress $\sqrt{3}\tau_c^p$.

We emphasize that this analysis assumes uniform deformation of the cell walls of the square honeycomb and only provides an upper bound to the shear stress versus strain response. The analytical prediction for the shear stress versus strain response, Equation (7), is valid up to the onset of wrinkling and has been added to the measurements plotted in Figures 6 and 8, with the curves truncated at the plastic buckling stress (Equation (8)). The analytical model is in good agreement with the measurements but predicts the onset of wrinkling slightly before that observed in the experiments.

4. Finite element predictions of the shear response

Finite element (FE) calculations of the shear response were performed using the general purpose finite element package ABAQUS Standard (Hibbitt, Karlsson & Sorensen, Inc.). All simulations reported here were performed on the unit cell shown in Figure 1b (as a cruciform section), including the nonlinear effects of large displacements. Additional calculations on larger repeating units comprising two and four unit cells gave nearly identical results to those presented here and are omitted for the sake of brevity.

The unit cell of the square honeycomb was modeled using linear 3D shell elements (S4R in the ABAQUS notation). Periodic boundary conditions were specified on the boundaries $x_1 = \pm l/2$ and $x_2 = \pm l/2$ by specifying that all degrees of freedom (both translational and rotational) on the edges $x_i = -l/2$ are equal to the corresponding ones on the edge $x_i = +l/2$, where the subscript i ranges from 1 to 2. The nodes on the plane $x_3 = 0$ were fully clamped. Loading was specified by prescribing the displacements $u_1 = \delta \cos \omega$ and $u_2 = \delta \sin \omega$, where δ is the applied displacement and ω is the loading angle², to all nodes on the plane $x_3 = h$. The displacements u_3 of all nodes on the plane $x_3 = h$ were constrained to be equal. The rotational degrees of the nodes on the planes $x_3 = h$ and $x_3 = 0$ were set to zero to simulate the constraint imposed by the honeycomb joint at the loading platens. These boundary conditions imply that the strain ε_{33} of the square honeycomb specimens is unconstrained with the average traction $T_3 = 0$. The single-lap shear tests discussed above provide negligible constraint to straining in the 3-direction, so the assumed boundary conditions described here are representative. Typically, the model comprised 30 shell elements in each of the x_1 , x_2 and x_3 -directions, giving a total of 1800 linear shell elements. Convergence studies revealed that increasing the number of elements above 1800 did not change the results appreciably.

² The applied displacements in the FE calculations are consistent with the experiments, where the shear test fixture prevents displacements in the x_1 and x_2 plane orthogonal to the ω direction.

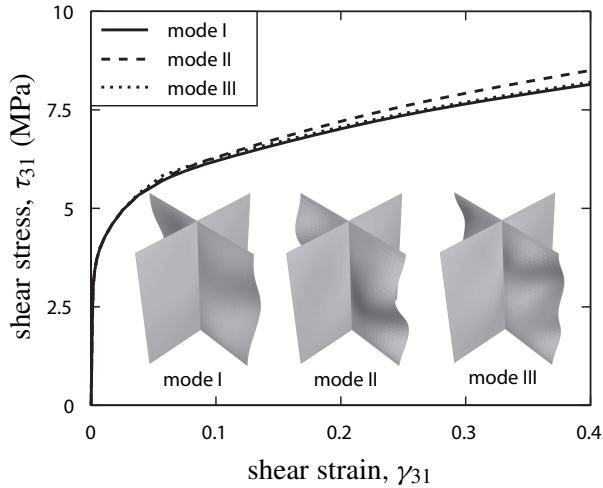


Figure 9. FE predictions of the shear stress τ_{31} versus shear strain γ_{31} response of the $\bar{\rho} = 0.05$ square honeycombs for three choices of the initial imperfection mode (shown in the inset). The nondimensional imperfection magnitude was taken to be $\zeta = 0.05$ in all cases.

The uniaxial true stress versus logarithmic plastic strain was tabulated in ABAQUS using the experimentally measured response (Figure 5). J2 flow-theory was adopted. Initial imperfections were introduced into the unit cell in the form of selected elastic eigenmodes of the structure. The three imperfection modes adopted are shown in the inset of Figure 9. Mode I is the lowest frequency mode, while mode II is the next harmonic. Mode III contains the first 2 eigenmodes, with an equal maximum deflection for each mode. The maximum transverse deflection of the webs of the honeycomb for each mode is set to $w = \zeta t$, where ζ is a prescribed nondimensional imperfection amplitude. The FE predictions of the $\omega = 0^\circ$ shear stress versus strain response of the $\bar{\rho} = 0.05$ square honeycombs are plotted in Figure 9 for the three selected modes of the initial imperfection with $\zeta = 0.05$. These calculations show that the response is relatively insensitive to the shape of initial imperfection. Scoping studies also revealed that the response is reasonably insensitive to the magnitude of the imperfection for $\zeta \leq 0.1$. In all calculations reported subsequently, we employed the mode I imperfection of Figure 9, with $\zeta = 0.05$.

4.1. Comparison with measurements. The FE predictions of the shear stress versus strain response of the square honeycombs are included in Figures 6 and 8, in which the predicted onset of wrinkling is marked by open circles. In all cases, the FE predictions agree with the experimental measurements to within about 10%. The onset of wrinkling is also accurately predicted by the FE calculations. The discrepancy between the measurements and FE predictions is greatest for the $\bar{\rho} = 0.11$ honeycombs (Figure 6d) and is attributed to tearing of the cell walls in the experiments. This was not accounted for in the FE calculations.

A comparison between the measurements and the predictions of both the analytical model and FE calculations is summarized in Figure 10. In Figure 10a, measurements and predictions are given for the normalized shear strength $\tau_{31}^y / (\bar{\rho} \sigma_y)$ versus $\bar{\rho}$, where τ_{31}^y is the shear stress at a shear strain $\gamma_{31} = 0.05$,

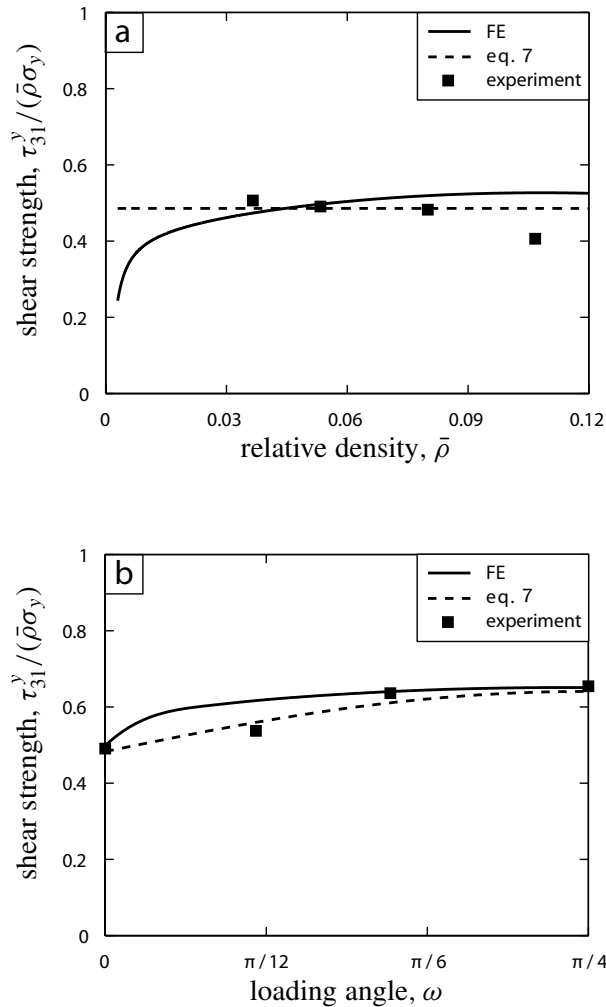


Figure 10. Comparison of the measured and predicted shear strengths. (a) The shear strength τ_{31}^y at a shear strain $\gamma_{31} = 0.05$ versus the honeycomb relative density $\bar{\rho}$, for $\omega = 0$; (b) the shear strength τ_{3n}^y at a shear strain $\gamma_{3n} = 0.05$ versus the loading angle ω , for $\bar{\rho} = 0.05$.

with $\omega = 0$. The value of 0.05 was selected for comparison purposes since the initial yield is difficult to define. Good agreement between the predictions and measurements is observed for the three lower values of $\bar{\rho}$, but as discussed above, tearing of the cell walls results in an over-prediction of the shear strength for the $\bar{\rho} = 0.11$ honeycomb. The FE calculations predict a sharp drop in the shear strength for $\bar{\rho} < 0.03$. At these low relative densities, elastic buckling of the cell walls is expected to control the shear strength of the square honeycombs. Note that experiments at such low relative densities are impractical for usual laboratory testing: for wall thickness of, for example, $t = 0.30$ mm, the cell size of a $\bar{\rho} = 0.03$ honeycomb is 20 mm. Figure 10b shows a comparison between the measurements and predictions of

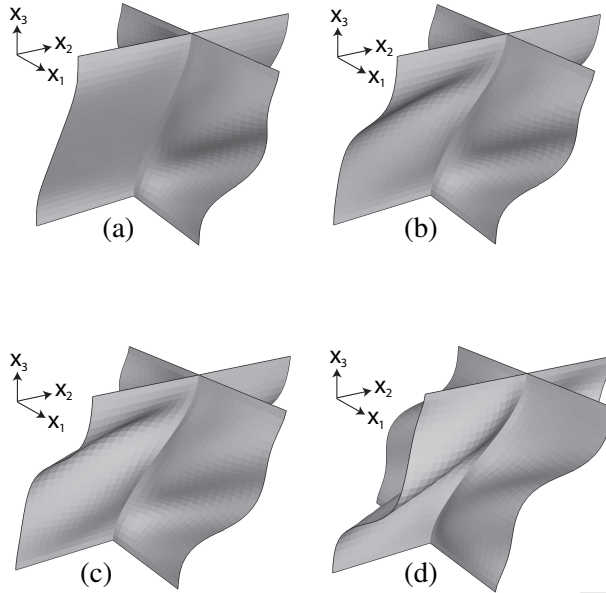


Figure 11. Finite element predictions of the deformation mode of the $\bar{\rho} = 0.05$ square honeycomb at a shear strain $\gamma_{3n} = 0.4$ for loading in the (a) $\omega = 0^\circ$, (b) $\omega = \tan^{-1}(1/4)$, (c) $\omega = \tan^{-1}(1/2)$, and (d) $\omega = \pi/4$ directions.

the shear strength τ_{3n}^y at a shear strain $\gamma_{3n} = 0.05$ for the $\bar{\rho} = 0.05$ square honeycombs, as a function of the loading angle ω . We observed excellent agreement between the measurements and both the FE and analytical predictions.

Figure 11 shows the FE predictions of the deformation modes of the $\bar{\rho} = 0.05$ square honeycomb at an applied shear strain $\gamma_{3n} = 0.4$ for the four loading directions studied experimentally. Consistent with the experimental observations, the degree of wrinkling of the cell walls parallel to the x_2 axis increases with increasing ω as the applied load is more evenly distributed between the cell walls of the square honeycomb.

In the FE calculations we assumed that the traction T_3 vanishes, with unconstrained straining of the specimen in the x_3 -direction. Specimen end effects in the single-lap shear test configuration mean that this boundary condition is not satisfied over the full length of the test specimens. To assess the significance of the constraint to straining in the 3-direction imposed in the single-lap shear configuration, we compare the measurements and FE predictions of the strain ε_{33} for the $\bar{\rho} = 0.04$ square honeycomb specimen tested in the $\omega = 0^\circ$ direction. The strain ε_{33} from experiments was evaluated from photographs taken at selected levels of applied shear strain. Figure 12 shows a plot of ε_{33} versus the applied shear strain γ_{31} . Good agreement between the FE predictions and measurements suggests that the $T_3 = 0$ boundary condition employed in the FE calculations is adequate to model our single-lap shear experiments.

4.2. Parametric finite element study. The FE model captures the experimental measurements within reasonable accuracy. Limitations on the specimen manufacturing and testing capabilities meant that we

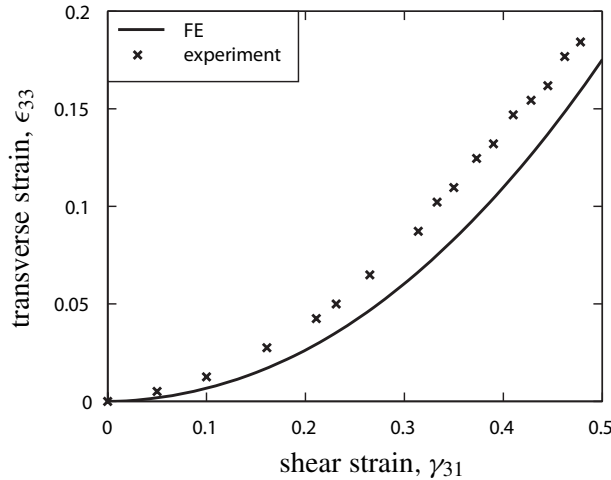


Figure 12. FE predictions and measurements of the through-thickness strain ϵ_{33} versus shear strain γ_{31} for a $\bar{\rho} = 0.04$ honeycomb loaded in the $\omega = 0^\circ$ direction.

did not investigate the effect of cell aspect ratio h/l on the shear response. Also, the effect of loading direction ω upon shear response was measured for a single value of relative density $\bar{\rho}$.

Figure 13a shows the FE predictions of the shear strength τ_{3n}^y at a shear strain $\gamma_{3n} = 0.05$ as a function of the cell aspect ratio h/l for three choices of loading angle ω , with $\bar{\rho}$ fixed at 0.05. The shear strength is only weakly dependent on h/l , with τ_{3n}^y decreasing by about 10% when h/l increases from 0.25 to 4. Note that the analytical model of Equation (7) predicts no dependence of τ_{3n}^y on h/l , which is why Figure 13a does not include these predictions. The effect of loading angle on the normalized shear strength $\tau_{3n}^y/(\bar{\rho}\sigma_y)$ is illustrated in Figure 13b for three choices of relative density $\bar{\rho}$. The FE calculations and analytical predictions of Equation (7) suggest that the shear strength is reasonably insensitive to the loading direction over the range of density $\bar{\rho}$ considered.

5. Comparison of the square honeycomb with competing sandwich cores

It is instructive to compare the shear strength of the stainless steel square honeycombs with competing cores. We were able to compare the measured shear strength of our stainless steel square honeycombs with data for commercially available aluminum hexagonal honeycombs, and with data for competing micro-architected sandwich cores also made from stainless steel.

The normalized shear strength $\tau^y/(\bar{\rho}\sigma_y)$ of 5052 H39 aluminum alloy hexagonal honeycombs manufactured by Hexcel Composites is plotted against relative density $\bar{\rho}$ in Figure 14a for loadings in two orthogonal directions. We assumed that the tensile yield strength of the parent aluminum is $\sigma_y = 255$ MPa, as reported by [Bhat and Wang 1990]. Our experimental measurements for the shear strength of the stainless steel square honeycombs are included in Figure 14a as well. Recall that we tested four relative densities for loading in the $\omega = 0^\circ$ direction, while the $\bar{\rho} = 0.05$ square honeycomb was tested in the $\omega = \pi/4$ direction. The shear strength τ^y is defined as the peak shear strength of the aluminum honeycombs. However, the stainless steel square honeycombs display no peak shear strength, so the

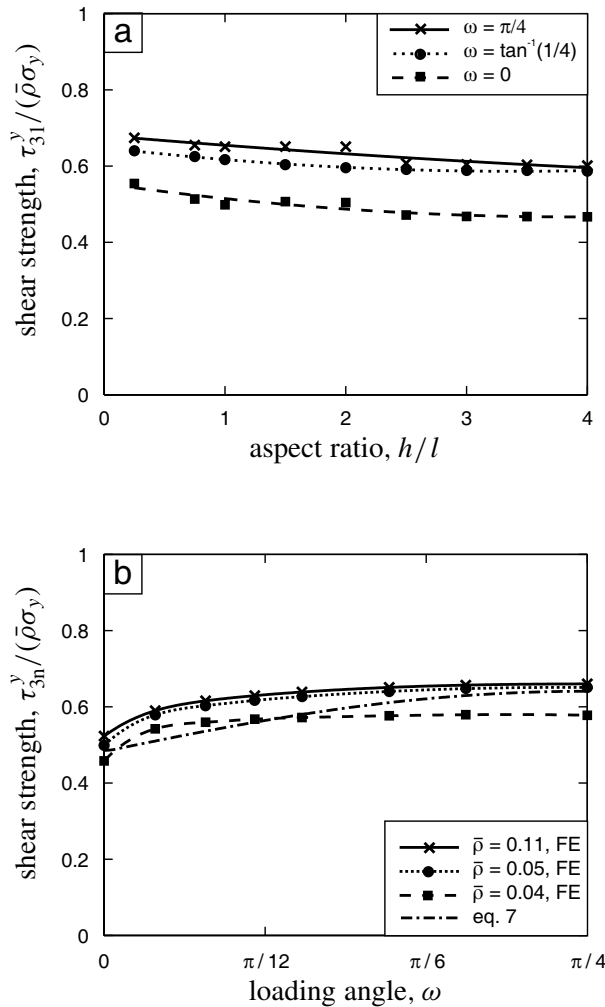


Figure 13. FE predictions of the shear strength of the stainless steel square honeycombs. (a) Shear strength τ_{31}^y at a shear strain $\gamma_{31} = 0.05$ versus cell aspect ratio h/l , for selected values of the loading angle ω , and $\bar{\rho} = 0.05$. (b) Shear strength τ_{3n}^y at a shear strain $\gamma_{3n} = 0.05$ versus loading angle ω , for selected values of $\bar{\rho}$.

shear strength τ^y is defined as the shear stress at a shear strain $\gamma = 0.05$. The normalized shear yield strength $\tau^y / (\bar{\rho}\sigma_y)$ of the stainless steel honeycombs is approximately equal to the Voigt upper bound value of 0.5 (assuming the Tresca yield criterion) over the full range of relative densities investigated here. The aluminum hexagonal honeycombs are clearly weaker especially for $\bar{\rho} < 0.06$.

Figure 14b illustrates the effect of the core topology upon out-of-plane shear strength τ^y . In the figure, the dependence of $\tau^y / (\bar{\rho}\sigma_y)$ upon the relative density $\bar{\rho}$ is given for the following cores:

- the stainless steel square honeycombs of the present study loaded in the $\omega = 0^\circ$ direction;
- stainless steel corrugated cores [Côté et al. 2006];

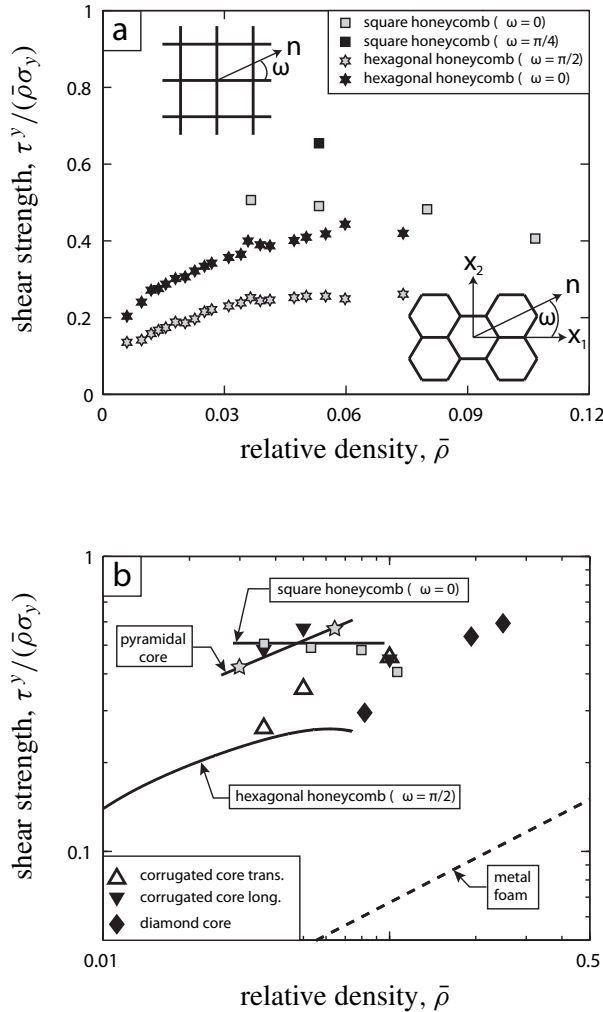


Figure 14. Comparison between the measured nondimensional shear strengths $\tau^y / (\bar{\rho} \sigma_y)$ of competing sandwich cores as a function of the relative density $\bar{\rho}$. (a) Comparison of aluminum hexagonal honeycombs with the stainless steel square honeycombs of the present study, and (b) comparison of stainless steel micro-architected sandwich core topologies.

- AL6XN stainless steel pyramidal cores [Zok et al. 2004; Côté et al. 2007];
- aluminum hexagonal honeycomb data ($\omega = \pi/2$) from Figure 14a; and
- aluminum alloy metal foams [Ashby et al. 2000].

The corrugated cores sheared in the longitudinal direction and the square honeycombs display no peak shear strength. Therefore, the shear strength τ^y in these cases is defined as the shear stress at a shear strain $\gamma = 0.05$. All other cores display a peak shear strength. In these cases we define τ^y as the peak strength.

The longitudinal shear strength of the corrugated core is comparable to that of the square honeycomb with $\tau^y/(\bar{\rho}\sigma_y)$ and is approximately equal to the upper bound value of 0.5 (assuming the Tresca yield criterion). In transverse shear, the corrugated and diamond cores are weaker than the square honeycomb.

6. Concluding remarks

We manufactured square honeycombs with a cell aspect ratio $h/l = 1$ by slotting together sheets of 304 stainless steel and then brazing the assembly. We then tested four relative densities of these honeycombs in out-of-plane shear in four loading directions. The measurements reveal that shear strength of the square honeycombs scales approximately linearly with the relative density $\bar{\rho}$ of the honeycomb. Moreover, the shear strength of these honeycombs is nearly isotropic.

A simple analytical model based upon uniform deformation of the cell walls is in good agreement with the measurements prior to wrinkling of the cell walls. A plastic buckling analysis predicts the onset of wrinkling with reasonable accuracy. FE calculations of the shear response of the square honeycombs agree with the test measurements, and show that the shear strength of the square honeycombs is relatively insensitive to the cell aspect ratio for aspect ratios in the range $0.5 \leq h/l \leq 4$.

The square honeycomb design exploits the strain hardening behavior of the parent material extremely efficiently in both out-of-plane compression [Côté et al. 2004] and in out-of-plane shear. In fact, the shear strength of these honeycombs is equal to that of the corrugated core sheared in the longitudinal direction. Unlike the corrugated core, which has a low transverse shear strength [Côté et al. 2006], the shear strength of the square honeycombs is nearly isotropic. Thus, square honeycombs have great potential for application in sandwich construction.

References

- [Ashby et al. 2000] M. Ashby, A. G. Evans, N. A. Fleck, L. J. Gibson, J. W. Hutchinson, and H. N. G. Wadley, *Metal foams: A design guide*, Butterworth Heinemann, Oxford, 2000.
- [ASTM 2000] “Standard test method for shear properties of sandwich core materials”, standard C273-00, American Society for Testing and Materials, 2000.
- [Bhat and Wang 1990] B. T. Bhat and T. G. Wang, “A comparison of mechanical properties of some foams and honeycombs”, *J. Mater. Sci.* **25**:12 (1990), 5157–5162.
- [Côté et al. 2004] F. Côté, V. S. Deshpande, N. A. Fleck, and A. G. Evans, “The out-of-plane compressive behavior of metallic honeycombs”, *Mater. Sci. Eng. A* **380**:1–2 (2004), 272–280.
- [Côté et al. 2006] F. Côté, V. S. Deshpande, N. A. Fleck, and A. G. Evans, “The compressive and shear responses of corrugated and diamond lattice materials”, *Int. J. Solids Struct.* **43**:20 (2006), 6220–6242.
- [Côté et al. 2007] F. Côté, N. A. Fleck, and V. S. Deshpande, “Fatigue performance of sandwich beams with a pyramidal core”, *Int. J. Fatigue* (2007). In press.
- [Doyoyo and Mohr 2003] M. Doyoyo and D. Mohr, “Microstructural response of aluminum honeycomb to combined out-of-plane loading”, *Mech. Mater.* **35**:9 (2003), 865–876.
- [Evans et al. 2001] A. G. Evans, J. W. Hutchinson, N. A. Fleck, M. F. Ashby, and H. N. G. Wadley, “The topological design of multifunctional cellular metals”, *Prog. Mater. Sci.* **46**:3–4 (2001), 309–327.
- [Fleck and Deshpande 2004] N. A. Fleck and V. S. Deshpande, “The resistance of clamped sandwich beams to shock loading”, *J. Appl. Mech. (ASME)* **71**:3 (2004), 386–401.
- [Gerard 1948] G. Gerard, “Critical shear stress of plates above the proportional limit”, *J. Appl. Mech. (ASME)* **15** (1948), 7–12.

- [Gibson and Ashby 1997] L. J. Gibson and M. F. Ashby, *Cellular solids, structure and properties*, 2nd ed., Cambridge University Press, Cambridge, 1997.
- [Hexcel 1999] “HexWeb honeycomb attributes and properties”, publication TSB-120, Hexcel Composites, Pleasanton, CA, 1999.
- [Kelsey et al. 1958] S. Kelsey, R. A. Gellatly, and B. W. Clark, “The shear modulus of foil honeycomb cores”, *Aircraft Eng.* **30** (1958), 294–302.
- [Mohr and Doyoyo 2004a] D. Mohr and M. Doyoyo, “Deformation-induced folding systems in thin-walled monolithic hexagonal metallic honeycomb”, *Int. J. Solids Struct.* **41**:11–12 (2004), 3353–3377.
- [Mohr and Doyoyo 2004b] D. Mohr and M. Doyoyo, “Experimental investigation on the plasticity of hexagonal aluminum honeycomb under multiaxial loading”, *J. Appl. Mech. (ASME)* **71**:3 (2004), 375–385.
- [Timoshenko and Gere 1963] S. P. Timoshenko and J. M. Gere, *Theory of elastic stability*, 2nd ed., McGraw Hill, New York, 1963.
- [Werren and Norris 1950] F. Werren and C. B. Norris, “Analysis of shear strength of honeycomb cores for sandwich constructions”, Technical Report 2208, NACA, 1950, Available at <http://hdl.handle.net/2060/19930082855>.
- [Xue and Hutchinson 2004] Z. Xue and J. W. Hutchinson, “A comparative study of impulse-resistant metal sandwich plates”, *Int. J. Impact Eng.* **30**:10 (2004), 1283–1305.
- [Zhang and Ashby 1992] J. Zhang and M. F. Ashby, “The out-of-plane properties of honeycombs”, *Int. J. Mech. Sci.* **34**:6 (1992), 475–489.
- [Zhuang and Eagar 1997] W. D. Zhuang and T. W. Eagar, “Transient liquid-phase bonding using coated metal powders”, *Weld. J.* **76**:4 (1997), 157s–162s.
- [Zok et al. 2004] F. W. Zok, S. A. Waltner, Z. Wei, H. J. Rathbun, R. M. McMeeking, and A. G. Evans, “A protocol for characterizing the structural performance of metallic sandwich panels: Application to pyramidal truss cores”, *Int. J. Solids Struct.* **41**:22–23 (2004), 6249–6271.

Received 17 Feb 2006. Accepted 12 May 2006.

FRANÇOIS COTE: fc248@eng.cam.ac.uk

Cambridge University Engineering Department, Trumpington Street, Cambridge, CB2 1PZ, United Kingdom

VIKRAM S. DESHPANDE: vsd@eng.cam.ac.uk

Cambridge University Engineering Department, Trumpington Street, Cambridge, CB2 1PZ, United Kingdom

NORMAN A. FLECK: naf1@eng.cam.ac.uk

Cambridge University Engineering Department, Trumpington Street, Cambridge, CB2 1PZ, United Kingdom

SUBMISSION GUIDELINES

ORIGINALITY

Authors may submit manuscripts in PDF format on-line. Submission of a manuscript acknowledges that the manuscript is *original and has neither previously, nor simultaneously, in whole or in part, been submitted elsewhere*. Information regarding the preparation of manuscripts is provided below. Correspondence by email is requested for convenience and speed. For further information, consult the web site at <http://www.jomms.org> or write to

Marie-Louise Steele

Division of Mechanics and Computation
Durand Building, Room 262
Stanford University
Stanford CA 94305

LANGUAGE

Manuscripts must be in English. A brief abstract of about 150 words or less must be included. The abstract should be self-contained and not make any reference to the bibliography. Also required are keywords and subject classification for the article, and, for each author, postal address, affiliation (if appropriate), and email address if available. A home-page URL is optional.

FORMAT

Authors are encouraged to use L^AT_EX and the standard article class, but submissions in other varieties of T_EX, and, exceptionally in other formats, are acceptable. Electronic submissions are strongly encouraged in PDF format only; after the refereeing process we will ask you to submit all source material.

REFERENCES

Bibliographical references should be listed alphabetically at the end of the paper and include the title of the article. All references in the bibliography should be cited in the text. The use of B^IB_T_EX is preferred but not required. Tags will be converted to the house format (see a current issue for examples), however, in the manuscript, the citation should be by first author's last name and year of publication, e.g. "as shown by Kramer, et al. (1994)". Links will be provided to all literature with known web locations and authors are encouraged to provide their own links on top of the ones provided by the editorial process.

FIGURES

Figures prepared electronically should be submitted in Encapsulated PostScript (EPS) or in a form that can be converted to EPS, such as GnuPlot, Maple, or Mathematica. Many drawing tools such as Adobe Illustrator and Aldus FreeHand can produce EPS output. Figures containing bitmaps should be generated at the highest possible resolution. If there is doubt whether a particular figure is in an acceptable format, the authors should check with production by sending an email to

production@mathscipub.org

Each figure should be captioned and numbered so that it can float. Small figures occupying no more than three lines of vertical space can be kept in the text ("the curve looks like this:"). It is acceptable to submit a manuscript with all figures at the end, if their placement is specified in the text by comments such as "Place Figure 1 here". The same considerations apply to tables.

WHITE SPACE

Forced line breaks or page breaks should not be inserted in the document. There is no point in your trying to optimize line and page breaks in the original manuscript. The manuscript will be reformatted to use the journal's preferred fonts and layout.

PROOFS

Page proofs will be made available to authors (or to the designated corresponding author) at a web site in PDF format. Failure to acknowledge the receipt of proofs or to return corrections within the requested deadline may cause publication to be postponed.

Journal of Mechanics of Materials and Structures

Volume 1, N^o 7 September 2006

- Antiplane deformation of orthotropic strips with multiple defects**
REZA TEYMORI FAAL, SHAHRIAR J. FARIBORZ and HAMID REZA DAGHYANI 1097
- Switching deformation modes in post-localization solutions with a quasibrittle material**
PIERRE BÉSUELLE, RENÉ CHAMBON and FRÉDÉRIC COLLIN 1115
- Incremental modeling of T-stub connections** MINAS E. LEMONIS and CHARIS J. GANTES 1135
- Effect of the order of plates on the ballistic resistance of ductile layered shields perforated by nonconical impactors**
G. BEN-DOR, A. DUBINSKY and T. ELPERIN 1161
- A numerical investigation of the effect of boundary conditions and representative volume element size for porous titanium**
HUI SHEN and L. CATHERINE BRINSON 1179
- Damage in domains and interfaces: a coupled predictive theory**
FRANCESCO FREDDI and MICHEL FRÉMOND 1205
- Elastic flexural-torsional buckling of circular arches under uniform compression and effects of load height**
MARK ANDREW BRADFORD and YONG-LIN PI 1235
- Transient analysis of a suddenly-opening crack in a coupled thermoelastic solid with thermal relaxation**
LOUIS MILTON BROCK and MARK TODD HANSON 1257
- 3D Green's functions for a steady point heat source interacting with a homogeneous imperfect interface**
X. WANG and L. J. SUDAK 1269
- The shear response of metallic square honeycombs**
FRANÇOIS COTE, VIKRAM S. DESHPANDE and NORMAN A. FLECK 1281